Design of molecules and materials for applications in clean energy, catalysis and molecular machines through quantum mechanics, molecular dynamics and Monte Carlo simulations

Thesis by

Jose L. Mendoza-Cortes

In Partial Fulfillment of the Requirements
for the Degree of
Doctor of Philosophy

California Institute of Technology
Pasadena, California

2012
(Defended May 17 2012)

Dedicated to:

Azucena A. Cortes-Gaspar

Acknowledgments

I am in debt to my advisor Prof. William A. Goddard for his patience and discussions during my doctoral studies. I am deeply thankful to him for allowing me to pursue an independent way of doing research and showing me how to be a better scientist.

I would like to thank also many collaborators during these years: Prof. Omar M. Yaghi, Dr. Hiroyasu Furukawa, Dr. Ravinder Abrol, Dr. Andres Jaramillo-Botero, Dr. Robert Nielsen, Dr. Tod A. Pascal and Prof. Theodor Agapie. I learnt many things about science through discussions with them.

My special thanks to Prof. Yaghi, who has been an exemplary scientist and helped me to improve as a scientist. I also would like to thank Dr. Furukawa who was patient and tough enough with his vast experience.

I would like to acknowledge some of my colleagues for fruitful discussions about different scientific topics; Dr. Jamil Tahir-Kheli, Wei-Guang Liu, Ted Yu, Fan Liu, Ross Fu, Jacob Kanady, Emily Y. Tsui, Vaclav Cvicek and Hai Xiao. It is amazing how much you can learn by discussing with your colleagues.

Also I would like to thank the support of my friends over the years; there are many of them spread over the world but specially Jorge Cholula, currently in Germany and Naoki Aratani from Japan. I would like to thank Ernie Mercado for allowing me to have some Mexican food on campus.

My gratitude to the California Institute of Technology which provided me with fellowship during my first year and also to the Roberto Rocca Program for providing support for two years.

Finally I would like to acknowledge my mother Azucena A. Cortes-Gaspar and Yuan Liu for being a great support in my life.

Abstract

We use a multiparadigm, multiscale strategy based on quantum mechanics (QM), first-principles QM-based molecular mechanics (MD) and grand canonical Monte Carlo (GCMC) to rationally design new molecules and materials for clean energy (H_2 and CH_4 storage), catalysis (O_2 evolution, metal-organic complexes) and molecular architectures (rotaxanes, hydrogels). This thesis is organized in seven chapters and shows that it is crucial to understand the scale of the system to be studied, the insight obtained can be used to rationally design new molecules and materials for desirable applications; as well as to guide and complement experimental studies. Chapter 1 discusses the specific details of the proposed methodology, including the theoretical underpinning of each modeling paradigm, potential limitations, and how we use these for in silico characterization and design optimization. Chapter 2 covers the structure prediction and characterization of metal-organic complex arrays (MOCA) through QM and force-field-based molecular mechanics. The methodology is inspired by the approach used for enzymatic systems, considering that experimentally determining their three-dimensional structure remains an open challenge. Chapter 3 describes the use of transition state theory for the calculation of reaction rates in polymer hydrogel network formation. This enables the determination of optimum concentrations for polymerization reactions and preparation of coarse-grained force fields. Chapter 4 describes the work performed on Stoddard's rotaxane dumbbells, where we explained origin for the template-directed synthesis through QM-derived free energies. We also give a consistent explanation for the role of the counter anion. Chapter 5 presents the simulation results for a tetranuclear cluster model for O_2 evolution, based on $CaMn_30_4$ and Mn_4O_4 clusters. We demonstrate how to calculate their oxidation potentials and propose new molecular designs that resemble the oxygen evolution complex (OEC) both structurally and electronically. Chapter 6 presents our findings for CH_4 storage. Using a second-order Møller-Plesset perturbation theory force field and GCMC we propose a framework for optimal delivery. Chapter 7 presents our designed materials for hydrogen storage and the validation of our methodology against experimental results. We based our predictions in QM and GCMC calculations through the development of our own first-principles vdW force field. Our results demonstrate novel frameworks capable of achieving the DOE energy density target for 2015. Finally, we show the generalization of adsorption phenomena for any porous material based on topological constraints.

Contents

List of Tables

List of Figures

Chapter 1

Introduction

The intention of this chapter is to give the reader a short introduction to the theory involved in the simulations described in every chapter. For a broader description of the theory the reader is encourage to consult the books by Jensen and the one by Cramer.[1, 3]

Our understanding of particles moving started with Newton's three laws and more specifically his second law:

$$\mathbf{F} = ma.$$

From this point of view we learned that since $\mathbf{p} = m\mathbf{v}$ then,

$$\mathbf{F} = \frac{d\mathbf{p}}{dt} = m\frac{d\mathbf{v}}{dt} = m\mathbf{a}$$

and we assumed at the time that $m = constant$. We also thought that we could predict the trajectory/interaction of every particle of the universe back and forward if we could determine the position and momentum at a given time in space of each one. However there were two revolutions that changed this view, the relativistic theory by Einstein and quantum mechanics.

The relativistic theory by Einstein found that at high velocities mass is no longer a constant, and that the maximum velocity any particle can reach is the velocity of light (c). This can be abstracted in the following equation:

$$m = \frac{m_0}{\sqrt{1 - v^2/c^2}}$$

where m_0 is the mass at rest, v the velocity of the particle and m is now the relativistic mass.

Quantum mechanics was the second revolution, and this theory was developed when the so-called classical mechanics theory of Newton/Einstein could not explain the phenomenon of small particles, such as the spectra of the hydrogen atom. The foundation of the old theory was that the energy was a continuum. It turned out that when the particles are small (as with electrons), other forces prevail in the interaction and another theory is needed. The explanation was then quantum mechanics, which at low velocities is represented in the Schrödinger equation:

$$\mathbf{H}\Psi = i\frac{d\Psi}{dt}$$

where

$$\mathbf{H} = \left(\frac{\mathbf{p}^2}{2m}\right) + \mathbf{V}.$$

This theory was further developed to include the relativistic postulate of Einstein. This was done by Dirac and the equation resembles the one at low velocities:

$$\mathbf{H}\Psi = i\frac{d\Psi}{dt}$$

but with a difference in the expression for the Hamiltonian operator:

$$\mathbf{H} = (c\boldsymbol{\alpha} \cdot \mathbf{p} + \boldsymbol{\beta} mc^2) + \mathbf{V}.$$

In here, the $\boldsymbol{\alpha}$ and $\boldsymbol{\beta}$ are 4×4 matrices and thus the relativistic wave function has three components. In the limit of $c \to \infty$, the Dirac equation reduced to the Schrödinger equation and the large components of the wave function reduce to the α and β spin-orbitals.[1]

From these equations, in principle, we could calculate all the kinetics of any one particle. However, there is the three-body problem, which means that we can solve analytically the expression for the interaction of two particles, but that if we have three particles, the equations are no longer solvable by exact methods, only by approximate methods. This is a big drawback to the initial belief that we can calculate all the interactions of all particles. All this view is syntesized in Figure 1.1a. It is commonly understood that relativistic effects started to be observed at 1/3 c and that quantum effects started to be observed at 1 atomic mass unit (amu).

Many techniques have been created to get to a certain degree of accuracy to a solution to the many-body problem. These techniques are created by using the formulas for classical and quantum mechanics and the power of computers to numerically calculate many interactions. Techniques in the domain of classical mechanics are included within the so-called molecular dynamics (MD) or molecular mechanics (MM), which basically uses Newtons equations, and treats every part with a model of balls and strings with a potential assigned to every interaction. Techniques in the domain of quantum mechanics include: the Hartree-Fock method (HF), density functional theory (DFT), Møller-Plesset perturbation theory (MP2,MP3,..), coupled cluster (CC), configuration interaction (CI), and so on. They use basis sets or plane waves to represent electrons and protons.[1, 3]

These are methods to calculate interaction between particles and the equation of motion. Now we will use these expressions to calculate the energy at different temperatures, and thus the entropy.

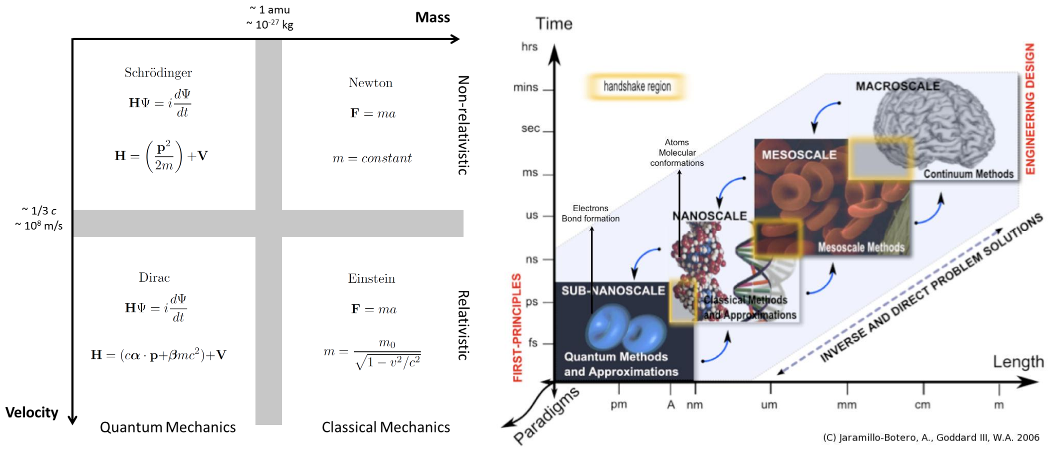

(a) Mass versus Velocity (b) Length versus Time

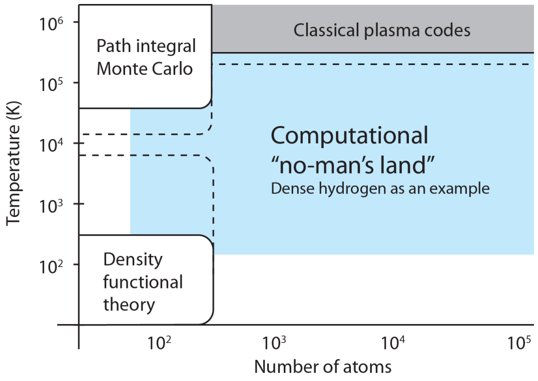

(c) Temperature versus number of atoms

Figure 1.1: Theoretical multiparadigms. (a) was adapted from [1], (b) is courtesy of Julius Su, and Part (c) is courtesy of Andres Jaramillo-Botero.

Entropy(S) is defined as the logarithm of the number of states accesible(g) to the system ($S = k_B \log g$). Thus the more states are available the higer the entropy. At absolute zero temperature, the ground state multiplicity ($g(0)$) has a well-defined multiplicitly. From the quantum point of view, at absolute zero the system is in its lowest sets of quantum states. And, the relation between temperature and entropy is given by $1/T = (\partial S/\partial U)_{N,V}$.[4] Therefore, at room temperature we can reduce the macroscopic problem two variables; length and time where the corresponding number of particles increase as shown in Figure 1.1b. If a higher temperature is used and the number of particles is increased, where the time is still in the nanosecond range, then the paradigms changes as it is shown in Figure 1.1c.

Now we review briefly some concepts of statistical mechanics to obtain temperature dependence. An statistical ensemble represents a probability distribution of microscopic states of the system. For a system taking only discrete values of energy, the probability distribution is characterized by the probability π_i of finding the system in a particular microscopic state i with energy level

E_i. Finding the probability distribution will give us the answer about the mean of any quantity (ensemble average) we want to know from the system. Since the ensemble average is dependent on the ensemble chosen, the expression is different and we show such properties on Table 1.1.

However, the mean obtained for a given physical quantity doesn't depend on the ensemble chosen at the thermodynamic limit. In this expression the denominator is known as the partition function and to obtain is the main goal of methods such as molecular dynamics trajectories or Monte Carlo methods. The denominators on Table 1.1; Ω, Q, Ξ and Δ are the partition function for each ensemble. This function allows us to calculate all the thermodynamically properties under the conditions of the ensemble. The derivation and expression of the partition function for each ensamble is beyond the scope of this chapter but there are many resources where this can be found.[5, 4]

Table 1.1: Ensembles for statistical mechanics. E stands for energy of the state; T, temperature; V, volume; N, number of particles; μ, chemical potential. β is given by $1/(kT)$, where k is the Boltzmann constant. The denominators Ω, Q, Ξ and Δ are the partition functions for each ensemble.

Ensemble	Independent variables	Probability distribution
Microcanonical	(E,V,N)	$\pi_i = \frac{1}{\Omega}$
Canonical	(T,V,N)	$\pi(E_i) = \frac{1}{Q} e^{-\beta E_i}$
Grand Canonical	(T,V,μ)	$\pi(E_i, N_i) = \frac{1}{\Xi} e^{-\beta(E_i + \mu N_i)}$
Isothermal isobaric	(T,P,N)	$\pi(E_i, V_i) = \frac{1}{\Delta} e^{-\beta(E_i + PV_i)}$

In Chapter 2, we use Molecular Mechanics (MM) combined with Quantum Mechanics (QM) to calculate different energies of structures. In Chapter 3, we use QM to calculate transition states and develop a coarse grained force field for molecular dynamics (MD). Chapters 4 and 5 uses QM based methods to predict the energetics of different molecules such as redox potential and electronic configurations. Finally, in Chapter 6 and Chapter 7, we use QM to calculate the interaction potential for many molecular components and then we use the Grand Canonical ensemble to obtain the number of interacting particles for a given chemical potential.

The highlight of Chapter 2 is that we can predict structures for this future catalyst and we enumerate the characteristics of the building parts in order to have a two- or three-centered reaction center. The most important results that we found in Chapter 3 is that we can predict the reactions rates for cross linking polymers and this can be compared to the brute-force coarse grained force field.

In Chapter 4 present the origin of the positive cooperativity with the results obtained from free energy. The origin is the optimal distance between the rotaxanes rings which allows them to interact to get positive cooperativity in the template-directed formation of these rotaxane/dumbbell complexes. We also found that the role of the counter anion is to tune the charge population on the -NH_2^+- recognition site so that the larger (softer) the counter anion the more charge on the recognition site and the more interaction with the rotaxane ring is obtained. The interaction with the recognition site serves as the first directed template mechanism (clipping) for the formation of the rotaxane rings. This has many implications for the future synthesis of rotaxanes because we predict that we can control the positive cooperativity by changing the charge population on the recognition site by tuning the softness of the counter anion.

In Chapter 5, presents new models that have oxidation states that are similar to the S_0, S_1 and S_2 states of the biological oxygen evolution complex (OEC). We have accomplished these different electronic states by modifying the original host ligand or by adding common linkers such as bipyridine or acetylacetonate. Thus we show that we can obtain compounds that resemble the OEC both structurally and electronically.

In chapter 6, I validated our methodology by comparing with experiments (Figure 1.2). I also report for the first time the methane uptake for benchmark MOF-177. Along the way I investigated for the first time the sorption mechanism by studying the ensemble for the methane uptake in Covalent-Organic Frameworks (COFs).

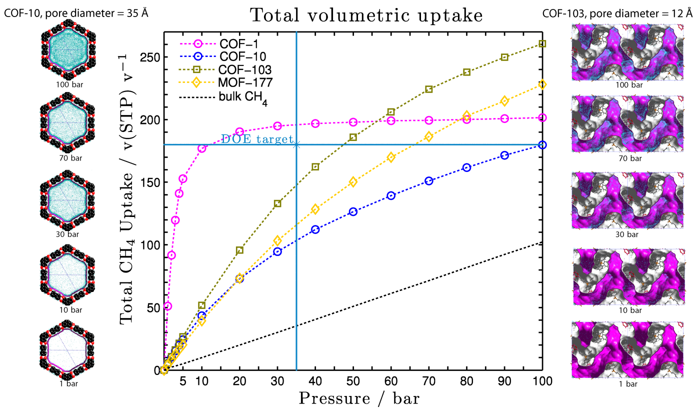

Figure 1.2: Uptake for CH_4 for COFs and MOFs and observation of the sorption mechanism for the uptake

In the second part of this chapter (Figure 1.3) I present predictions for new COFs that have an optimal structure for methane uptake that reach the DOE target. I calculate the uptake up to 300 bar and found that two new structures COF-102-Ant and COF-103-Eth-trans have an optimal pore diameter for an optimal delivery amount of methane.

In Chapter 7, I present for the first time the H_2 uptake for the new generation of Metal-Organic Frameworks and we compare them to the most representative COFs (Figure 1.4). I then propose a method to increase the H_2 uptake at room temperature by metaling the organic linkers with alkaline metals. I found that MOF-200-Li and COF-102-Li reach the 2015 DOE target. In the second part of this chapter we present another metalation strategy using transition metals (TM). I found that for delivery amount (real amount usable) metalation is another option to obtain higher binding energy

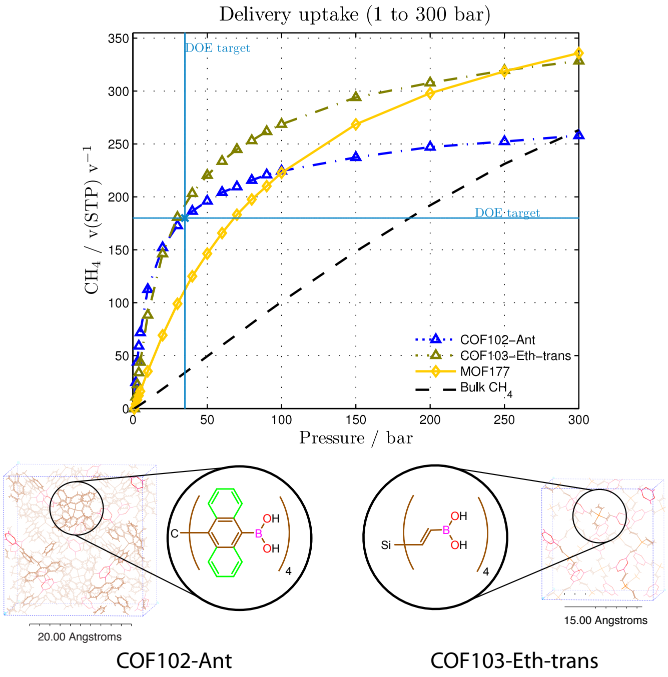

Figure 1.3: The design of two new COFs that overcome the DOE target at room temperature. They perform better than MOF-177, currently on the market.

with H_2. I use Quantum Mechanical calculations to obtain the binding energy and to predict a new strategy to metalate ligand sites.

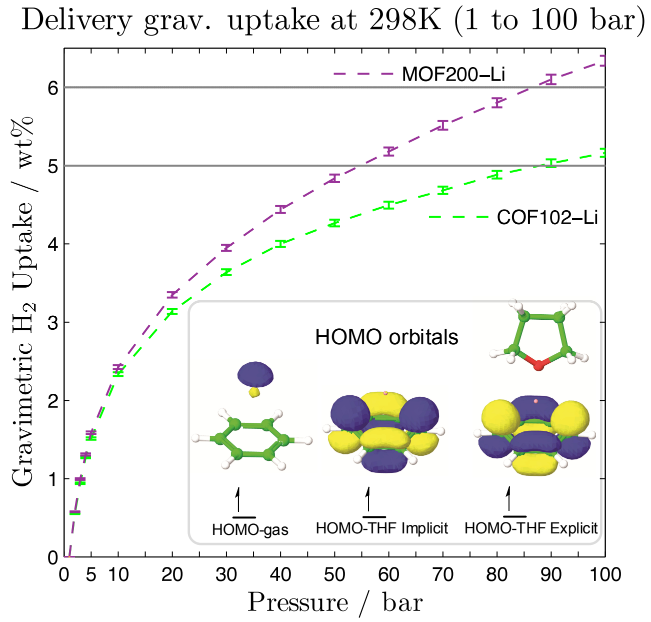

Figure 1.4: MOF200-Li and COF102-Li reach the 2015 DOE target.

Chapter 2

Prediction of Structures of Metal-Organic Complex Arrays (MOCA)

Jose L. Mendoza-Cortes, Vaclav Cvicek, Ravinder Abrol, William A. Goddard III

2.1 Introduction

We implement two methods with the objective of finding the most stable conformational state of the structures denominated as metal-organic complex arrays (MOCA). The main objective is to understand such possible structures in order to predict possible enzymatic activity.

MOCA are terpyridine appended and L-tyrosine protected with Fluorenylmethyloxycarbonyl (Fmoc) molecules that are metalated selectively with Pt(II), Rh(III) or Ru(II) ions. These building block then are assembled into a sequence using protocols of solid state peptide synthesis.[6]

The structures that are available experimentally are mono-, di-, tri-, tetra-, penta- and hexamers containing one of the three previously selected transition metals.[6] The structures used in this study are shown in Figure 2.1. However the 3D coordinates of such structures are not available experimentally. Such knowledge is important because we can predict the possible catalytic activity due to the folding of structure and possible accessible sites for a specific molecule. The structure can be studied by NMR but the 3D-dimensional coordinates can be very challenging due to the difficulty in crystalizing such molecules.

This chapter is divided in two parts; each part offers a different approach to the problem. The first part uses a quantum mechanics – molecular mechanics (QM/MM) approach, while the second part uses a method inspired from enzyme structure prediction.

2.2 Method I: QM/MM

Method I uses a hybrid method combining quantum mechanics (QM) and molecular mechanics (MM). It is important to mention that we are not interested in the boundary between the QM and MM Hamiltonian; we are only interested in the bonding and position of the monomers. Therefore, this method is a simple generation of the coordinates around the metal with QM, while the rest is handled by MM (Figure 2.1).

2.2.1 Methodology

Quantum Mechanics (QM). We used density functional theory (DFT) with a functional that has been corrected for dispersion interaction: M06-2X[7]. In some cases we used B3LYP[8] hybrid DFT functional as comparison. All the calculations we performed in the Jaguar code.[9] Here we used the 6-31G** basis set. We used mainly M06-2X because it gives the best estimation for $\pi - \pi$ interaction energies and in this problem we will have many such interactions. For the TM we used the Los Alamos LACVP**++, which includes relativistic effective core potentials.[10] The unrestricted open-shell procedure for the self-consistent field calculations was used. All geometries were optimized using the analytic Hessian to determine that the local minimum has no negative curvatures (imaginary frequencies).

Molecular Mechanics (MM). During minimization the organics were optimized with universal force field (UFF) [11] but the QM structures were kept constant. We use a cutoff of 12 Å, for the noncovalent interactions. The charges used for the QM part are the Mulliken charges; while the MM part is from the QeQ calculations.[12]

2.2.2 Quantum Mechanical Calculations

We first optimize the geometries from QM for the metal centers. We realized that there are only three metallic centers needed to construct all the present MOCA. These units are shown in Figure 2.2. It is important to note that these structures have charges due to the metallic center, and the counter anion is present in the liquid solution. However, in our calculations in the gas phase of these complexes we use a total charge of +1 for Pt, 0 for Rh and +2 for Ru. This way our optimization reaches equilibrium faster and we do not have to deal with the different configuration interactions that the counter anion could have with the metallic complex. The charge is dispersed over the entire structure and this is close to have a soft anion such as $CO_2CF_3^-$. Thus we do not expect to have a major difference in the structure versus using explicit counter anion.

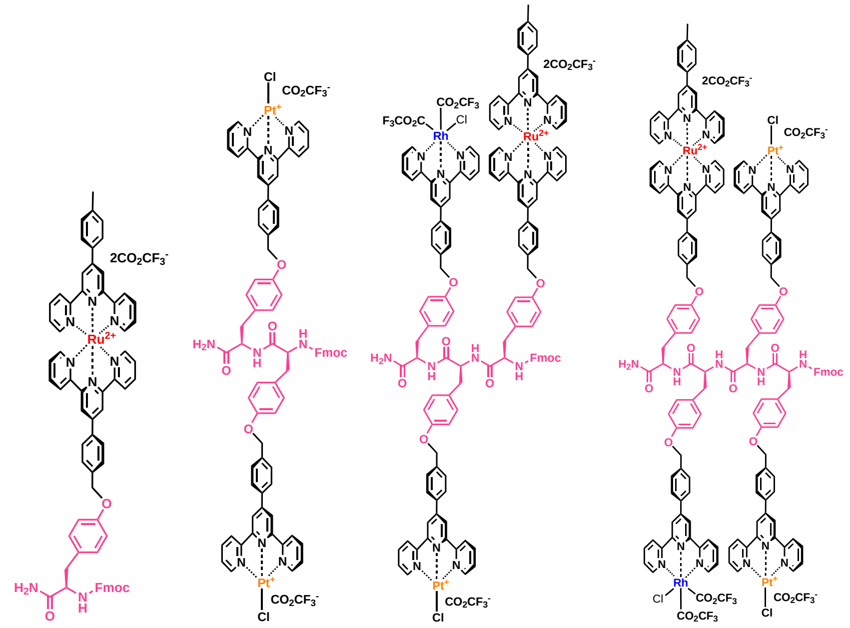

(a) Compound A (b) Compound B (c) Compound C (d) Compound D

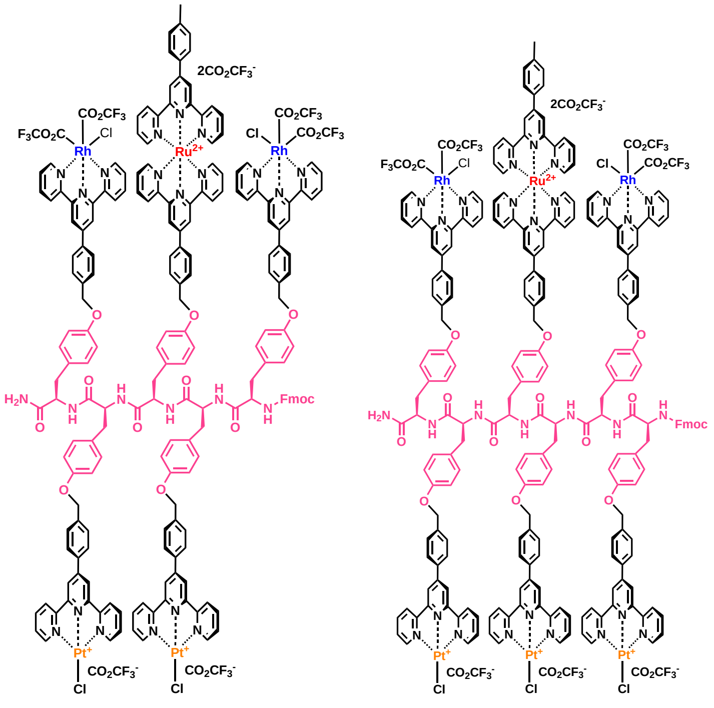

(e) Compound E (f) Compound F

Figure 2.1: Metal-organic complex arrays (MOCA). QM was used for the black part, including the metal. MM was used for the pink part. Fmoc stands for fluorenylmethyloxycarbonyl.

2.2.2.1 The case of Platinum (Pt)

The first compound we studied was the Pt complex. We started by optimizing the structure with our QM method and we checked that there were not imaginary frequencies. Once we reached the

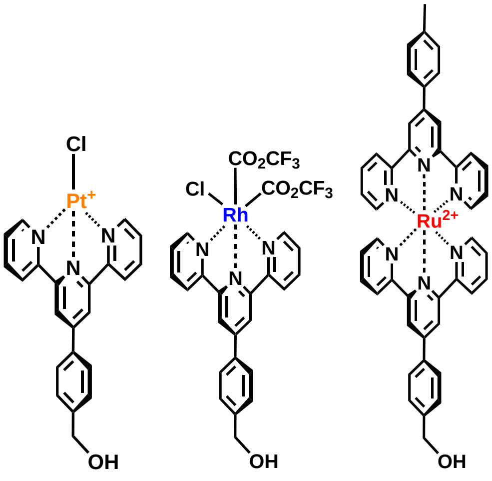
(a) Pt (b) Rh (c) Ru

Figure 2.2: Structures used for the QM calculations. For the calculations in gas phase we did not use the counter anion but the absolute charge that is shown.

optimized structure we realized that we might have obtained a local minimum. This compound has two main degrees of freedom: the dihedral angles between the benzenes (CCCC) and the one including a benzene and the OH (CCCO). Such dihedrals are illustrated in Figure 2.3.

In order to find the global minimum we assume that the dihedral conformer would be the major differentiator. Thus we carried a coordinate scan for these dihedral angles, each step of 30°.

The first dihedral angle studied is the CCCC angle. The results are shown in Figure 2.3a and b. The plot suggests that the most stable configurations are at 30, 150, 210 and 330°. We can see that the barriers are different between 30 and 150° versus 150 and 210°. For the first one we have a high barrier of 3.5 kcal/mol while for the second one we have a barrier of 2.1 kcal/mol. The same values are repeated for the 210 and 330° and for 330 and 30°. We would expect to see only one type of barrier but this suggests that the OH might be playing a role. This is a low-resolution scan to give us an idea of the kind of energy surface for this degree of freedom. Next we optimize the structure starting with the dihedral angle mentioned before. For a specific example, we arbitrarily start with the 330° and find that optimized structure has a value of 324°. For our purposes the plot suggests that the profile for the 4 states is equivalent and we do not need to optimize this dihedral angle to a higher resolution. This information can be stored in our structure generator code to give the same probability to each of these angles.

Secondly, we studied the CCCO dihedral as shown in Figure 2.3c and the results are shown in Figure 2.3d. We used the same procedure as for CCCC and we found a more standard dihedral profile: one type of barrier with three equivalent angles. We can see from the plot that under consideration of the resolution of the conformer scan, there are two equivalent angles at 0 and 180° (where the angle at 0° is the same as at 360°.) Each of these has a difference of 0.1 kcal/mol.

The barrier for the dihedral rotation is 2.6 kcal/mol. This is intermediate to the one obtained for the CCCC dihedral. This can be understood as the OH wanting to be in the same place as the benzene since the free electrons of the oxygen atom can interact with the π electrons from the benzene ring. To make sure that we found the correct angles we performed an optimization of the structure, arbitrarily choosing the 0°. The optimized structure had a value of 1.1° suggesting that our resolution is good enough to use these three angles as equivalent in our generator of structures.

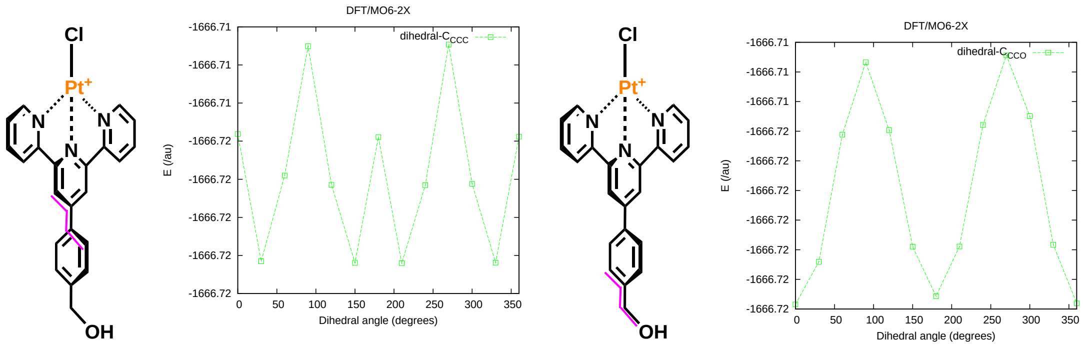

(a) Dihedral (b) Dihedral CCCC (c) Dihedral (d) Dihedral CCCO

Figure 2.3: Coordinate scan for the dihedrals CCCC and CCCO of the Pt case. The pink lines indicate the dihedral angle used.

2.2.2.2 The case of Rhodium (Rh)

The next case we study is the Rh complex. This particular complex can have two isomers due to one Cl^- and two $CO_2CF_3^-$. QM calculations with MO6-2X and B3LYP were performed to discern which isomer is the most stable. The results are shown in Table 2.1. We found that the most stable isomer is the *cis* conformation by more than 10 kcal/mol. When we observed the optimized structure of the *cis* configuration we found there is an interaction between the C-H from one of the pyridines and the O from the ester of the equatorial $CO_2CF_3^-$ groups at a distance of 2.17 Å. The Mulliken charge on the H is of +0.22 and the O is -0.45. The atomic electrostatic potential charge (ESP) for the H is +0.20 and for the O is -0.52. This interaction can be characterize it as a hydrogen bond with a C-H···O nature.[13, 14] Thus we used the *cis* isomer for all the following calculations.

Table 2.1: DFT energies for the Rh *cis* and *trans*

Functional	E_{cis} (kcal/mol)	E_{trans} (kcal/mol)
MO6-2X	0.0	12.1
B3LYP	0.0	10.3

We then proceeded to find the most stable configuration for the two dihedral angles present in the linker. The linker is the same as the one used for Pt^{+1}, however this time the metal center, Rh, has a formal charge of zero.

The first dihedral we calculated is the CCCC of the adjacent benzene ring, as it is shown in Figure 2.4a. The result for the scan is shown in Figure 2.4b and it was as we expected: similar to the Pt^{+1} case, with four major local minima. However, for this case we found that all the barriers are basically equivalent (2.7 kcal/mol) and the local minima are similar (different by 0.5 kcal/mol). The barrier for the Rh case is smaller compared to the highest barrier (3.5 kcal/mol) and larger than the lowest barrier (2.1 kcal/mol) of the Pt^{+1} case. We should remember that the resolution to explore this dihedral was of a 30° step. Therefore we use 30, 150, 210 and 330° dihedrals as equivalent in our structure generator code.

Our next explored dihedral CCCO is shown in Figure 2.4c. We expected this profile for Rh(0) to be similar to the one obtained for Pt^{+1}. We observed such a case; however this time we calculated a higher-resolution energy profile. We measured the energy every 10°. The results are shown in Figure 2.4d. As we can see, the dihedral has two equivalent barriers but this depends on the initial state. That is, from 0 to 90° the barrier is 1.9 kcal/mol, but if we start from 180° then the barrier to either 0 or 360° is 2.1 kcal/mol. These barriers are smaller than the Pt^{+1} case of 2.6 kcal/mol. This is still within the intrinsic error of our QM calculations because the state at 0 and 180° differ by only 0.2 kcal/mol. It is important to mention that with our current approach we get an equivalent energy between 170, 180 and 190°. All these angles, 0, 170, 180 and 190 have the same probability of being generated when used in our random structure generator.

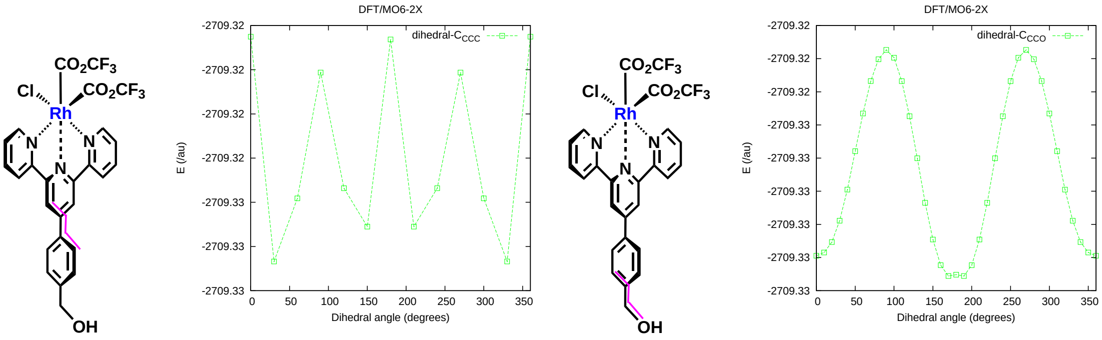

(a) Dihedral (b) Dihedral CCCC (c) Dihedral (d) Dihedral CCCO

Figure 2.4: Different dihedral angles tested for the Rh complex. The pink lines indicate the dihedral angle used.

2.2.2.3 The case of Ruthenium (Ru)

The last unit we studied was the Ru^{+2} case. We followed the same procedure as the one used for Pt^{+1} and Rh(0). For this compound we have two linkers that differ only on the tails, CH_2OH versus CH_3. Therefore we have three different dihedral angles.

The first dihedral angle we studied was the CCCC formed by the pyridine and benzene group as shown in Figure 2.5a. Our QM results for this scan are shown in Figure 2.5b. As we can see, the profile is very similar to the one we encountered in the Pt^{+1} case with two kinds of barriers. We found four minima which are at 30, 150, 210 and 330° and we found two barriers. The first barrier of 3.6 kcal/mol is between 30 and 150°(repeated between 210 and 330°) and the second barrier of 2.5 kcal/mol is between 150 and 210° (repeated between 330 and 30°). These are similar in magnitude to the barriers calculated for the Pt^{+1} compound: 3.5 and 2.1, respectively.

We also explored the energetics of the other CCCC dihedral bond as it is shown in Figure 2.5c. The results are almost identical to the former CCCC dihedral of the same compound, as we should expect, and this is shown in Figure 2.5d. There are four minima at 30, 150, 210 and 330°. There are also two kinds of barrier, a high barrier of 3.6 kcal/mol (between 30–150°, as well as in between 210–330°) and a low one of 2.3 kcal/mol (between 150–210° and in between 330 and 30°). As we expect, it is basically the same as the dihedral CCCC shown in Figure 2.5a and b. Therefore all these angles are used as equivalent when generating random structures.

Finally, we also explored the CCCO dihedral in the tail of linker containing the OH group (Figure 2.5e). The results are plotted in Figure 2.5d. We can see that the profile of the energetics are very similar to the Pt^{+1} and Rh(0) cases. The barrier is 1.4 kcal/mol, and this is the lowest among the CCCO studied cases.

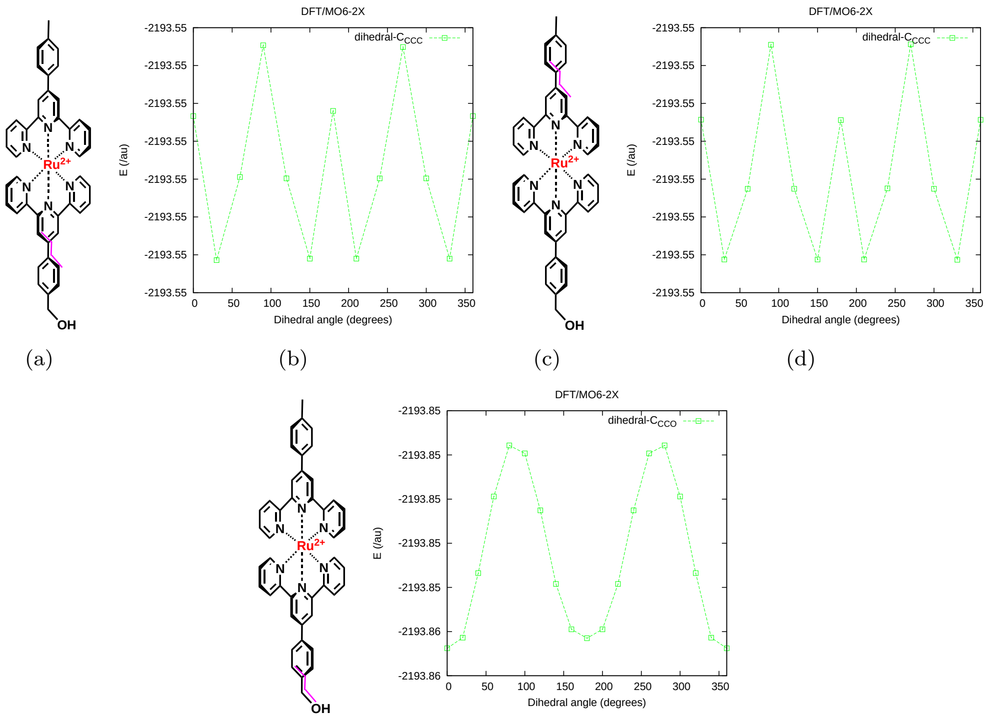

(a) (b) (c) (d)

(e) (f) Scan 3 CCCO

Figure 2.5: Ru complex

2.2.2.4 Dimers

The last parameters we obtained from QM calculations are the energy interactions between dimers. We calculated such interaction because when observing Figure 2.2 we can observe that such interaction will play an important role in the folding or general structure of the MOCA.

Thus, we optimize the geometry for all possible dimer interactions. There are only 6 possible dimer interactions; Pt^{+1}-Pt^{+1}, Pt^{+1}-Rh(0), Pt^{+1}-Ru^{+2}, Rh(0)-Rh(0), Rh(0)-Ru^{+2} and Ru^{+2}-Ru^{+2}. Our DFT/MO6-2X results are shown in Table 2.2.

Since we did not use counter anion for the positively charged complexes, we obtain a repulsive energy for the interaction containing two positively charged molecules. Such is the case of Pt^{+1}-Pt^{+1}, Pt^{+1}-Ru^{+2} and Ru^{+2}-Ru^{+2}. The magnitude of the repulsion is positively correlated with the magnitude of the charge present in the dimers. The least repulsion interaction is for the Pt^{+1}-Pt^{+1} dimer (12.6 kcal/mol), followed by the Pt^{+1}-Ru^{+2} (33.2 kcal/mol) and Ru^{+2}-Ru^{+2} (119.3 kcal/mol).

On the other hand, when only one of the complexes is a charged species then the energy is attractive. This is the case for the Pt^{+1}-Rh(0), Rh(0)-Rh(0) and Rh(0)-Ru^{+2} interactions. All the magnitude of the attractive interactions are very similar; around 35 kcal/mol.

Table 2.2: Binding energies (E_{bind}) for the different dimers obtained from DFT/MO6-2X and basis set LACVP**/6-31G**

Dimer	Functional	E_{bind} (kcal/mol)
Pt^{+1}-Pt^{+1}	MO6-2X	12.6
Pt^{+1}-Rh(0)	MO6-2X	-36.9
Pt^{+1}-Ru^{+2}	MO6-2X	33.2
Rh(0)-Rh(0)	MO6-2X	-33.6
Rh(0)-Ru^{+2}	MO6-2X	-35.7
Ru^{+2}-Ru^{+2}	MO6-2X	119.3

The geometry obtained for the Pt^{+1}-Pt^{+1} dimer is shown in Figure 2.6a. The energetics for the dimers is repulsive, however the intramolecular distance of the optimized structure is around 3.3 Å. This might sound contradictory; however it can be explained in the following manner. During minimization we started from an initial state and we found a minimum, this bottom of the well can be above zero or below zero in magnitude. Therefore we obtained a minimum but the magnitude of the well is above zero. If molecular dynamics (MD) were to be performed this dimer would fall apart because the bottom of the well can be escaped and the repulsion forces would prevail. We did not calculate the effect of having counter anions around the dimer to see if the forces would become attractive. This is because in our generator of structures we keep a positive charge, therefore these calculations are in accordance with our intentions of not using counter anions when building the full MOCA.

The optimized dimer structure for Pt^{+1}-Rh(0) dimer is shown in Figure 2.6b. The nature of this interaction is attractive and this binding energy is 36.9 kcal/mol. For this structure we found three sources of attractive interactions. First there are $\pi - \pi$ interactions between two pyridine molecules separated by almost 3.5 Å. The magnitude of this interaction is not considerable when compared to H bond. For example, the benzene dimer has binding energy of 2–3 kcal/mol.[15] The second source is a hydrogen bond interaction between the F of the $CO_2CF_3{}^-$ ligand linked to Rh(0) and the H from the pyridine ring bounded to Pt^{+1}. This hydrogen bond can be represented as a typical C-H$\cdots$F. The distance between these atoms is around 3.0 Å. This is a typical distance for a moderate hydrogen bond with mostly electrostatic interactions.[13, 14]. The Mulliken population charge for the C-H from pyridine is +0.19 and for the F from equatorial CF_3 is -0.29. The atomic electrostatic potential charge (ESP) for H from pyridine is +0.13 and -0.17 for F in the same hydrogen bond. Finally, the third source of interaction is another hydrogen bond that occurs between the OH at the tails of both linkers. This H bond can be thought of as a typical O-H$\cdots$O interaction. In this interaction the hydrogen bond donor, OH, is from the linker from the Pt^{+1}, and the acceptor, O, from the Rh(0) linker. The distance between H and the acceptor O is 2.0 Å, this is typical distance for this interaction.[14] The Mulliken charge for H is +0.36 (ESP=+0.40) and for O is -0.57 (ESP=-0.60). This is more evidence of such hydrogen bond. These three attractive interactions can count for the binding of 36.9 kcal/mol for this dimer.

The next dimer interaction we studied was the Pt^{+1}-Ru^{+2} and the optimized structure is shown in Figure 2.6c. The energy for this interaction is very repulsive (33.2 kcal/mol). The value is three times more repulsive than the Pt^{+1}-Pt^{+1} case; this is because there are more positive charges involved. The layers formed by the ligands from both metals is separated by 3.3 Å. This distance is between the only two pyridines that interact. The optimized dimer structure is again a local minima that depends on our initial guess, and it has a positive value. The optimized value finds the bottom of the well even if the bottom of the well is above zero. To put it another way, we went from very repulsive interaction to the least repulsive configuration. Classical MD or ab initio MD would then escape this local minima and the dimer would fall apart. For our purposes, we need the charges and the nature of the interaction for our structure generator. In the optimized local minimal obtained we found two interactions that can be considered as a hydrogen bond. This occurs between the O in the tail of the ligand of Ru and the C-H from the ligand bound to Pt. The distance of the H to the O for this C-H$\cdots$O interaction is 3.2 Å. The Mulliken charge for H is +0.18 (ESP charge=+0.19) and for O is -0.48 (ESP charge=-0.56). The second interaction is between the H from the C-H belonging to a benzene ring of the Ru^{+2} and the Cl bound to the Pt. The separation of this C-H$\cdots$Cl interaction is 2.9 Å. The Mulliken charge for H is +0.16 (ESP charge=+0.04) and for Cl is -0.33 (ESP charge=-0.46). The ESP charges for H give a qualitatively different result than Mulliken charges for the hydrogen in this case.

Next, we studied the interaction of the Rh(0)-Rh(0) dimer. The optimized structure is shown in Figure 2.6d. This interaction is attractive, with a magnitude of 33.6 kcal/mol. For this case, we no longer have the O-H$\cdots$O interaction as in the Pt^{+1}-Rh(0) case. However, in this dimer there are still three types of interactions: dispersion forces and two types of hydrogen bonds. The dispersion forces are responsible for the close distances between the benzene and the pyridine rings of both linkers. This distance varies from 3.1 Åfor the benzene-benzene interaction, and 3.4 Åfor pyridine-pyridine. The contribution to the binding should not be significant since the value for the benzene dimer is 2–3 kcal/mol [15], however for the H bond, this interaction can go from less than 4 to 40 kcal/mol.[16] Also the first type of hydrogen bond that we observed is a three-centered hydrogen bond that has the form C-H1$\cdots$Cl$\cdots$H2-C, with the C-H belonging to the same pyridine ring. The distance for this interaction is around 2.7 Å. To corroborate that there is a hydrogen bond we also calculated the Mulliken and ESP charges. We found that H1 and H2 have Mulliken charges of +0.15 and +0.16, respectively. On the other hand, Cl has a Mulliken charge of -0.38. The ESP charges for H1, H2 and Cl are +0.15, +0.16 and -0.46, respectively, which are very similar to the Mulliken charges. Finally, the second type of hydrogen bond occurring in this dimer is rather interesting. It is a four-centered hydrogen bond which involves three different H atoms (H1, H2 and H3) interacting with a single Cl atom. Each of these H atoms belongs to a different pyridine ring. The C-H...Cl distances are around 2.5 Å. In order to fully characterize such an H bond, we calculate its Mulliken and ESP charges. The Mulliken charges for H1, H2, H3 and Cl are +0.12, +0.14, +0.13 and -0.41, respectively, while the ESP charges are +0.13, +0.13, +0.15 and -0.41 for the same atoms. Both methods give the same result: the electronegative atom Cl is forming a hydrogen bond with the H of the C-H present in three different pyridines. This can be characterized as a strong hydrogen bond.[13, 14]

The fifth dimer we studied was the interaction of the Rh(0)-Ru^{+2}. The optimized structure is shown in Figure 2.6e. This interaction is attractive, as we can see from the binding energy: -35.7 kcal/mol. There are three main types of interaction that are responsible for this, dispersion interaction and two types of hydrogen bonds, just as in the case of the other dimers with attractive interactions. First, the dispersion interactions can be observed because of the $\pi - \pi$ stacking formed by the pyridines rings from both metal complexes. The distance for their separation is 3.2 Å. This interaction is not typically very strong in magnitude; for example, for the benzene-benzene dimer the binding energy is 2–3 kcal/mol in gas phase.[15] Therefore most of the contribution should come from the hydrogen bonding. The first strong interaction we have in this dimer is a three-centered hydrogen bond C1-H1$\cdots$O$\cdots$H2-C2 formed by the two C-H from a pyridine of Rh(0) and the O from the OH tail present in the Ru ligand. The separation for the H1$\cdots$O bond is 2.6 Å, and the separation for the H2$\cdots$O is 2.5 Å. The Mulliken charges for the H1, H2 and O are +0.15, +0.17 and -0.57, respectively, while the ESP charges are +0.15, +0.13 and -0.61 for the same atoms. The second strong interaction is a three-centered hydrogen bond that includes H10, H11 and H12 from different pyridine in the same linker bound to Ru^{+2}, interacting with a Cl bound to Rh(0). The distances for H10$\cdots$Cl, H11$\cdots$Cl and H12$\cdots$Cl are 2.8, 2.4 and 2.4 Å. The Mulliken charges for H10, H11, H12 and Cl are +0.12, +0.18, +0.19 and -0.46 (ESP charges are +0.11, +0.16, +0.14 and -0.50), respectively. The H10$\cdots$Cl can be considered weaker than the other two hydrogen bonds because of their longer distance and lower charge difference, either Mulliken or ESP charges.

Finally, we studied the dimer which is formed by complexes with the Ru^{+2}-Ru^{+2} metal centers. We started with a guess of this interaction and we minimized the structure, then we found the geometry that is shown in 2.6f. As we discussed above, even we get a repulsive energy of 119.4 kcal/mol we obtain this dimer separated by only 3.4 Å, this is because we found a local minima which is above zero in magnitude. If the true global minima needs to be found then an MD method is necessary, with this we will observe the dimer going apart from each other. This dimer is a case where the small dispersion interaction is competing against a strong Coulomb repulsion of a charge +2 interacting with another charge +2.

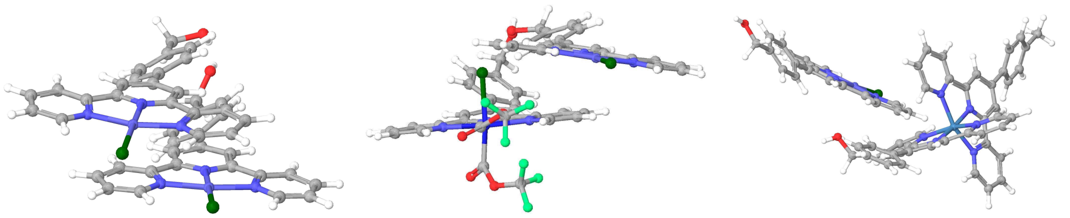

(a) Pt^{+1}-Pt^{+1} dimer (b) Pt^{+1}-Rh(0) dimer (c) Pt^{+1}-Ru^{+2} dimer

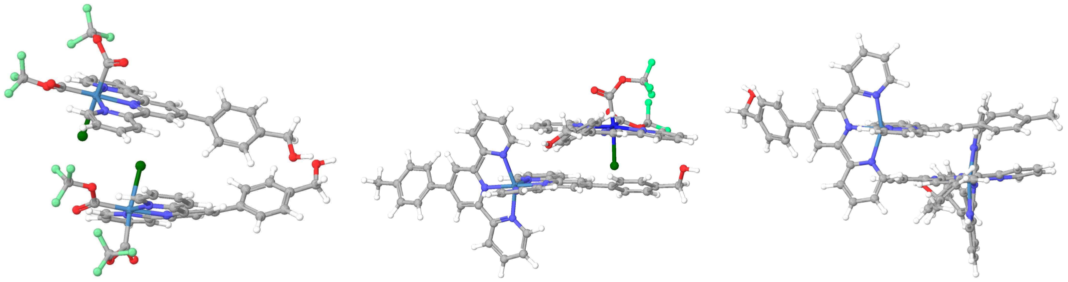

(d) Rh(0)-Rh(0) dimer (e) Rh(0)-Ru^{+2} dimer (f) Ru^{+2}-Ru^{+2} dimer

Figure 2.6: 3D-representation of the optimized structure obtained for each of the dimers considered in this study.

2.2.3 Structures Obtained from QM/MM

Using all this knowledge we have obtained from QM calculation we then proceeded to generate structures for the MOCA. As it was discussed before, the QM structures were used with the MM part calculated for the peptides. The partition for the interactions are shown in Figure 2.1. The big problem with the QM/MM method is how to define the interface between the two methods. In order to avoid such problem, we use the geometries generated by QM as described above and we only allow relaxing the atoms from the peptide. This way we keep the information from QM and we do not have to define the Hessian in the interface. Therefore, this method is more like a constrained MM. Next we defined a cutoff for the van der Waals of 12 Å, these interactions are assigned even for the structure obtained from the QM. The purpose is to capture any noncovalent interaction within this MM scheme. We minimized the structures using the UFF force field and a conjugated gradient minimization scheme with at least 5,000,000 steps. From this we obtained the structures shown in Figure 2.7. In these structures we used the Mulliken charges into the MM code, while we use Qeq[12] charges for the peptides. Before the minimization we equilibrate the charges in order to keep a proper global consistency.

The perspective used for these structures does not show all the details about the interactions having place. For example for the compound A (Figure 2.7a) the aromatic ring of Fluorenylmethyloxycarbonyl (Fmoc) is interacting with the benzene ring of the L-tyrosine, the closest distance for the benzene-benzene of these two entities is 3.5 Å. There is also a small interaction between the C-H from Fmoc and the O of L-tyrosine. The C-H$\cdots$O interaction distance is 3.6 Å, and the charges for the H and O atoms after minimization are +0.11 and -0.32, respectively.

Compound B has an array than can be described as Fmoc-(L-tyrosine-Pt)-(L-tyrosine-Pt). We also found other interactions that are not easy to see for the optimized compound B (Figure 2.7b). The first interaction is between the aromatic ring of Fmoc and the benzene of the linker of the farthest Pt^{+1}. The closest distances for these rings are 3.5 and 3.7 Å. The second interaction is a weak hydrogen bond between the H in the CH_2 of the Fmoc group and the O in the tail of the farthest L-tyrosine. The separation for the C-H$\cdots$O is 3.2 Å, and the charges for these atoms are +0.11 for the H and -0.33 for the O. The Pt^{+1} are far apart with a distance of 28.6 Å, which suggest that it might have low catalytic activity.

Compound C can be described as an Fmoc-(L-tyrosine-Ru)-(L-tyrosine-Pt)-(L-tyrosine-Rh) array. The optimized structure for this compound is shown in Figure 2.7c. The Fmoc in compound D interacts slightly with the benzene of the Pt^{+1} ligand, their separation at the closest range is of 3.9 Å. There is also a hydrogen bond between the H of the CH_2 from the tail of the Ru^{+2} ligand and the O of the carbonyl from the L-tyrosine-Pt. The distance for this C-H$\cdots$O is of 2.8 Å. The charges for the H and O involved in the H bond are +0.14 and -0.51, respectively. The distance between the metal centers are as follows: the Ru-Pt distance is 32.3 Å, the Pt-Rh distance is 32.1 Å, and the Rh-Ru distance is 18.5 Å.

Compound D is formed by four metal centers and the array is described as Fmoc-(L-tyrosine-Pt1)-(L-tyrosine-Pt2)-(L-tyrosine-Rh)-(L-tyrosine-Ru). The optimized structure is shown in Figure 2.7d. For these compounds we do not observe an obvious intramolecular interaction except for the aromatic ring of Fmoc interacting with the benzene ring present in linker of Pt1. The arrangement formed by the four metallic centers of this molecule resembles a distorted rectangle with each metallic center in one of the corners. The distorted square then has the following distances between metallic centers: Pt1-Pt2; 28.2, Pt2-Ru; 17.2, Ru-Rh; 30.1 and Rh-Pt1; 20.7 Å. Thus, this array looks less promising for a catalytic multicenter. We can see that the Rh for this case does not interact with the Ru because it is too close for the dihedral to align in this interaction.

Compound E is formed by five metal centers and the array is described as Fmoc-(L-tyrosine-Rh1)-(L-tyrosine-Pt1)-(L-tyrosine-Ru)-(L-tyrosine-Pt2)-(L-tyrosine-Rh2). The aromatic ring of Fmoc in this molecule is interacting with the benzene ring of the linker bound to Pt1. We also found two interesting H bond between a cabonyl and the H of an amine. The first C=O$\cdots$H-N interaction is at the distance of 2.4 Å, with the O having a charge of -0.42 and the H a charge of +0.21. The carbonyl belongs to the Fmoc group and the -NH belong to the peptide of L-tyrosine-Pt1. The second of this type of interaction is between the C=O from the 3rd peptide; (L-tyrosine-Ru) and the NH from the 5th peptide (L-tyrosine-Rh2). The distance for the C=O$\cdots$H-N interaction is 2.6 Å, and the charges for the O and for the H are -0.51 and +0.21, respectively. The distances between the closest metallic centers are as follow: Rh1-Ru; 12.3, Ru-Rh2; 12.1, Pt1-Pt2; 16.3 with all units in Å. All the other distances between metal centers is beyond 26 Å. The Rh is more likely to interact with the second nearest neighbors, as we can observe for this case and Rh1 interacting with Ru or Ru interacting with Rh1 which are separated for one monomer with Pt.

Compund F is the final array we studied, the sequence is described as Fmoc-(L-tyrosine-Pt1)-(L-tyrosine-Rh1)-(L-tyrosine-Pt2)- (L-tyrosine-Ru)-(L-tyrosine-Pt3)-(L-tyrosine-Rh2). The aromatic ring of Fmoc is interacting this time with the benzene ring of the linker bound to Pt1. We also found a hydrogen bond C=O$\cdots$H-N that is apart by a distance of 2.4 Å, with the O having a charge of -0.51 and the H a charge of +0.21. The carbonyl belongs to the 1st peptide (L-tyrosine-Pt1) and the -NH belong to the 3rd peptide (L-tyrosine-Pt2). However, the most relevant interaction found for this structure is the H bond of nature F$\cdots$H-C, with the F from the $CO_2CF_3^-$ ligand bound to Rh2 and H from one of the pyridines bound to the Ru. The H bond between the F and H is of 2.7 Å. The charges for H and F are +0.19 and -0.32, respectively. This interaction makes the Ru-Rh2 distance only 10.9 Å apart! The other other relevant distances are: Pt1-Pt2; 14.4, Pt2-Pt3; 12.7, and Rh1-Ru; 21.9 Å. All the other intermetallic distances are over 25 Å.

2.2.4 Conclusions

Our procedure suggest that the more Rh(0) we put in our array, more closer interactions will occur, thus more chances of generating catalytic activity. The monomer containing Rh(0) will interact with the second nearest neighbor because it is at the perfect distance so that the dihedrals can align for optimal interaction. We observed this for compound E and F, where the Rh are separated from Ru by 1 monomer. We found that when Rh(0) is used, the F of the $CO_2CF_3^-$ ligand can form moderate,

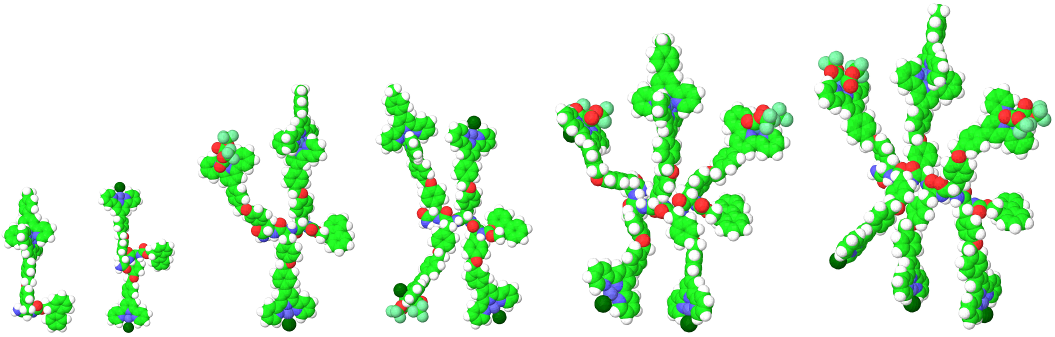
(a) A (b) B (c) C (d) D (e) E (f) F

Figure 2.7: Final configuration obtained using the QM/MM method for all the arrays denominated MOCA A, B, C, D, E and F

mostly electrostatic H bonds between the linkers of the metallic centers and this can help to create a multicenter multi catalytic region. We also found that the hydrogen bond network happens mostly in the polypeptide chain when $CO_2CF_3^-$ of the Rh(0) is not involved. The metallic centers do not interact with peptidic part due to the rigidity of their ligands.

2.3 Method II: Structure Prediction Inspired in Enzymes

This method uses a random generator in order to sample completely random structures. This is in order to capture the folding and most likely interaction in the MOCA compounds.

2.3.1 Methodology

The QM structures obtained from QM were used here. This means that all the most stable dihedral angles, as well as the bond lengths were conserved. These optimized structures were attached to the backbone peptide (organic part) and the conformers were generated with a random generator approach. This code generates 2,000–20,000 conformers of the compounds A, B, C, D, E and F. We then run 1,000 steps minimization of the whole structure with the Universal Force Field[11] while the structures obtained from QM were left constant. We then analyze the different conformers and classify them according to their energies with the lowest being the most favorable.

2.3.2 Generation of Conformers for All Compounds

We randomly generated a large number of possible conformations of the considered structures by sampling all the possible orientations of the rotatable torsions. First, we generated the peptide backbone with torsions from the Ramachandran distribution, then we added the tyrosine side chain. Dihedral N-C_A-C_B-C_G was chosen randomly from the three local minima. Finally, we added the functional groups with metal, again randomly sampling the rotatable torsions, which were described in the previous section.

Because the number of conformers is proportional to the number of degrees of freedom we generated 2,000 to 20,000 configurations for the compounds A to F, where A has less degree of freedom than B, and so on. Then we executed 1,000 steps with the conjugated gradient minimization scheme. This allows us to scan through a big database of structures.

The landscape for the ranking of all the generated structures can be observed in Figure 2.8. We assume there are enough configurations because there is a low enough dip in the beginning of the plot. In other words, there are a few structures with energy lower than the energy of a typical randomly generated structure.

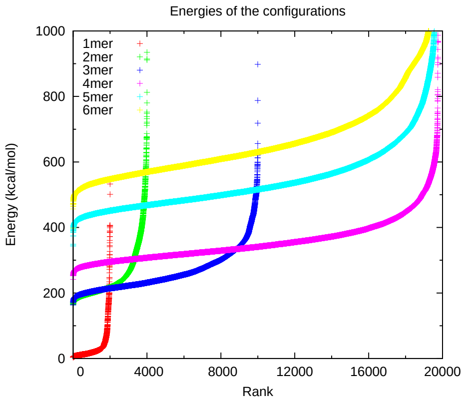

Figure 2.8: Population of all conformers generated for MOCA A to F. Color code: 1mer(A), red; 2mer(B), green; 3mer(C), navy blue; 4mer(D), cyan; 5mer(E), light blue; and 6mer(F), yellow.

In order to determine our best configuration we take the 10 most stable configurations. We can see that we obtain the most stable configuration when we zoom in for the first ranks. In Figure 2.9a and b, we can see that how the configurations for A converges to the most stable ones with 2,000 structures. This is the same case for compound B which the convergence plot can be observed in Figure 2.9c and d for 4,000 structures. For compound C, 10,000 structures were used (Figure 2.9e and f) For compounds D, E and F; 20,000 conformers were used and the convergence curve can be seen in Figure 2.9g-f.

The top 10 structures based on the energies are shown on Table 2.3. The energies presented in this Table are with respect to the UFF parameters. Thus we present these numbers taking into account that the relative values are the ones with physical meaning. That is the more positive the number, the more unstable the structure and the relative value between two structures represent which one is the most stable; with the lowest being the most stable. We can see that for compound A, the conformer ranked 1st differs from rank 2nd by 0.65 kcal/mol. For compound B, this difference is 1.27 kcal/mol. Compound C shows a gap of 1.83 kcal/mol. Compund D, E, F shows bigger gaps

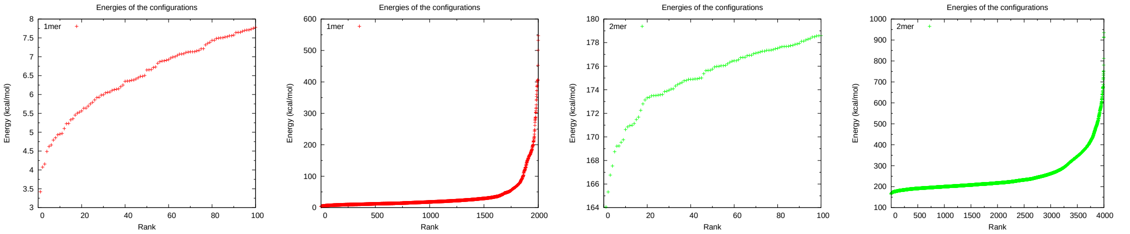

(a) Compound A (b) Compound A (c) Compound B (d) Compound B

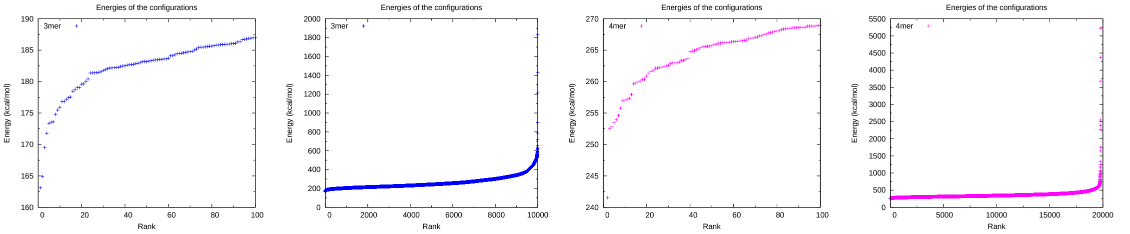

(e) Compound C (f) Compound C (g) Compound D (h) Compound D

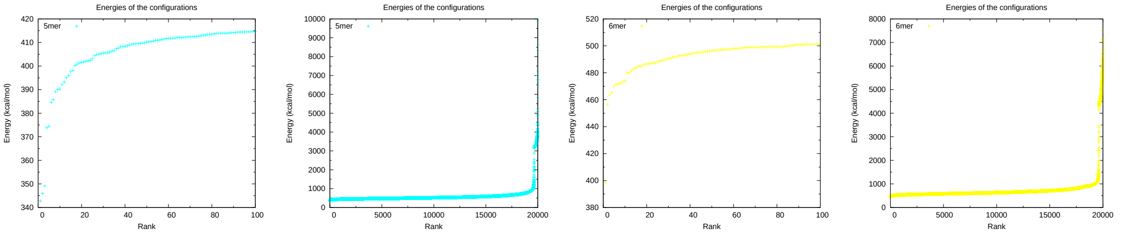

(i) Compound E (j) Compound E (k) Compound F (l) Compound F

Figure 2.9: Population of conformers generated for Compound A, B, C, D, E and F

of 11.0, 3.23 and 58.2 kca/mol, respectively. This demonstrates that for compound D and F, we have a very low relative minima compared to the second choice, while for compounds E; the top three conformers are closer in energy. Compound A, B and C have fewer degrees of freedom which causes the energy states to be closer.

Table 2.3: Energies for the top 10 conformers. R stands for rank. All the energies are in kcal/mol.

Compound A		Compound B		Compound C		Compound D		Compound E		Compound F	
R	Energy	R	Energy	R	Energy	R	Energy	R	Energy	R	Energy
1	3.42	1	164.06	1	163.10	1	241.53	1	342.78	1	398.44
2	4.07	2	165.33	2	164.93	2	252.53	2	346.01	2	456.65
3	4.15	3	166.76	3	169.54	3	252.80	3	349.11	3	463.54
4	4.48	4	167.54	4	171.79	4	253.48	4	373.82	4	465.39
5	4.62	5	168.75	5	173.32	5	253.94	5	374.46	5	469.89
6	4.66	6	169.22	6	173.56	6	254.60	6	384.65	6	471.33
7	4.79	7	169.23	7	173.59	7	255.78	7	385.80	7	471.89
8	4.85	8	169.54	8	174.79	8	256.94	8	389.10	8	472.14
9	4.93	9	169.76	9	175.47	9	257.07	9	389.99	9	473.19
10	4.95	10	170.63	10	175.92	10	257.22	10	390.24	10	474.18

The structures ranked as 1st for each of the compounds are shown in Figure 2.10. Compound A obtained by this method (Figure 2.10a) resembles the one obtained by method I (Figure 2.7a). The main difference is the structure obtained by method II does not have the Fmoc interacting with the O of L-tyrosine. The distance for C-H···O interaction is 5.0 Å (compared to 3.6 Å from method I). The root mean square (RMS) for the comparison between these two structures is 4.2.

The structure obtained for B is shown in Figure 2.10b. In this structure we do not find any interaction between the Fmoc and the benzene ring of the L-tyrosine or the linkers. There are not hydrogen bonds as in the structure for B found by method I (Figure 2.7b). The Pt^{+1}-Pt^{+1} distances are 22.6 Å which is a smaller distance to the one obtained from method I; 28.6 Å. When overlapping the structures obtained for B from method I and II, we found that the RMS is 7.86.

Method II gives for Compound C the structure shown in 2.10c. The structure obtained with method II does not show C-H···O Hydrogen bond as the one obtained from Method I (Figure 2.7c). However, there is a very interesting feature found for this structure. The distance between the center Rh to Ru is of only 10.1 Å! This is similar to this type of interaction found for compound E and F from method I. Compound C can be defines as the array : Fmoc-(L-tyrosine-Ru)-(L-tyrosine-Pt)-(L-tyrosine-Rh). From our conclusions of method I, we found that the Rh-Ru interaction can be found once the Rh and the Ru are separated by one monomer. We did not find this interaction from method I for compound C but we found such configuration as the most stable from method II. This shows the complementary of both methods to gives a nearly full representation of the important interactions and most stable structures. This suggests that also compound C can have catalytic processes where these two metals can be involved at the same time. The structures for C from the two different methods give similar structures with a RMS of 7.28.

The optimized structure obtained for compound D obtained from method II is shown in Figure 2.10d. Compound D can be described as an Fmoc-(L-tyrosine-Pt1)-(L-tyrosine-Pt2)-(L-tyrosine-Rh)-(L-tyrosine-Ru) sequence. In the most stable structure generated from this method we observe a very interesting interaction between the Rh and Pt1 at a distance 10.3 Å. This is the main difference with the structure generated from method I, where such interaction was not found (Figure 2.7d). This also corroborates our postulate that Rh can interact with a second nearest neighbor, and in this case is the monomer with Pt1. The RMS for the overlap of the structures of D obtained from Method I and II is 10.1, which indicates they are not very similar.

Compound E can be represented as follows; Fmoc-(L-tyrosine1-Rh1)-(L-tyrosine2-Pt1)-(L-tyrosine3-Ru)-(L-tyrosine4-Pt2)-(L-tyrosine5-Rh2) and the optimized structure obtained from method I is shown in Figure 2.10e. The Fmoc interacts slightly with the benzene ring from the L-tyrosine binded to Rh1, their separation is about 3.7 Å. There are also two hydrogen bonds of nature N-H···O=C between L-tyrosine1(C=O) and L-tyrosine3(N-H), as well as between L-tyrosine3(C=O) and L-tyrosine5(N-H). The separations are 2.9 and 3.3 Å, respectively. However the most important feature found in this structure is the interaction between Rh1 and Pt1. The separation for this metallic center is 7.1 Å, which is the closest interaction we found for any structure. In this interaction of dimers we found a hydrogen bond between the F from the CO_2CF_3 ligand bounded to Rh1 and the C-H from the pyridine bounded to Pt1. The separation for this C-H$\cdots$F interaction is 2.9 Å with charges for F of -0.32 and for H of +0.17. This kind of interaction in a dimer was already suggested by our QM calculations but it was not observed for the structure E obtained from method I (Figure 2.7e). The RMS for the overlap of the most stable structures obtained from method I and method II is 9.3. This would suggest they are very different however they mostly differ in one dihedral that contains Rh1 and Rh2. This explains why we do not observe the Rh-Ru close interaction but the Rh-Pt interaction with this method.

Compound F is described by the array Fmoc-(L-tyrosine-Pt1)-(L-tyrosine-Rh1)-(L-tyrosine-Pt2)-(L-tyrosine-Ru)-(L-tyrosine-Pt3)-(L-tyrosine-Rh2) and the structure obtained from method II is shown in Figure 2.10f. The main interaction observed for this structure is the presence of the dimer interaction between Pt1 and Rh2. It is the same type of interaction observed for compound E. The Pt1 and Rh2 centers are separated by 7.9 Å. There is also a hydrogen bond between the C-H from the pyridine bounded to Pt1 and the F from the CO_2CF_3 ligand bounded to Rh2. The separation for the C-H$\cdots$F interaction is 3.1 Å with charges for H of +0.18 and for F of -0.32. It is also interesting to note that the adjacent F interacts with the Pt1 center since they are separated by 3.3 Å. The structure from method I and II when overlapped gives a RMS of 16.0 which suggest that these structures are very different.

2.3.3 Conclusions

Compound C have a structure with the Rh-Ru distance of 10.1 Å, similar to the distance for this interaction found for compound E and F obtained from Method I. We did not find this interaction from method I for compound C but we found such configuration as the most stable from method II. This also strongly supports our earlier conclusions that Rh(0) is necessary to obtain close distances between metallic centers and if Rh-Ru interaction were to occur, they should be separated by one monomer. Method II also shows for the first time that compound D can present interactions between Rh and Pt. For this type of interaction they do not necessarily need to be second nearest neighbors since the Rh-Pt is not as restricted as the Rh-Ru interaction. This interaction is also observed for compound E and F between Rh and Pt, however we did not observe the Rh-Ru close interactions given by method I for these cases. Our observations show the complementary of both methods, method I observes the Rh-Rh interactions and method II observes the Rh-Pt interactions.

If Rh is used as a way to increase interactions in the MOCA, the next generation of arrays may try to contain earth abundant elements for catalysis in energy production such as Cu for oxidation of methane, [17, 18] Ni/Fe for production of molecular hydrogen, [19] or Mn/Ca for production of

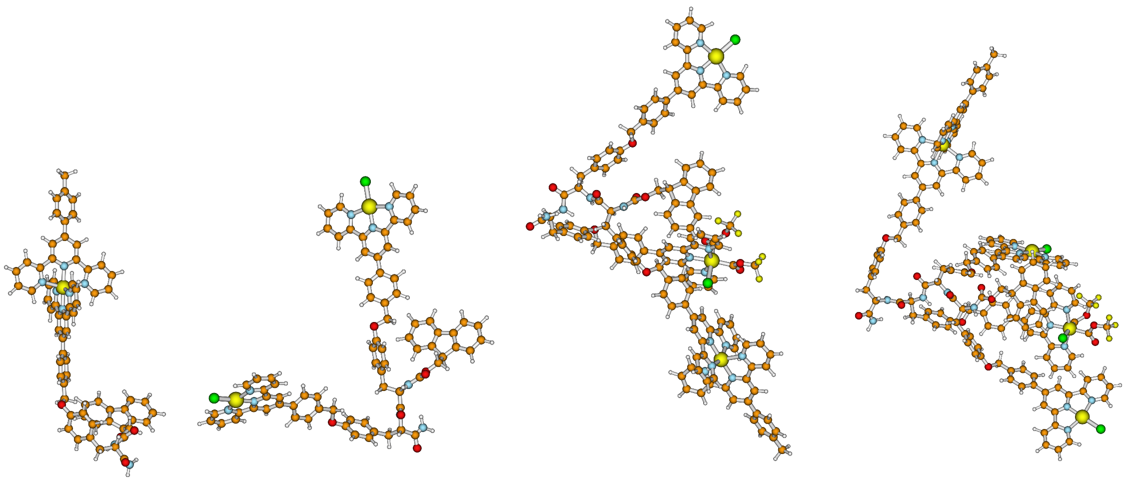

(a) 1st A (b) 1st B (c) 1st C (d) 1st D

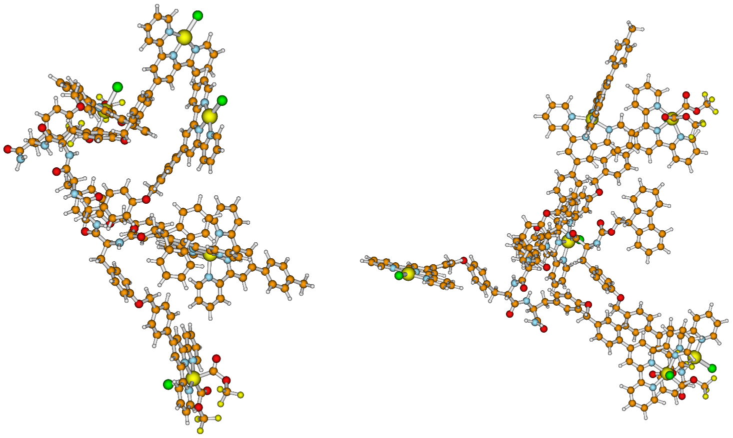

(e) 1st E (f) 1st F

Figure 2.10: Top 1st conformer for all compounds obtained by using method II

molecular oxygen. [20].

Chapter 3

Coarse-Grained Potential for Hydrogels from Quantum Mechanics

Jose L. Mendoza-Cortes, Andres Jaramillo-Botero, William A. Goddard III

3.1 Introduction

Hydrogels are aqueous polymer systems that may exhibit significant strength depending on their composition and structure (e.g. crosslinking). The equilibrium between strength and elasticity makes these materials a potential scaffolding material for cartilage, tendons and ligaments.[21]

There have been many attempts to understand the source of the strength in double network polymer hydrogels at the molecular level, and through the use of atomistic molecular simulations.[22] However, modeling and simulation of important events that occur during the synthesis process, such as percolation, are beyond the capabilities of current atomistic Molecular Dynamics (MD) simulations. To overcome some of these limitations, in particular those associated with the large length and time scales, we proposed the use of a coarse-grained model parameterized from the finer atomistic scale. [23, 24]

Thus, this chapter describes a coarse grained Force Field parameterized from quantum mechanics (QM) in order to understand the dynamics of polymer hydrogels. The specific polymers described as an example of the parameterization procedure are poly-acrylamide (poly-[aam]) and poly-2-acrylamido-2-2methylpropanesulfonic acid (poly-[amps]).

We also provide insights from Transition State Theory (TST) theory on the reaction rates required for cross-linking polymerization. From the reaction constants we determine to which degree the concentration of each monomer is optimal for cross-linking and how this relates to percolation and strength of the model hydrogels.

3.2 Methodology

This section present the methods used from Quantum Mechanics (QM) to calculate the potential energy that can be fitted to a functional form which defines the coarse grained potential.

3.2.1 Molecular Mechanics and Quantum Mechanics

In order to have a good initial guess of the structural features of monomers, dimers, trimers, or even tetramers, we minimized these with the Dreiding force field. [25] The initial guess obtained from molecular mechanics were used to calculate the potential curve of bond breaking and dihedral angles using first principles QM. For this, we used Unrestricted Density Functional Theory (UDFT) with the M06-2X[7] functional as implemented in the Jaguar code[9] and a 6-31G** basis set. All geometries were optimized using the analytic Hessian to confirm that the local minimum had no negative curvature (imaginary frequencies). By studying the transition state we confirm that there is one and only one imaginary frequency.

3.2.2 The Finite Extensible No Linear Elastic (FENE) Potential

FENE stands for Finite Extensible Nonlinear Elastic. It was initially proposed by Kremer and Grest.[26]

$$E = -0.5KR_0^2 \ln\left[1 - \left(\frac{r}{R_0}\right)^2\right] + 4\epsilon\left[\left(\frac{\sigma}{r}\right)^{12} - \left(\frac{\sigma}{r}\right)^6\right] + \epsilon \tag{3.1}$$

The first term extends to R_0, the maximum extent of the bond. The 2nd term is a cutoff at $2^{1/6}\sigma$, the minimum of the Lennard-Jones (LJ) potential. Where, ϵ and σ are obtained from QM and the other terms are derived from these two terms, this is $K = 30\ \epsilon/\sigma^2$ and $R_0 = 1.5\ \sigma$. The units are ϵ = energy, σ = distance, K = energy/distance^2, and R_0 = distance.

A basic example of this functional form is shown in Figure 3.1. The plot of the FENE potential contains the following parameters $\epsilon = 1.0$ and $\sigma = 1.0$. With this parameter we can derive the rest, $K = 30\ \epsilon/\sigma^2 = 30$, $R_0 = 1.5\ \sigma = 1.5$ and the cuttoff for the LJ is $2^{1/6}\sigma = 1.12$. In other words, when a particle A is described by the FENE potential, anything that is within a distance of 1.5 is going to have interaction with this particle A (mainly attraction). That is if a particle B gets in this range of another particle, particle B will continue to get closer due to the attractive interaction. At 1.12, a repulsive force will start acting on particle B. If particle B gets closer, it will experiment a stronger repulsive force, just as in the LJ potential. So far we have not defined the units, so we can assume for now they are atomic units.

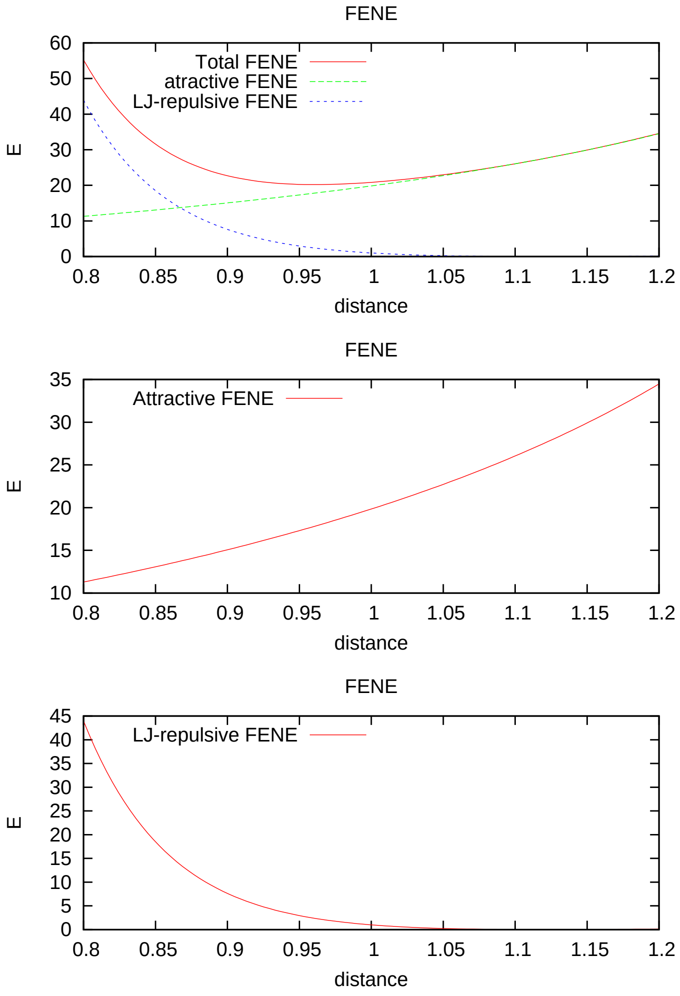

Figure 3.1: Example of the FENE potential. The repulsive part acts from 0 to $2^{1/6}\sigma$ (bottom). The attractive potential acts from 0 to $R_0 = 1.5\ \sigma$ (middle). The combination of both terms make the FENE potential (top). In this case, $\epsilon = 1.0$, $\sigma = 1.0$, thus $K = 30$, $R_0 = 1.5$, and $2^{1/6}\sigma = 1.12$.

3.3 FENE Potential

We describe our results obtained for the different models of monomers used and their bond strength. The potential curve obtained was used to fit the terms of the FENE potential.

The monomers used on this study are acrylamide ([aam]), 2-acrylamido-2-methyl propane sulfonate ($[\text{amps}]^{-1}$), sodium 2-acrylamido-2-methyl propane sulfonate ([amps]) and N,N'-methylenediacrylamide ([xlinker]). Their chemical structure are shown in Figure 3.2.

We studied both the anion and neutral version of [amps] and we will show that this matters for the parameters obtained for the FENE potential. In general we are interested in a neutral oligomer to model the hydrogels properties, however the partially charged hydrogel could exist when the water concentration is low, hence we report both parameters.

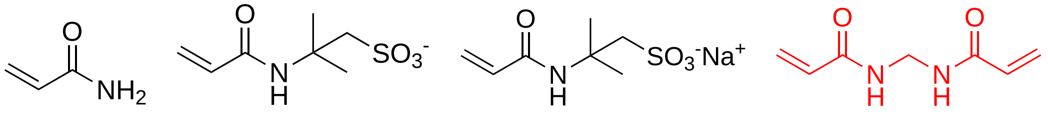

(a) aam (b) amps^{-1} (c) amps (d) xlinker

Figure 3.2: All monomers used are presented: (a) acrylamide (71.08) (b) 2-acrylamido-2-methyl propane sulfonate^{-1} (206.24 g/mol) (c) sodium 2-acrylamido-2-methyl propane sulfonate (229.23 g/mol) and (d) N,N'-methylenediacryl amide(154.17 g/mol).

As we can see from the structure, the dihedral angles are key in describing the larger-scale conformal motions of polymers built from these units. Therefore we first study if the dihedral angle correlation with the FENE potential form. Next, we study the parameters obtained when dimers, trimers and tetramers are formed and how the FENE parameters correlates with the type of interaction.

3.3.1 Dihedral Conformation and the FENE Potential

Dihedral are the principal degree of freedom necessary to develop accurate FENE parameters from QM. The advantage of these monomers is that when the double bond is converted into a radical for the polymerization and formation of the dimer or higher olygomers, each dimer creates only one new dihedral bond.

To show such interaction we show in Figure 3.3a-b the dihedral angle created when the aam-aam dimer is formed. We executed QM calculation with the procedure described to calculate the energy surface for this dihedral. The result is shown in Figure 3.3c. The dihedral surface energy is not symetrical.

3.3.1.1 Quantum Mechanics for the Dihedral Angles in the [aam-aam] Dimer

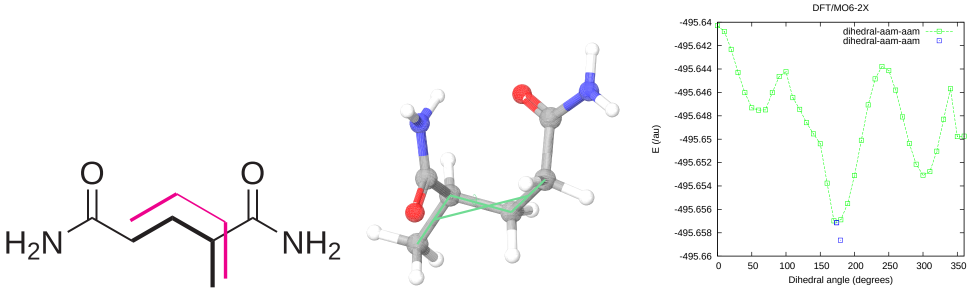

(a) aam-aam dihedral (b) aam-aam dihedral (c) aam-aam dihedral

Figure 3.3: The dihedral used for the aam-aam dimer is shown in (a) and (b) with magenta and green colors, respectively. The 360° point should be equivalent to the O° for a constrained dihedral scan, however we executed a relaxed scan.

The value for the dihedral of the starting optimized structure shown in Figure 3.3b is $\angle_{dihedral}$

= 204.1°. However, the scan showed there are other conformers with lower energies: $\angle_{dihe} = 170°$, $\angle_{dihe} = 180°$ and $\angle_{dihe} = 187°$. Thus, optimizations with these starting geometries were performed and the results are depicted by the blue squares in Figure 3.3c.

After further optimization we found that: $\angle_{dihe} = 170.0°$ goes to $\angle_{dihe} = 173.9°$, $\angle_{dihe} = 180.0°$ goes to $\angle_{dihe} = 174.0°$, $\angle_{dihe} = 187.0°$ goes to $\angle_{dihe} = 179.4°$. We observed that two structures converge to almost the same dihedral angle and almost the same energy, see Table 3.1. We pick the geometry with lowest energy, i.e. dihedral 173.9°.

Table 3.1: Energies for dihedral in the aam-aam

Angle (/degrees)	Energy (/au)
$\angle_{dihe} = 173.9°$	-495.657144
$\angle_{dihe} = 174.0°$	-495.657138

We then explored how the different most stable dihedral correlates to the FENE potential terms. The QM curve for investigating the bond strength is shown in Figure 3.4. We can see that the dihedrals have a different well depth, however both have the same equilibrium value. This is expected considering it represents the same C-C bond as shown in Figure 3.7.

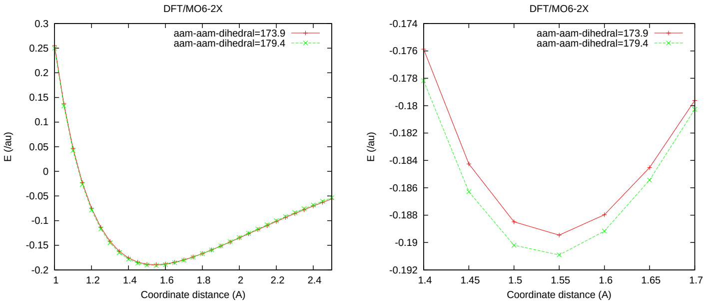

(a) aam-aam dihedrals (b) aam-aam dihedrals

Figure 3.4: Bond energies for aam-aam with dihedrals 173.9° and 179.4°

Table 3.2 shows the FENE parameters obtained by fitting to the dihedral terms described. For comparison we also include the FENE parameters obtained from another optimized structure with less stable dihedral (204.1°).

As we discussed earlier, the QM results shows that the same distance for the C-C bond should be expected independently of the configuration used. This is captured by the FENE σ parameters, i.e. it is the same for all configurations. On the other hand, our QM results suggested that the different configurations would result in a different well depth, which also captured by the FENE potential and the different values for the ϵ parameter.

From this we can conclude that the FENE potential capture the qualitative parts of QM. From this we can conclude that the dihedral configuration used does not influe significatively the result

Table 3.2: FENE parameters obtained for different dihedral for the [aam-aam] dimer

Combination	Bond	σ (Å)	ϵ (au)	R_0 (Å)	K (au/Å^2)
[aam-aam] (204.1°)	(C-C)	1.55	0.188	2.33	2.35
[aam-aam] (173.9°)	(C-C)	1.55	0.189	2.33	2.36
[aam-aam] (179.4°)	(C-C)	1.55	0.191	2.33	2.38

obtained for the FENE terms. The absolute numbers of the FENE potential does not have a physical meaning but the relative quantities does.

3.3.1.2 Quantum Mechanics for the Dihedral Angles in the [xlinker] Monomer

We repeat the process for the different units involved in the polymerization, this section corresponds to the xlinker. The dihedral is shown in Figure 3.5a.

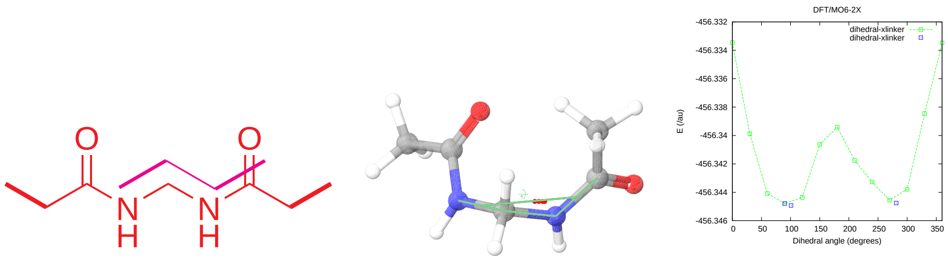

(a) xlinker dihedral (b) xlinker dihedral (c) xlinker dihedral

Figure 3.5: xlinker dihedral used. (a) The structure used is shown in red and the dihedral angle explored is magenta. (b) 3D representation of the xlinker with the dihedral used shown in green. The blue dots in (c) are reoptimized structures with the dihedrals shown in green.

We started with the optimized geometry shown in Figure 3.5b. The value for the dihedral of this structure is $\angle_{dihedral} = 103.4°$. The results of a full dihedral scan are shown in Figure 3.5b. The lowest laying conformers have a dihedral value of, $\angle_{dihe} = 103.4°$, $\angle_{dihe} = 90.0°$, $\angle_{dihe} = 270.0°$. Dihedral angles of 90.0° and 270.0° should be similar in energy, however we re-optimize the geometries. The results for this second optimization is shown in Figure 3.6c as blue dots. Some of the dihedral angles change slightly while one remains the same. This is, the starting $\angle_{dihe} = 90.0°$ reconverged to $\angle_{dihe} = 90.0°$, while the starting $\angle_{dihe} = 103.4°$ reconverged to $\angle_{dihe} = 100.8°$ and the starting $\angle_{dihe} = 270.0°$ reconverged to $\angle_{dihe} = 281.3°$.

Then we scan the bond strength for the most stable dihedral angles with our QM procedure. The scanned bond is shown in Figure 3.13. The results for the three dihedral angles are show in Figure 3.6. We observe that all the energies, minima and distance to the minima are the same. This is different to the dimer [aam-aam] case where there is a small difference in the depth well.

Therefore, the corresponding xlinker dihedral does not affect the FENE potential parameters.

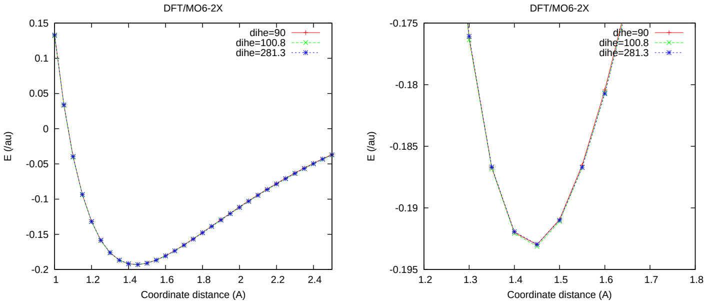

(a) xlinker dihedrals (b) xlinker dihedrals

Figure 3.6: Bond scan for most stable xlinker dihedrals

Table 3.3: [xlinker] FENE parameters for the FENE potential from QM

Combination	bond	σ (Å)	ϵ (au)	R_0 (Å)	K (au/Å^2)
[xlinker] (90.0°)	(N-C)	1.45	0.192	2.175	2.74
[xlinker] (100.8°)	(N-C)	1.45	0.192	2.175	2.74
[xlinker] (281.3°)	(N-C)	1.45	0.192	2.175	2.74

3.3.2 Bond Strength and the FENE Potential

This section describes in more detail the QM results for the monomer and dimer bonds involved in the hydrogel polymerization. We will use only one dihedral angle of one optimized geometry since we demonstrated in the previous section that any optimized structure with a given dihedral angle will give FENE terms that do not vary considerably from the the dihedral global minima. The FENE potential is intended for coarse grained systems, which means that many vibrational modes are smeared out, in order to make the calculation faster. Therefore small variation in the ϵ for a given interaction will not have a big effect when the full simulation is considered.

3.3.2.1 Quantum Mechanics of [aam-aam]

The first interaction we considered is the bond strength in the formation of a aam-aam dimer. The structure of such dimer is shown in Figure 3.7a. As we discussed previously the different dihedral angle gives essentially the same FENE parameters. As an example we show the optimized structure with dihedral 204.1° in Figure 3.7b. The energy surface for the C-C bond for the union of two dimers is shown in 3.7c.

After fittting, the FENE terms obtained for this bond in this interaction we obtained $K = 2.35$, $R_0 = 2.33$, $\epsilon = 0.188$ and $\sigma = 1.55$. The FENE potential for these parameters are shown in Figure 3.7. We discussed the other FENE terms obtained for other dihedral angles and all the results are shown Table 3.5.

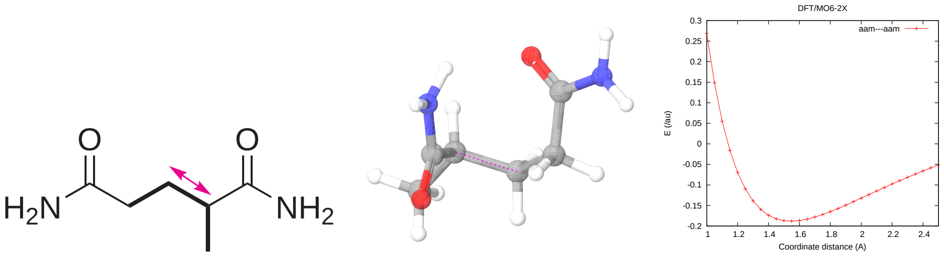

(a) aam-aam (b) aam-aam (c) aam-aam

Figure 3.7: Bond strength for a used conformation of aam-aam

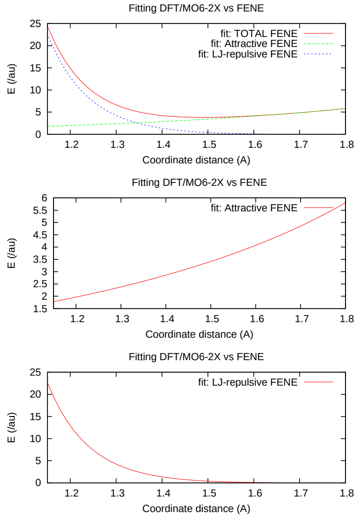

Figure 3.8: [aam-aam] FENE potential for structures in Figure 3.7

3.3.2.2 Quantum Mechanics of [amps-aam]

Next, we calculated the bond energy surface for the C-C bond in the amps-aam dimer. We must remember that the amps monomer can be neutral o anionic. The interactions used for the study of the C-C bond between aam and amps are shown in Figure 3.9a and d. We optimized the configuration with our QM scheme and we obtained the structures shown in Figure 3.9b and e. The conformation obtained for the neutral case and anionic case are slightly different. Then we calculated the energy surface for the same C-C bond and the results are shown in 3.9c and f.

The energy surface was then fitted to the FENE potential (Figure 3.10) and we obtained the parameters shown in Table 3.4. The parameters for both cases are basically the same. Therefore, we conclude that the use of anion or neutral species in the aam-amps formation does not change the final FENE parameters. Another way to look at it is that the FENE potential can not differentiate between the charged molecule and the anion molecules when this dimer forms.

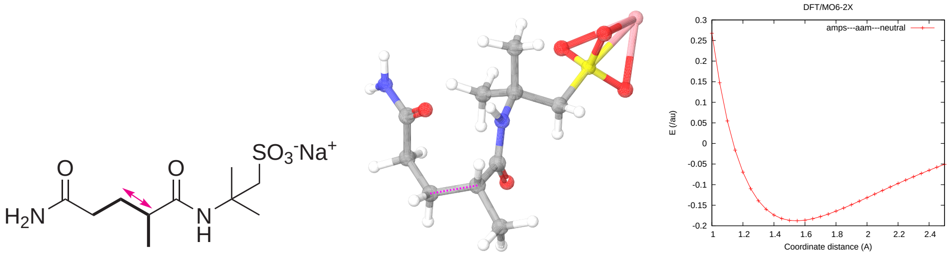

(a) aam-amps(0) (b) aam-amps(0) (c) aam-amps(0)

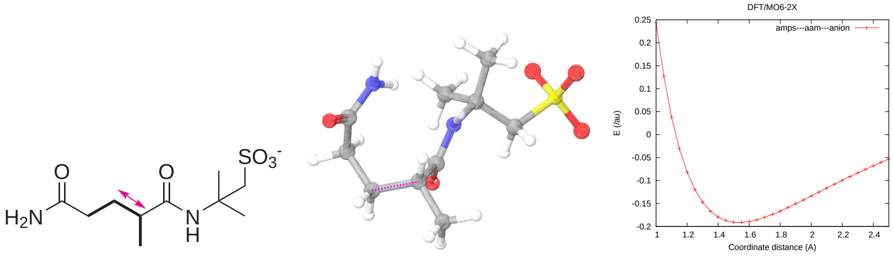

(d) aam-amps^{-1} (e) aam-amps^{-1} (f) aam-amps^{-1}

Figure 3.9: amps-aam used. The scan used is shown with a magenta arrow.

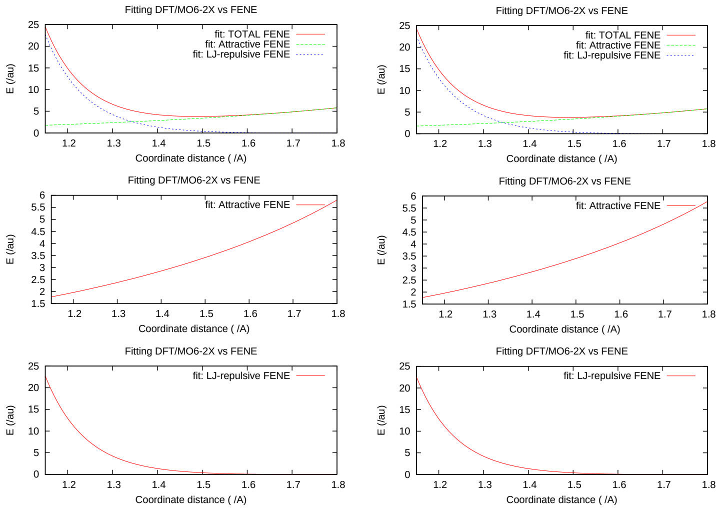

(a) aam-amps(0) (b) aam-amps^{-1}

Figure 3.10: [amps-aam] FENE potential for structures in Figure 3.9

Table 3.4: [aam-amps] FENE parameters for the FENE potential from QM

Combination	Bond	σ (Å)	ϵ (au)	R_0 (Å)	K (au/Å^2)
[aam-amps](0)	(C-C)	1.55	0.194	2.33	2.42
[aam-amps]$^{-1}$	(C-C)	1.55	0.193	2.33	2.41

3.3.2.3 Quantum Mechanics of [amps-amps]

We then proceed to calculate the strength for the amps-amps dimer. This interaction can have three types of species: amps-amps(0), amps-amps^{-1} and amps^{-1}-amps^{-1}. However, for our purposes we only considered the [amps-amps(0)] and [amps-amps^{-2}] species as it shown in Figure 3.11a and d. We built these models with the DREIDING force field and then we optimized them with our QM method. The resulting structures are shown in Figure 3.11b and e. We can see that for the case of the neutral species, the Na$^+$ atoms used remains around the SO_3^- group as we should expect. Then we proceed to break the C-C bond that connects both monomers. The surface energy obtained for this bond is shown in Figure 3.11c and f.

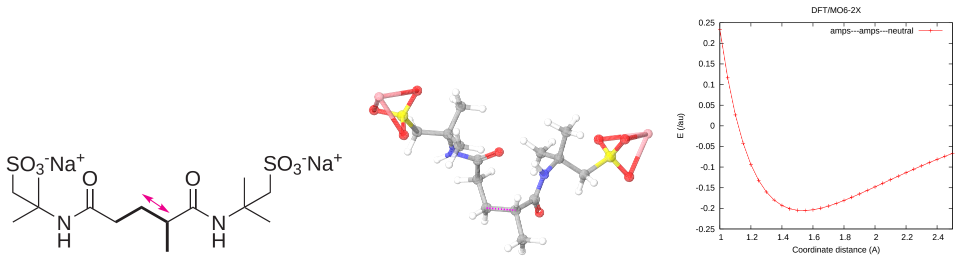

(a) amps-amps(0)   (b) amps-amps(0)   (c) amps-amps(0)

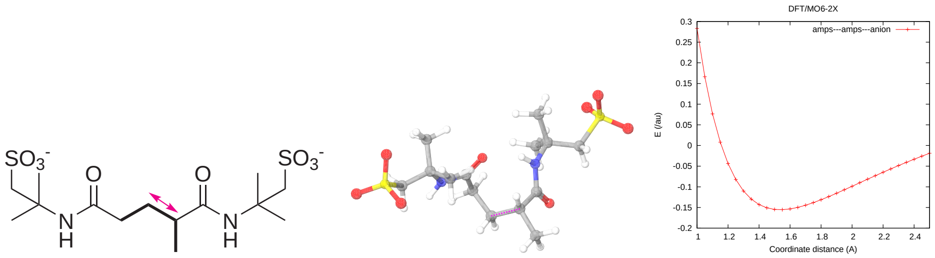

(d) amps-amps^{-2} (e) amps-amps^{-2} (f) amps-amps^{-2}

Figure 3.11: amps-amps neutral and anion used. The scan used is shown with a magenta arrow.

Using these energy surfaces, we fitted them into the FENE potential form. The results are shown in Table 3.5. The parameter for this interactions change drastically from the neutral to the full anionic forms in the ϵ parameter, 0.205 for the neutral case and 0.155 for the anionic case. As in the other interactions the σ remains 1.55 as we expected. Since K is directly correlated to the ϵ, we also obtained different K values. The stronger bond is for the neutral form as we can see from the larger value for ϵ. This can be understood from the interaction between Na$^+$ and the SO_3^- group, which makes it more harder to pull two species with larger masses apart. Thus, when used in MD, this potential should include different relative masses for each species.

Table 3.5: [amps-amps] parameters for the FENE potential from QM

Combination	Bond	σ (Å)	ϵ (au)	R_0 (Å)	K (au/Å^2)
[amps-amps](0)	(C-C)	1.55	0.205	2.33	2.56
[amps-amps]$^{-2}$	(C-C)	1.55	0.155	2.33	1.94

The FENE form for these parameters is shown in Figure 3.12. This indicates that the FENE parameters are able to differentiate between a full anionic form and the neutral form but is not specific enough to differentiate the aam-amps interaction when either anion or neutral species is used for amps.

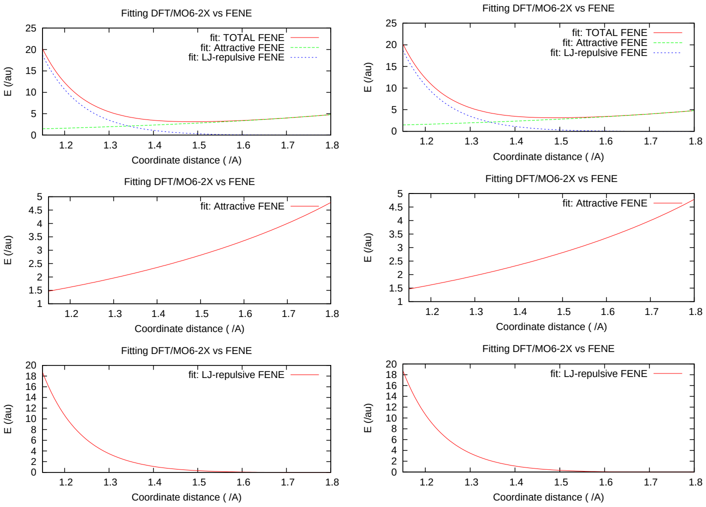

(a) amps-amps(0)

(b) amps-amps^{-2}

Figure 3.12: [amps-amps] FENE potential for structures in Figure 3.11

3.3.2.4 Quantum Mechanics of [xlinker]

We studied the strength of the N-C bond in the xlinker. This is in case we need to study C-N bond breaking during the polymerization reaction. The bond explored in xlinker is shown in Figure 3.13a. while the optimized structure used for the construction of the bond surface energy is shown in Figure 3.13b. The results for the scan from 1 to 2.5 Å is show in Figure 3.13c.

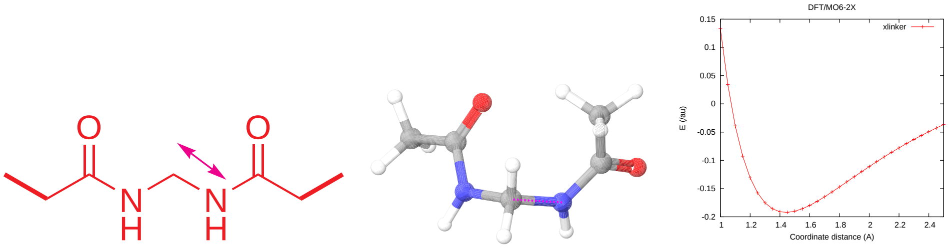

(a) xlinker

(b) xlinker

(c) xlinker

Figure 3.13: xlinker used. The scan used is shown with a magenta arrow.

Again, we used these QM results to fit the FENE potential. The parameters obtained are shown in Table 3.6. We observe that N-C bond is shorter then the C-C bond according to the σ FENE parameter. However, so far the C-N bond strength from this monomer is not stronger or weaker than the C-C bonds explored. The ϵ value is between the values obtained for the C-C bonds. Since the C-N bond is not participating in the polymerization, there could be a case where we need to separate the xlinker slightly, and this term would serve for such purpose. However for our current MD purposes we will not use these FENE term but only the C-C term. The FENE potential from fitting these parameters are shown in Figure 3.14.

Table 3.6: FENE parameters

Combination	Bond	σ (Å)	ϵ (au)	R_0 (Å)	K (au/Å^2)
[xlinker]	(N-C)	1.45	0.192	2.175	2.74

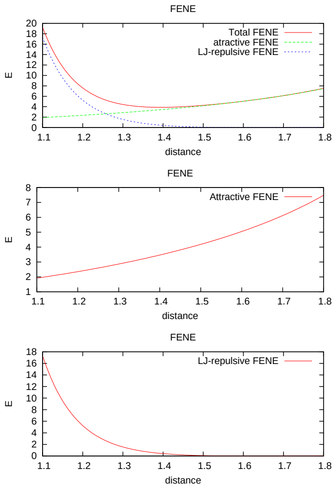

Figure 3.14: [amps-amps] FENE potential for structures in Figure 3.13

3.3.2.5 Quantum Mechanics of [xlinker-xlinker]

In this section we show the C-C FENE terms derived from QM. The C-C bond chosen is shown in Figure 3.15a. As in the other cases we built this dimer using the Dreiding force field and optimized the structure with molecular mechanics. Then we optimized the resulting structure with our QM method. The structure obtained from this procedure is shown in Figure 3.15b. We then scan the C-C bond to obtain the potential surface shown in Figure 3.15c.

Table 3.7: [xlinker-xlinker] parameters for the FENE potential from QM

Combination	σ (Å)	ϵ (au)	R_0 (Å)	K (au/Å^2)
[xlinker-xlinker]	1.55	0.173	2.33	2.16

This is the form of FENE with the parameters: $K = 2.16$, $R_0 = 2.33$, $\epsilon = 0.173$, $\sigma = 1.55$. Fitting the energy surface for the C-C bond shown, we obtain the FENE parameters in Table

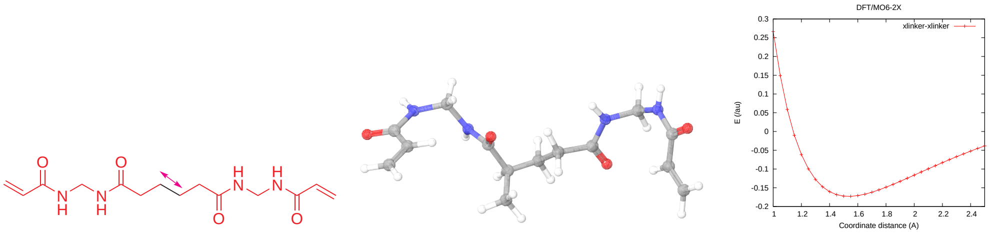

(a) xlinker-xlinker (b) xlinker-xlinker (c) xlinker-xlinker

Figure 3.15: xlinker-xlinker used. The C-C bond scan used is shown with a magenta arrow.

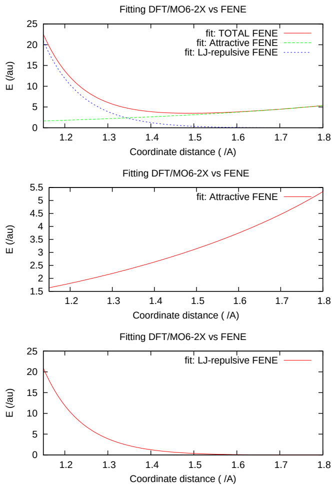

Figure 3.16: [amps-amps] FENE potential for structures in Figure 3.15

3.7. Just like all other cases the σ value is the same for the C-C bond, however we found that the ϵ is the lowest value from all the interaction considered so far. This could be an indication that self-polymerization of [xlinker] is not the main interaction but the cross linking of [xlinker] with [aam] and [amps]. In this sense the FENE potential is able to capture such trend since in real experiments, when the [xlinker] is added to the mixture of [aam] or [amps] the cross linking occurs but the [xlinker-xlinker] formation is not seen in big quantities in the product. The parameters obtained for this interaction in the FENE potential are shown in Figure 3.16.

3.3.2.6 Quantum Mechanics of [xlinker-aam]

Calculations for the [xlinker-aam] interactions were also executed. For this interaction we decided to study the two types of bonds between [xlinker] and [aam] (Figure 3.17a and d). Although in the coarse grained potential every monomer will be represented as a bead, we need to make sure that at the atomistic level we capture the most stable configuration with the FENE description. We optimized the geometry for the [xlinker-aam] with the procedure described before and we obtained the configuration shown in Figure 3.17b, which is the same as Figure 3.17e. We then scan the strength of the two types of C-C bonds that occur between these two monomers. The results are shown in Figure 3.17c and f.

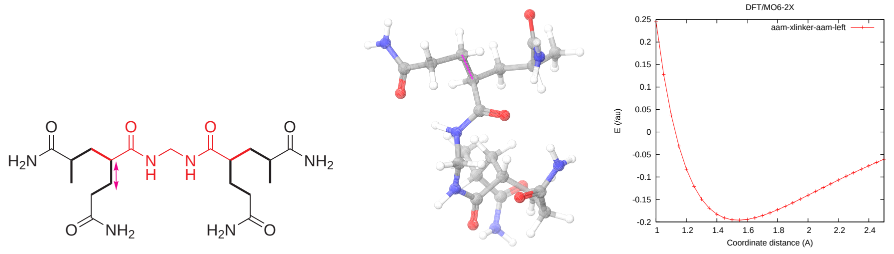

(a) xlinker-aam-I (b) xlinker-aam-I (c) xlinker-aam-I

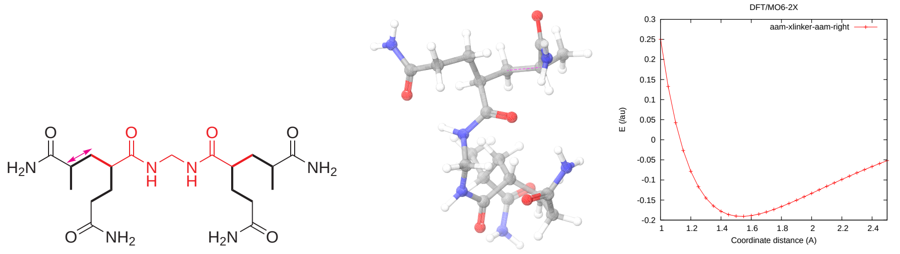

(d) xlinker-aam-II (e) xlinker-aam-II (f) xlinker-aam-II

Figure 3.17: xlinker-aam used. The scan used is shown with a magenta arrow.

From fitting our QM results to the FENE potential we obtained the parameters shown in Table 3.8. As we can see, the C-C distance represented by the FENE potential by σ are the same. And the depth of the well for the two types of C-C bonds are very similar. We found that the the C-C bond type I is stronger than the type II (ϵ is larger; 0.196 versus 0.191). However there is not a considerable difference. Therefore, it is a good approximation to use either C-C bond possibility, as we did in the last cases. Since the coarse grain MD is not going to capture the type of C-C bond between these two monomers, we will use the terms with the largest ϵ, in this case 0.196.

Table 3.8: [xlinker-aam] parameters for the FENE potential from QM

Combination	Bond	σ (Å)	ϵ (au)	R_0 (Å)	K (au/Å^2)
[xlinker-aam]-I	(C-C)	1.55	0.196	2.33	2.45
[xlinker-aam]-II	(C-C)	1.55	0.191	2.33	2.38

3.3.2.7 Quantum Mechanics of [xlinker-amps]

Just as in the [aam-amps] and [amps-amps] interaction, in the [xlinker-amps] interaction we can have two types of species, neutral or anionic. However we found that for the case of [amps-amps], the neutral dimers results in the strongest interactions ($\epsilon = 0.205$ for the neutral versus 0.155 for the anionic dimer). Therefore we use the neutral dimer to estimate the FENE parameters. We studied

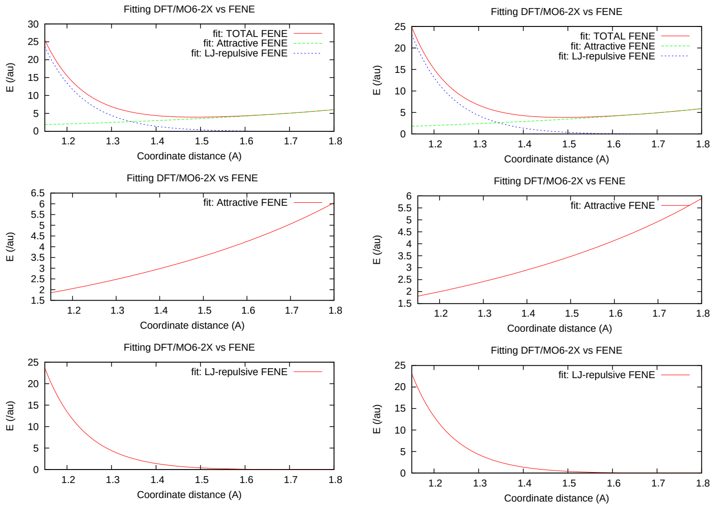

(a) Neutral (b) Anion

Figure 3.18: [xlinker-aam] FENE potential for structures in Figure 3.17

the two forms in which [xlinker] can bind to [amps]. The bonds explored are shown in Figure 3.19a and d. We optimized the structure with our MM method, and then with the QM scheme. The final structure is shown in Figure 3.19b and e. Then we proceeded to build the bond energy curve for the two types of C-C bonds. The results from QM are shown in Figure 3.19c and f.

We used these results to construct the FENE parameters. The terms obtained are shown in Table 3.9 and plotted in Figure 3.20. Just like the other cases and as we should expect the σ is the same for both cases, 1.55. However we observe that in this case we obtain different values for the ϵ, 0.192 for bond I and 0.208 for bond II. The difference is 0.016 and this is the largest difference observed for the same conformation. Thus, we use ϵ of 0.208 for our future calculations. This value of ϵ is comparable to the one obtained for the $amps - amps$ neutral interaction, which we found was 0.205. This suggest that the bond were amps is involved has a stronger interaction with xlinker and itself than with the [aam] monomer.

Table 3.9: [xlinker-amps] parameters for the FENE potential from QM

Combination	Bond	σ (Å)	ϵ (au)	R_0 (Å)	K (au/Å^2)
[xlinker-amps]-I	(C-C)	1.55	0.192	2.33	2.40
[xlinker-amps]-II	(C-C)	1.55	0.208	2.33	2.60

3.3.3 Conclusions

The obtained FENE potential parameters are shown in Table 3.10. The σ is the same for all cases considering they are C-C bond types. However the depth of the well changes depending on the

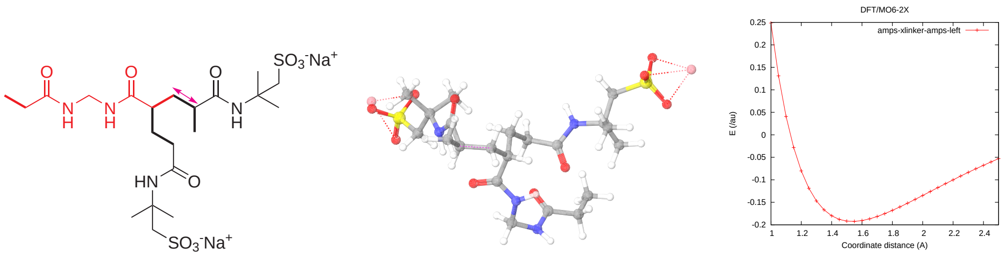

(a) xlinker-amps-I (b) xlinker-amps-I (c) xlinker-amps-I

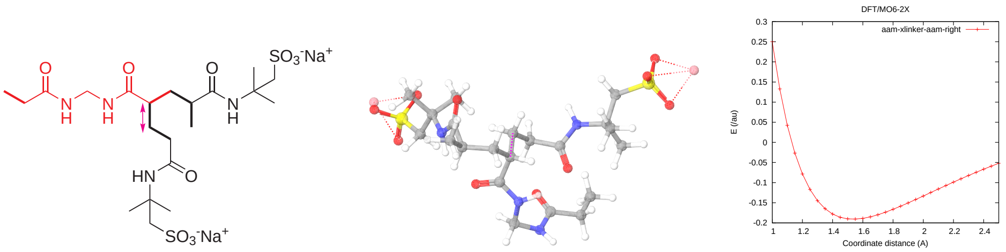

(d) xlinker-amps-II (e) xlinker-amps-II (f) xlinker-amps-II

Figure 3.19: xlinker-amps used. The scan used is shown with a magenta arrow. (b) and (e) are equivalent.

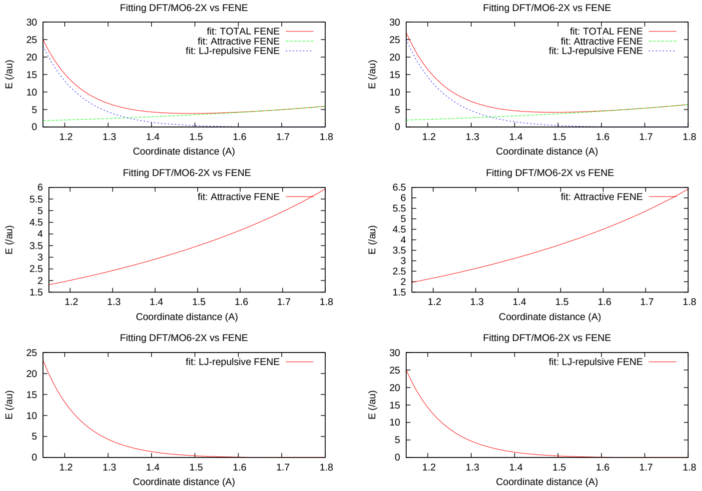

(a) Neutral (b) Anion

Figure 3.20: [xlinker-aam] FENE potential for structures in Figure 3.19

interacting monomers. All these terms are obtained for either the neutral, which indicates that the Na$^+$ has been included for the [amps], and the anionic species (absence of Na$^+$). The bigger the depth the stronger the bond. Since K depends proportionally to ϵ and all the σ are the same, then will also be larger for the larger depth.

A fast way to compare the quality of the FENE potential is to compare the QM trends with the FENE trend. In Figure 3.21a we show the neutral species for the interaction between [aam] and [amps]. We can see that the stronger interaction is for [amps-amps], followed by [amps-aam] and

Table 3.10: All the parameters for the FENE potential from QM. I and II stand for different explored C-C bonds

Combination	(bond)	σ (Å)	ϵ (au)	R_0 (Å)	K (au/Å^2)
[xlinker-amps]-I	(C-C)	1.55	0.192	2.33	2.40
[xlinker-amps]-II	(C-C)	1.55	0.208	2.33	2.60
[xlinker-aam]-I	(C-C)	1.55	0.196	2.33	2.45
[xlinker-aam]-II	(C-C)	1.55	0.191	2.33	2.38
[xlinker-xlinker]	(C-C)	1.55	0.173	2.33	2.16
[amps-amps](0)	(C-C)	1.55	0.205	2.33	2.56
[amps-amps]$^{-2}$	(C-C)	1.55	0.155	2.33	1.94
[aam-amps](0)	(C-C)	1.55	0.194	2.33	2.42
[aam-amps]$^{-1}$	(C-C)	1.55	0.193	2.33	2.41
[aam-aam]	(C-C)	1.55	0.191	2.33	2.38

the weakest among these three is the [aam-aam]. For the FENE potential terms, the strength of the bond for each interaction is given by the value of ϵ. For the [amps-amps] we have the largest value for ϵ (0.205) followed by [amps-aam](0.194) and then [aam-aam] (0.191). This is the same trend obtained for the QM calculation.

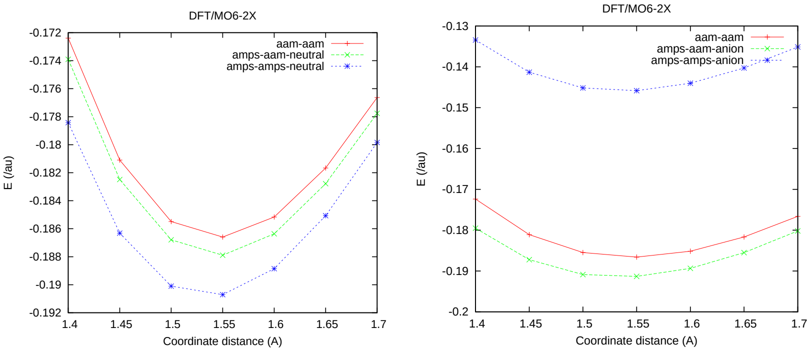

(a) Neutral

(b) Anion

Figure 3.21: All QM results around the equilibration point

Our main objective was to calculate the interaction between neutral species. However, the FENE potential is able to capture the trend obtained from QM for anionic species. In Figure 3.21b we show the energy surface for the C-C for the interaction between [aam] and [amps]$^{-1}$. We can see that QM predicts the interaction in the [amps-aam]^1 dimer to be the strongest followed by [aam-aam] and finally [amps-amps]^2 as the weakest. If we observe the FENE terms we found that the [amps-aam]^1 interaction has the the largest ϵ (0.193), therefore the strongest interaction, followed by [aam-aam]^1(0.191) and [amps-amps]^2 (0.155).

Conclusions for [xlinker-aam] and [xlinker-amps]

Finally the FENE terms obtained from QM determines that for the cross-linking reaction when the xlinker is used the [xlinker-amps] will be dominant due to the largest ϵ = 0.208 followed by [xlinker-aam]^2 with $\epsilon = 0.196$. The values for these two species are almost the same so there will be no an evident preference for either one and the concentration for each species will play the main role, just as in the experiments. The FENE parameters predict that there will not be much self-polymerization for the xlinker as we can see from the small $\epsilon = 0.173$, this is also observed in experiments. When the three species [amps], [aam] and [xlinker] are mixed in the same concentration, the FENE parameters predicts that the main reaction is between [xlinker] and [amps], as well as self-polymerization of [amps] since they have the largest ϵ. In experiments however, smaller concentration of [amps] is used, compared to [aam], perhaps because of this reason and since cross-polymerization is needed.

A coarse grain bead model used in an MD scheme with the developed FENE interactions enables an improved sampling, over a fully atomistic model, of the conformational space of the polymers. Appropriate bead masses should be set for each monomer bead, and from our analysis we suggest a mass of 1 for aam, 4 for amps, and 2 for the xlinker.

3.4 Reaction Rates from Transition State Theory

Here we calculate the reaction rates between the different species discussed in the previous section from Transition State Theory (TST). Using Eyring equation of TST [27] for calculating rates of reaction we have:

$$A + B \rightleftharpoons [AB]^{\ddagger} \rightarrow P$$

TST assumes that even when the reactants and products are not in equilibrium with each other, the activated complexes are in quasi-equilibrium with the reactants. The equilibrium constant $K^{\ddagger}$ for the quasi-equilibrium can be written as

$$K^{\ddagger} = \frac{[AB]^{\ddagger}}{[A][B]}$$

where [ ] = concentration mol/L, thus the concentration of the transition state is $[AB]^{\ddagger} = K^{\ddagger}[A][B]$ and the rate equation for the production of product is $\frac{d[P]}{dt} = k^{\ddagger}[AB]^{\ddagger} = k^{\ddagger}K^{\ddagger}[A][B] = k[A][B]$ Here, the rate constant k is given by $k = k^{\ddagger}K^{\ddagger}$. $k^{\ddagger}$ is directly proportional to the frequency of the vibrational mode responsible for converting the activated complex to the product; the frequency of this vibrational mode is ν. Every vibration does not necessarily lead to the formation of product, so a proportionality constant κ, referred to as the transmission coefficient, is introduced to account for this effect. So $k^{\ddagger}$ can be rewritten as $k^{\ddagger} = \kappa\nu$.

For the equilibrium constant $K^{\ddagger}$, statistical mechanics leads to a temperature dependent expression given as $K^{\ddagger} = [(k_BT)/(h\nu)]e^{-(\Delta G^{\ddagger})/(RT)}$. Combining the new expressions for $k^{\ddagger}$ and $K^{\ddagger}$, a new rate constant expression can be written, which is given as

$$k = k^{\ddagger} K^{\ddagger} = \kappa[(k_B T)/(h)]e^{-(\Delta G^{\ddagger})/(RT)}$$

Since $\Delta G = \Delta H - T\Delta S$, the rate constant expression can be expanded, giving the Eyring equation $k = \kappa[(k_B T)/(h)]e^{(-\Delta S^{\ddagger})/(R)} e^{(-\Delta H^{\ddagger})/(RT)}$. In order to determine the reaction rates we calculate the transition state energy and then apply TST to obtain the reaction constant.

3.4.1 Reaction Rates in Gas Phase and Water

The polymerization reaction used in the synthesis of hydrogels is a free radical mechanism. In real experiments, first one monomer is polymerized with excess xlinker [21]. This way cross-linking polymers of only [aam] and [xlinker] is created first which we call P[aam,xlinker] and in a different reaction, the cross linking polymers of only [amps] and [xlinker] is created, which we call P[amps,xlinker]. If double network polymers are needed, normally one would prepare a single network first, wash excess x-linker, and add the second component in linear form with a low xlinker concentration.

The concentration of the monomers in any case is very low since the water content is about 90%. Therefore our QM calculation in gas phase and implicit water solvent can capture the reaction rates for real experiments because low concentration of reactants are required. This is because in the implicit solvent case we assume low concentration of the reactant, since we do not consider multiple monomer-monomer interactions. The reactions we studied are shown in Figure 3.22. We do not consider the aam-aam and the amps-amps interaction since we assume that all the interactions will come from the x-linker interaction with these two monomers or with itself since x-linker is the initiator of the reaction and generally present in a higher concentration. If higher concentrations of [aam] or [amps] compared to [xlinker] are used, then the energies for this interaction should be calculated.

Since the free radical polymerization reaction is used in real experiments we calculate the possible reactions when the xlinker is the initiator, 3.22a, c and e. Also we considered the case that the polymerization continues with the free radical now in the [aam] or [amps]. As we discussed before, in real experiment the concentration of [aam] and [amps] are relatively small compared to the [xlinker]. Thus this new free radical will have more probability of finding [xlinker] and this case is calculated in the second possibility illustrated in Figure 3.22b, d and f.

For our implicit solvent calculations we used the Poisson-Boltzmann solvation model (PBF) approximation [28, 29] and the parameters for these calculation are shown in Table 3.11. We first optimized the structure in gas phase and then the solvent correction was added. Then we found the transition state for each geometry and the results are show in Figure 3.23. This is a plot were the

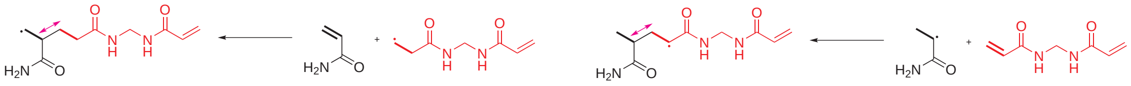

(a) aam-xlinker, Reaction 1 (b) aam-xlinker, Reaction 2

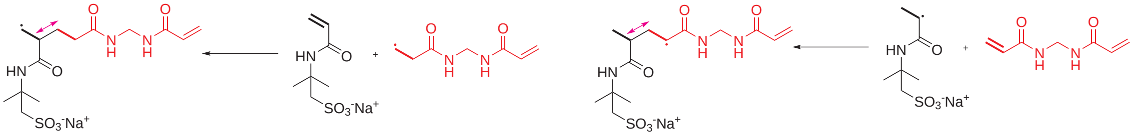

(c) amps-xlinker, Reaction 1 (d) amps-xlinker, Reaction 2

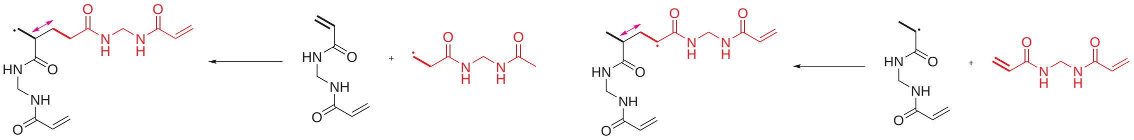

(e) xlinker-xlinker, Reaction 1 (f) xlinker-xlinker, Reaction 2

Figure 3.22: For all studied reactions, the free radical polymerization mechanism is assumed

doublet was calculated for the transition state and the full scan for the formation of reactants and products is shown. The plots for the water cases are not shown but the free energies calculation with water solvent were performed and all the results are shown in Table 3.12.

Table 3.11: Parameters for water

Dielectric constant	80.37
Probe Radius	1.40 A

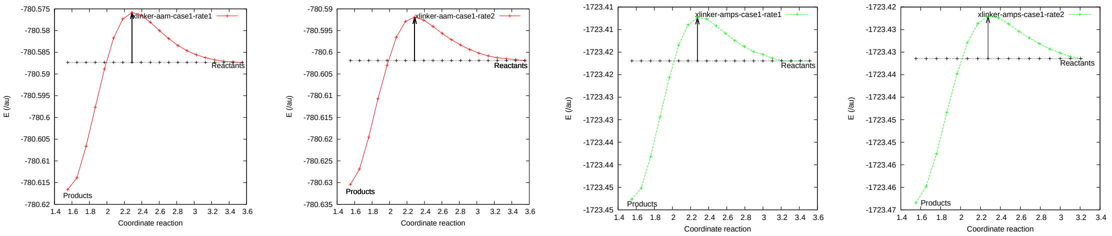

(a) aam-xlinker,rxn-1 (b) aam-xlinker,rxn-2 (c) amps-xlinker,rxn-1 (d) amps-xlinker,rxn-2

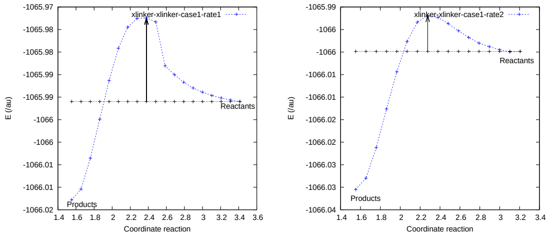

(e) xlinker-xlinker,rxn-1 (f) xlinker-xlinker,rxn-1

Figure 3.23: This plot shows the product (left) and reactant (right)

The Free energies (ΔG) for the gas phase changes when solvation is used as we should expected.

The degree of this change should depend on the charge and size of each species, since these are the main factors that are affected by the solvation. For example, the free energies for the [xlinker-aam] we found that the main changes in the free energy are for the radical and neutral [xlinker].

An important factor that should be pointed out is that due to the nature of the free radical polymerization, we can have different modes of reaction for a given asymmetrical double (C1 = C2) that reacts with a another asymmetrical double bound (C1' = C2'). This is because the free radical can be in either of the carbons and reacts with any of the carbons of the other double bond. This four modes can be represented as: C1-C2·—C1' = C2', C1-C2·—C2' = C1', C2-C1·—C1' = C2', and C2-C1·—C2' = C1'.

For our calculations we only consider one mode, assuming that the other modes will be very similar in energy. This is because even the carbons that are acting in the double bond are not identical, they are primarily CH=CH_2 bonds. This point is shown when we consider two modes for the xlinker-xlinker interaction (Figure 3.22e and f). The radical can be in the primary or secondary carbon in the xlinker, then we calculate the energy when they react with the secondary carbon of another xlinker. The activation energy for both cases are very similar, for the primary C· reacting with the secondary C in the double bond we have $\Delta G^{\ddagger}$ = +12.7 while for the secondary C· reacting with the secondary C in the double bond we obtained $\Delta G^{\ddagger}$ = +14.1. The distance between these two cases in water gets reduced even further $\Delta G^{\ddagger}$ = +20.6 for the former case and $\Delta G^{\ddagger}$ = +21.7 for the latter. This suggests that our assumption of considering only one mode of reaction is acceptable, specially when solvation is used.

3.4.2 Conclusions

The calculation of the activation energy gives us several insights about the kinetics of this polymerization. Using the Eyring equation from TST we can estimate the reaction constant. The results are shown in Table 3.13. The reactions are slower in water solvent. This is because the organic part of the monomers does not interact strongly with the polar water. This can be seen clearly in Table 3.12, where all the structures gets destabilized by the water solvent. However in both scenarios, [xlinker]· is ten times slower than the reaction that starts [aam]· or the analog that starts with [amps]·. The implication is that since the initiation for the reaction ([xlinker]· reacting with [aam] or [amps]) is slower than the propagation (reaction of [aam]· or [amps]· with [xlinker]). I assume that the propagation is a reaction with [xlinker] because it is in higher concentration.

From the reaction constants, we found that in the initiation with the ([xlinker]· species in water the reaction with [amps] is slightly faster than with [aam]. Our results also indicate that the self polymerization reaction for the [xlinker] is not important since it is two orders of magnitude slower than the cross linking polymerization. All these observation are relevant to experimental results when low concentrations of [amps] or [aam] are used, with respect to xlinker concentration. Water

Table 3.12: Free energy (G) of all the reactions in gas phase. Energies are in kcal/mol.

xlinker-aam (Gas phase)				xlinker-aam (In water)			
reaction 1		reaction 2		reaction 1		reaction 2	
$G^{\ddagger}$	-30.4	$G^{\ddagger}$	-31.2	$G^{\ddagger}$	-24.4	$G^{\ddagger}$	-23.9
G_{aam}	-18.7	$G_{aam\cdot}$	-19.5	G_{aam}	-17.8	$G_{aam\cdot}$	-18.8
$G_{xlinker\cdot}$	-26.4	$G_{xlinker}$	-24.5	$G_{xlinker\cdot}$	-25.9	$G_{xlinker}$	-23.0
$\Delta G_1^{\ddagger}$	+14.7	$\Delta G_2^{\ddagger}$	+12.8	$\Delta G_1^{\ddagger}$	+19.3	$\Delta G_2^{\ddagger}$	+17.9

xlinker-amps (Gas phase)				xlinker-amps (In water)			
reaction 1		reaction 2		reaction 1		reaction 2	
$G^{\ddagger}$	-38.6	$G^{\ddagger}$	-39.1	$G^{\ddagger}$	-33.3	$G^{\ddagger}$	-32.2
G_{amps}	-28.1	$G_{amps\cdot}$	-29.3	G_{amps}	-26.4	$G_{amps\cdot}$	-27.3
$G_{xlinker\cdot}$	-26.4	$G_{xlinker}$	-24.5	$G_{xlinker\cdot}$	-25.9	$G_{xlinker}$	-23.0
$\Delta G_3^{\ddagger}$	+16.6	$\Delta G_4^{\ddagger}$	+14.7	$\Delta G_3^{\ddagger}$	+19.0	$\Delta G_4^{\ddagger}$	+18.1

xlinker-xlinker (Gas phase)				xlinker-xlinker (In water)			
reaction 1		reaction 2		reaction 1		reaction 2	
$G^{\ddagger}$	-38.2	$G^{\ddagger}$	-37.4	$G^{\ddagger}$	-28.3	$G^{\ddagger}$	-27.7
$G_{xlinker}$	-24.5	$G_{xlinker\cdot}$	-27.0	$G_{xlinker}$	-23.0	$G_{xlinker\cdot}$	-26.4
$G_{xlinker\cdot}$	-26.4	$G_{xlinker}$	-24.5	$G_{xlinker\cdot}$	-25.9	$G_{xlinker}$	-23.0
$\Delta G_5^{\ddagger}$	+12.7	$\Delta G_6^{\ddagger}$	+14.1	$\Delta G_5^{\ddagger}$	+20.6	$\Delta G_6^{\ddagger}$	+21.7

Table 3.13: Free energy obtained from QM and the derived reaction constant (k) from TST

Gas phase		In Water		
$\Delta G^{\ddagger}_{rxn}$	k	$\Delta G^{\ddagger}_{rxn}$	k	Reaction rates
+14.7	1.03E+02	+19.3	4.33E-02	$v_1 = k_{a-x\cdot}[aam][xlinker\cdot]$
+12.8	2.54E+03	+17.9	4.61E-01	$v_2 = k_{a\cdot-x}[aam\cdot][xlinker]$
+15.9	1.35E+01	+19.0	7.19E-02	$v_3 = k_{m-x\cdot}[amps][xlinker\cdot]$
+14.7	1.03E+02	+18.1	3.29E-01	$v_4 = k_{m\cdot-x}[amps\cdot][xlinker]$
+12.7	3.01E+03	+20.6	4.82E-03	$v_5 = k_{x-x\cdot}[xlinker][xlinker\cdot]$
+14.1	2.82E+02	+21.7	7.52E-04	$v_6 = k_{x\cdot-x}[xlinker\cdot][xlinker]$

content in a hydrogel is normally high, i.e. 80-90 weight percent content.

Our results also suggest that for the propagation reaction in water, the reaction between [aam]· and [xlinker] is slightly faster than [amps]· and [xlinker]. This is in the opposite order for the initiation reaction with [xlinker]·. This might be a source for getting close reaction rates when equimolar quantities of [aam] and [amps] are used with an excess of [xlinker].

Therefore, the coarse grained MD obtained with the FENE potential should find the same trends obtained from TST and the same relative energies.

Chapter 4

Origin of the Positive Cooperativity in the Template-Directed Formation of Molecular Machines

Jose L. Mendoza-Cortes, William A. Goddard III

4.1 Introduction

Molecules with mechanical bonds are of great interest for synthetic chemists. This lead to the creation of the field termed mechanically interlocked molecules.[30] Rotaxanes are macromolecules that interacts trough noncovalent interactions with another host molecule. This pair is usually subject to chemical changes that make the rotaxane change the position on the host molecule without forming new bond between the rotaxane and the host.

The most common strategies by which rotaxanes can be synthesized are capping, clipping and slipping.[31] The discovery of highly efficient protocols through the clipping mechanism made feasible the preparation of rotaxanes of different order and complexity.[32, 33, 34] One of the most popular clipping reactions is the reversible imine bond formation, that when combined to template directed interactions (noncovalent interactions such as dispersion and coulombic) leads to a high yield synthesis.[35]

We investigate the formation of rotaxanes through imine bonds formation which interacts with Dumbbells (D and Dp) as it is shown in Figure 4.1.[36] Both hosts D and Dp have the recognition sites -NH_2^+- and C_6H_4-$(OCH_3)_2$ stoppers at each end, however they differ in their separation. For D: the separation fragments is given by -[$CH_2CH_2NH_2^+CH_2$]n- while for Dp is -[$C_6H_4CH_2NH_2^+CH_2$]n- (Figure 4.1). This separation seems to play a crucial role in the thermodynamics and kinetics (Figure 4.1 and Figure 4.2). On one side the template directed synthesis is observed while in the other case is not. Although the experiments have been able to differentiate both cases, the quantitative energetics for this phenomenon is not clear. Thus, in this chapter we present the role of the dispersion forces (pi-pi interaction, hydrogen bonds) as well as Coulombic interactions (counteranion) in the formation of these rotaxanes and we compare our results to the experimental observations.

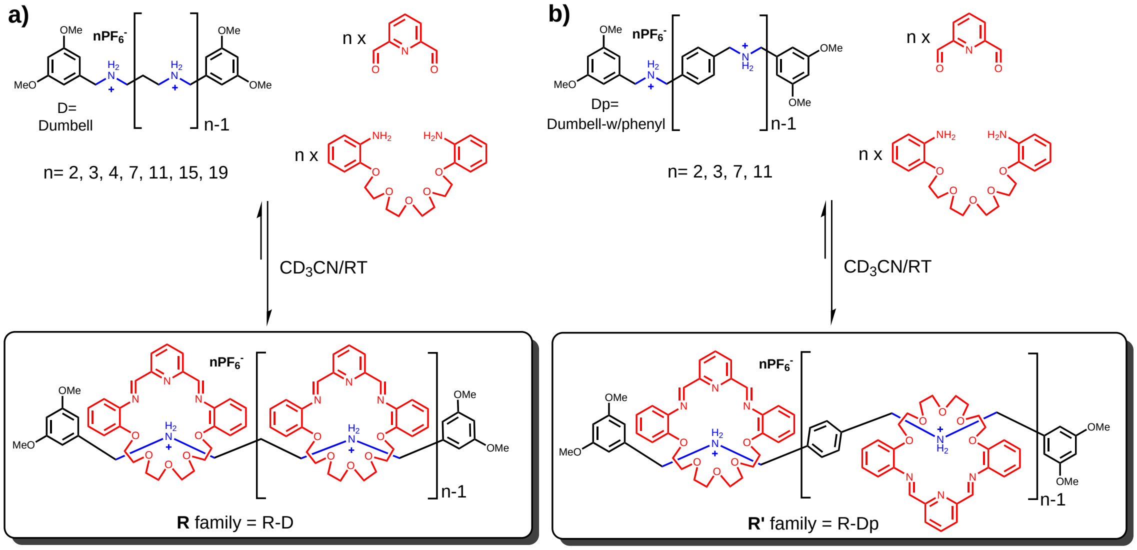

Figure 4.1: Reaction for the template directed formation of rotaxanes for the (a) **R** Family and for the (b) **R'** family

Table 4.1: Reaction kinetics on the formation of the **R** family, which is the combination of nR + D

compound no.	[n] rotaxane	rings	time to reach equilibrium [a]	isolated yield (%)	no. of imine bonds	yield per imine bond (%)
$2R^{2+}$	3	2	<5min	93	4	98.2
$3R^{3+}$	4	3	<5min	90	6	98.3
$4R^{4+}$	5	4	<5min	88	8	98.4
$7R^{7+}$	8	7	6h	94	14	99.6
$11R^{11+}$	12	11	10h	98	22	99.9
$15R^{15+}$	16	15	12h	93	30	99.8
$19R^{19+}$	20	19	14h	90	38	99.7

[a] Equilibrium times were determined by monitoring the clipping reaction by ^{1}H NMR spectroscopy until no changes in the spectra were observed

4.2 Methodology

Quantum Mechanics (QM) We start with the experimental structures and the optimized them using the MO6-L functional[7] and for C, H, O, N, P, F we used the 6-31G** basis set[37, 38] and electron Core potential for I: LAV3P**[10] as implemented in Jaguar[9]. All geometries were optimized using the analytic Hessian to determine that the local minima have no negative curvatures (imaginary

Table 4.2: Reaction kinetics on the formation of the **R'** family, which is the combination of nR + Dp

compound no.	[n] rotaxane	rings	time to reach equilibriumb [a]	isolated yield (%)	no. of imine bonds	yield per imine bond (%)
$2R'^{2+}$	3	2	<5min	86	4	96.3
$3R'^{3+}$	4	3	<5min	72	6	94.7
$7R'^{7+}$	8	7	20min	78	8	98.2
$11R'^{11+}$	12	11	30min	85	14	99.3

[a] Equilibrium times were determined by monitoring the clipping reaction by ^{1}H NMR spectroscopy until no changes in the spectra were observed

frequencies). The vibrational frequencies from the analytic Hessian were used to calculate the zero-point energy correction at 0 K. Solvent corrections were applied using the single point self-consistent Poisson-Boltzmann continuum solvation model for acetonitrile (ϵ=37.5 and R_0=2.18) as implemented in the PBF module[28] in the Jaguar code. This methodology has proved to give the best agreement with experiments.[39]

Molecular Mechanics (MM) For higher order rotaxanes, it is necessary to use molecular mechanics (QM) and the force field (FF) validation is the key for generating plausible structures. In this case we analyze the Dreiding[25] as well as the OPLS[40] Force Field and we compare with the quantum mechanical calculations. We used the conjugated gradient minimization scheme with at least 5000 steps or until convergence criteria of 0.05 kcal/mol were obtained. The charges for Dreiding were obtained from Qeq[12] while for OPLS they are inbuilt in this FF.

4.3 Results and Discussion

4.3.1 Experimental Coordinates vs MM vs QM

In order to validate our methodology for these systems we compare the Xray diffraction coordinates (XRD) with the minimized structures obtained from QM and MM. We show the results on Figure 4.2 and Figure 4.3. We found that MM gives a good estimate of the general geometry since it gives a small root mean square distance (RMSD) of around 0.35. On the other hand the QM method gives a larger error (RMSD=0.638). However as we expected the QM method gives the best estimation of the pi-pi interaction followed by the Dreiding FF, while the worst estimation of this interaction is given by the OPLS-FF (Figure 4.3). Because we suspect that the pi-pi interactions as well as other dispersion interactions are the main factor to determine the formation of these structures, we prefer to use the QM methodology.

Furthermore, the QM method is the only one which can gives physically meaningful energetics in gas phase as it can be seen in Figure 4.4. The MM method does not give binding energies for the Dreiding FF while the OPLS FF presents an strange behavior of an extremely high binding energy

(-500 kcal/mol) for the first rotaxane while a repulsive energy for the second ring (+149 kcal/mol). However the QM method is very consistent, giving a binding energy for the first and second rotaxane of -26.1 and -60.6 kcal/mol, respectively. Thus QM is the only method to represent correctly the energetics of these systems.

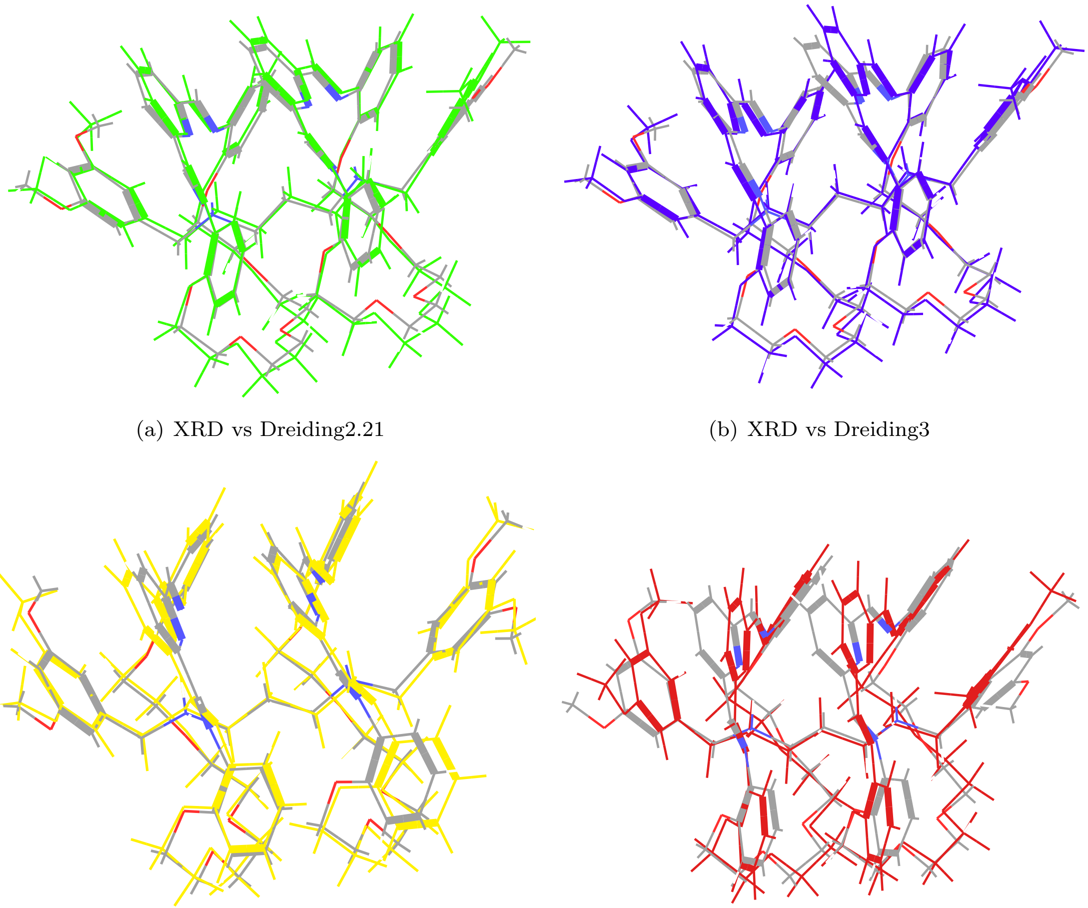
(a) XRD vs Dreiding2.21

(b) XRD vs Dreiding3

(c) XRD vs OPLS2005

(d) XRD vs M06-L

Figure 4.2: Comparison of XRD experimental determined structure versus different theoretical methods used. Colors are C: grey, O:red, N:blue and H: white. In the figures the unicolor represents the structure obtained after minimization with MM or QM

4.3.2 Origin of the Positive Cooperativity

The most puzzling part of these compounds is to find the reason behind the loose of positive cooperativity when the different Dumbbells are used (D versus Dp). Thus, we also calculate the geometries and energetics for the R's family up to 2 rotaxanes and they are shown in Figure 4.3. The geometries for the R' family (Dp + rotaxanes) are not available from crystal diffraction experiments but our QM methodology can estimate these structures with acceptable accuracy.

The main difference between the dumbbells D and Dp is the extra phenyl in the latter case.

Table 4.3: Root mean square distance (RMSD) for the comparison between experimental structure for 2R·$2PF_6$ and the QM and MM methods. Column 2 and 3 shows the estimation of the $R(_{\pi-\pi})$ interaction for benzene (Bz) in the stopper of the dumbbell (D), first rotaxane (R1) and second rotaxane (R2)

2R·$2PF_6$	RMSD Bz(D)-Bz(R1)	RMSD Bz(R1)-Bz(R2)	RMSD All atoms
Experimental XRD	0	0	0
Dreiding2.21/Qeq	0.153	0.109	0.375
Dreiding3/Qeq	0.186	0.608	0.311
OPLS2005	0.235	0.446	0.320
MO6L/6-31G**	0.152	0.106	0.638

Table 4.4: Comparison of binding energies for the Formation of 1R-$2PF_6$ and 2R-$2PF_6$. All the units are in kcal/mol.

Method	[1R]$2PF_6$ Gas phase	[2R]$2PF_6$ Gas phase
Dreiding2.21/Qeq	35.7	52.5
Dreiding3/Qeq	32.7	22.8
OPLS2005	-500	149
MO6L/6-31G**	-26.1	-60.6

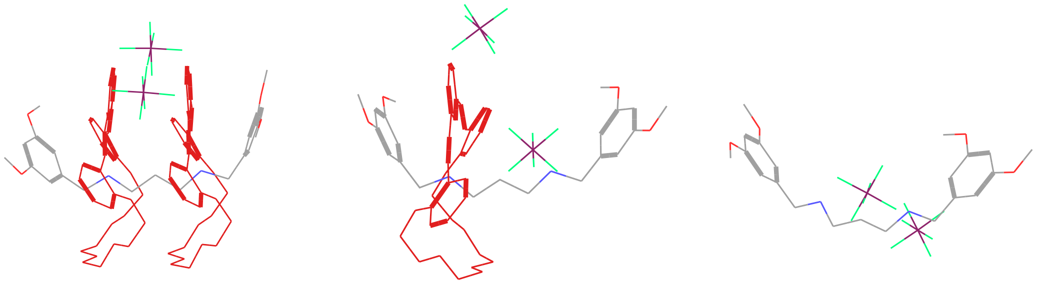

(a) 2R-D-$2PF_6$ (b) 1R-D-$2PF_6$ (c) 0R-D-$2PF_6$

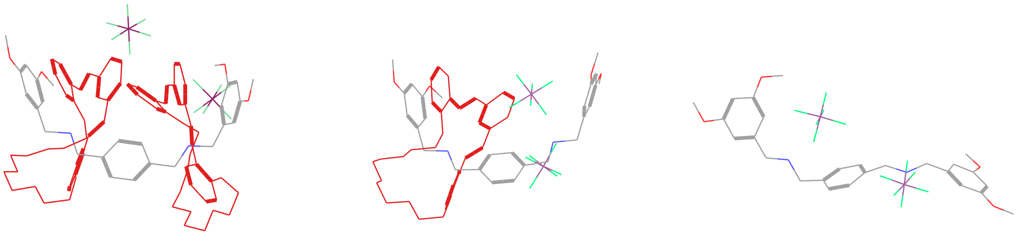

(d) 2R-Dp-$2PF_6$ (e) 1R-Dp-$2PF_6$ (f) 0R-Dp-$2PF_6$

Figure 4.3: Compounds for the R family (a,b and c; xR-D-$2PF_6$) and for the R' family (d,e and f; xR-Dp-$2PF_6$). Colors are C: grey, O:red, N:blue, F: green, P:purple and H:not shown. rotaxanes are colored in full red in order to distinguish them from the atoms in the dumbbell.

This makes the rotaxanes rings to be more separated and most likely this determines the interaction strength between these rings. To the best of our knowledge, the quantification for the forces being involved in these compounds has not been determined. In other words, we do not know the energetics (enthalpies or free energies) for the interaction of the -$(CH_2)NH_2^+(CH_2)$- site or the -$(C_6H_4CH_2)NH_2^+(CH_2)$- site with the rotaxane. There are several hydrogen bond being involved in this interaction of the types N-H$\cdots$O and N-H$\cdots$N which is important to quantify.

Thus, we calculate the strength of the interactions between a rotaxane ring and the -NH_2^+- site as well as the interaction with the stopper for the **R** and **R'** compounds. The results are shown in Figure 4.5. We can see that the interaction of the rotaxane ring with the stopper is almost negligible, since the ΔG^{gas} is -1.7 kcal/mol while with CH_3CN is -3.2. We must remember that interaction is the same for the the **R** and **R'** family of compounds. Also the interaction of the rotaxane ring with the $(CH_3)NH_2^+(CH_3)$ (-NH_2^+-) site or the -$(C_6H_5CH_2)NH_2^+(CH_3)$- (-NH_2^+'-) site is very similar ΔG^{gas} -26.7 and -25.4 kcal/mol, respectively. The values for $\Delta G^{solvated}$ are more different because of the inherent difference in the size for the -NH_2^+- and the -NH_2^+'- site so the bigger molecule gains more energy when it is solvated in CH_3CN, this gives -22.3 and -26.4 kcal/mol, respectively.

Next we compare this partition of interaction to the full system of 2 rotaxanes, 2 stoppers and 2 recognition sites -NH_2- for the **R** family in order to find the source of the positive cooperativity. Our results show that in gas phase, the first rotaxane ring in the 1R-D-2PF_6 systems only interacts with the recognition site, since the strength of this interaction is almost the same as isolate strength of the -NH_2^+- site; ΔG^{gas} -26.7 and -26.1 kcal, respectively. This implies that there is not interaction between the rotaxane ring and the stopper when the first rotaxane ring is added. This can be observed from the optimized structure shown in Figure 4.3b, where the benzene ring of the rotaxane have a distance of the 4.1 Å with the benzene ring of the stopper (The optimal interaction distance is 3.4 Å). The ΔG^{solv} for the isolated -NH_2^+- site and the full system with the -NH_2^+- recognition site differ for more than 10 kcal/mol, most likely because the difference in the size of the systems, the full system 1R-D-2PF_6 has more surface than the 1R-$NH_2^+(CH_3)_2$, thus the solvation is more favorable for the full system than for the individual parts. However when the second rotaxane ring is added to the sys-tem (2R-D-2PF6 system), the interaction between the rotaxane rings and the stopper is recovered. This can be deduced because the energetics for the full system 2R-D-2PF6 contains 2 interactions of rotaxane/-NH_2^+- nature, 2 interactions of rotaxane/stopper type and one interaction of Rotaxane-Rotaxane (R-R). This correspond to a partition of ΔG^{gas} of -26.7 x 2 kcal/mol (2 rotax-ane/-NH_2^+-) + -1.7 x 2 kcal/mol (2 rotaxane/stopper) and -8.6 kcal/mol (1 R-R) equals to -65.4 kcal/mol [the full system gives -25.4(first rotaxane)-60.6(second rotaxane) = -86.0 kcal/mol]. If the solvation is included this can be partitioned as ΔG^{solv} of -22.3 x 2 kcal/mol (2 rotax-ane/-NH_2^+-) plus -3.2 x 2 kcal/mol (2 rotaxane/stopper) and -8.8 kcal/mol (1 R-R) equals to -59.8 kcal/mol [the QM calculations for the full system gives -51.4 (first rotaxane) - 33.1 (second rotaxane) = -84.5 kcal/mol]. The total free energy of the full system should more than the sum of the individual components for the positive-cooperativity to be present. Thus is an example where the sum of interaction when all the components are together is more than the sum of the individual ones.

On the other hand for the **R'** family, the first rotaxane ring interacts strongly not only with the benzene ring of the stopper but also with the benzene ring of the dumbbell Dp. This can be better observed in Figure 4.3b. The distance of the pyridine ring from the rotaxane ring with the benzene ring of the stopper is 3.9 Å, while the distance with the benzene ring of the Dumbbell Dp is 3.6 Å. This is reflected in the energetics of the system. Figure 4.5 shows that for the system 1R-Dp-2PF$_6$ we obtain ΔG^{gas} equals to -60.6 kcal/mol and ΔG^{solv} equals to -48.2 kcal/mol. The energetics obtained for the full system cannot be described as 1 rotaxane/-NH$_2^+$'- interaction (ΔG^{gas}=-25.4 kcal/mol, ΔG^{solv}=-26.4 kcal/mol) and 1 rotaxane/stopper interaction (ΔG^{gas}=-1.7, ΔG^{solv}=-3.2 kcal/mol). The difference of ΔG^{gas}=-33.5 and ΔG^{solv}=-18.6 can be assigned to the extra interaction of the rotaxane ring with the benzene ring next to the -NH$_2^+$'- site of the Dumbbell Dp. When the second rotaxane ring is added the main difference between the **R** and the **R'** family becomes obvious. For the second rotaxane ring in the 2R-Dp-2PF6 compound, we have the interaction energy of only ΔG^{gas}=-20.5 kcal/mol, this is almost the same interaction strength as the rotaxane/-NH$_2^+$'- interaction site which is ΔG^{gas}=-25.4 kcal/mol. When the species are solvated, the same comparison is valid, for the extra rotaxane ring in the full system the interaction is ΔG^{solv}=-25.1 kcal/mol, this is very similar to the rotaxane/-NH$_2^+$'- interaction site with ΔG^{solv}=-26.4 kcal/mol. This shows that there is not Rotoxane-Rotoxane interaction for the **R'** family due to the long distance between these rotaxane rings. This is also observed from the thermodynamics for this rotaxane - rotaxane interaction at 5.0 Å, that gives positive $\Delta \mathrm{H}^{\mathrm{gas}}$, ΔG^{gas} and ΔG^{solv} (Table 4.5).

Thus we have found the origin of the positive cooperativity in the Template-directed formation of these rotaxane/dumbbell complexes; the distance between the rotaxanes rings should be optimal for them to interact and this is will give the positive interaction. This can be better visualized in Figure 4.4 where the important interaction distances are shown. The distance between the first and second -NH$_2$- site of the 2R-D-2PF$_6$ (**R** family) is of 4.8 Å, while the distance between the first and the second rotaxane ring is of 4.0 Å, this is because the rotaxane ring are slightly twisted trying to interact with each other (Figure 4.3a). This rotaxane-rotaxane distance is close to the ideal value of 3.6 Å. On the other hand, for the 2R-Dp-2PF$_6$ (**R'** family), the distance between the first and the second -NH$_2$'- site increase to 7.1 Å, because the extra phenyl ring in between. This makes the distance between the first and second rotaxane to be longer for this compound; 5.0 Å. This is a long even though the rotaxane rings are twisted to a small degree to maximize interactions (Figure 4.3d). This is a difference of 1 Å; between the distance among rotaxanes in the **R** versus the **R'** family. This long distance between rotaxanes in the **R'** compound makes their interactions to be negligible.

Table 4.5: ΔG^{gas} and ΔG^{solv} with respect to isolated rotaxanes rings and dumbbell. The solvent used is CH_3CN. All the units are in kcal/mol.

Compound	$\Delta \mathrm{H}^{\mathrm{gas}}$	ΔG^{gas}	ΔG^{solv}
1R—(Stopper site)	-16.3	-1.7	-3.2
R family			
1R—1R (4.0 Å) [a]	-26.6	-8.6	-8.8
1R—(NH_2 site)[b]	-45.9	-26.7	-22.3
1R-D-2PF$_6$	-41.2	-26.1	-33.1
2R-D-2PF$_6$	-85.7	-60.6	-51.4
R' family			
1R—1R (5.0 Å) [c]	1.9	4.7	3.2
1R—(NH_2' site)[d]	-43.3	-25.4	-26.4
1R-Dp-2PF$_6$	-75.7	-60.6	-48.2
2R-Dp-2PF$_6$	-45.7	-20.5	-25.1

[a] This is the distance for rotaxana - rotaxane interaction distance for the 2R-D-2PF$_6$.

[b] To estimate the strength of this site, we have used the compound $(CH_3)_2NH_2{}^+$

[c] This is the rotaxane-rotaxane interaction distance for the 2R-Dp-2PF$_6$ system.

[d] To estimate the strength of this site, we have used the compound $(CH_3)(C_6H_5CH_2)NH_2{}^+$

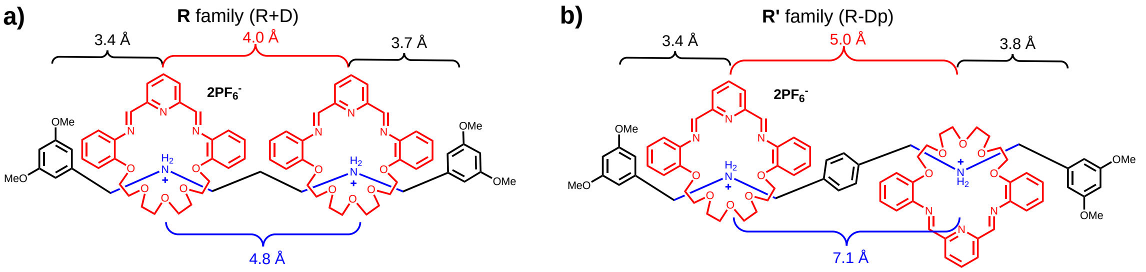

Figure 4.4: Distances for the optimized structure for the (a) 2R-D-2PF$_6$ (**R** family) and for (b) 2R-Dp-2PF$_6$ (**R'** family). In the **R** family we observe rotaxane-rotaxane interaction while in the **R'** family, the distance between rotaxane rings is too large for them to interact. Distance between stopper and rotoxane ring is marked in black. Distance between first and second rotoxane is marked in red. Distance between first and second -NH_2- site is marked in blue. The optimal rotaxane-rotaxane interaction distance is 3.6 Å.

4.3.3 Role of the Counter Anion

Once we have found the source of the positive cooperativity, we decide to study the role of the counteranion in these systems. For that purpose, we calculate the geometries of the 2R-D, 1R-D and D systems with different anions beside PF_6^-; I^-, F^- and with overall charge of +2 (Figure 4.5). This is also done with the 2R-Dp, 1R-Dp and Dp systems (Figure 4.7).

In general the rotaxane - rotaxane distance is affected while the position of the anion are closer to the -NH_2^+- site of each compound. When we compared the optimized structures for the **R** family

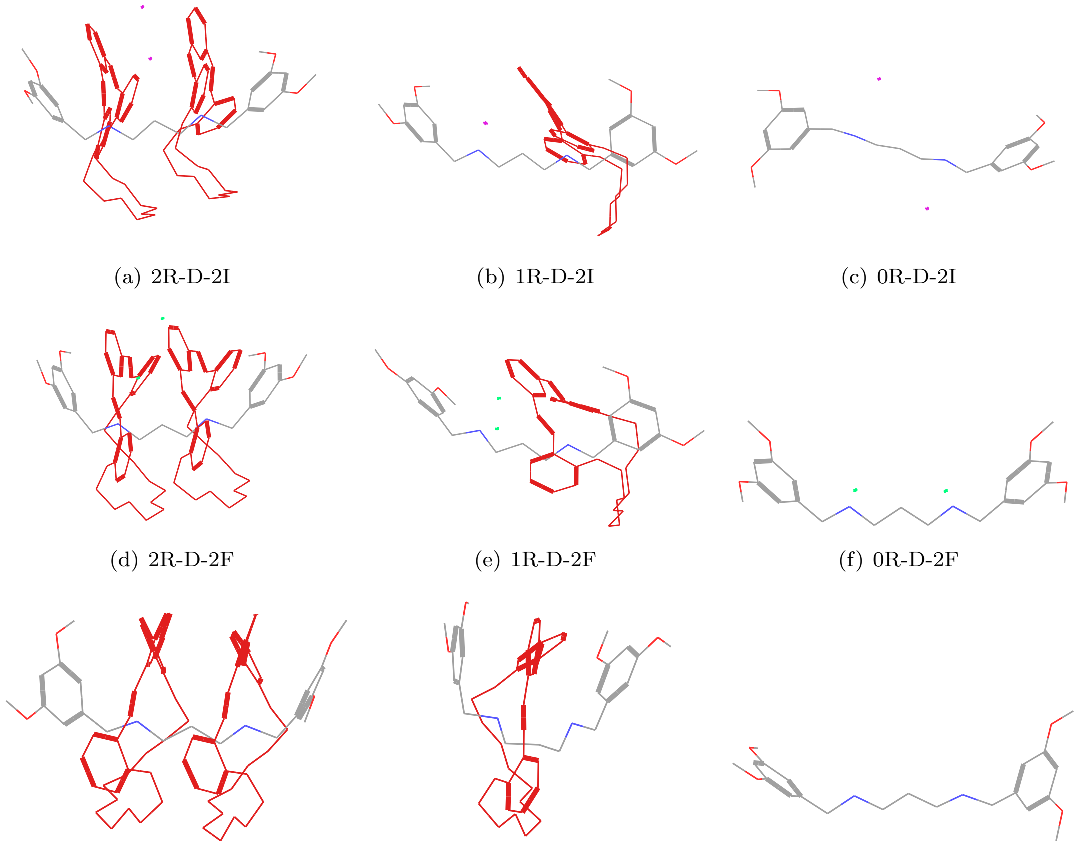

(a) 2R-D-2I (b) 1R-D-2I (c) 0R-D-2I

(d) 2R-D-2F (e) 1R-D-2F (f) 0R-D-2F

(g) 2R-D-2 (h) 1R-D-2 (i) 0R-D-2

Figure 4.5: xR-D-2anion compounds. Colors are C: grey, O:red, N:blue, F: green, P:purple and H:not shown. rotaxanes are colored in full red in order to distinguish them from the atoms in the dumbbell.

with the $2PF_6^-$ counter anion (Figure 4.3a), we can see that the skeleton is very similar to the one obtained for the 2R-D-2I system and derivatives. However, when we use the F^- counter anion for this family of compounds we see that the rotaxane-rotaxane distance is the more affected. This is correlated to the thermodynamics and to the electron density as we will see below. In the same manner, we calculate the optimized structures for the **R'** family and we found similar trends. The structures where $2PF_6^-$ were used (Figure 4.3b) resemble the ones where I^- has been used. On the other hand, the structures were F^- is used are more different to those with $2PF_6^-$ and I^-. We calculate the structures with no counter anions but a total charge of +2 to explore the effect of a homogeneous field versus a counter anion to neutralize the system. It is difficult to quantify the difference based on pure rotaxane - rotaxane distances or counter anion - NH_2^+ site distances so thermodynamics and electron densities are needed.

Therefore, we also calculate the thermodynamics of these systems and the results are shown in Figure 4.6. We found that for the 2R-D compounds (**R** family) the positive cooperativity only

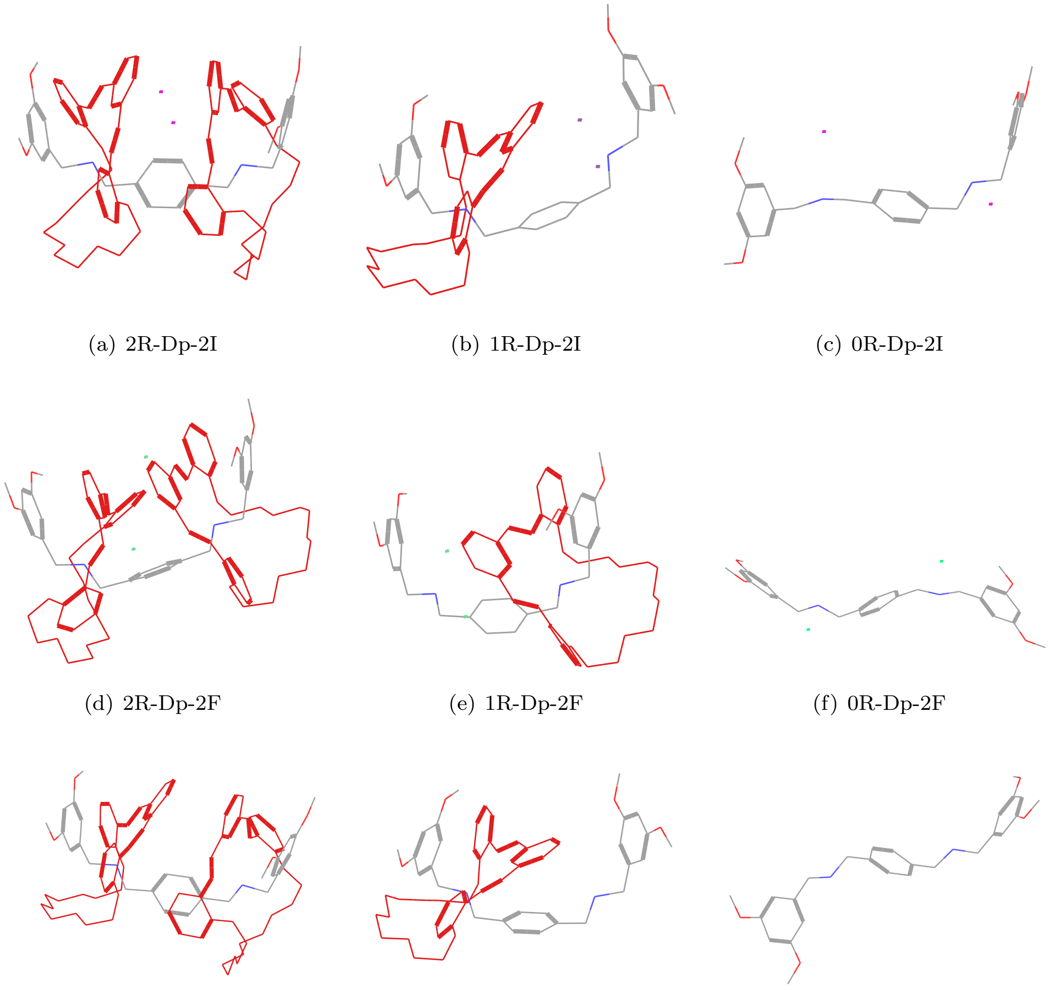
(a) 2R-Dp-2I (b) 1R-Dp-2I (c) 0R-Dp-2I

(d) 2R-Dp-2F (e) 1R-Dp-2F (f) 0R-Dp-2F

(g) 2R-Dp-2 (h) 1R-Dp-2 (i) 0R-Dp-2

Figure 4.6: xR-Dp-2anion compounds. Colors are C: grey, O:red, N:blue, F: green, P:purple and H:not shown. rotaxanes are colored in full red in order to distinguish them from the atoms in the dumbbell.

occurs when the counter anions PF_6^- or I^- is used. In other words we get more negative free energy when the second rotaxane ring is added than with the first one. However, when the anions F^- are used, the positive cooperativity disappears as it shown in Figure 4.7. This phenomenon happens in gas phase and solvated phase. Therefore the counteranion should be playing a central role in the positive cooperativity for the **R** family. For the 2R-Dp compounds (**R'** family) there was never a positive cooperativity with the PF_6^- counter anion and this remains for I^-, F^- and no counter anion (field of +2) as it can be observed in Figure 4.6 and at the bottom of Figure 4.7.

In order to investigate further the role of the counter anion, we calculate the Electrostatic potential (ESP) and the Mulliken Charges for these systems. Then we use these charges to calculate the dipole moments. The results are shown in Figure 4.7. The results obtained from ESP charges are similar to the ones obtained with Mulliken charges however we use the ESP results in this discus-

Table 4.6: ΔG^{gas} and ΔG^{solv} with respect to isolated rotaxanes rings and dumbbell. All the units are in kcal/mol.

Compound	$\Delta \mathrm{H}^{\mathrm{gas}}$	ΔG^{gas}	ΔG^{solv}
1R-D-2I	-37.0	-22.0	-1.5
2R-D-2I	-79.0	-53.8	-54.9
1R-D-2F	-37.8	-22.8	-20.4
2R-D-2F	-39.3	-14.1	-21.4
1R-D-2	-114.1	-99.1	-46.3
2R-D-2	-88.4	-63.3	-44.1
1R-Dp-2I	-74.3	-59.3	-45.1
2R-Dp-2I	-32.9	-7.7	-6.5
1R-Dp-2F	-29.7	-14.6	-16.9
2R-Dp-2F	-32.5	-7.3	-2.5
1R-Dp-2	-89.1	-74.0	-40.7
2R-Dp-2	-85.0	-59.9	-37.6

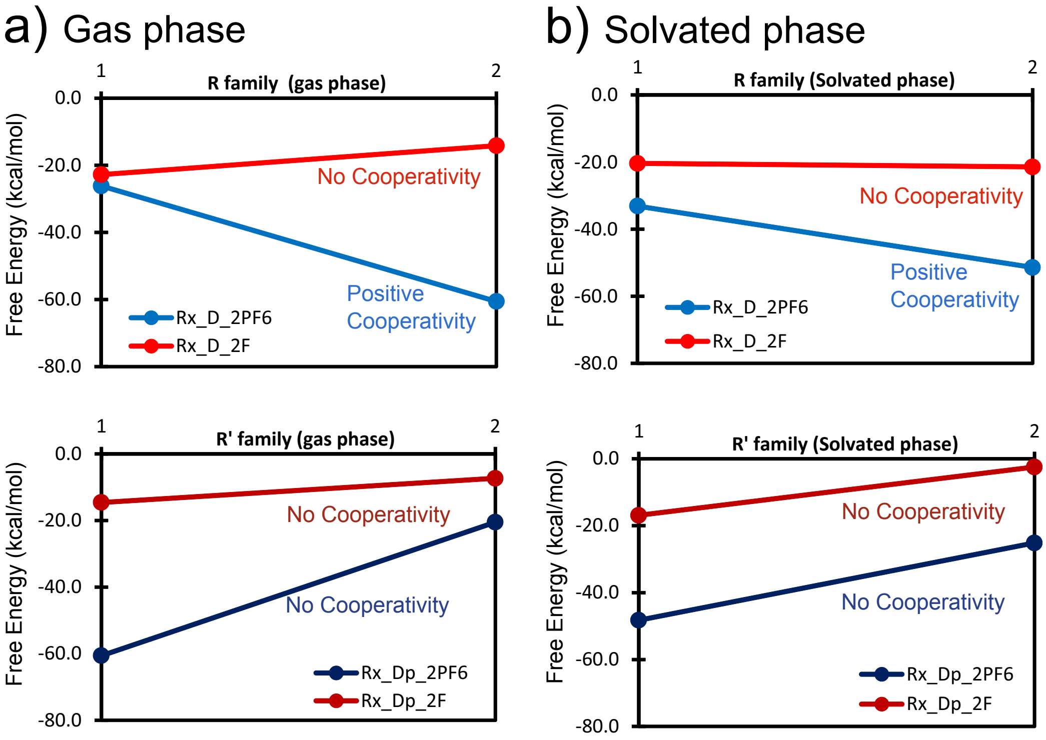

Figure 4.7: Free energies in the gas phase for (a) gas phase and (b) solvated phase for the **R** Family: 2R-D-2PF$_6$ and 2R-D-2F (top) and for the **R’** Family: 2R-Dp-2PF$_6$ and 2R-Dp-2F (bottom). The positive cooperativity is only observed with the PF$_6^-$ (or I$^-$, not shown) counter anion.

sion. We can observe that the dipole moment (μ) increase as the size of the counter anion increase for both **R** and (**R’** family of compounds. This is; the dipole moment is related to the size of the counteranion. This can be visualized better in Figure 4.8. The highest dipole moment is with the counteranion PF$_6^-$ ($\mu = 28$ Debye) where the electrostatic potential is very well defined by localized charges. On the hand, the dipole decrease when using F$^-$ ($\mu = 14.8$ Debye) because the electrostatic potential is more spread due to the high contact/interaction between this small counter anion and the -NH$_2^+$- site. This contact make the ESP charges to go for the first and second -NH$_2^+$- from +1.00 and +0.67 (with PF$_6^-$) to +0.49 and +0.36 (with F$^-$), respectively. This means that the smaller counteranion lowers the strength of the interaction between the rotaxane ring and the recognition site -NH$_2^+$- by virtue of lessening the charge on N, which then cause the disappearances of the positive effect even if there is still rotaxane - rotaxane interaction. We must note that the -NH$_2^+$- serves as a site where the rotaxane can form by imine bond formation. The same effect happens for the **R'** family of compounds, the dipole moment is larger for the counter anion PF$_6^-$ ($\mu = 24.9$ Debye) than with F$^-$ ($\mu = 5.8$ Debye) as it is shown in Figure 4.8b.

Table 4.7: Dipole moments (μ, /Debye) obtained from Electrostatic potential (ESP) charges and Mulliken charges. The ESP and Mulliken charges have been normalized.

	μ from ESP (/Debye)				ESP charges for N	
Compound	X	Y	Z	**Total**	1st -NH$_2^+$-	2nd -NH$_2^+$-
2R-D-2PF$_6$	25.4	11.7	-0.2	28.0	1.00	0.67
2R-D-2I	18.1	9.5	-2.8	20.6	0.58	0.65
2R-D-2F	13.4	6.3	-0.2	14.8	0.49	0.36
2R-D-2	0.1	-1.7	-0.2	1.7	0.40	0.23
2R-Dp-2PF$_6$	16.7	17.8	-5.0	24.9	0.82	0.51
2R-Dp-2I	11.1	9.8	-0.2	14.8	0.73	0.42
2R-Dp-2F	3.0	4.8	-1.3	5.8	0.45	0.32
2R-Dp-2	1.0	0.1	0.5	1.2	0.37	0.21

	μ from Mulliken (/Debye)				Mullikan charges for N	
Compound	X	Y	Z	**Total**	1st -NH$_2^+$'-	2nd -NH$_2^+$'-
2R-D-2PF$_6$	26.0	16.3	-0.4	30.7	0.98	0.97
2R-D-2I	20.6	13.5	-2.5	24.8	0.98	0.97
2R-D-2F	14.5	10.2	-0.2	17.7	0.96	0.95
2R-D-2	4.0	2.8	-0.2	4.9	0.97	0.95
2R-Dp-2PF$_6$	16.0	22.5	-5.4	28.1	1.00	0.99
2R-Dp-2I	11.7	14.1	-1.2	18.4	0.98	0.98
2R-Dp-2F	2.9	9.4	-0.3	9.8	0.95	0.97
2R-Dp-2	2.6	5.4	0.3	6.0	0.96	0.96

Thus the role of the counter anion is to control the charge population on the -NH$_2^+$- recognition site which determines the interaction with the rotaxane ring. Then the larger (softer) the counter anion the less interaction with the recognition site and the more interaction between -NH$_2^+$- and the rotaxane ring will be. To the best of our knowledge this is the first time this effect have been observed.

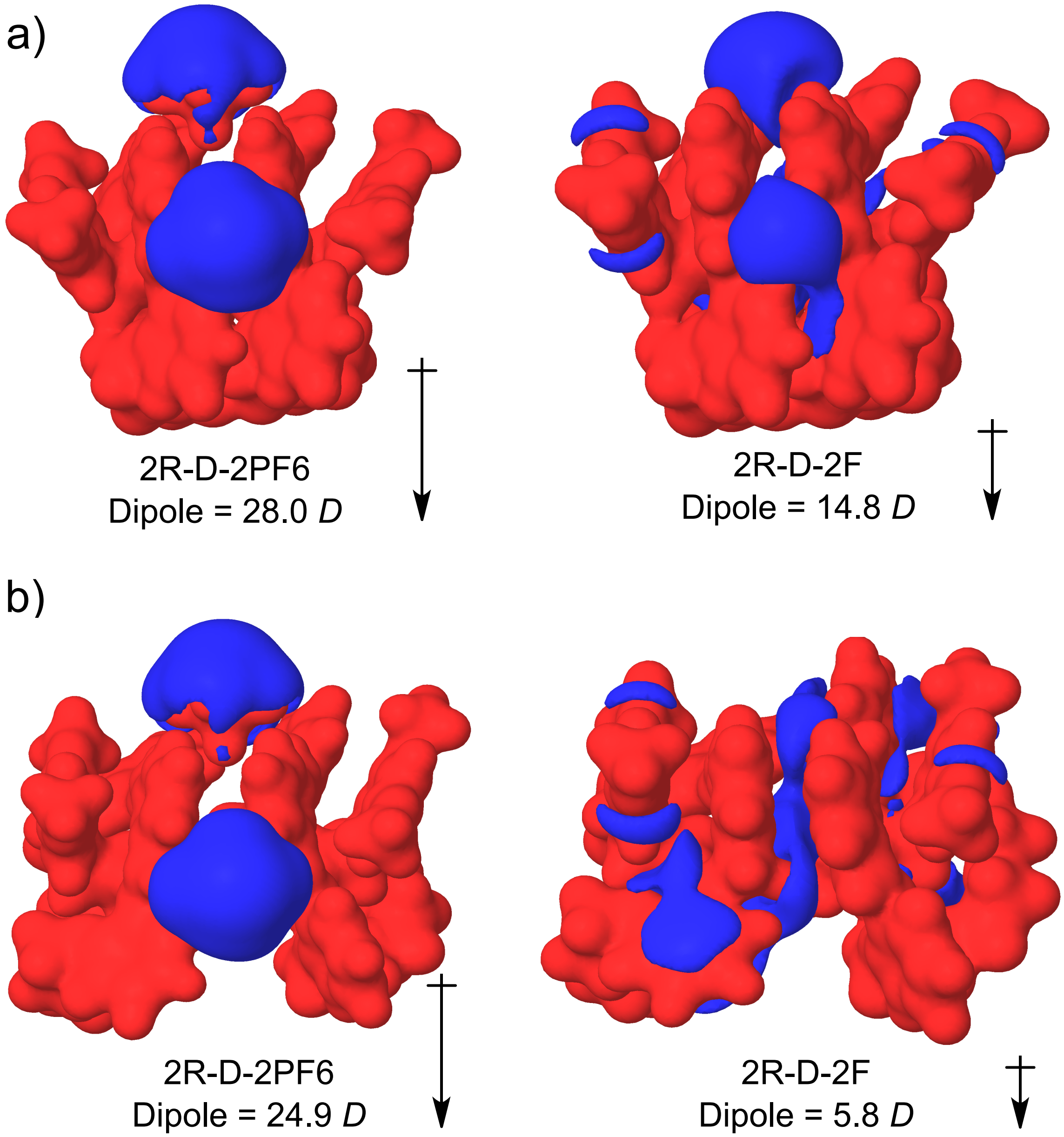

Figure 4.8: Dipole moments (μ) from ESP charges obtained for the (a) **R** Family (2R-D-2PF$_6$ and 2R-D-2F) and for the (b) **R'** family (2R-Dp-2PF$_6$ and 2R-Dp-2F)

4.4 Conclusions

In general, all FFs studied (Dreiding and OPLS) give poor representation of the thermodynamics but acceptable representation of the geometries. On the other hand the QM method gives a better representation of the pi-pi interactions as well as a more consistent and physically meaningful thermodynamics.

The distance between the rotaxanes rings should be optimal for them to interact and this origin of the positive cooperativity in the template-directed formation of these rotaxane/dumbbell complexes.

The rotaxane-rotaxane distance in the **R** family is of 4.0 Å, this is close to the optimal value of 3.6 Å. On the other hand, this distance is 5.0 Å for the **R'** family making this interaction to be negligible. Thus the efficiency for the template directed synthesis is tuned by controlling the distance between recognition sites.

Most importantly, we found that the role of the counter anion is to tune the charge population on the -NH_2^+- recognition site so that the larger (softer) the counter anion the more charge on the recognition site and the more interaction with the rotaxane ring is obtained. The interaction with the recognition site serves as the first directed template mechanism (clipping) for the formation of the rotaxane rings. This has many implications for the future synthesis of rotaxanes because we predict that we can control the positive cooperativity by changing the charge population on the recognition site by tuning the softness of the counter anion. Thus we can control the efficiency of future directed synthesis of rotaxanes for the clipping mechanism by using different degree of softness for the counter anion.

Chapter 5

Design of New Models for the Oxygen Evolving Complex

Jose L. Mendoza-Cortes, Robert Nielsen, Jacob Kanady, Emily Y. Tsui, Theodor Agapie, William A. Goddard III

5.1 Introduction

Photosystem II is a homodimer where photosynthetic water oxidation occurs.[41] Each monomer contains 20 subunits with a total molecular mass of 350 kDa. Besides the protein subunits, there are other cofactors such as four manganese atoms, three to four calcium atoms (one of which is in the Mn_4Ca cluster) and others such as chlorophylls and β-carotenes.[41] Water oxidation is catalyzed by a center containing the Mn_4Ca cluster, which is known as the Oxygen Evolution Complex (OEC). The OEC is one of nature's capacitors. It couples successive one-electron reductions of an adjacent chlorophyll center (known as P_{680}) to four-electron oxidation of water to dioxygen.[42] At a fundamental level, the chemical reactions taking place are shown in Figure 5.1. First, the most reduced OEC state is oxidized four units by P_{680}^{+}, giving a state that can be characterized as OEC(+4) or S_4. The S_4 state reacts with water to produce dioxygen (Figure 5.1a). However, the path that the OEC undergoes to reach this virtual OEC(+4) is not well understood and it has been a matter of debate.[42] On the other hand, there is a consensus that the oxidation of the OEC is stepwise; each of the oxidation steps are shown in Figure 5.1b. Each oxidation state of the OEC is known as S-state or Storage-state (S_n) with S_4 being the most oxidized and S_0 the most reduced state. The transition from S_4 to S_0 is the most important and more controversial step because it is when the water is converted to dioxygen.

Many mechanisms have been proposed for the transition from S_4 to S_0 but almost all of them proposed the need for high oxidation state for Mn, such as Mn(IV) or even Mn(V).[43] This is consistent with the necessary transfer of $4e^-$ to the OEC from the water oxidation. This transition, however, has proven to be challenging to observe because it happens very quickly, but some progress have been made in observing S_3 to S_0 but not the S_4 itself.[44, 45, 46]

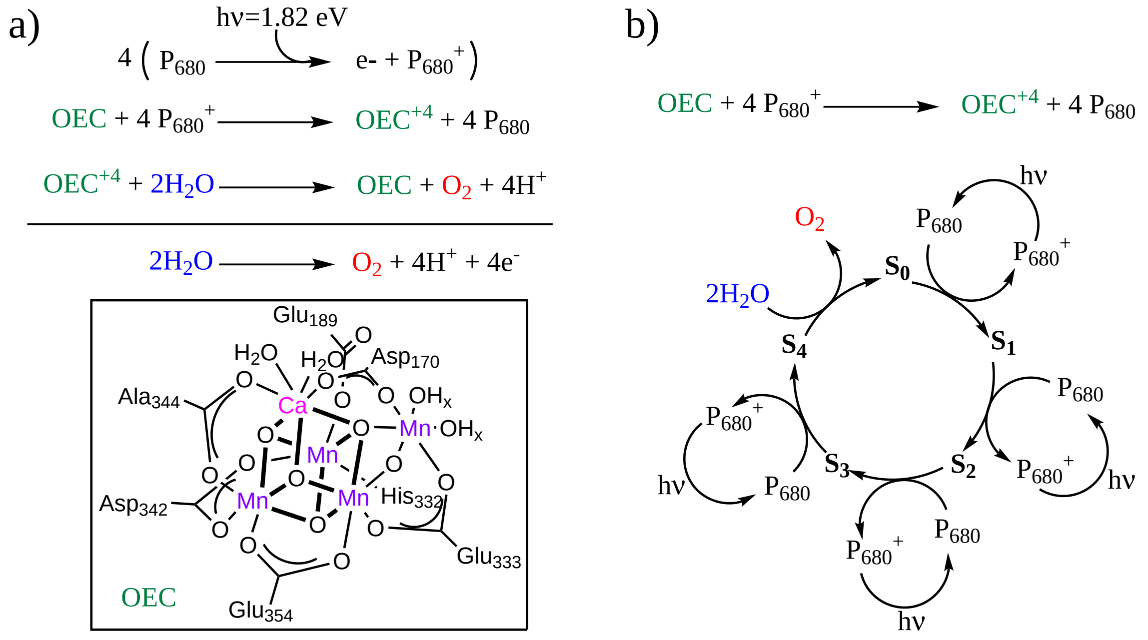

Figure 5.1: (a) Fundamental chemical reactions that take place in the production of O_2 that start with the conversion of solar energy ($h\nu$) to an electron and a hole in the chlorophyll center called P_{680}. (b) The catalytic cycle of the Oxygen-evolving complex (OEC) is shown where every oxidation is defined as a S-state (S_n). (Inset) The full description of the OEC is shown.

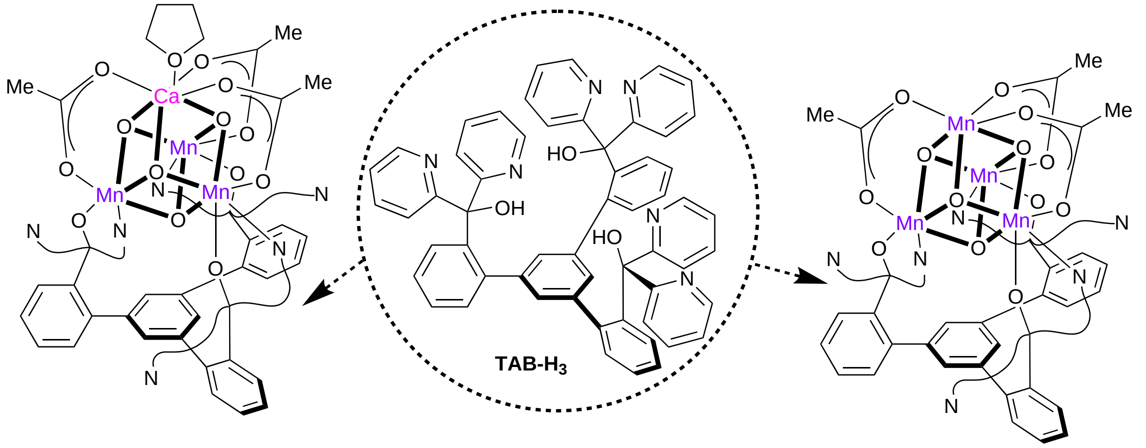

Figure 5.2: Complexes synthesized in the Agapie group containing (left) a Mn_3Ca and (right) a Mn_4 cubane. Notice how the Ca in Mn_3 at the top have been substituted by one Mn to give Mn_4.

A molecular model of the Mn_4Ca cluster would allow study of the electronic structures involved in all the oxidation states of the OEC. The synthesis of such a biomimetic compound can be attained by designing ancillary ligands. One such approach performed by the Apapie group was able to obtain a Mn_3Ca complex. It is the first example where the Ca atom has been incorporated with Mn into a cubane that resembles the OEC (Figure 5.2). They were also able to synthesize an all Mn cubane Mn_4. This opens the possibility of studying the role of the Ca in the oxidation states of the Mn.

Thus in this work we validate a methodology to reproduce and predict the reduction potential of the biomimetic model for the OEC using the rigid ligand 1,3,5-triarylbenzene spacer which incorporates six pyridine and three alcohol groups (TAB-H_3) shown in Figure 5.2. We then can use this method to design new compounds that structurally and electronically resemble to a high degree the most oxidized state of the OEC.

5.2 Methodology

Quantum Mechanics (QM) Nonperiodic QM calculations were carried out using the B3LYP,[47, 48] M06 and M06-L[7] hybrid DFT functionals with the Jaguar code.[9] Here we used the 6-31G** for C, H, O, N while and LACVP**[10] basis set for Mn and Ca as implemented in Jaguar. All geometries were optimized with B3LYP and using the analytic Hessian to determine that the local minima have no negative curvatures (imaginary frequencies). The vibrational frequencies from the analytic Hessian were used to calculate the zero-point energy corrections at 0 K. Solvent corrections were applied using the single point self-consistent Poisson-Boltzmann continuum solvation model as implemented in the PBF module1[29] in the Jaguar code.

5.3 Results and Discussion

5.3.1 Validation of the Computational Methodology: Geometry

In order to validate our methodology to predict and reproduce the properties of these compounds, we compare the X-ray diffraction (XRD) coordinates with the minimized structures obtained from QM calculations.

We first calculated the optimized structure with our QM method of the $CaMn_3O_4$-Full ligand compound as it is shown in Figure 5.3a. We measured the deviation of the experimental structure by virtue of the root mean square (RMS). The larger the RMS between the experimental structure and the geometry obtained from QM calculations, the worse the methodology. For this compound which has 147 atoms, we found a RMS of 0.417 Å. This means that we can reproduce the geometry of the compound with the entire ligand within 1.0 Å of accuracy. We found the biggest difference in the atoms of the tetrahydrofuran bound to the Ca. There are also some small differences in the unbound pyridines of the full ligand. These are atoms that are unlikely to participate in the important processes of this compound. In other words, it is very plausible that most of the chemistry will be happening in the core $CaMn_3O_4$, thus accuracy in this area is most important. Thus we calculate the RMS on the core and the first coordination shell of this cluster; 20 atoms. The comparison of positions between experimental and the calculated geometry give us an RMS of 0.114 Å. This can be broken down to RMS of 0.007 Å for the comparison of bonds and RMS of 0.384° in the estimation of bond angles. This gives us confidence that our QM methodology can reproduce the geometry of the $CaMn_3O_4$-Full ligand compound.

Next, we use our QM methodology to calculate the optimized structure of the Mn_4O_4-Full ligand as it is shown in Figure 5.3b. We found that when comparing the position of the 134 atoms between the experimental and the QM structure, the RMS is 0.530 Å. The main difference between these structures is again between the unbound pyridines. When comparing only the Mn_4O_4 cluster and the first coordination shell between the experimental and QM structure it is found an RMS of 0.086 Å. This is composed from the estimation of bonds with an RMS of 0.012 Å and RMS of 0.060° for the estimation of bond angles. In general, the estimation of the general structure for the Mn_4 is slightly worse than for the $CaMn_3$ case, however when estimating the core cluster the reverse happens.

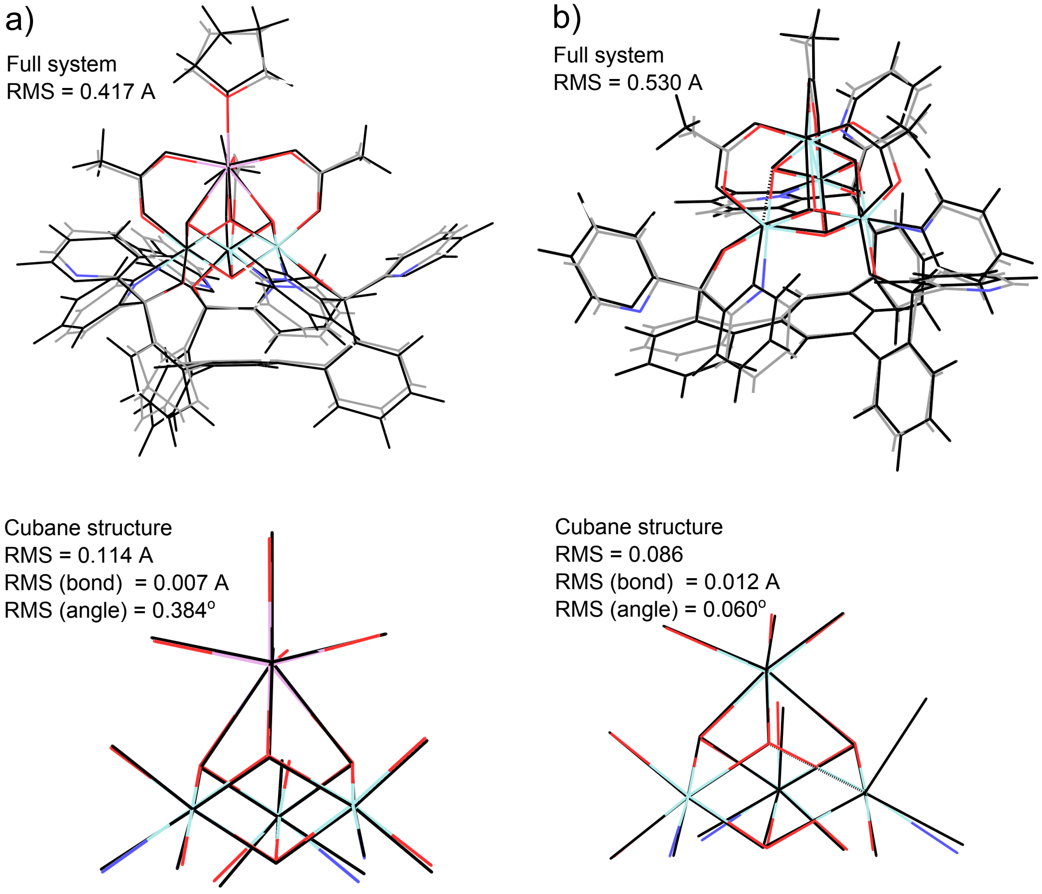

Figure 5.3: Comparison of geometries obtained from experiment (colored: Ca; magenta, Mn; light blue, O; red, C; grey, H; white) and theory (black) using the full ligand. We show the root mean square (RMS) to compare all the atoms in the structure (top) and the cubane (bottom).

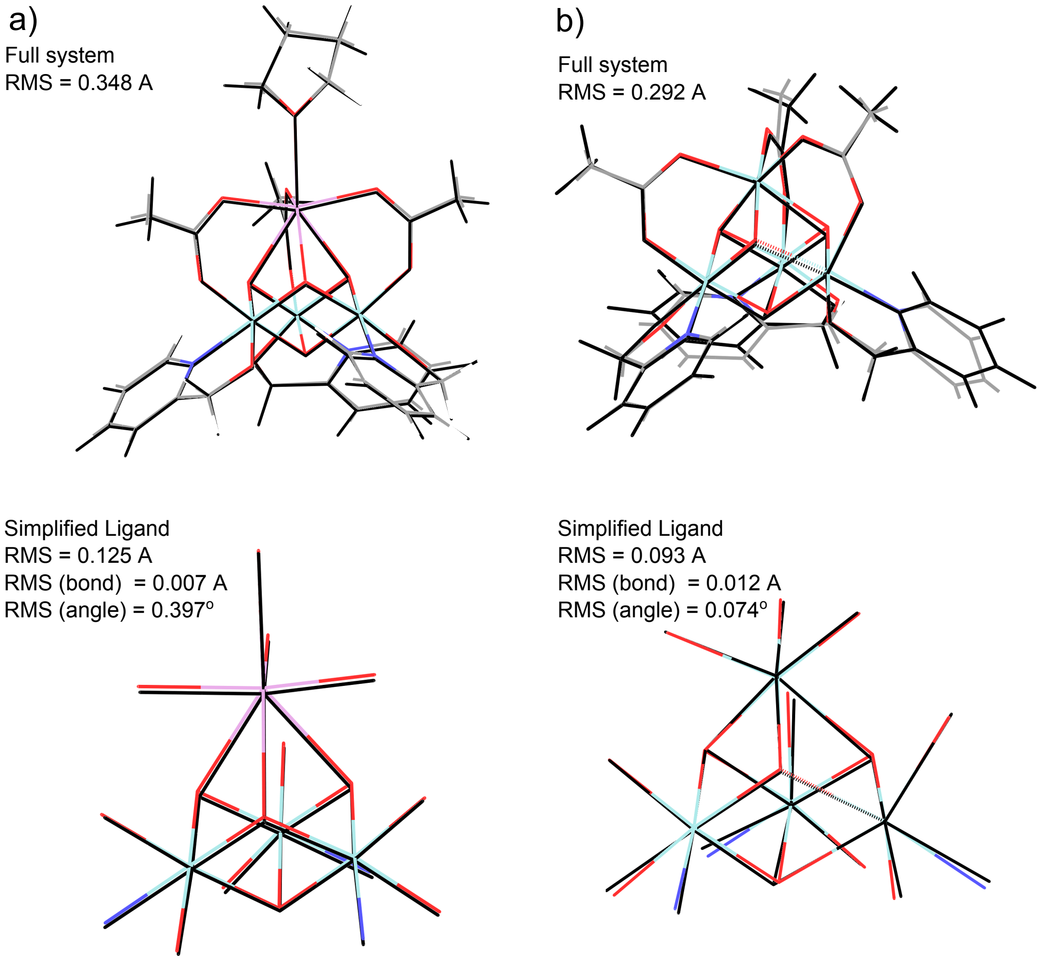

Figure 5.4: Comparison of geometries obtained from experiment (colored: Ca; magenta, Mn; light blue, O; red, C; grey, H; white) and theory (black) using the simplified ligand. We show the root mean square (RMS) to compare all the atoms in the structure (top) and the cubane (bottom). The structures with this simplified ligand are almost identical to the ones obtained with the full ligand (Figure 5.3).

However, we need to calculate many properties of these compounds such as the vibrational modes and having to do this for 147 or 134 atoms is too expensive computationally. We postulate that the TAB ligand, although serving to support the metallic cluster, should not participate in the important electrochemical reactions. Thus we simplified our compound by removing the four benzene rings at the bottom and the three unbound pyridines. In addition we fix the carbon that bridges the oxo and bound pyridine in order to mimic the presence of the stiffness of the full TAB ligand. The results are shown in Figure 5.4. The first simplification was done on the $CaMn_3O_4$ containing compound as it is shown in Figure 5.4a. By comparing the position of atoms between the geometry obtained from experiments with the one obtained from the simplified ligand, we obtained a RMS of 0.348 Å. This is a smaller number than the one obtained from QM with the full ligand because there are less atoms. In the case of the simplified ligand we have 84 atoms while with the full ligand we treated

147 atoms. Since we are most interested in the estimation of the metallic core, we compared the geometry between this core including the first coordination shell, and the RMS obtained is 0.125 Å. In a more detailed fashion, this is a RMS of 0.007 Å for the estimation of bonds and RMS of 0.397° for the estimation of angles. This is basically the same accuracy as with the full ligand model.

We performed a similar simplification for the Mn_4O_4 containing compound as it is shown in Figure 5.4b. When comparing the structure from experiment and the one obtained with this simplified ligand, we found a RMS for the position of the atoms of 0.292 Å. This is smaller than with the full ligand due to the smaller number of atoms being compared. With the full ligand we treat 134 atoms while with this simplification on the ligand we only need to handle 71 atoms. In this case, we are also interested in how accurate we can predict the geometry of the Mn_4O_4 cluster and the first coordination shell, since we believe most of the electrochemical processes occur there. By comparing the experimental and the computational geometry of the cluster obtained with the simplified ligand we obtained an RMS of 0.093 Å for the estimation of the geometry. The RMS is 0.012 Å for estimation of bonds and the RMS is 0.074 ° for the estimation of angles. This is practically the same as with the full ligand. With the simplified ligand we obtain a better estimation of the geometry for the Mn_4 case than for the $CaMn_3$ structure, including when only taking into account the cluster and its first coordination shell.

Thus, the models with the simplified ligand gives an accurate description of the geometry observed in experiments and speeds up our calculation by reducing the number of atoms to be treated to almost a half.

5.3.2 Validation of the Computational Methodology: Redox Potentials

We also calculated the redox potential with our QM calculations and then compared the results to the ones obtained experimentally. We started by calculating the redox potential obtained for the $CaMn_3O_4$ containing compound (Table 5.1). The potentials obtained with B3LYP and M06 contains ZPE, vibrational and solvent terms applied to the model with the simplified ligand. We see that B3LYP gives a good estimation of the redox potential when dimethylacetamide (DMA) is used. However it is off almost 0.2 V when dimethylformamide (DMF) is used. On the other hand, M06 gives the best estimation of potential for both cases with a difference of 0.1 V with DMA and of 0.03 V with DMF. The addition of a new electron affects the geometry of the $[Mn^{IV}{}_3CaO_4]$ compound as it is shown in Figure 5.5. The extra electron reduces one of the Mn^{IV} to Mn^{III}, and this electron populates one of the e_g orbital that affects the bond distance along an arbitrary z-axis. These bonds are the Mn_3-O_8 and the Mn_3-O_{16} bonds as it is shown in Figure 5.5. The magnitude of the changes is the following: the oxidized compound has a Mn_3-O_8 bond distance of 1.91 Å, while the reduced one have a bond distance of 2.38 Å. The same elongation happens for the Mn_3-O_{16}, the oxidized species has a bond distance of 1.93 Å, while the reduced one has a bond distance of 2.27 Å. In other words, the oxidized species have bond distances at least 0.33 Å shorter than the reduced compound along an arbitrary z-axis.

Table 5.1: Oxidation/reduction potentials for the Mn_3CaO_4 compound with respect to ferrocene/ferrocenium. Solvents: dimethylacetamide (DMA) and dimethylformamide (DMF).

Mn_3Ca Compound	Solvent	E°_{redox}/V Exp	E°_{redox}/V B3LYP	E°_{redox}/V M06
$[Mn^{IV}{}_2Mn^{III}CaO_4]/[Mn^{IV}{}_3CaO_4]$	DMA	-0.94	-1.07	-0.84
$[Mn^{IV}{}_2Mn^{III}CaO_4]/[Mn^{IV}{}_3CaO_4]$	DMF	-0.89	-1.16	-0.92

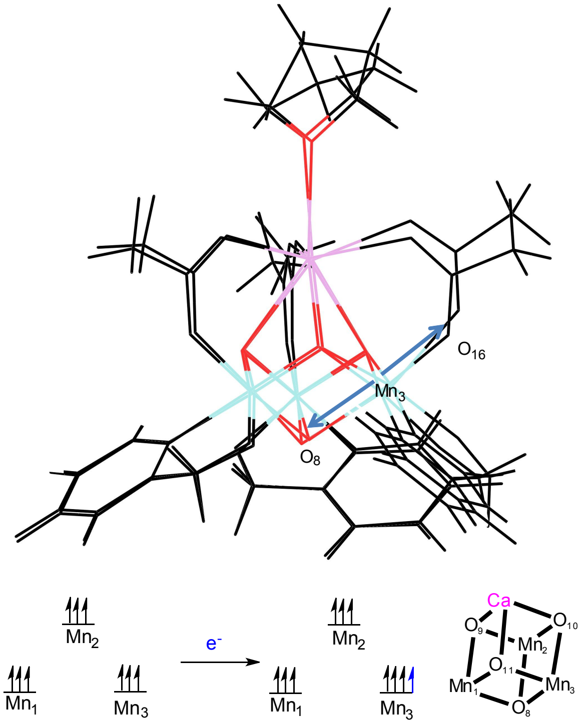

Figure 5.5: Oxidation/reduction for the Mn_3CaO_4 compound. Color code: Ca; magenta, Mn; light blue, O; red, C and H; black.

Next we calculated the redox potential for the compound containing the Mn_4O_4 cluster. The results are shown in Table 5.2. In this case, B3LYP still gives a poor estimation of the experimental redox potential with a difference of at least 0.17 V. On the other hand, M06 gives a closer estimation of the potentials with a difference of at most 0.06 V. The experimental redox potential for the couple $[Mn^{IV}{}_2Mn^{III}{}_2O_4]/[Mn^{IV}{}_3Mn^{III}O_4]$ is 0.29 V, while M06 predicts 0.35 V. The next redox pair; $[Mn^{IV}{}_2Mn^{III}{}_2O_4]/[Mn^{IV}Mn^{III}{}_3O_4]$ gives an experimental redox potential of -0.70 V, while M06 predicts -0.67 V. These redox processes have geometrical changes associated. The structural changes can be observed in Figure 5.6. In the reduction process, the addition of one electron to the $[Mn^{IV}{}_3Mn^{III}O_4]$ compound, populates one of the e_g orbitals, elongating the Mn-O bond along an arbitrary z-axis. This elongation happens in the bonds between Mn_1-O_5 and Mn_1-O_{12}. The oxidized species has a bond distance for Mn_1-O_5 of 1.92 Å and for Mn_1-O_{12} of 1.99 Å. The reduced complex increases these bonds by more than 0.24 Å. The Mn_1-O_5 bond increases to 2.41 Å while the Mn_1-O_{12} bond increases to 2.23 Å. In the further reduction another of the Mn^{IV} centers is reduced to Mn^{III} and one of its e_g orbitals is populated, changing the bond distance along that axis (Figure 5.6). This time the modified bonds are Mn_2-O_7 and Mn_2-N_{19}. The changes are as follows: Mn_2-O_7 bond distance increase from 1.85 Å to 2.21 Å when reduced, while the Mn_2-N_{19} increases from 2.07 Å to 2.29 Å.

Table 5.2: Oxidation/reduction potentials for the Mn_4O_4 compounds with respect to ferrocene/ ferrocenium. Solvent: dimethylacetamide (DMA).

Mn_4 Compound	Solvent	$E°_{redox}$/V Exp	$E°_{redox}$/V B3LYP	$E°_{redox}$/V M06
$[Mn^{IV}_2Mn^{III}_2O_4]/[Mn^{IV}_3Mn^{III}O_4]$	DMA	0.29	0.11	0.35
$[Mn^{IV}_2Mn^{III}_2O_4]/[Mn^{IV}Mn^{III}_3O_4]$	DMA	-0.70	-0.93	-0.67

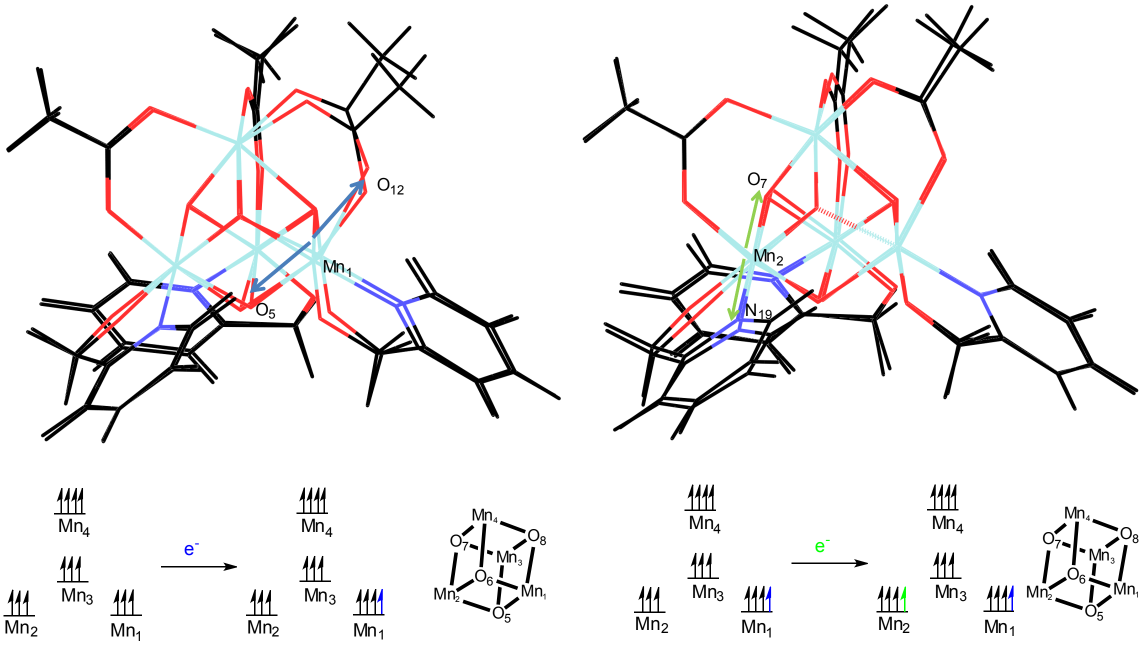

Figure 5.6: Oxidations/reductions for the Mn_4O_4 compound. Color code: Ca; magenta, Mn; light blue, O; red, N; dark blue, C and H; black

Thus we have validated our QM methodology by reproducing the experimental redox potential for these systems. We were also able to determine how the redox processes affects the geometry of the structure by reducing the Mn^{IV} atoms to Mn^{III}.

5.3.3 Prediction of New Models that Resemble the OEC Both Structurally and Electronically

Unfortunately the molecular models described by the Agapie group do not produce O_2. However they were able to prove that the presence of a Ca center facilitates the formation of highly oxidized Mn^{IV} species at lower potentials (>1V more negative when comparing $Mn^{IV}{}_3CaO_4$ and $Mn^{IV}{}_4O_4$, Table 5.1 and Table 5.2). The highly oxidized Mn^{IV} centers have been proposed to be necessary in the catalytic process because the compound needs to receive 4 electrons in the last step.[43] However, the main difference with the biological OEC is a fourth dangling manganese in the same plane as the other Mn of the cubane (Figure 5.1), thus we can improve the model compound by finding a way to put that fourth Mn in the already proposed model and determine if we can observe a highly oxidized Mn species.

Table 5.3: Bond distances for the fourth Mn shown and its first coordination shell as it is shown in Figure 5.7.

$CaMn_4$-NH_2		$CaMn_4$-bipy		$CaMn_4$-acac	
Type	Bond (Å)	Type	Bond (Å)	Type	Bond (Å)
Mn_4-O_1	2.28	Mn_4-O_1	2.27	Mn_4-O_1	2.02
Mn_4-O_2	2.31	Mn_4-O_2	1.94	Mn_4-O_2	2.19
Mn_4-O_3	2.02	Mn_4-O_3	1.75	Mn_4-O_3	1.81
Mn_4-N_5	2.49	Mn_4-O_5	2.38	Mn_4-O_5	2.17
Mn_4-O_6	2.23	Mn_4-N_6	2.14	Mn_4-O_6	2.13
Mn_4-O_7	2.26	Mn_4-N_7	2.14	Mn_4-O_7	1.96

The first model we created was modifying the linker in order to have a binding group on the side. We decided to modify one of the unbounded pyridines and create a point of extension CH_2NH_2 that can host the fourth Mn center. This is shown in Figure 5.7a. We also added another oxygen, O_3, in order to complete the coordination shell of the fourth manganese (Mn_4). The electronic state of this compound shows that we have three Mn^{IV} and one Mn^{II} which resembles S_1 of the biological OEC. The bond distances for this fourth manganese and its first coordination shell is shown in Table 5.3. All of the bond distances are too long in all axes, which is larger than 2 Å. We also found that the geometry for the central Mn_4 is not octahedral but a distorted trigonal bipyramidal with the oxygen O_1 from the carboxylate occupying a site that can be described as one of the faces of the pyramid. This suggests that putting a point of extension on the ligand might constrain the system too much and the binding of the fourth manganese can be unstable.

We decided to keep the original ligand but using another additional ligand that can bind a fourth Mn. Thus we use the bipyridine (bipy) molecule as it is shown in Figure 5.7b. Besides the addition of the bipyridine ligand and the fourth Mn (Mn_4) we also add another oxo oxygen, O_3. We complete the coordination shell of the added Mn with H_2O. By analyzing the electronic state of this compound we found that there are two Mn^{IV} and two Mn^{III}, similar to S_1 of the biological OEC. The bond

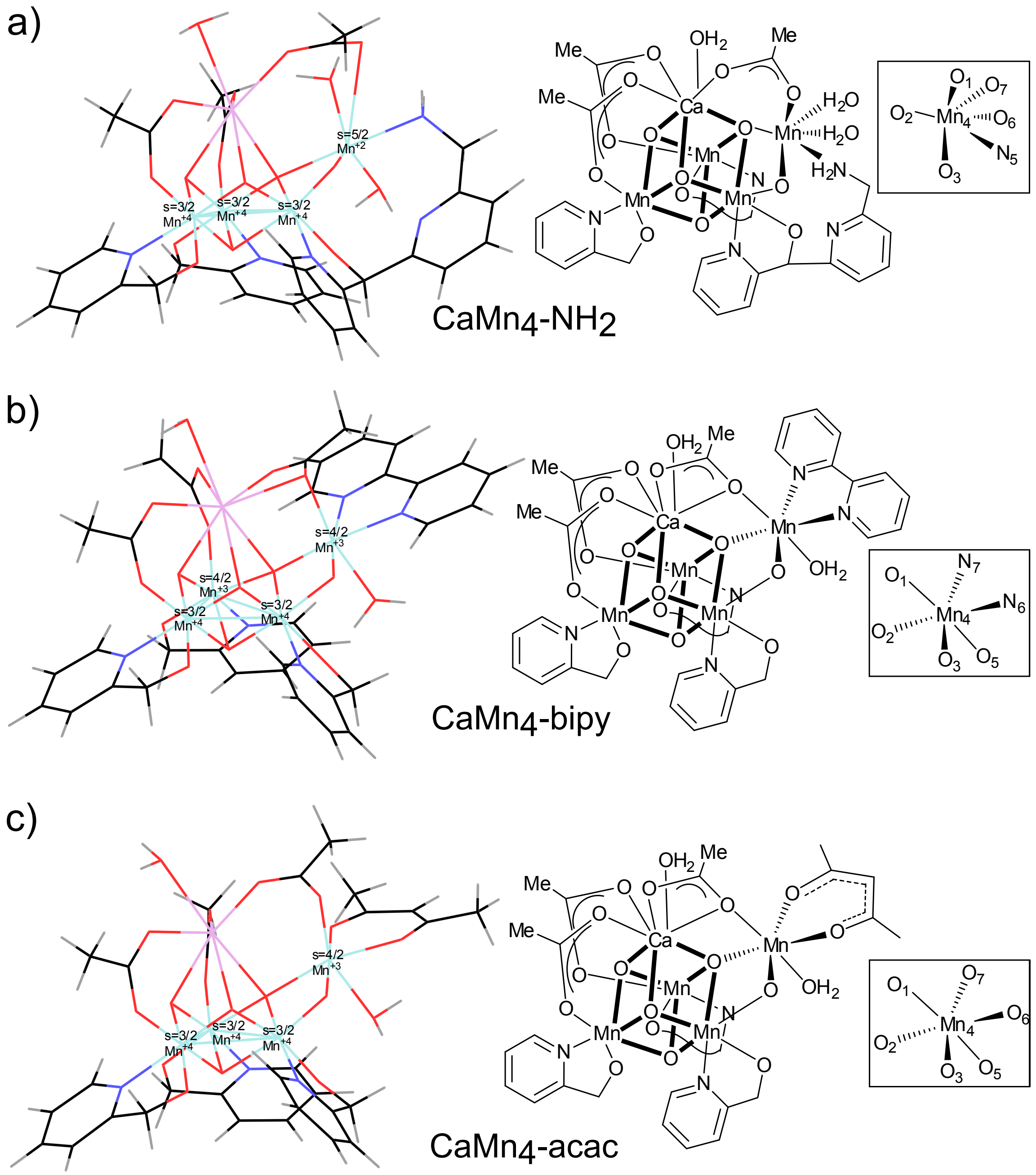

Figure 5.7: New models for the OEC that includes the fourth Mn giving a $CaMn_4O_4$ type cluster; (a) $CaMn_4$-NH_2, similar to S_1 (b) $CaMn_4$-bipy, similar to S_1 and (c) $CaMn_4$-acac, similar to S_2. Color code: Ca; magenta, Mn; light blue, O; red, N; dark blue, C; black and H; grey

distances for the fourth Mn and surrounding atoms are shown in Table 5.3. We can see that we have two long bonds along an arbitrary z-axis and four short bonds in the xy plane which is consistent with Mn^{III} and one populated e_g orbital. Therefore this system is not constrained and the neutral state resembles one of the steps in the OEC catalytic cycle.

Finally, we designed another molecule with the acetylacetonate (acac) ligand. Because acac has a formal charge of -1, we can modify the electronic structure of the $CaMn_4$ compound and at the same time coordinate the fourth Mn as it is shown in Figure 5.7c. We found that the electronic state of this model gives three Mn^{IV} and one Mn^{III}, which resembles the S_2 state of the biological OEC. The fourth Mn has an octahedral environment with two short bond along the z-axis (O_3 and O_7) as it is shown in Table 5.3. This compound does not show constraints in the fourth manganese or the bridging oxygen (O_3) which suggest that its synthesis can be viable. This $CaMn_4$ with the acac in the equatorial position can also have another isomer where the acac binds along the z-axis in the site where the water is bound, giving the axial isomer. Our calculations show that the axial isomer is 10 kcal/mol less stable than the equatorial isomer shown in Figure 5.7c.

Although in all our new models we only add one extra dangling Mn, there is not an obvious reason to think that other two extra dangling Mn cannot be added due to the symmetry of the ligand and metal cluster.

5.4 Conclusions

We have validated a QM methodology that can reproduce the geometries and redox potential of the system described by Agapie et al. We found that in this redox process, the Mn^{IV} atoms gets reduced to Mn^{III} and the extra electron populates one of the e_g orbitals which elongates the bonds along the z-axis of the Mn^{IV}.

Using this methodology we have designed new molecules with the $Mn^{IV}{}_4CaO_4$ architecture. These new models have oxidation states that are similar to the S_1 and S_2 states of the biological OEC. We have accomplished these different electronic states by modifying the original host ligand or by adding common linkers such as bipyridine or acetylacetonate. Thus we have proven that we can obtain compounds that resemble the OEC both structurally and electronically.

Chapter 6

Methane Storage in Metal-Organic Frameworks and Covalent-Organic Frameworks

In this chapter we validate our theoretical methodology by comparing our results with experimental measurements (COF-5 and COF-8). We describe the sorption mechanism for CH_4 and developed a first principle based van der Waals Force Field for the interaction of Covalent Organic Frameworks (COFs) that was extended to Metal-Organic Frameworks (MOFs).[49] Then we proceed to use the this methodology to design new types of materials with optimal characteristic for methane delivery at room temperature. We found that Two new frameworks, COF-103-Eth-trans and COF-102-Ant, are found to exceed the DOE target of 180 v(STP)/v at 35 bar for methane storage. [50]

6.1 Adsorption Mechanism and Uptake of Methane (CH_4) in Covalent-Organic Frameworks: Theory and Experiment

Reproduced with permission from American Chemical Society, Copyright 2010. Jose L. Mendoza-Cortes, Sang Soo Han, Hiroyasu Furukawa, Omar M. Yaghi, and William A. Goddard, III J. Phys. Chem. A, **2010**, *114* (40), pp 10824 - 10833. .

6.1.1 Introduction

Although gasoline is the current fuel of choice for personal transportation because of its low-cost and the fuel supply structure, it generates pollutants by combustion and evaporation, including nitrogen oxides, sulfur oxide, carbon monoxide, and traces of carcinogens chemicals.[51] This has motivated the search for alternative routes toward new energy sources. Methane is a good candidate for an alternative fuel because it is inexpensive with clean-burning characteristics.[52] Moreover, the huge reserves of natural gas (NG) (>95% CH_4, with some ethane, nitrogen, higher hydrocarbons, and carbon dioxide)[52] around the world are comparable to the energy content of the worlds petroleum reserves. However, to utilize this CH_4, inexpensive means of transporting and storing are required. Since methane has a critical temperature of 191 K and critical pressure of 46.6 bar, it cannot be liquefied at room temperature, increasing the cost of its transportation.[53] Attempts to overcome this disadvantage include

- storing methane as liquefied natural gas (LNG, at ∼112 K) or compressed natural gas (CNG, at 200 bar),[54]
- converting methane to oxygenates such as methanol or higher hydrocarbons such as ethane,[55, 56, 57] and
- storing in porous materials.[58]

Among these alternatives, we believe that storing methane via adsorption on porous materials is the most promising near-term route because it allows operation at reasonable pressure (1-300 bar) and temperature (77-298 K) and does not require extra energy input for conversion to higher hydrocarbons or methanol.

Recently, the new covalent-organic frameworks (COFs) family of porous materials was reported, based on boronic acid building blocks (Figure 6.1).(9-12)[59, 60, 61, 62] COFs are held together by strong covalent bonds between light elements such as B, C, O, H, and Si. They have high surface areas (as high as 6450 m^2/g), large pore volumes (as high as 5.4 cm^3/g), and the lowest densities for any known crystalline material (as low as 0.17 g/cm^3),[61] all of which are prerequisites for high uptake of methane (Table 6.1). In principle, an immense number of COFs using various building units and various numbers of points of extension and functionality to attain various topologies could be synthesized and tested for methane adsorption. Such empirical processes have been effective, but we explore here the alternate procedure in which theory and computation is used to predict the most promising candidates, followed by experimental synthesis and characterization only on the most promising cases. Of course, this is only possible if the results from the theory and computation are sufficiently reliable that one can with confidence reject low performance systems without the need for experiment. Grand canonical Monte Carlo (GCMC) provides the accuracy required to predict accurate adsorption isotherms. However, GCMC requires a force field (FF) accurate for predicting the structure of the COF and for predicting the weak intermolecular interactions with CH_4. The covalent bonds of the framework for COF systems are well treated by generic FF such as Dreiding[25] and UFF,[11] and by more specialized FF such as OPLS.[40] However, these FF do not generally provide the accuracy required to predict adsorption isotherms.[63] GCMC coupled to these generic FF have been used to reproduce experimental isotherms reported by our group in some 2D-COFs[64] and 3D-COFs[65] finding disagreements between our experiments and this theory of 10%

and 25%, respectively. The same approach has been used to study MOF-5, and they were compared to experiments and the absolute error ranges from +5 to -16%.[66, 67, 68] (19-21) Here it is essential to account for the van der Waals (vdW) attraction (London dispersion) and electrostatic interactions that dominate the interaction of CH_4 with surfaces. The vdW terms have been a problem because the powerful density-functional theory (DFT) methods underlying most quantum mechanics (QM) calculations today are notoriously inaccurate for vdW.[69, 70] Consequently, we focused here on developing and validating the vdW part of the force field using QM methods (MP2) expected to be accurate.

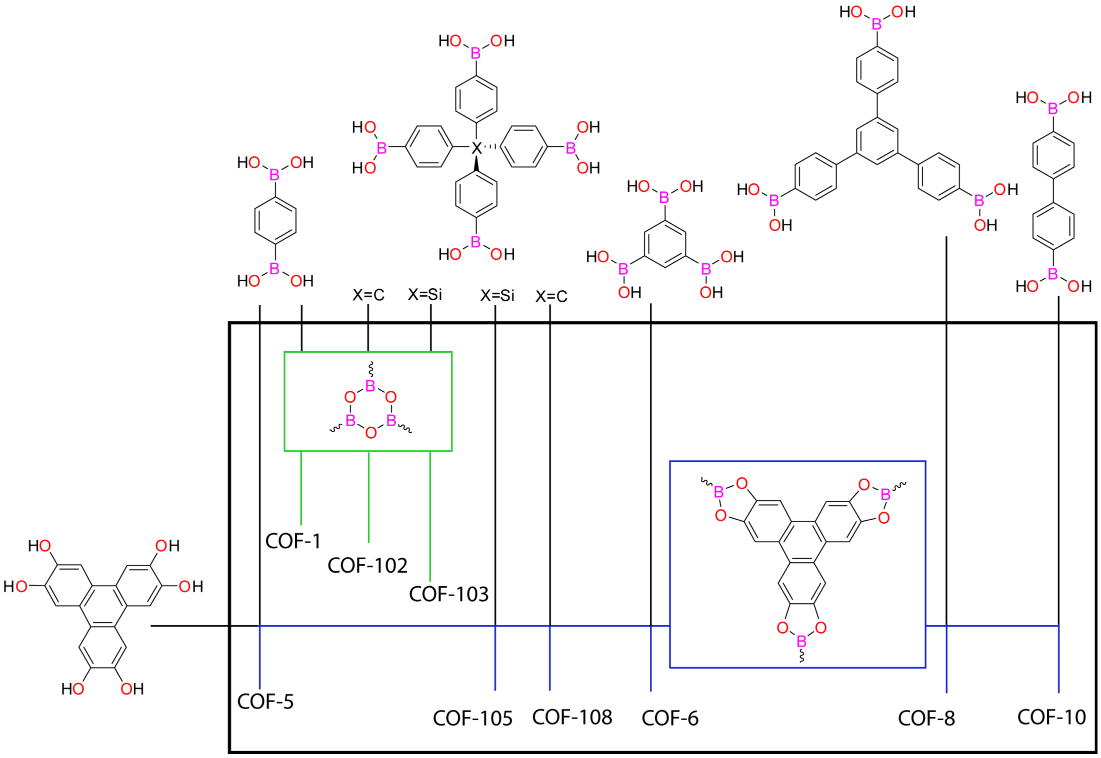

Figure 6.1: Molecular structures of building units used for COF synthesis (outside black box) and their COF formation reactions (green box, boroxine; blue box, ester)

In this work, we predict the methane uptake for five 2D-COFs (COF-1, COF-5, COF-6, COF-8, and COF-10) and four 3D-COFs (COF-102, COF-103, COF-105, and COF-108), as shown in Figure 6.2. However, a better adjective for 2D- is two-periodic-COFs and for 3D- is three-periodic-COFs. These predicted isotherms are in excellent agreement with our experimental results (within 2%) for the two systems for which the experimental data show that the pores of the structures have been completely cleaned (COF-5 and COF-8 up to 85 bar), validating our computational methodology. Then we use this method to show that COF-102 and 103 are excellent materials for practical methane storage.

Table 6.1: Pore size (P_{Size}), surface area (S_A), pore volume (V_P), and density of the Framework without guest molecules (ρ) for the studied COF series[a]

material	P_{Size}, Å	S_A, m^2g^{-1}	V_P, cm^3g^{-1}	ρ, g cm^{-3}	topology	space group
COF-1	7	1230	0.38	0.91	**gra**	$P6_3/mmc$
COF-5	27	1520	1.17	0.58	**bnn**	$P6/mmm$
COF-6	11	1050	0.55	1.03	**bnn**	$P6/mmm$
COF-8	16	1320	0.87	0.71	**bnn**	$P6/mmm$
COF-10	35	1830	1.65	0.49	**bnn**	$P6/mmm$
COF-102	12	4940	1.81	0.42	**ctn**	$I\bar{4}3d$
COF-103	12	5230	2.05	0.38	**ctn**	$I\bar{4}3d$
COF-105	19	6450	4.94	0.18	**ctn**	$I\bar{4}3d$
COF-108	20,11	6280	5.4	0.17	**bor**	$P\bar{4}3m$

[a] P_{Size} was calculated by placing a sphere in the center of the largest cavity and measuring its diameter considering the van der Waals radii of atoms in the framework. S_A and V_P were estimated from rolling an Ar molecule with diameter of 3.42 Å[71] over the frameworks surface.

6.1.2 Methodology

6.1.2.1 Force Field

For geometry optimization, we used the quadruple-ζ valence basis (QZV) supplemented with polarization functions from the cc-pVTZ basis, which is denoted as QZVPP. To develop the FF to be used in describing the interactions of methane with the COF (CH_4-COF) and the interaction between methane molecules (CH_4-CH_4), we used QM at the MP2 level with the approximate resolution of the identity (RI-MP2).[72, 73, 74] Quantum mechanical calculations were performed using the Turbomole code. The auxiliary-QZVPP basis set was used for the RI-MP2 calculations.[75] We did not include excitations out of the 1s core orbital in the MP2 calculation.

The binding energies between CH_4-CH_4 and CH_4-COFs were corrected using basis-set superposition error (BSSE) by the full counterpoise procedure (eq 6.1).

$$E_{interaction}^{CP} = E_{super} - \sum_{i=1}^{n} E_{m_{opt}^{i}} + \sum_{i=1}^{n} (E_{m_f^i} - E_{m_f^{i*}}) \tag{6.1}$$

Where the E_{m^s} represent the energies of the individual monomers. The subscripts *opt* and f denote the individually optimized monomers and those frozen in their supermolecular geometries and the asterisk ($*$) denotes monomers calculated with ghost orbitals.[76]

Using the accurate RI-MP2 results, we developed FF parameters for nonbonded interactions between CH_4-CH_4 and CH_4-COFs where for the functional form the Morse potential (eq 6.2) was used. Here the parameter D is the well depth, r_0 is the equilibrium bond distance, and α determines the stiffness (force constant).

$$\boldsymbol{U}_{ij}^{Morse}(r_{ij}) = D\left\{e^{\alpha(1-\frac{r_{ij}}{r_0})} - 2e^{-\frac{\alpha}{2}(1-\frac{r_{ij}}{r_0})}\right\} \tag{6.2}$$

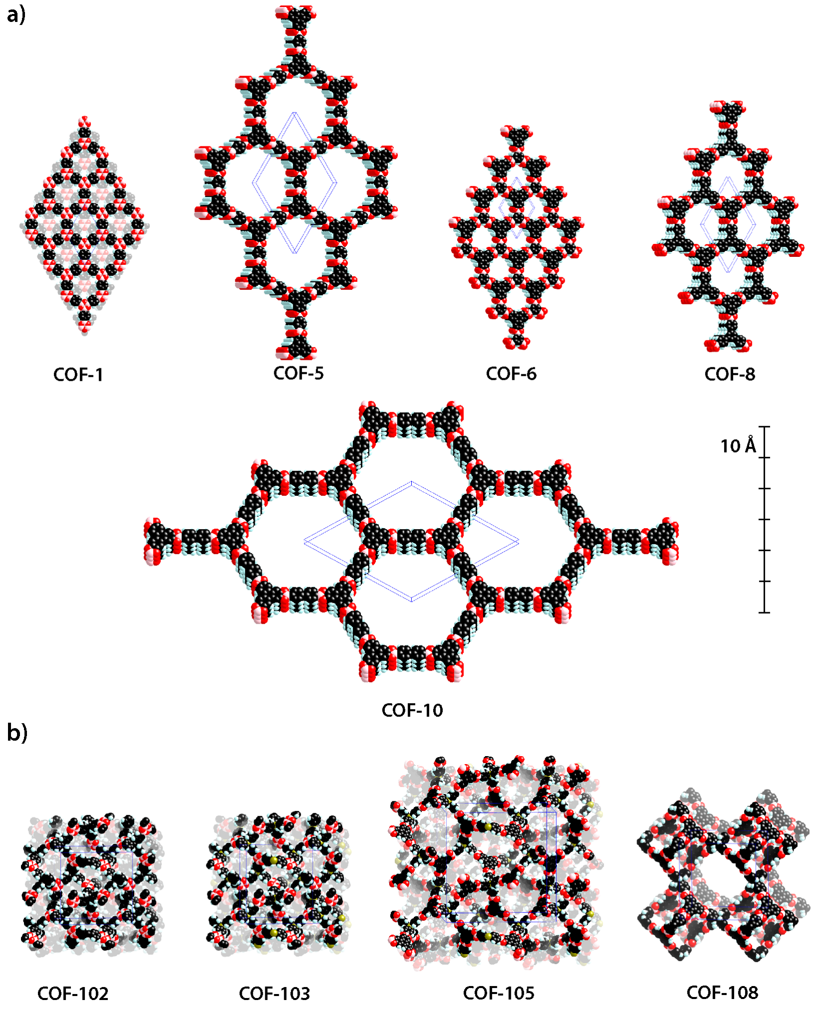

Figure 6.2: Atomic connectivity and structure of crystalline products for (a) 2D-COFs and (b) 3D-COFs. Unit cells are shown in blue lines. Atom colors: C, black; O, red; B, pink; Si, yellow; H, blue

It is more common to use Lennard-Jones (LJ-12-6) and exponential-6 (exp-6) functional forms for such studies,[25] because it is believed that the long-range form should have $1/\mathrm{R}^6$ character. However, our experience is that LJ-12-6 and exp-6 have inner walls that are too stiff and that the region of true $1/\mathrm{R}^6$ character is only at much longer distances than relevant here. Thus, we believe that the Morse function is the most suitable for studying gas adsorption in porous frameworks. For the electrostatic interactions, we used the atomic charges (C -0.43820 and H +0.10955) of methane from our QM calculations. For the charges of the COFs framework we used the QEq charge equilibration method.[12]

6.1.2.2 QM Determination of the vdW Force Field Parameters

The parameters (D, α, and r_0 in eq 6.2) were developed to fit QM results. Since all COF systems considered here are composed only of B, C, H, O, and Si, we developed 13 sets of interaction parameters:

- C_{CH_4}-C_{CH_4}, H_{CH_4}-H_{CH_4}, C_{CH_4}-H_{CH_4}
- C_{COF}-C_{CH_4}, C_{COF}-H_{CH_4}, H_{COF}-C_{CH_4}, H_{COF}-H_{CH_4}
- O_{COF}-C_{CH_4}, O_{COF}-H_{CH_4}, B_{COF}-C_{CH_4}, B_{COF}-H_{CH_4}
- Si_{COF}-C_{CH_4}, Si_{COF}-H_{CH_4}

To obtain these parameters, we considered four different geometrical configurations for each cluster: CH_4-CH_4, C_6H_6-CH_4, $B_3O_3H_3$-CH_4, and $Si(CH_4)4$-CH_4 (Figure 6.3) as well as the interaction with the edges. [77]

Table 6.2: Nonbonded FF parameters developed to fit the RI-MP2 calculations[a]

term	D/kJ mol^{-1}	r_0/Å	α
C_{CH4}-C_{CH4}	3.21×10^1	3.92	12.7
H_{CH4}-H_{CH4}	1.34×10^2	3.13	11.4
C_{CH4}-H_{CH4}	2.18×10^1	3.46	11
C_{COF}-C_{CH4}	2.09×10^1	4.23	13.2
H_{COF}-C_{CH4}	3.67×10^3	3.25	12
O_{COF}-C_{CH4}	2.02×10^1	3.59	11.3
B_{COF}-C_{CH4}	1.95×10^1	4.11	12.3
C_{COF}-H_{CH4}	4.79×10^1	3.08	9.07
H_{COF}-H_{CH4}	3.67×10^3	3.26	12
O_{COF}-H_{CH4}	3.85×10^1	2.55	8.99
B_{COF}-H_{CH4}	3.84×10^1	3.28	11.7
Si_{COF}-H_{CH4}	4.58×10^1	4.06	7.19
Si_{COF}-C_{CH4}	3.58×10^1	4.78	16.5

[a] The function form (Morse) is given in eq 6.2. D is the well depth, r_0 is the equilibrium bond distance, and a determines the force constant. Each parameter has been rounded to three significant figures.

Our RI-MP2/QZVPP calculation finds that the energy for CH_4 binding (E_{bind}) to the face of the organic linker for the most stable configuration is higher than when it interacts with the edge; also the equilibrium distance (R_{eq}) to the face is shorter. The face E_{bind} of CH_4-C_6H_6 is 7.0 kJ mol^{-1} with R_{eq} equal to 3.7 Å, while the edge E_{bind} is 3.8 kJ mol^{-1} and R_{eq} is 5.0 Å. Also, the face E_{bind} for CH_4-$B_3O_3H_3$ is 5.2 kJ mol^{-1} and R_{eq} is 3.4 Å, whereas its edge E_{bind} is 1.5 kJ mol^{-1} and R_{eq} is 4.9 Å.

The energy as a function of distance from QM was calculated near the equilibration distance for each type of interaction and fitted to eq 6.2 using larger weights at the equilibrium distances (insets in Figure 6.3). The predominant configurations interactions for the clusters are $D3d$ for CH_4-CH_4, ANTI for C_6H_6-CH_4, SYN for $B_3O_3H_3$-CH_4, and ANTI2 for $Si(CH_4)_4$-CH_4. Our new

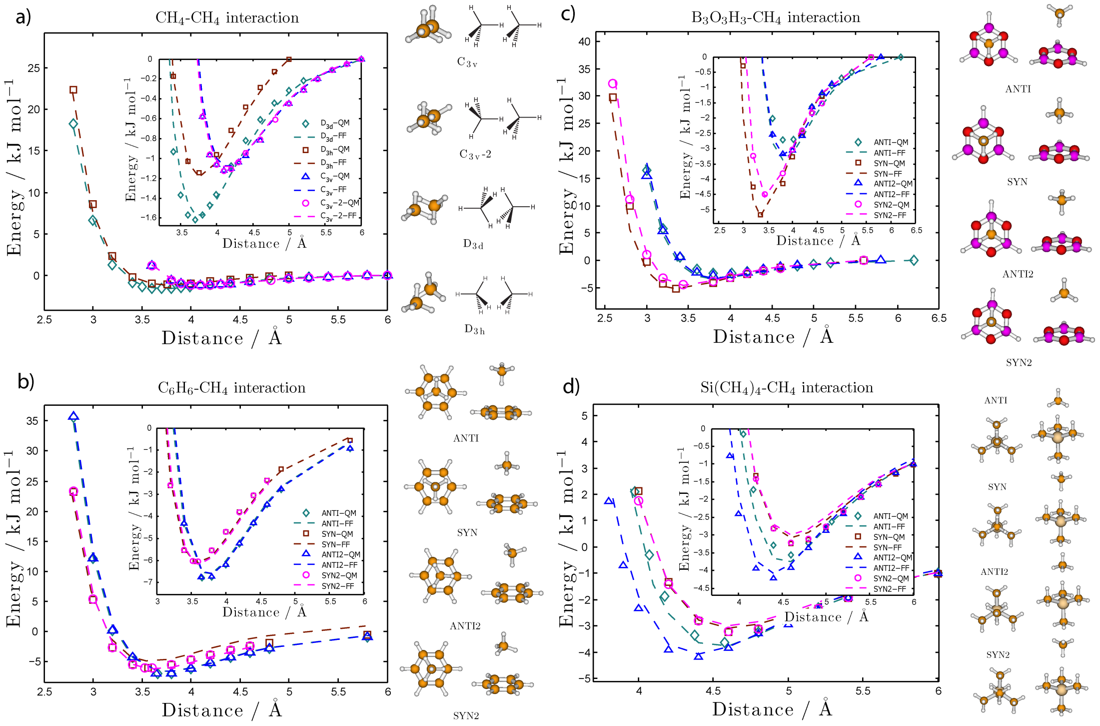

Figure 6.3: Comparison of the optimized FF energies with QM (MP2-RI) for four configurations: (a) CH$_4$-CH$_4$; (b) C$_6$H$_6$-CH$_4$; (c) B$_3$O$_3$H$_3$-CH$_4$; (d) Si(CH$_4$)4-CH$_4$. FF results are shown as dashed lines while the QM results are shown by empty symbols. Each configuration has four plausible geometrical structures shown to the right, where C atoms are brown, B pink, O red, Si yellow, and H white. Configurations interacting through the edges are not shown. The insets show the accuracy in fitting to the equilibrium distance. Data plotted here as the BSSE corrections are included in the Supporting Information.

FF parameters (Figure 6.2) reproduce well these binding energies and the QM energy profile (Figure 6.3). We validated the FF for CH$_4$ by calculating the CH$_4$ equation of state at various temperatures (260-400 K) and pressures (1, 10, and 100 bar, see Supporting Information) and by comparing the sorption isotherms to our experimental results for two COFs.

Table 6.3: Most-stable interaction geometries for clusters considered in this work[a]

interaction	geometry	r_0/Å	QM/kJ mol^{-1}	FF/kJ mol^{-1}
CH$_4$-CH$_4$	*D3d*	3.710	1.61	1.59
C$_6$H$_6$-CH$_4$	ANTI	3.657	7.01	6.83
B$_3$O$_3$H$_3$-CH$_4$	SYN	3.352	5.16	5.22
Si(CH$_4$)$_4$-CH$_4$	ANTI2	4.401	4.44	4.28

[a] r_0 is the equilibrium bond distance defined as the distance between the barycenter of every molecule.

6.1.2.3 GCMC Procedure

To determine methane storage capacity in COFs, we used the GCMC method with the ab initio based FF developed herein. At each step of the GCMC, one of four events (translation, rotation, creation, and annihilation of methane molecules) is applied using the Monte Carlo criteria for acceptance. Details can be found elsewhere.[78, 79]

To obtain an accurate measure of methane loading, we constructed 3 000 000 configurations to compute the average loading for each thermodynamic condition. The equilibrium conditions were verified for every loading curve.

6.1.2.4 Structural Characteristics of COFs

These simulations used the experimental structures of 2D-COF (COF-1, COF-5, COF-6, COF-8, and COF-10) and 3D-COF (COF-102, COF-103, COF-105, and COF-108) shown in Figure 6.2. The surface area, pore volume, density, and pore aperture of studied COFs are summarized in Figure 6.1.[71]

There are two classes of 2D-COFs, one in which the layers are eclipsed and the other with them staggered.

- COF-1 has an underlying graphite topology (**gra**) given by the“ABAB” stacking sequence of its layers with interlayer spacing of 3.35 Å, leading to the $P6_3/mmc$ space group. This leads to compartments with pore apertures of 7 Å.[59]
- In contrast, COF-5, COF-6, COF-8, and COF-10 have a boron-nitride (**bnn**) topology with an“AAA” stacking sequence of layers and $P6/mmm$ space group.(9, 10)[59, 60] The pore diameters for these COFs are controlled by the building blocks (Table 6.1).

For the 3D-COFs, the simplest two topologies plausible from the connectivity of these building units are the carbon-nitride (**ctn**) and boracite (**bor**) topologies.[80, 81]

- COF-102, COF-103, and COF-105 have the **ctn** topology with $I\bar{4}3d$ $I\bar{4}3d$ space group. The pore structures for these materials are similar with pore diameters varying from 12 to 19 Å.[82]
- COF-108 has the **bor** topology with the $P\bar{4}3m$ space group leading to two classes of pores with diameters of 11 and 20 Å.

6.1.3 Results and Discussion

6.1.3.1 Comparison Between Theoretical and Experimental Methane Adsorption

To validate our FF and simulation procedure, we additionally compare the predicted and experimental methane uptakes for COF-5 and COF-8, the two systems for which we had already confirmed to be properly activated. This was done by comparing the measured pore volume with Ar at low pressure and the measured pore volume from He at high pressure (see Supporting Information). It is very important to note that if solvent molecules remain in the pore or COF framework or are partially decomposed, it is not possible to obtain an accurate measure of the adsorption. Indeed, this is the value of the simulations, in that adsorption performance can be obtained prior to confirming proper activation. Furukawa et al.[83] reported that there are some COFs that still need to be further activated, a possible solution could the CO2 method developed by Nelson et al.[84] The GCMC-predicted total methane adsorption isotherms for COF-5 and COF-8 at 298 K based on the new FF were converted to obtain the excess isotherms because total uptakes are not experimentally accessible.[85]

Figure 6.4 compares the excess isotherms in gravimetric unit (wt %) from simulations and experiments. Here wt % = (mass of gas) × 100/[(mass of framework) + (mass of the gas)]. The predicted excess methane uptake in COF-5 is 11.3 wt % at 80 bar, in excellent agreement with the experimental value of 11.1 wt % at 78 bar. Similarly, the predicted excess uptake in COF-8 of 10.6 wt % at 80 bar is very close to the experimental result of 10.3 wt % at 78 bar. These results validate our theoretical methodology for these large pore materials; indeed, COF-5 can be classified as mesoporous while COF-8 is microporous. This indicates that our FF provides a good estimation of the COF-methane interaction at 298 K. This validation of our simulation procedures allows us to determine the performance of the other COF systems, providing a guide to determine the optimal materials for methane uptake.

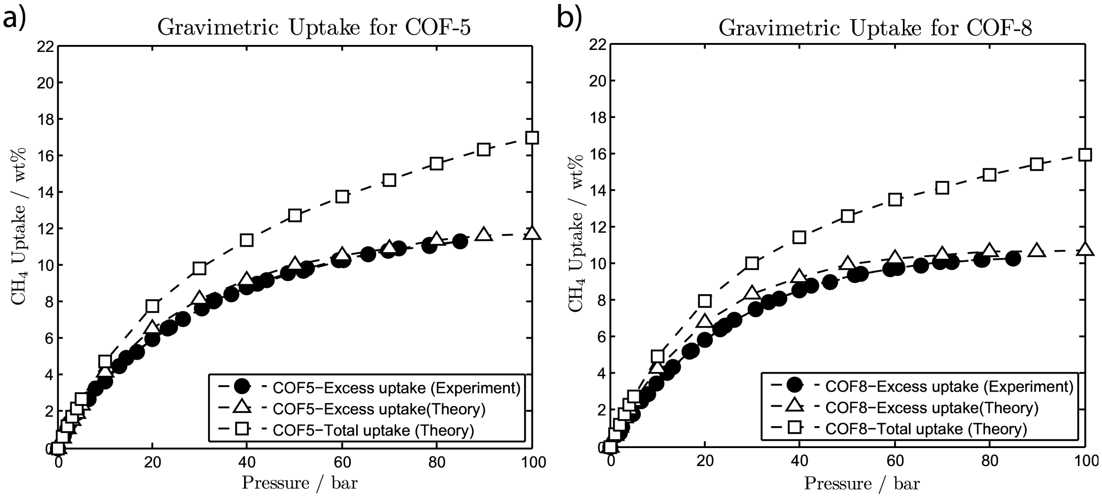

Figure 6.4: Predicted (open triangles) and experimental (closed circles) methane isotherms at 298 K in excess uptake gravimetric units (wt %): (a) COF-5; (b) COF-8. The total predicted uptake is shown by open squares.

6.1.3.2 Gravimetric Methane Uptake in Other COFs

The predicted gravimetric methane uptakes in other COFs at 298 K are shown in Figure 6.5. To show superior capability of several COFs over MOFs, we have also included the experimental and theoretical methane uptake of MOF-177, which have not been reported in the literature yet. MOF-177 has been a benchmark for the MOFs compounds because of the high surface area (4700 m^2/g)[85] and the large amount of exposed edges of the organic ligands that has been suggested to be the reason of the high permance for gas adsorption, as well as its microporosity.[86] The simulated methane adsorption isotherms of the MOF-177 are compared to the experimental data, giving a good agreement as for COFs where the combination rules have been used as well as our accurate parameters previous developed for Zn (see Supporting Information).[87] As expected, all COFs show type I for total and excess isotherms, with profiles that depend strongly on the materials. The highest total gravimetric methane uptake was found in COF-108 (41.5 wt %) and COF-105 (40.5 wt %), followed by COF-103 (31.0 wt %), COF-102 (28.4 wt %), MOF-177 (25.9%), COF-10 (19.6 wt %), COF-8 (15.9 wt %), COF-6 (12.3 wt %), COF-5 (16.9 wt %), and COF-1 (10.9 wt %) all at 100 bar. This is in disagreement with a recent report by Lan et al.[88] where it is shown that at 100 bar the total gravimetric uptake is 54.39% for COF-105 and 54.68% for COF-108. This is an overestimation of 31% with repect to our values. This might be due to the fact that only one configuration was used for the organic linker-CH_4 interaction and the CH_4-CH_4 parameters were not obtained with the same methodology as the other parameters.

In terms of excess methane uptake (the quantity measured experimentally), the best at 100 bar are the 3D-COFs [COF-105 (27.6 wt %), COF-103 (26.6 wt %), COF-108 (24.2 wt %), and COF-102 (23.8 wt %)] followed by MOF-177 (22.8%) and 2D-COFs [COF-10 (12.2 wt %), COF-5 (11.7 wt %), COF-6 (11.1 wt %), COF-1 (10.9 wt %), and COF-8 (10.7 wt %)]. Most COFs have much smaller excess/total uptake ratios, generally in inverse proportion to the free volume (see Supporting Information): 0.81 for COF-5, 0.95 for COF-6, 0.81 for COF-8, 0.77 for COF-10, 0.89 for COF-102, 0.90 for COF-103, 0.76 for COF-105, and 0.71 for COF-108 and 0.92 for MOF-177. However, COF-1 shows an unusual behavior. It has the best performance below 30 bar, with a total uptake amount very close to the excess uptake with no additional adsorption above 30 bar. The reason is that COF-1 has parallel exposed faces of boroxine rings spaced at 12 Å (Figure 6.2) and part of the benzene rings inside the pores. This leads to saturation at lower pressure and low total uptakes. The pores in COF-1 have small diameters (7 Å) and are isolated due to the "ABAB" stacking sequence; therefore, the COF-1 might have kinetically inaccessible regions. However, the GCMC simulation assumes that any points within the simulation cell can be accessed so that our results for the case of COF-1 might overestimate the adsorption observed experimentally. This implies that the difussion rate of methane in the COF-1 pores is not very high.

In sorption experiments, the absolute adsorbed amount can be estimated by using eq 3,[85]

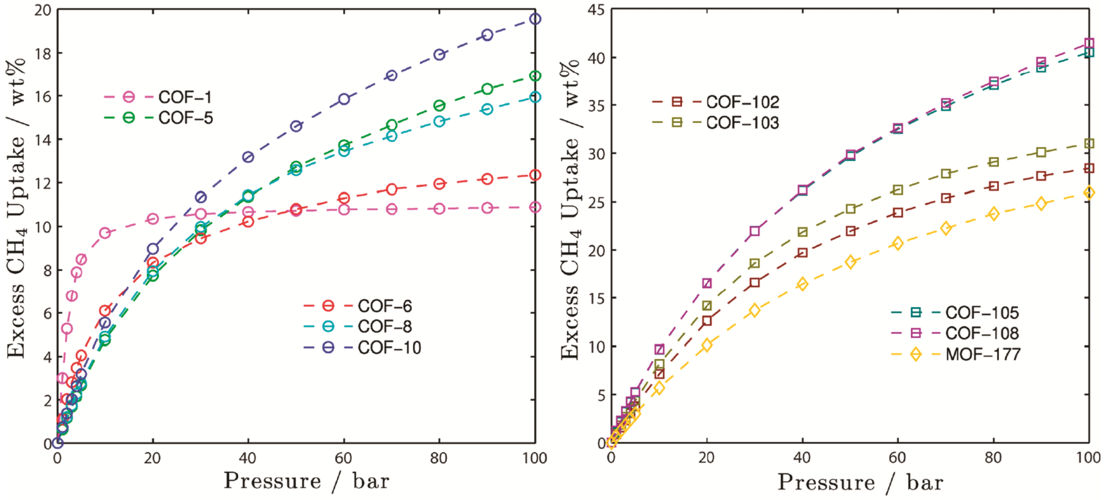
a) Total gravimetric uptake

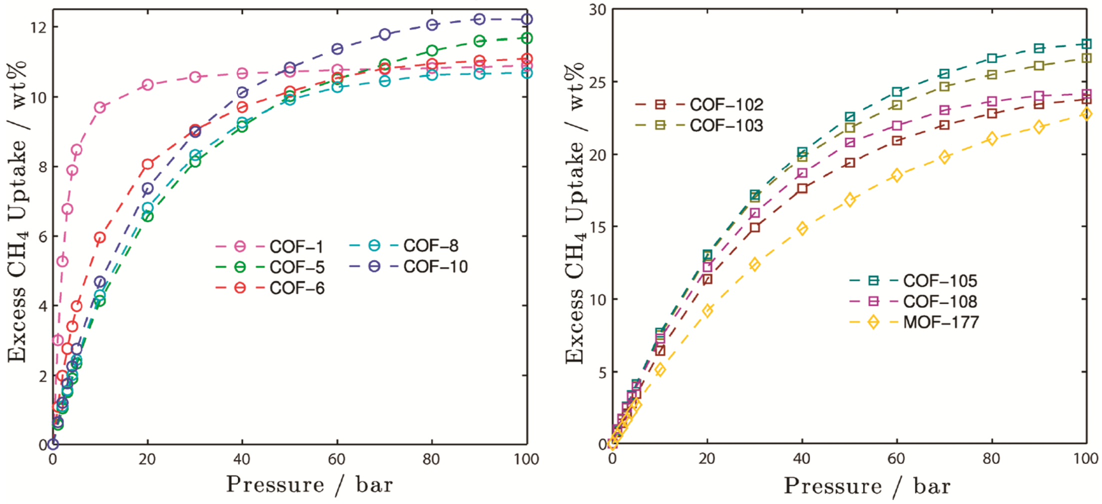
b) Excess gravimetric uptake

Figure 6.5: Predicted gravimetric methane isotherms at 298 K: (a) total and (b) excess uptake isotherms. We have also validated our calculations for MOF-177 with experiments and these are included for comparison.

$$N_{total} = N_{excess} + V_p \times \rho_{bulk} \tag{6.3}$$

where N_{excess} is the excess mass, V_p is the pore volume, N_{total} is total adsorbed amount of methane, ρ_{bulk} is the bulk density of methane. Using eq 6.3, we recalculated the total uptake based on the experimental excess isotherms and experimental methane density (see Supporting Information). Calculated total uptakes from eq 3 are greater than simulated ones over the entire range of pressure. The error is <10% below 50 bar, but it is >20% for COF-1 at 100 bar. The reason is that the deviation is not negligible in the high-pressure region and for smaller pore COFs, since eq 3 does not compensate for the volume of adsorbed guests. Thus although eq 6.3 is convenient for a rough estimate of total uptake from experimental data, it can lead to an error in estimating total uptake, especially at high pressure.

6.1.3.3 Adsorption Mechanism of Methane in COFs

At cryogenic temperatures (below 20 K), entropic effects in gas adsorption are not significant, so that the specific adsorption sites of guest molecules can be observed with diffraction experiments.[89] The change in electron density is related to the strength of the adsorbent-adsorbate interaction since the electron density reflects the occupancy of the adsorption sites. However, at room temperature, such diffraction experiments do not provide clear-cut location of the guest molecules due to thermal disorder.[90] Therefore, the average of the snapshots obtained from the GCMC simulations provide new insights into the methane adsorption behavior in COFs.

Figures 6 and 7 show the average of all snapshots for every COFs under each thermodynamic condition. Figure 6.6 shows that the COFs with the larger pores (COF-5, 8, 10) are not filled completely even at 100 bar, although their excess isotherms show saturation, while COF-6 reaches saturation at 60 bar. Another smaller pore material, COF-1, reaches saturation at 40 bar since it can only store three methane molecules per pore (see Supporting Information). The average of the GCMC snapshots show that the joint of two edges is more populated than the center of the pore at higher pressures. Surprisingly, we find that adsorption in 2D-COFs can even occur at room temperature with the coexistence of layer formation and pore filling. The formation of some pattenrs at higher pressures suggest the formation of a second layer for those pores that can hold them; however, a third layer is not observed even for COF-10.

Unlike 2D-COFs, the adsorption sites of 3D-COFs can be on the surface of aromatic and boroxine rings. Figure 6.7 shows that the layer formation and pore filling mechanism is again present even though we are dealing with topologically different compounds. The average of the GCMC steps shows that sites that are more populated are those where two edges converge. A similar trend was observed for COF-108, although it has two different kinds of pores.

6.1.3.4 Isosteric Heat of Adsorption

The adsorption enthalpy is one of the most important parameters to evaluate the performance of COFs, in addition to surface area and pore volume. We calculated the Q_{st} for COFs from their total uptake isotherms (Figure 6.8a). These Q_{st} values do not depend strongly on the pressure (i.e., adsorbed amounts of methane); however, we do see some interesting trends. We expect the COF-methane interaction to decrease with increasing adsorption of methane, since the stronger binding sites would be occupied first.[91] Indeed, this is the case for COF-5, COF-10, COF-105, and COF-108 (group A). However, the Q_{st} values for COF-1, COF-6, COF-8, COF-102, and COF-103 (group B) increase directly with pressure. We interpret this phenomenon as related to the pore diameters

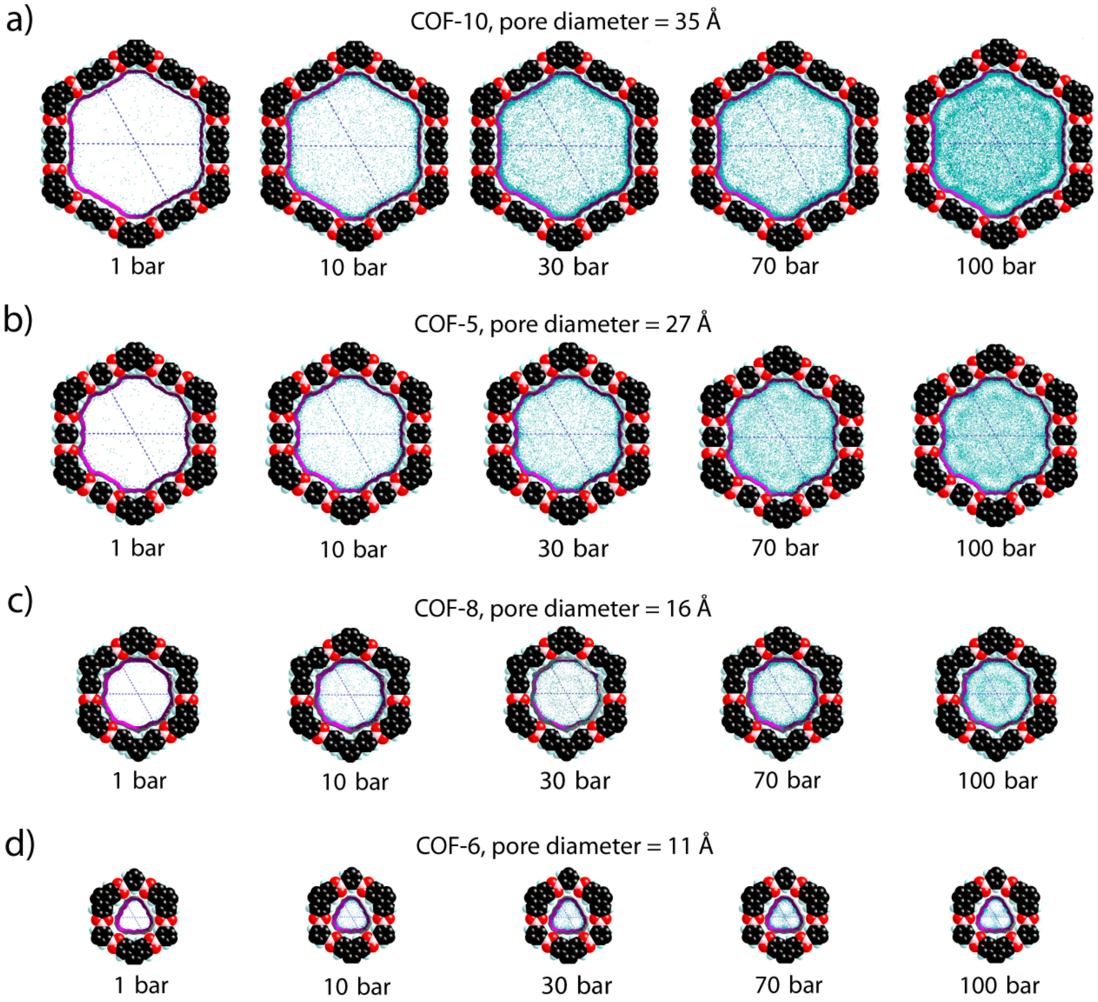

Figure 6.6: Ensemble average from the GCMC steps for methane adsorption in 2D-COFs at various pressures. Atom colors are the same as in Figure 6.2; the average of the methane gas molecules is shown in blue. The accessible surface is shown in purple and was calculated using the vdw radii of every atom of the framework and the methane kinetic radii: (a) COF-10, pore diameter = 35 Å; (b) COF-5, pore diameter = 27 Å; (c) COF-8, pore diameter = 16 Å; (d) COF-6, pore diameter = 11 Å.

because the space is not getting wasted, this suggests that interaction of framework methane is more effective than in the bulk gas. This assumption is supported by the larger Q_{st} values of the COF-methane versus methane alone (Figure 6.8a). Thus group B (Psize below 18 Å) have an steady increase in the Q_{st} values as more methane is added to the structure, while group A (Psize above 18 Å) have a decrease in Q_{st} values at higher pressure; i.e., there is more space so methane can interact more, as in the bulk (see Figure 6.8a). MOF-177 could be classified in group B since it has a Psize of 10.8 Å and V_P of 1.55 cm^3/g.[86] Although it seems that the desirable pore diameter should be smaller than 18 Å, it is not always necessary to design narrow pore materials, because large Q_{st} values could have a negative impact on both heat management and diffusion rate in practical use.[92]

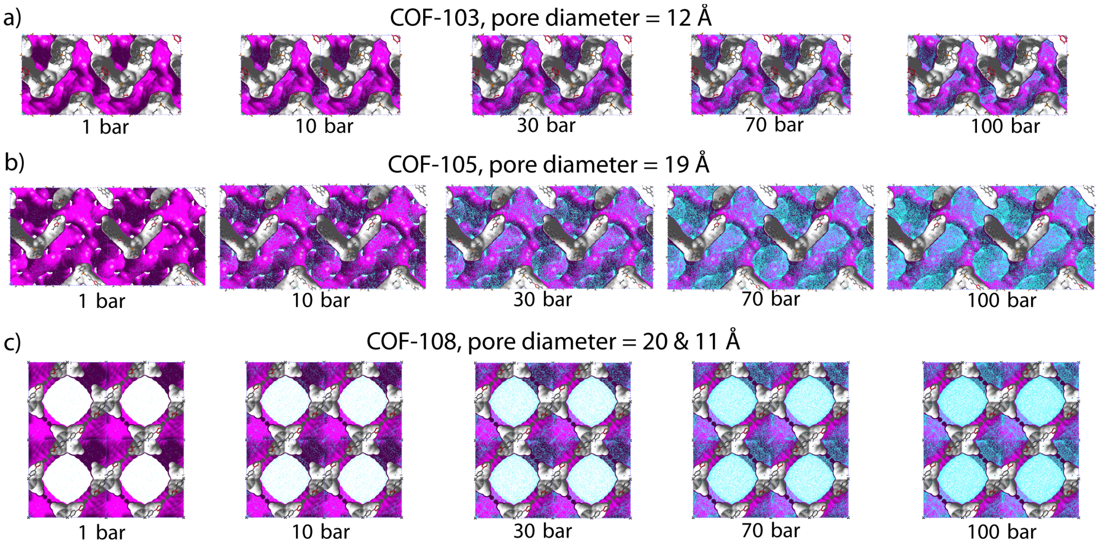

Figure 6.7: Ensemble average of methane molecules at different pressures: (a) COF-103; (b) COF-105; (b) COF-108. Atom colors: C, gray; O, red; Si, yellow; B, pink. The average of the methane gas molecules is in blue. The accessible surface was calculated as in Figure 6.6. COF-102 has the same sorption profile as COF-103 and it is not shown.

In this sense, we believe that COF-102 and COF-103 having reasonable pore diameters and their $Q_{\rm st}$ values place them are among the promising materials. From the relation of $Q_{\rm st}$ with V$_P$ we can find that the best materials for methane adsorption (COF-102, COF-103, and MOF-177) are found at around 1.53 cm^3/g and 10.6 kJ/mol, suggesting a maximum value of performance for these connectivities and chemical composition (Figure 6.8b).

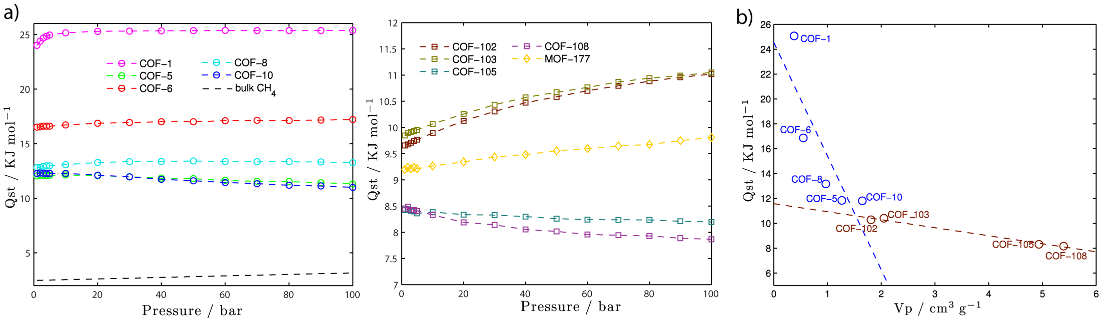

Figure 6.8: (a)Predicted $Q_{\rm st}$ values for COFs as a function of pressure. We have added the calculated values for MOF-177 for comparison. (b) V$_P$ versus $Q_{\rm st}$ for COFs. There are two groups, based on the structural analysis: 2D-COFs (-1, -5, -6, -8, -10), which laid in a line with the same slope. Also the 3D-COFs (-102, -103, -105, -108) have a common line. Both lines coincide at V$_P$ ~ 1.53 cm^3/g and $Q_{\rm st}$ ~ 10.6 kJ/mol.

6.1.3.5 Delivery Amount in COFs

In practical applications of porous material for gas storage, the delivery amount (that is, the difference in the amount adsorbed at 100 bar vs the amount, e.g., at 5 bar) is the important quantity. Although the delivery amount can be measured experimentally,[93, 94] it is not easy to predict delivery amounts from excess isotherms, rather one needs total uptake isotherms. However, the simulations lead directly to this value. We choose 5 bar as the releasing pressure of cylinders and compare estimated delivery amounts to the targets set by the U.S. Department of Energy (DOE): release 180 L at standard temperature and pressure (STP), defined as 298 K and 1.01 bar, of methane per liter of storage vessel (Figure 6.9). The standard temperature and pressure in the DOE targets are 298 K and 1 atm. However, in the field of chemistry, one usually chooses 273 K and 1 atm as STP, so that all volumetric uptake is converted to the volume at 298 K.[95]

We see that COF-1 reaches the DOE target in a total volumetric uptake basis (195 v(STP)/v at 30 bar), but the delivery amount is very poor (42 v(STP)/v at 30 bar), making it a bad candidate for practical applications of methane storage. We predict that COF-102 and COF-103 perform very nicely in both total uptake (255 and 260 v(STP)/v at 100 bar) and delivery amount (229 and 234 v(STP)/v at 100 bar), suggesting that they are suitable for practical applications of methane storage. This results from a combination of factors such as small pore diameter, high surface area, low density, and high pore volume.

6.1.4 Concluding Remarks

To predict reliable methane adsorption isotherms, we developed FFs on the basis of accurate ab initio calculations for interactions of methane with COF subunits involving C, O, B, Si, and H. We confirmed that these calculations predict methane adsorption isotherms for COF-5 and COF-8 in good agreement with experiment. This validates that ab initio based FF can be used to obtain accurate predictions of gas adsorption isotherms. And the developed FF can be effectively used to design new materials prior to experiments.

From our GCMC trajectory, we found the multilayer formations coexist with the pore filling mechanism. We find that a pore diameter (∼12 Å), large pore volume (∼5 cm^3/g), and a high surface area (>5000 m^2/g) can lead to large volumetric methane uptakes. We also demonstrate that a high Q_{st} value can improve the initial slope for the isotherm. However, this behavior reduces the delivery amount of methane, which is more important for practical applications. There may be the misconception that a weak binding energy will necessarily result in poor methane storage capacity. However, we find that the volumetric uptake and the total uptakes in COF-102 and COF-103 outperform other 2D and 3D-COFs at high pressure, even the benchmark MOF-177. The high delivery/storage amount ratios for these COFs again support the importance of reasonable Q_{st}

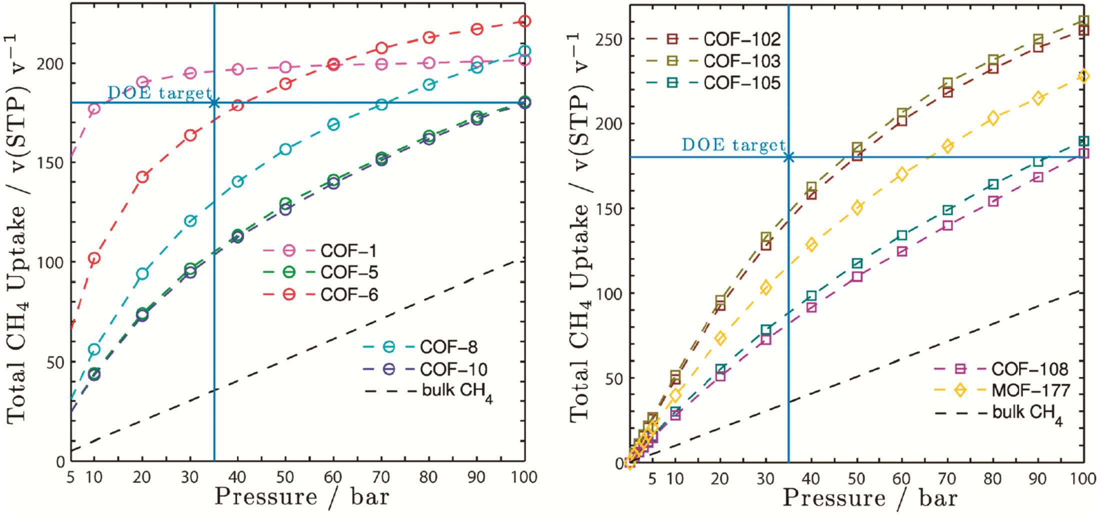

a) Total volumetric uptake

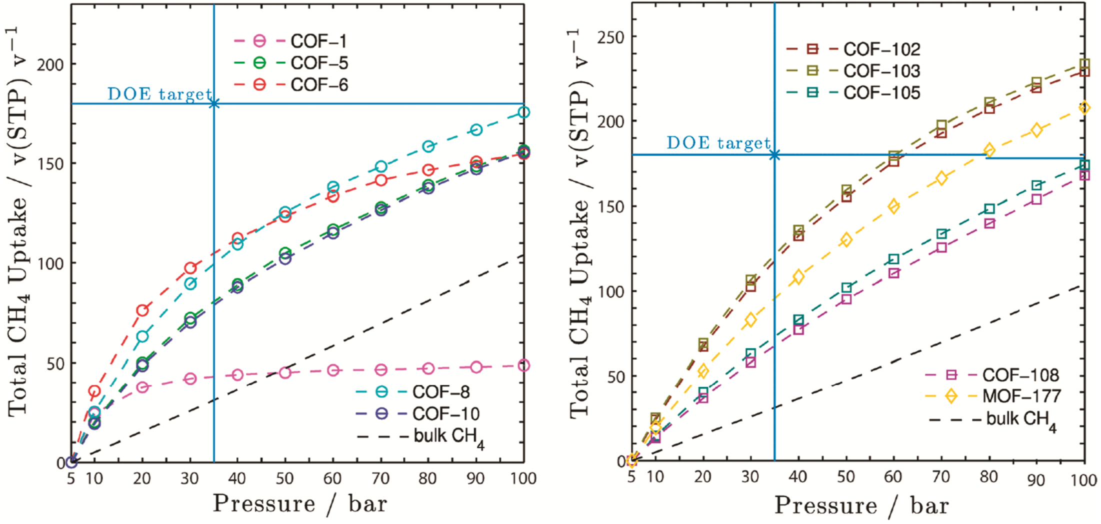

b) Delivery uptake

Figure 6.9: Predicted volumetric methane isotherms at 298 K for COFs: (a) total uptake isotherm and (b) delivery uptake isotherm (the difference between the total amount at pressure p and that at 5 bar). Here the black dashed line indicates the uptake for free CH_4 gas. MOF-177 uptake is added for comparison.

values. These results indicate the value of having an additional fused aromatic ring, because the methane molecules interact strongly with the faces of the aromatic or boroxine ring and weakly to the edges.

This study focused on representative crystalline COFs that have been structurally characterized. These results suggest that crystalline framework structures composed of triazines or triphosphorines instead of the boroxine rings might lead to improved properties.

6.2 Design of Covalent Organic Frameworks for Methane Storage

Reproduced with permission from American Chemical Society, Copyright 2011. Jose L. Mendoza-Cortes, Tod A. Pascal, and William A. Goddard, III J. Phys. Chem. A, **2011**, *115* (47), pp 13852 - 13857.

6.2.1 Introduction

Crystalline microporous materials systems such as the metal-organic frameworks (MOF) and covalent organic frameworks (COF) are valuable for trapping enormous amounts of gases such as H_2, CO_2, and CH_4 at modest pressures,[49, 83, 85, 96, 97, 98, 99] due to their outstanding porosity. Thus COF-105 has a surface area of 6450 m^2/g (equivalent to 1.4 American football fields per gram) and COF-108 has a pore volume of 5.4 cm^3/g with the lowest density crystalline material known (0.17 g/cm_3).[59, 60, 61, 100, 101] We are interested in COFs because they contain light elements (B, C, O, H, and Si). Such materials could be useful in automotive applications (storing CH_4 rather than gasoline[52]) and in CH_4 capture to prevent this greenhouse gas for getting into the atmosphere, of critical importance because methane is 21 times more effective in trapping heat in the atmosphere than CO_2.[102]

We are also interested in the *delivery* amount of gas rather than the *excess* uptake because delivery is more important for industrial application. We define the delivery amount as the difference in the total amount adsorbed at certain pressure compared to the base pressure of the system, for example, atmospheric pressure.[49] Much effort has been focused on reaching the DOE target of storing methane at 35 bar, because this is the pressure in natural gas pipelines. However, current commercial tanks can now hold pressures up to 250 bar, and hence we are interested in which frameworks are useful in this pressure range. Here we use virtual screening of candidate materials to discover new designs for COFs that can produce better CH_4 delivery methane uptake than current materials.

Our previous results showed that small pore diameter plus a high content of accessible aromatic rings give a heat of adsorption (Q_{st}) suitable for binding CH_4 at 298 K.[49] On the other hand, too low a pore diameter leads to quick saturation at low pressures, as was found for COF-1. We also found[49] that methane-methane interactions are important in achieving good sorption performance with increasing pressure. On the basis of these lessons, we designed 15 new COFs containing alkyl substituents that we expected to take advantage of these interactions.

We based the new designs on building blocks with a 3,4-connectivity, shown previously to yield carbon-nitride (**ctn**) and boracite (**bor**) topologies.[61, 80, 81] Figure 6.10 shows the building block used for this study as well as the chemistry of the condensation reactions. Scheme 6.2.1 summarizes

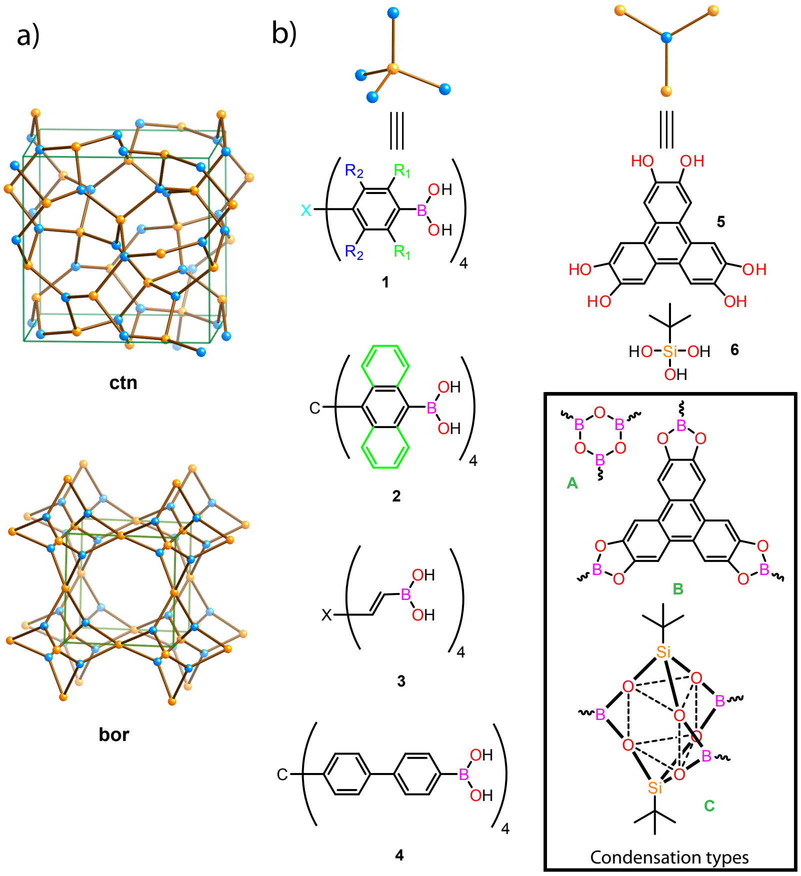

Figure 6.10: Building blocks used in this study for designing new COFs. The inset shows the types of condensation.

the topologies and the kind of substituents used for the frameworks.

This paper is organized as follows. Section describes the details about the methodology used for each simulation. It also includes the criteria used for the topological design of the new COFs. Section presents the results about the volumetric delivery performances as well as Q_{st} values of our compounds versus representatives COFs and MOFs without open metal sites (COF-102, COF-103, COF-105, COF-108, COF-202, MOF-177, and MOF-200). We also discussed the comparison of our results with previous studies. Finally, section summarizes our main findings.

6.2.2 Methodology

6.2.2.1 Force Field

Nonbonding terms. Previously we developed a force field for nonbonded interactions (vdW-FF) of COFs and CH_4 based on quantum mechanics (QM) calculations at the MP2-IR/QZVPP level expected to be accurate for London dispersion forces (van der Waals attraction). We validated this FF with the CH_4 equation of state at various temperatures (260-400 K) and pressures (1, 10, and

Reactants	Type		R_1	R_2	Name	topology
1	A	X=C	—H	—H	COF102	**ctn**
1	A	X=C	—CH_2CH_3	—H	COF102-Et-H	**ctn**
1	A	X=C	—$CH(CH_3)_2$	—H	COF102-iPr-H	**ctn**
1	A	X=C	—$(CH_2)_2CH_3$	—H	COF102-Pr-H	**ctn**
1	A	X=C	—$C(CH_3)_3$	—H	COF102-tBu-H	**ctn**
1	A	X=C	—$C(CH_3)_3$	—$C(CH_3)_3$	COF102-tBu-tBu	**ctn**
1	A	X=C	—CH_3	—CH_3	COF102-Me-Me	**ctn**
1	A	X=Si	—CH_3	—CH_3	COF103-Me-Me	**ctn**
2	A	X=C	N/A	N/A	COF102-Ant	**ctn**
3	A	X=C	N/A	N/A	COF102-Eth-trans	**ctn**
3	A	X=Si	N/A	N/A	COF103-Eth-trans	**ctn**
5+1	B	X=Si	—CH_3	—CH_3	COF105-Me-Me	**ctn**
5+1	B	X=C	—H	—H	COF108	**bor**
5+1	B	X=C	—$(CH_2)_5CH_3$	—H	COF108-nHex-H	**bor**
5+1	B	X=C	—CH_3	—CH_3	COF108-Me-Me	**bor**
5+3	B	X=C	N/A	N/A	COF105-Eth-trans	**ctn**
6+1	C	X=C	—H	—H	COF202	**ctn**
6+4	C	X=C	—H	—H	COF212	**ctn**

Scheme 6.2.1: Reactions Involving the New COFs. The first column shows the building blocks used and the second column shows the type of condensation undergone. Note that between COF-102 and COF-103 analogs the only difference is the central atoms of the tetrahedral, C and Si, respectively

100 bar) and with experimental loading curves.[49] This vdW-FF was used to calculate the loading curves.

Covalent Terms. For this work we are interested in studying the stability of the frameworks using molecular dynamics (MD). Thus we have combined our vdW-FF with the covalent terms from the DREIDING force field[25] for use in the MD studies.

6.2.2.2 Electrostatic Interactions

We described the electrostatic interactions using used the Mulliken charges from QM for the CH_4 molecule (C, -0.43820; H, +0.10955) and the QEq (charges equilibration) charges for the framework.[12]

6.2.2.3 Grand Canonical Monte Carlo

We used grand canonical Monte Carlo (GCMC) simulations to calculate the loading curves for these frameworks. Here we use our vdW-FF with QEq charges for the framework and QM charges for the CH_4. At each pressure we considered 3 000 000 GCMC steps and tested that convergence was attained in each simulation. Every GCMC step allows four possible events: translation, rotation, creation, and annihilation each at equal probability.[78, 79] We used the GCMC code as implemented in Cerius2.

6.2.2.4 Molecular Dynamics

To test the stability of the compounds, we performed molecular dynamics (MD) simulations using the LAMMPS simulation engine with a 1 fs time step.[103] We used the combined force field (vdW-FF plus Dreiding) to treat the interactions. The long-range electrostatics were treated using the particle-particle particle-mesh Ewald[104] technique, with a real space cutoff of 10 Å and an accuracy tolerance of 10^{-5}. For each MD simulation we started with the equilibrium geometry from 500 steps of conjugated gradient (CG) minimization (cell coordinates and atom positions) followed by 10 ps of NVT dynamics to heat the system from 10 to 298 K. Finally, we ran NPT dynamics at 1 atm and 298 K for 7.5 ns from which we collect all relevant data. The temperature damping constant was 0.1 ps, and the pressure damping constant was 2.0 ps. The equations of motion used are those of Shinoda et al.,[105] which combine the hydrostatic equations of Martyna et al.[106] with the strain energy proposed by Parrinello and Rahman.[107] The time integration schemes closely follow the time-reversible measurepreserving Verlet integrators derived by Tuckerman et al.[108]

6.2.2.5 Topological Consideration in the Design of COFs

For the design of the 3,4 frameworks we used only the **ctn** ($I\bar{4}3d$ space group) and **bor** ($P\bar{4}3m$ space group) topologies because they have been shown to be the most stable.[61, 80, 81] To build each structure, we used the corresponding space group and add the irreducible representation of the ligand into it. None of the ligands produces lower symmetry frameworks.

We minimize these frameworks with CG for 500 steps, which always led to convergence. During the design of COF-102- Eth-trans, COF-103-Eth-trans, and COF-105-Eth-trans, we found that the *cis* version is incompatible with these constraints and that the framework is unstable after minimization, leaving the trans isomer as the only choice. The optimized structures coordinates are reported in the Supporting Information.

6.2.3 Results and Discussion

6.2.3.1 Delivery Volumetric Uptake in Designed COFs

The DOE goal for methane storage is 180 v(STP)/v at 35 bar. Here, v(STP)/v denotes the volume of methane per volume of system, where STP is the standard temperature and pressure of 298 K and 1.01 bar.[95] Only two materials have been reported to satisfy the methane uptake DOE requirements at 35 bar: Ni-MOF-74 and PCN-14. In the experimental reports, 1 atm and 273 K were used as the standard units. Thus, Ni-MOF-74[109] reached 190 *excess* v(273 K, 1 atm)/v and PCN-14[110] reached 220 *excess* v(273 K, 1 atm)/v, the latter measured at 290 K. To make a fair comparison in the following discussions, we multiply these experimental quantities by 1.09 (or 298/273) to get our defined STP. Therefore, after conversion, we obtain 207 v(STP)/v for and Ni-

MOF-74 and 240 v(STP)/v for PCN-14.

The representative MOF-177,[86] which is now in industrial production for automotive applications, [111] achieves only 91 *excess* v(STP)/v at 35 bar. The excess and total uptakes are summarized in Table 6.4, where we used standard definitions for these quantities.[85, 112] We use only experimental uptakes for PCN-14 and Ni-MOF-74 because our vdW-FF does not deal yet with open metal sites.

The results for the delivery amount of methane for our four best new designs for up to 35 bar are shown in Figure 6.11, whereas the performance for the remaining 11 systems are in the Supporting Information. At 35 bar (in v(STP)/v delivery units) the best performers are

COF-103-Eth-trans (192 ± 4), exceeding the DOE target,

COF-102-Ant (180 ± 3),

COF-102-Eth-trans (172 ± 3), and

COF-105-Eth-trans (110 ± 2).

Thus COF-103-Eth-trans stores 5.6 times as much as bulk CH_4 at the same pressure (bulk CH_4 reaches 34 ± 1). All our designed COFs have superior performance to previously reported COFs and MOFs, such as COF-102 (137 ± 3), MOF-177 (112 ± 2), and MOF-200 (81 ± 2).

The new materials were designed for best performance at 35 bar. At higher pressures, the trend in performance (at 300 bar and in v(STP)/v delivery units) changes: COF-105-Eth-trans (350 ± 7),

COF-103-Eht-trans (328 ± 7),

COF-102-Eht-trans (306 ± 6), and

COF-103-Ant (258 ± 5).

Therefore, at 300 bar, COF-105-Eth-trans stores 1.3 times as much as an empty container (bulk CH_4 takes 263 ± 3). Other good performers over the range of 1-300 bar are shown in the Supporting Information. For example, at 300 bar, COF-103 reaches 352 ± 7 delivery v(STP)/v, followed by COF-105 (327 ± 7), COF-108 (318 ± 6), COF-212 (310 ± 6), COF-105-Met-Met (308 ± 6), and COF-108-Met-Met (302 ± 6). We see that some of these new designs perform better than the archetypal frameworks: COF-102 (340 ± 7), MOF-177 (336 ± 7), and MOF-200 (321 ± 6). Figure 6.11 shows that COF-102-Ant performs comparable to bulk CH_4 container at 300 bar whereas under 35 bar it approaches the DOE target.

Our results show that attaching alkyl substituents such as -CH_3, -CH_2CH_3, -$CH_2CH_2CH_3$, -$CH(CH_3)_2$, -$C(CH_3)_3$, or -$(CH_2)_5CH_3$ to the benzene rings does not increase the binding over having the simple H substituent. Among alkyl-substituted benzenes, the type of isomer matters because the one with higher surface area performs better, in particular when propyl (2590 m^2/g) and isopropyl (1420 m^2/g) are compared. The propyl substituent has a higher uptake when compared to isopropyl because more atoms are available to interact with a sorbent molecule and gives higher surface area even though they have the same components.

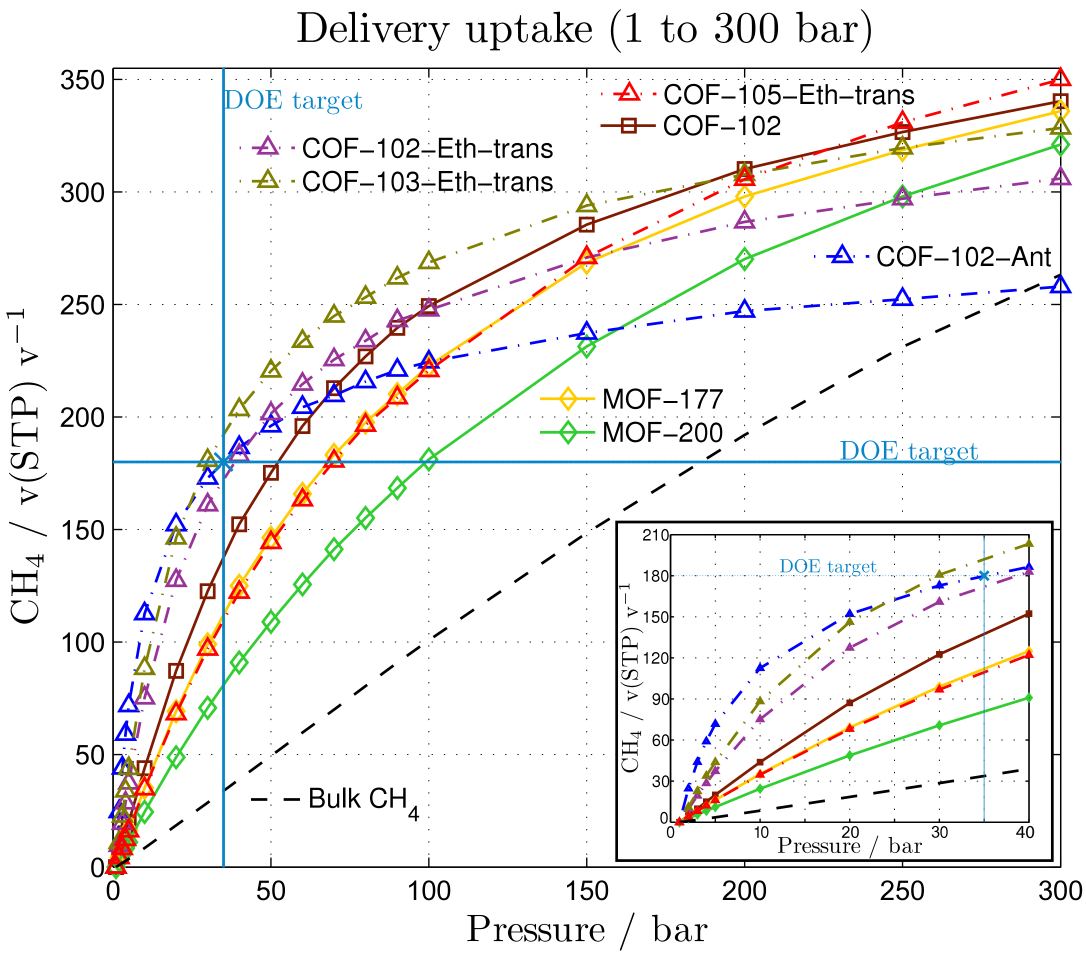

Figure 6.11: CH_4 uptake for the best COF performers. The delivery amount using a base pressure of 1 bar is reported. The best performers at 35 bar are shown along with some that perform best at 300 bar. Solid lines indicate published compounds.

6.2.3.2 Isosteric Heat of Adsorption

Our calculated Q_{st} values are shown in Figure 6.12. These trends can be understood from a comparison of COF-1, COF-102-Ant, and COF-103-Eth-trans (Table 6.4). COF-1 has the highest Q_{st} among COFs, but it is saturated by 40 bar, giving the poorest delivery uptake. COF-102-Ant outperforms COF-1 despite a smaller Q_{st} value due to the higher and V_{P}. Finally, COF-103-Eth-trans is the best performer due to its balance of mild Q_{st}, high S_{A} and high V_{P}.

High Q_{st} (>20 kJ/mol) at low pressures and low S_{A} and V_{P} lead to low delivery amount. The same analysis was done for PCN-14 and Ni-MOF-74 where experiments found high Q_{st} (30.0 and 20.2 kJ/mol, respectively, at nearly 0 bar) but poor S_{A} (1753 and 1033 m^2/g, respectively) and V_{P} (0.87 and 0.54 cm^3/g, respectively). Thus we expect that PCN-14 and Ni-MOF-74 will saturate by 100 bar, consistent with their experimental sorption isotherm curves trend. We did not simulate PCN-14 and Ni-MOF-74 in this study because we have not yet developed a FF to deal with the

Table 6.4: Isosteric heat of adsorption (Q_{st}), surface area (S_A), pore volume (V_P), and uptake of the framework series at 298 K (Where Tot = total, Exc = excess, and Del = delivery)[a]

material	Q_{st} (kJ/mol)	S_A (m^2/g)	V_P (cm^3 g^{-1})	$^{Tot}CH_4$ [v(STP)/v] at 35 bar	$^{Exc}CH_4$ [v(STP)/v] at 35 bar	$^{Del}CH_4$ [v(STP)/v] at 35 bar	$^{Del}CH_4$ [v(STP)/v] at 300 bar
PCN14[110]	30	1753	0.87	251[b](230[c])	240[b](220[c])		
Ni-MOF74[109]	20.2	1033	0.54	218[b](200[c])	207[b](190[c])		
COF1	25.1	1230	0.38	196	196	145	150
COF102	10.5	4940	1.81	143	120	137	340
COF102-Ant	18.4	2720	0.75	215	200	180	258
COF102-Eth-trans	13.1	4640	1.2	184	166	172	306
COF103-Eth-trans	13.3	4920	1.36	206	187	192	328
COF105-Eth-trans	9.3	6350	3.62	114	86	110	350
MOF177	9.6	4800	1.93	116	91	112	336
MOF200	7.9	5730	4.04	84	54	81	321
Pure CH_4	3			35		34	263

[a] Q_{st} values are reported as an average from 1 to 300 bar. S_A and V_P were estimated from rolling an Ar molecule with diameter of 3.42 Å6 over the frameworks surface. The GCMC predicts an uncertainty of 2% in our reported uptakes but for clarity it is not shown. For PCN14 and Ni-MOF74 we use the experimental Q_{st} at low pressure (nearly zero coverage).[109, 110] The S_A and V_P for PCN-14 and Ni-MOF-74 were also obtained from literature.

[b] We have converted the experimental uptake (273 K, 1 atm) to our STP units (298 K, 1.01 bar) by multiplying by the factor 1.09 to get a better comparison.

[c] Experimental value (273 K, 1 atm).[109, 110]

open metal sites, which are an important feature in these compounds. The trends in performance at higher pressure are also shown for archetypal MOF-177 and MOF-200, which have lower Q_{st} of 9.7 ± 0.5 and 8.0 ± 0.2, respectively. However, the higher S_A (4800 and 5730 m^2/g, respectively) and V_P (1.93 and 4.04 cm^3/g, respectively) give them an advantage at pressure beyond 100 bar.

In this work we are focused on getting the best performance in delivery units and this requires a low interaction methane-COF in the low-pressure range. In other words, we want to get a low Q_{st} at low pressure. We have succeeded in obtaining this behavior for COF-102-Eth-trans and COF-103-Eth-trans by using the tiny vinyl link, as demonstrated by the shape of their Q_{st} curves, which are similar to that of COF-102 but more marked for the entire pressure range. Eventually, methane-methane interactions compensate to show moderate Q_{st}. This is opposite to the Q_{st} profile of COF-102-Ant where the link being used gives a high interaction at low loading (Figure 6.12). Therefore, our new designs using vinyl linkers present a new way to maximize delivery uptake, which is different from the approach of using fused phenyl rings.

6.2.3.3 Stability of COFs

Recently, it was suggested[113] that COF-108 and even COF-102 might collapse due to instability of the frameworks; however, the same study suggested that for COF1 the "AA" conformation is more

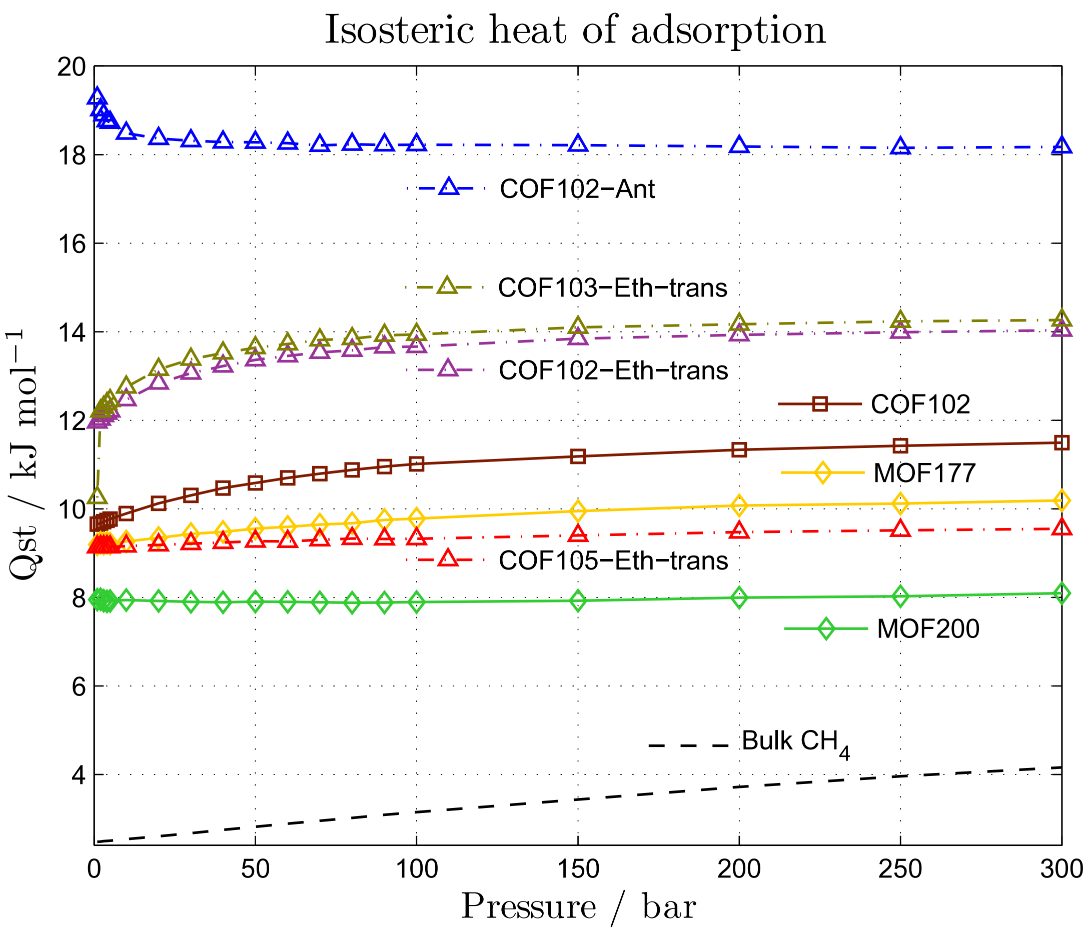

Figure 6.12: Heat of adsorption calculated for the compounds in Figure 6.11. The results for the remaining compounds are in the Supporting Information.

stable than the experimentally observed “AB” conformer.[113] Therefore, we decided to study the stability of our newly designed COFs with MD simulations. Our results show that cell parameters of our new COFs change only slightly (0.130-0.142%) throughout the entire dynamics while the cell angles stayed at 90° (orthorhombic) as shown in Table 6.5 and Figure 6.13.

For comparison, we also performed MD on the characteristic MOF-5 because it is very well documented experimentally that the lattice parameters change from 25.670 to 25.910 Å over a temperature range of 3.5-300 K but remain stable under these conditions.[89, 114, 115] We find that MOF-5 has a change of 0.219% in the lattice parameters, larger than our new COFs (Table 6.5). This indicates that our new COFs and the experimental COFs are stable without guest molecules at 298 K and 1 atm.

Table 6.5: MD statistics for the frameworks obtained at 298 K[a]

material	^{MD}lattice (Å)	^{MD}std dev (%)	^{Exp}lattice (Å)
COF-102	27.444	0.0268 (0.098)	27.177
COF-103	27.86	0.0280 (0.101)	28.248
COF-108	28.917	0.0402 (0.139)	28.401
COF-102-Ant	27.759	0.0389 (0.140)	
COF-102-Eth-trans	19.82	0.0274 (0.138)	
COF-103-Eth-trans	20.371	0.0290 (0.142)	
COF-105-Eth-trans	37.043	0.0483 (0.130)	
MOF-5	24.286	0.0533 (0.219)	25.790 (0.46%)[b]

[a] The standard deviation was calculated after 10 ps. All these frameworks have a cubic lattice.

[b] The experimental lattice value for MOF-5 is taken as the median of most representative experimental conditions reported (the average for these experiments is 25.833 Å). For comparison we show in parentheses the percentage from upper and bottom bounds.[89, 114, 115]

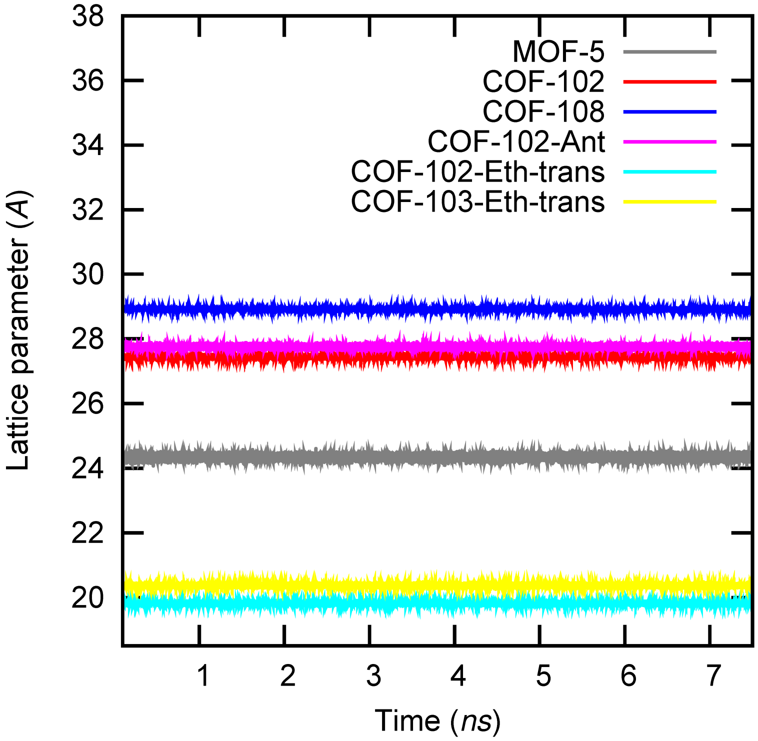

Figure 6.13: Lattice parameter variations obtained from MD for several COFs. The lattice parameters are in Angstroms (Å) and time in nanoseconds (ns). COF-103 and COF-105-Eth-trans are not shown; the statistics are summarized in Table 6.5.

6.2.3.4 Comparisons to Previous Computational Studies

previous computational report about sorption of CH_4 on MOFs showed that increasing the number of fused benzene rings increases the $Q_{\rm st}$ value.[66] However, they reported that their empirical vdW attraction terms led to errors of 5.7-9.9% greater than experiments. This study did not report the stability of their designed compound IRMOF-993, and experimentalists attempted to synthesize the proposed IRMOF-993 but could only create the analog PCN-13. The synthesized framework has the same components but a different topology with a smaller pore size (almost half of the originally proposed MOF-993).[116] MOF-993 was reported to be topologically stable on the basis of studies of Snurr et al.;[66] however, it was found by experimentalists not to be thermodynamically accessible. Even so, these studies showed that enhancement of CH_4 storage at pressures below 35 bar on MOFs can be attained by increasing the Q_{st} value by putting fused rings into the framework, assuming the structure is stable. Our study shows that this is also the case for CH_4 in COFs; however, we found that this is a poor strategy if we want to obtain a good delivery uptake at higher pressures and it does not help beyond 250 bar.

To avoid such problems, we performed MD calculations on our proposed topological stable frameworks to show that they are also dynamically stable. Our current study shows that enhancement of the CH_4 delivery amount can by attained reducing the interaction at low-pressure of methane-COF while also demonstrating stability of the proposed frameworks. We found that this behavior is opposite to that of putting fused benzene rings when looking at the interaction profile over the entire pressure range.

6.2.4 Concluding Remarks

In summary, we have also shown two ways to produce improved absorbents for higher delivery methane up to 35 bar: by using skinny ligands to minimize the methane-COF interaction in the low-pressure range (COF-102-Ethtrans and COF-103-Eth-trans) and by increasing the heat of adsorption (COF-102-Ant).

We also found that the performance at 300 bar can be improved by frameworks with larger pore volumes and surface areas. Our results show that attaching systematically alkyl substituents to the benzene rings does not increase the binding over having a simple -H substituent. These conclusions should apply also to metal-organic frameworks and zeolite imidazolate frameworks.

Chapter 7

Clean Energy (H_2) Storage in Metal-Organic Frameworks and Covalent-Organic Frameworks

In this chapter I describe my work on the design of new Covalent-Organic Frameworks (COFs) and Metal-Organic Frameworks (MOFs) in order to store H_2. In the first section we validate our methodology by comparing our results with the experimental uptake of the latest MOFs and COFs. We then propose to metalate the frameworkss with Li, Na or K in order to obtain a higher H_2 uptake. For the gravimetric delivery amount from 1 to 100 bar, we find that eleven of these compounds reach the 2010 DOE target of 4.5 wt % at 298 K. The best of these compounds are MOF200-Li (6.34) and MOF200-Na (5.94), both reaching the 2015 DOE target of 5.5 wt % at 298 K. Among the undoped systems, we find that MOF200 gives a delivery amount as high as 3.24 wt % while MOF210 gives 2.90 wt % both from 1 to 100 bar and 298 K. However, none of these compounds reach the volumetric 2010 DOE target of 28 g H_2/L. The best volumetric performance is for COF102-Na (24.9), COF102-Li (23.8), COF103-Na (22.8), and COF103-Li (21.7), all using delivery g H_2/L units for 1-100 bar. These are the highest volumetric molecular hydrogen uptakes for a porous material under these thermodynamic conditions.

In the second section we use accurate quantum mechanical (QM) methods to find the H_2 binding energy to six different common organic linkers as well as their metalated analogs (60 compounds). Precious transitions metals (Pd, Pt) give comparable energies to first row transition metals (Sc to Cu). We report that metalating certain linkers can give the desired binding energy (>10kJ/mol and <15.3 kJ/mol) to reach the maximum delivery amount for the DOE targets. We also show a new route for metalating organic linkers with the use of metallic Pd(0) and we prove that this reaction is favorable, with the new compound serving as a site for chemisorption and physisorption of H_2. With these results we propose that these linkers and transition metals can be used to create the next generation of H_2 storage porous materials

7.1 High H_2 Uptake in Li-, Na-, K- Metalated Covalent-Organic Frameworks and Metal-Organic Frameworks at 298 K

Reproduced with permission from American Chemical Society, Copyright 2012. Jose L. Mendoza-Cortes, Sang Soo Han and William A. Goddard, III J. Phys. Chem. A, **2012**, *116* (6), pp 1621-1631.

7.1.1 Introduction

A current major obstacle to molecular hydrogen (H_2) as an alternative source of energy is the difficulty of storage at operational temperatures. The U.S. Department of Energy (DOE) has set the 2010 targets of 4.5 wt % and 28 g/L at room temperature (and 5.5 wt % and 40 g/L for 2015).[117, 118] Many materials have been proposed that might approach these demanding goals. Chemisorption of H_2 in solid systems can lead to the required capacities; however chemisorption generally leads to interaction energies that are too strong (>30 kJ/mol) compounded by additional barriers that lead to very slow kinetics. On the other hand, physisorption generally has good kinetics (no barrier), but the net bonding is too weak (interaction energy <10 kJ/mol) for substantial storage at room temperature.[119] The discovery of robust microporous covalent organic frameworks (COFs)[59, 61, 100] and metal-organic frameworks (MOFs)[86, 101, 114] have brought excitement that these systems might lead to a solution to this problem due to their (1) high surface area: MOF210 has the world record in Brunauer-Emmett-Teller (BET) surface area of 6240 m^2/g, and Langmuir surface area of 10400 m^2/g;[101] (2) low density: 0.17 g/cm^3 for COF108, the lowest for a crystalline material,[61] while 0.22 g/cm^3 for MOF200;[101] and (3) high porosity: as high as 3.59 cm^3/g for MOF200, 3.60 cm^3/g for MOF210, 1.81 for COF102 and 2.05 for COF103.

However, these compounds show a poor uptake of H_2 at room temperature due to the weak interactions between the frameworks and H_2. As a way to obtain higher interaction energies we proposed metalating MOFs, such as MOF5[120] and MOF177,[121] with Li and we showed that this could increase the uptake sufficiently to achieve up to 5.5 wt % excess H_2 at 300 K.[121]

In the current study, we report the excess and delivery sorption curve from 1 to 100 bar at room temperature for the latest generation of MOF and COFs, including the Li-, Na-, and K-metalated analogs. We also calculate the thermodynamics for the formation of the alkaline species in the gas phase and in tetrahydrofuran (THF), including the possibility of clustering and adducts (Li-benzene vs Li-Li), to explore the plausibility for the experimental synthesis under room temperature. We then propose that metalating the new COFs and MOFs with alkali metals (Li, Na, and K) can dramatically increase the binding energy and, thus, the H_2 uptake.

For this study, we used FF parameters developed from accurate quantum mechanics (CCSD(T) and MP2) for describing the physisorption of H_2 onto the alkali-aromatic complex adducts. We then used GCMC based on this first principles FF to calculate the loading curves of H_2 versus pressure at room temperature. These simulations demonstrate that the metalated versions of these materials can achieve the major DOE gravimetric targets for 2010 and even 2015. We report H_2 uptake using total, delivery, and excess units resulting from metalating the highest surface areas (S_A) and the highest pore volume (V_P) frameworks with Li, Na, or K, as well as the pristine analogs. This includes the latest generation of COFs (COF102, COF103, and COF202) and MOFs (MOF177, MOF180, MOF200, MOF205, and MOF210), which physical properties are summarized in Table 7.1.

Table 7.1: Properties of the frameworks used in this work: surface area (S_A), pore volume (V_P), and density (ρ)[a]

material	S_A, m2g-1	V_P, cm3g-1	ρ, g cm-3	material	S_A, m2g-1	V_P, cm3g-1	ρ, g cm-3
COF102	4940	1.81	0.42	COF102-Na	4930	1.35	0.5
COF103	5230	2.05	0.38	COF103-Na	5090	1.54	0.46
COF202	4500	1.37	0.54	COF202-Na	3950	1.09	0.59
MOF177	4800 (4500)	1.93 (1.89)	0.43	MOF177-Na	4710	1.49	0.46
MOF180	5940	3.5	0.25	MOF180-Na	6010	2.92	0.28
MOF200	5730 (4530)	4.04 (3.59)	0.22	MOF200-Na	6020	3.17	0.26
MOF205	4630 (4460)	2.21 (2.16)	0.38	MOF205-Na	4950	1.75	0.44
MOF210	5570 (6240)	3.61 (3.60)	0.25	MOF210-Na	5610	3.05	0.28
COF102-Li	5360	1.65	0.44	COF102-K	4380	1.1	0.56
COF103-Li	5500	1.85	0.38	COF103-K	4800	1.27	0.52
COF202-Li	4250	1.25	0.54	COF202-K	3570	0.94	0.64
MOF177-Li	5100	1.74	0.39	MOF177-K	4220	1.27	0.51
MOF180-Li	6440	3.26	0.26	MOF180-K	5630	2.6	0.31
MOF200-Li	6480	3.69	0.23	MOF200-K	5600	2.73	0.29
MOF205-Li	5270	2	0.4	MOF205-K	4340	1.5	0.49
MOF210-Li	6130	3.39	0.26	MOF210-K	5140	2.73	0.31

[a] The values in parentheses were reported in the literature.[101]S_A and V_P were estimated from rolling an Ar molecule with a diameter of 3.42 Å [71] over the frameworks surface.

7.1.2 Computational Details

7.1.2.1 Quantum Mechanics Calculations and Development of the Parameters for Nonbond Interactions

To develop FF parameters for the nonbonded interactions between H_2 and MOF/COFs, we used DFT/M06[122] with the 6-311G**++ basis set calculations as implemented in Jaguar[9] to determine the locations and numbers of Li, Na, or K atoms on the aromatic linkers. We then used these geometries to calculate the binding energies from accurate quantum mechanical methods (CCSD(T) and MP2) which are capable of accurately describing the London dispersion forces The FF were then fitted to these QM energies and geometries.

We use the Morse potential (eq 7.1), which we found to describe well the nonbond interaction of H_2. The Morse function involves three parameters: the well depth D, the equilibrium bond distance r_0, and the stiffness α.

$$\boldsymbol{U}_{ij}^{Morse}(r_{ij}) = D\left\{e^{\alpha(1-\frac{r_{ij}}{r_0})} - 2e^{-\frac{\alpha}{2}(1-\frac{r_{ij}}{r_0})}\right\} \tag{7.1}$$

Our experience is that the Morse function gives a slightly better description than exponential-6, which performs much better than Lennard-Jones 12-6 potential.[123, 124] Table 7.2 shows the parameters used for this work.[96, 120, 125]

Table 7.2: Nonbonded FF parameters used for this study based on MP2 for Li and CCSD(T) for Na and K[a]

term	D, kJ mol^{-1}	r_0, Å	α
H_{H2}-H_{H2}	7.60 10-2	3.57	10.7
H_{H2}-CCOF/MOF	4.22 10-1	3.12	12
H_{H2}-HCOF/MOF	3.63 10-3	3.25	12
H_{H2}-ZnCOF/MOF	5.21 10-1	2.76	13.4
H_{H2}-OCOF/MOF	1.05 10-1	3.32	12
H_{H2}-BCOF/MOF	2.02 10-1	3.49	10.6
H_{H2}-SiCOF/MOF	4.61 10-1	3.53	14.2
H_{H2}-LiCOF/MOF	9.03	2.02	7.13
H_{H2}-NaCOF/MOF	5.73	2.49	7.71
H_{H2}-KCOF/MOF	2.71	3.13	8.04

[a] The function form (Morse) is given in eq 7.1. D is the well depth, r_0 is the equilibrium bond distance, and α determines the force constant.[120, 96, 125]

7.1.2.2 Valence Bond Force Field

The equilibrium structures of the pristine MOFs and COFs used in this study were optimized with the Dreiding force field[25] starting with the reported experimental structures. We have shown that the resulting structures are in very good agreement with experiment.[120, 96] The coordinates of the optimized metalated structures are shown in the Supporting Information.

7.1.2.3 Grand Canonical Monte Carlo Loading Curves

We used the first principles based force field described above in grand canonical Monte Carlo (GCMC) ensemble simulations. Here for each temperature and pressure, we constructed 3,000,000 configurations to compute the average loading for which we observed convergence was obtained. Every GCMC step allows four possible events, translation, rotation, creation, and annihilation, each at equal probability. We used the GCMC code as implemented in Cerius2. The structures of the optimized frameworks are shown in Figure 7.1.

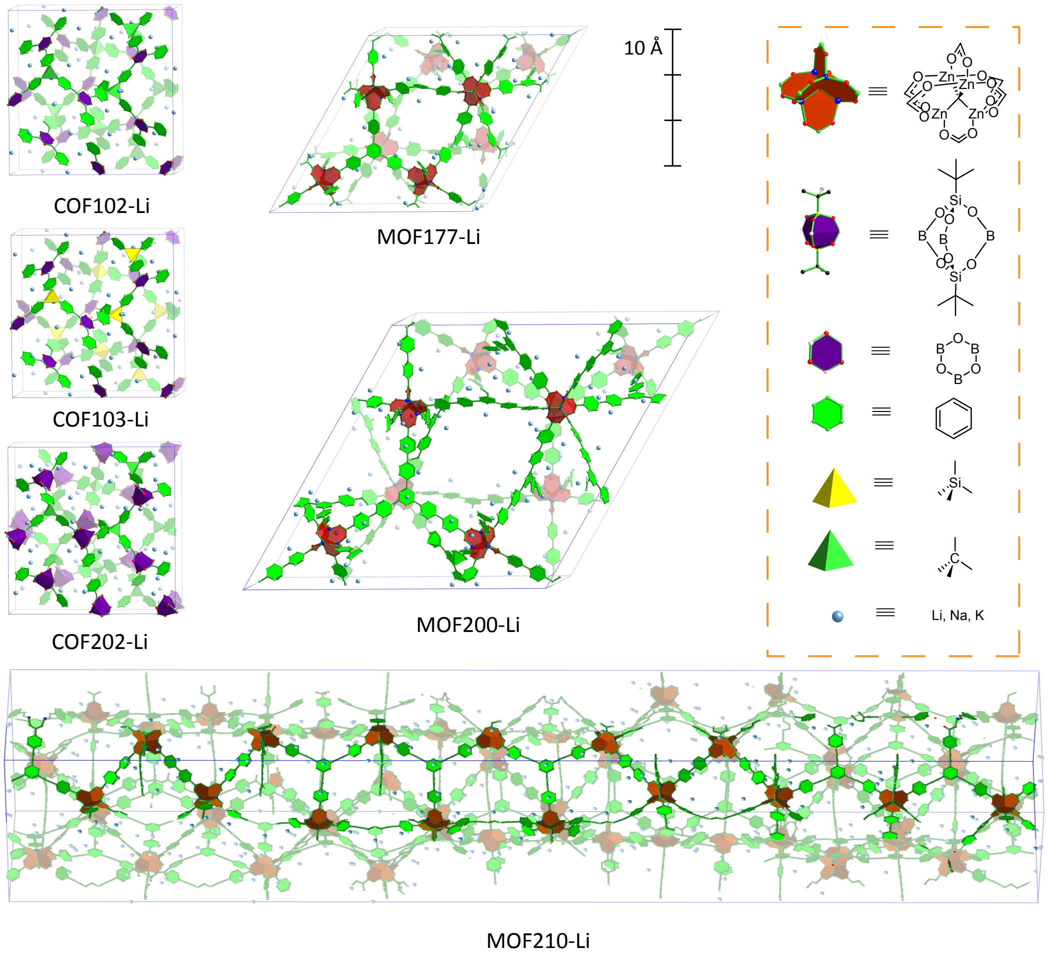

Figure 7.1: Structures of the Li-doped COFs and MOFs studied in this work. Hydrogen atoms have been omitted for clarity.

7.1.3 Results and Discussion

7.1.3.1 Nature of the Chemical Bond for the Li-Benzene (Li-Bz) Systems

To investigate the plausibility on the formation of Li-Bz adduct, we calculated their thermodynamics from quantum mechanics in the gas phase and in tetrahydrofuran (THF). Nonperiodic QM calculations were carried out using the B3LYP[47, 48] and M06[122] hybrid DFT functionals with the Jaguar code.[9] Here we used the 6-31G**++ and 6-311G**++ basis sets. All geometries were optimized using the analytic Hessian to determine that the local minima have no negative curvatures (imaginary frequencies). The vibrational frequencies from the analytic Hessian were used to calculate the zero-point energy corrections at 0 K (Tables 7.3 and 7.4). To explore the solvation, we consider two different approaches explicit THF and implicit THF (for which we used the Poisson-Boltzmann continuum approximation; with $\epsilon = 7.6$, $R_0 = 2.52$ Å).[28] When we compared the binding energy for the Li-Li compounds, we found that M06 is closer than B3LYP to the CCSD(T) calculations (Figure S1). The results for the thermodynamics at 298.15 K and 1.01 bar are shown in Figure 7.2. We observed that, in the gas phase, the Li-Bz is not thermodynamically favorable; however, MO6 predicts that the Li-Bz-Li compound is favorable in the gas phase with respect to Li(g) and Bz(g). This observation prompted us to calculate the thermodynamics in THF since this might help to stabilize the polarized Li species and, therefore, have a favorable thermodynamics under these conditions. As predicted, we can see from Figure 7.2, if we are able to form Li(g) as well as Bz(g) and dissolve them in THF, we will observe the formation of Li-Bz adduct is thermodynamically favorable (ΔG = -22.4 kcal/mol). Although such an experimental setup might be difficult, a good approximation could be attained by dissolving Li(s) and Bz(l) in THF at very low concentrations. On the other hand, Tacke[126] has shown experimentally and theoretically that when concentrated quantities of Bz and Li in THF are used at 77 K; C-H activation occurs and Li-Ph + Li-H compounds are formed. In a related work, they also showed that the formation of R-Li$\cdots$Bz adducts (R = H, CH_3, and Ph) is possible when R-Li is used as the source for Li.[127] This suggests that the concentration of Bz and Li, as well as the source of Li is key to obtain the structures here proposed and also confirms that Li clustering is not a major issue.

Table 7.3: Electronic energy for the optimized systems using different basis sets (6-31G**++ and 6-311G**++) and different functionals (M06 and B3LYP) is presented[a]

	M06/6-31**++		M06/6-311**++		B3LYP/6-31**++		B3LYP/6-311**++	
compound	E_{SCF} (kcal/ mol)	BSSE (kcal/ mol)	E_{SCF} (kcal/ mol)	BSSE (kcal/ mol)	E_{SCF} (kcal/ mol)	BSSE (kcal/ mol)	E_{SCF} (kcal/ mol)	BSSE (kcal/ mol)
1Li	-4696.9	N/A	-4696.8	N/A	-4700.7	N/A	-4700.9	N/A
2Li	-9416.2	0.1	-9418.2	0	-9421.7	0.1	-9422.6	0.1
Bz	-145624.2	N/A	-145653.8	N/A	-145747.5	N/A	-145777.4	N/A
Li-Bz	-150323.8	0.3	-150353.6	0.3	-150449.1	0.4	-150479.6	0.5
Li-Bz-Li	-155032.6	1.1	-155066.2	0.9	-155153.2	0.7	-155188.3	0.5

[a] We also show the basis set superposition error (BSSE)[129] for the addition of a Li atom.

In a remarkable work, Krieck et al.[128] have been able to synthesized the $(THF)_3Na(\mu\text{-}\nu^6\text{-}C_6H_3\text{-}2,4,6\text{-}Ph_3)$ and $(THF)_4K(\mu\text{-}\nu^6\text{-}C_6H_3\text{-}Ph_3)$, see inset of Figure 7.2. They were able to characterize these compounds by crystallography. This report shows that these systems can be synthesized but more remarkable it is the fact that the linkers used are the building blocks of MOF-177 and the precursor of MOF-200.

An interesting question to ask is where the electron goes once the Li-Bz adduct is formed. We calculated the HOMO and LUMO for these species and the results are shown in Figure 7.3. The molecular orbital diagram shows that the HOMO-LUMO gap narrows when THF is used (Figure 7.3a). The HOMO shows that the electron remains in the Li in the gas phase; however, if explicit

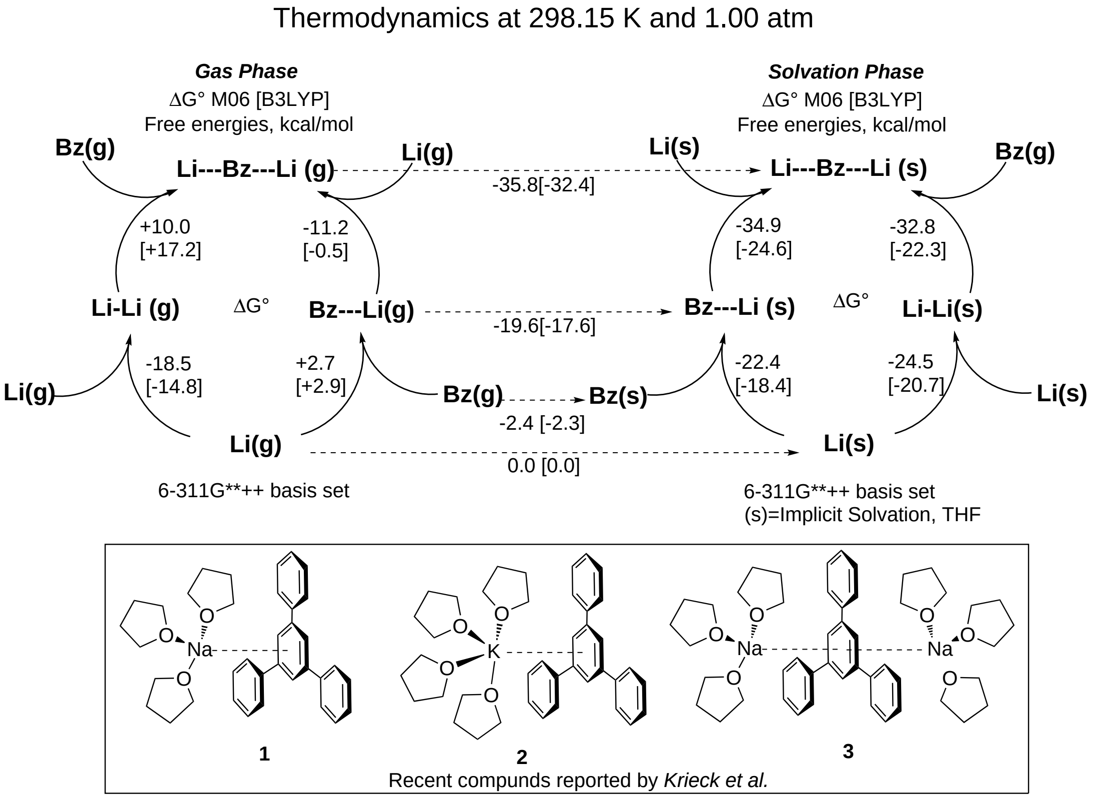

Figure 7.2: Calculations of the thermodynamics for the Li species were obtained using M06/6-311G**++ and B3LYP/6-311G**++. We defined the following quantities as ${}_{\text{gas}}G^{298\text{K}} = E_{\text{SCF}} + E_{\text{ZPE}} + H_{\text{TOT}} - T \times S_{\text{TOT}}$, and ${}_{\text{solv}}G^{298\text{K}} = E_{\text{SCF}} + E_{\text{SOLV}} + E_{\text{ZPE}} + H_{\text{VIB}} + 6RT - T(0.5\ S_{\text{TOT}} + 0.5\ S_{\text{TOT}})$. All the numerical data is shown in Tables 7.3 and 7.4. (Inset) **1**, **2**, and **3** are experimental compounds reported by Krieck et al.[128].

Table 7.4: Zero-point energy (ZPE), vibrational enthalpy (H$_{vib}$), total enthalpy (H$_{tot}$), vibrational entropy (S$_{vib}$), total entropy (S$_{tot}$), and solvation energy (E$_{solv}$) obtained for the different compounds for 298.15 K[a]

compound	M06 ZPE (kcal/mol)	B3LYP ZPE (kcal/mol)	M06 H$_{\text{vib}}$ (kcal/mol)	M06 H$_{\text{tot}}$ (kcal/mol)	B3LYP H$_{\text{vib}}$ (kcal/mol)	B3LYP H$_{\text{tot}}$ (kcal/mol)	M06 S$_{\text{vib}}$ (kcal/mol)	M06 S$_{\text{tot}}$ (kcal/mol)	B3LYP S$_{\text{vib}}$ (kcal/mol)	B3LYP S$_{\text{tot}}$ (kcal/mol)	M06 E$_{\text{solv}}$ (kcal/mol	B3LYP E$_{\text{solv}}$ (kcal/mol
1Li	0	0	0	1.5	0	1.5	0	33.9	0	33.9	0	0
2Li	0.5	0.5	0.2	2.3	0.2	2.3	1.2	47.2	1.2	47.2	0	0
Bz	62.8	63.1	1	3.4	1	3.3	4.5	64.2	4.4	64.1	-2.4	-2.3
Li-Bz	62.7	63.1	1.6	3.9	2.6	5	21	75.7	17.9	84.9	-19.6	-17.6
Li-Bz-Li	58.9	59.9	3.1	5.4	2.7	5.1	29.4	81.6	26.4	78.7	-35.8	-32.4

[a] ZPE energy corrections were obtained from the vibrational frequencies using the respective functional.

or implicit THF is used, the electron is transferred the benzene ring (Figure 7.3b). This suggests that the transfer of electron is promoted by the solvent as expected.

A very important question for experimentalists is how to remove the THF from inside the structure in case it is strongly coordinate to the alkaline metal. The approach discussed so far uses an implicit model approximation (Poisson-Boltzmann continuum approximation) and this approach takes into account the entire accessible surface area of the Li-Bz adduct but it does not consider explicit THF molecules for the calculation. Therefore, we have performed M06/6-311**++ calculations to study how strongly the explicit oxygen of THF can coordinate with the Li from the Li-Bz adduct. We found that the free energy for this case is in the order of ΔG = -1.0 kcal/mol compared to the Li-Bz (implicit THF). Thus, if the THF is coordinated to the Li-Bz adduct, it can be removed. The M06 functional predicts that in gas phase the Li-Bz-Li would be stable while the Li-Bz would unstable by 2 kcal. This is still within the level of accuracy for current DFT approach. However, B3LYP and M06 predict that 1 THF is necessary to stabilize the Bz-Li system if necessary.

A promising method to remove solvents from MOFs structures have been published by Hupp et al.[84] This method uses supercritical CO_2 to activate the frameworks. They reported a spectacular 1200% uptake increase in some cases. This has been proven to lead to the successful activation in MOF-200, for example.[101] This method can be potentially used for the removal of THF since the molecules of THF are not strongly coordinated to the Li-Bz adduct as we have shown in our calculations. The supercritical CO_2 can be ultimately use to remove the most THF molecules and this approach could be tuned to avoid removing also the Li.

7.1.3.2 Gravimetric Uptake

We calculated the total wt% (see SI) gravimetric uptake of the frameworks at 298 K, which we used to estimate the *delivery* amount; this is the difference in the amount adsorbed at 100 bar versus a basis, say, 1 or 5 bar. The delivery amount is difficult to estimate experimentally;[93, 94] however, it is very important for practical applications because it allows us to estimate the maximum amount that can be obtained if we unload the gas to, for example, ambient temperature and pressure.

Figure 7.4a shows the gravimetric delivery amount using 1 bar as the basis for pure and Li, Na, and K metalated COFs and MOFs. Here we see that the Li-metalated cases have a better performance than the Na-metalated cases, while Na-analogs lead to better performance than the K-cases. We can see that from 1 to 100 bar, 11 compounds reach an uptake higher than the 2010 DOE gravimetric target of 4.5 wt %: MOF200-Li (6.34), MOF200-Na (5.94), COF102-Li (5.16), MOF180-Li (5.16), MOF180-Na (4.91), MOF210-Li (4.80), COF103-Li (4.75), COF102-Na (4.75), COF103-Na (4.72), MOF210-Na (4.68), and MOF205-Li (4.58). From these compounds, only MOF200-Li and MOF200-Na reach an uptake over 5.5 wt % delivery. It is interesting to note that pure MOF200 gives a delivery amount as high as of 3.24 wt %, while MOF210 gives 2.90 wt % both at 100 bar and using 1 bar as the basis.

Figure 7.4b shows the gravimetric delivery amount using 5 bar as the basis at 298 K. Under these units, metalated cases lead to a different trend, with the uptake for Na-metalated > Li-metalated

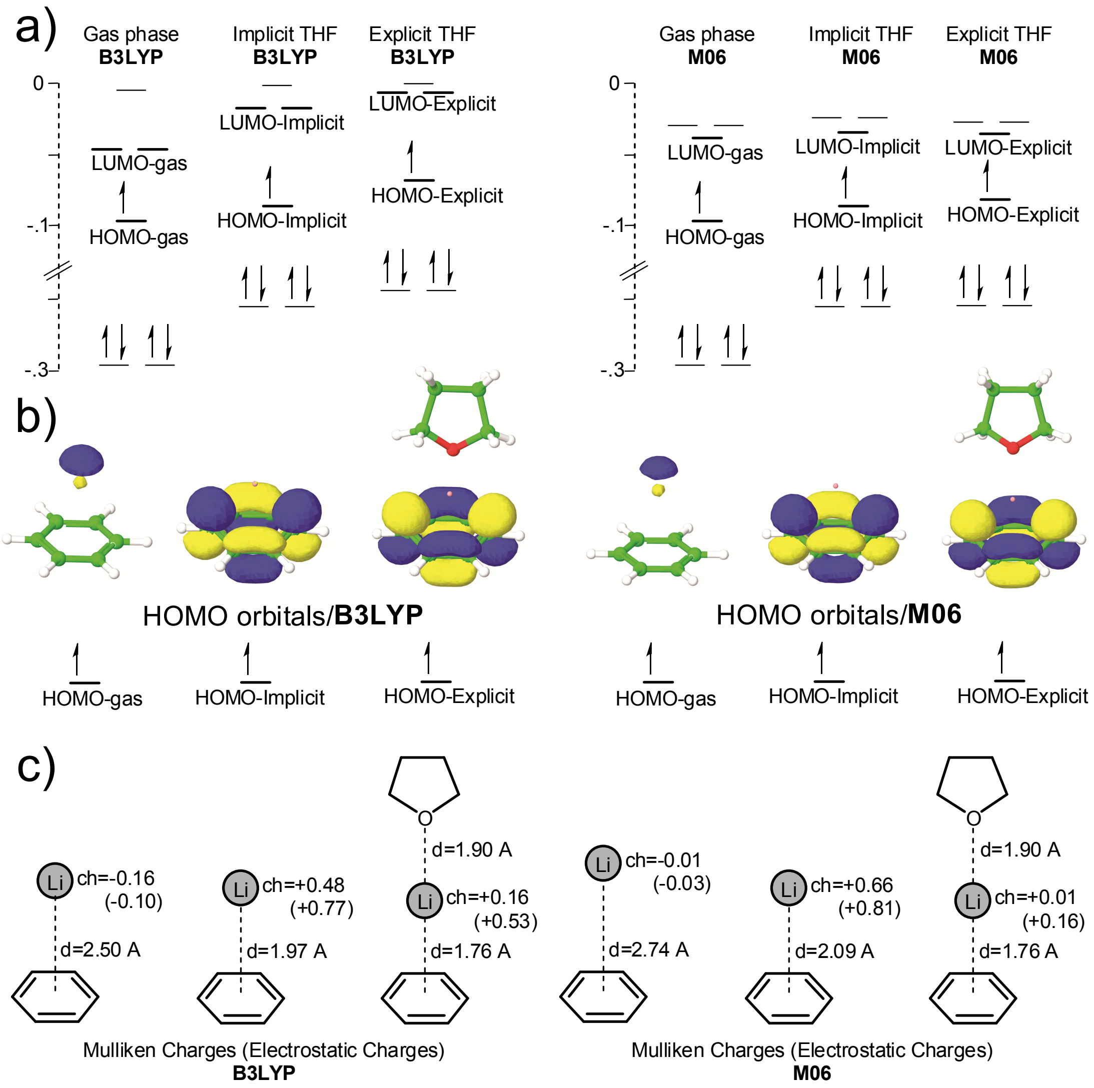

Figure 7.3: (a) Molecular orbital (MO) diagram for Li-Bz system. Units for the vertical axis are Hartrees. (b) Highest occupied molecular orbital (HOMO) for the Li-Bz for the gas phase, for the implicit THF and for explicit THF obtained from M06 and B3LYP. Atoms colors are C, green; H, white; and Li, pink. The colors of the orbitals yellow and dark blue represent an arbitrary positive and negative sign. (c) Mulliken and electrostatic charges for Li-Bz (g), Li-Bz (implicit THF), and Li-Bz (explicit THF)

> K-metalated at pressures higher than 30 bar. Therefore, the best performance for gravimetric delivery (5-100 bar) is for MOF200-Na (5.25 wt %), followed by MOF200-Li (4.90 wt %), COF102-Na (4.75 wt %), COF103-Na (4.71 wt %), and MOF210-Na (4.11 wt %). This shows another way to tune the properties to attain better delivery amounts for different basis (1 vs 5 bar). It is also worthwhile to highlight that, even with 5 bar as basis and 100 bar as the limit, pure MOF200 and pure MOF210 have a delivery amount of 3.11 and 2.77 wt %, respectively.

A possible explanation for this behavior is shown in Figure 7.5, where we plot V_P versus wt% delivery amount using 1 and 5 bar as the delivery basis for all COFs. For this figure, MOFs were omitted for clarity, but the following discussion also applies (see Figures S19 and S20). Figure 7.5a,b shows that performance at higher pressures depends on the basis used to estimate the delivery amount. We found that the gravimetric uptake depends generally in higher degree on the V_{P} than on the S_{A} (Figure S21 vs S22), the same was suggested independently for the H_2 uptake in zeolitic imidizolate frameworks.[125] We also observed that the pore volume decreases as the size of the metalated atoms increases. Thus, the V_{P} is bigger for the pure framework > Li-metalated > Na-metalated > K-metalated.

Figure 7.5a shows that when using 1 bar as the basis, the Li-metalated COFs gives a better delivery uptake at every pressure (10, 30, 50, 80, and 100 bar). Thus, at every coordinate, the uptake is higher for the Li-cases, with the difference getting smaller at 100 bar.

Figure 7.5b shows the delivery uptake with 5 bar as the basis, where we can see that at 10 bar the Li cases barely exceed the Na cases, and at 30 bar and above, the Na-analogs overcome any other counterparts. The K cases start performing closer to the Na cases with increasing pressure, while performing almost as good as the Li cases at 100 bar.

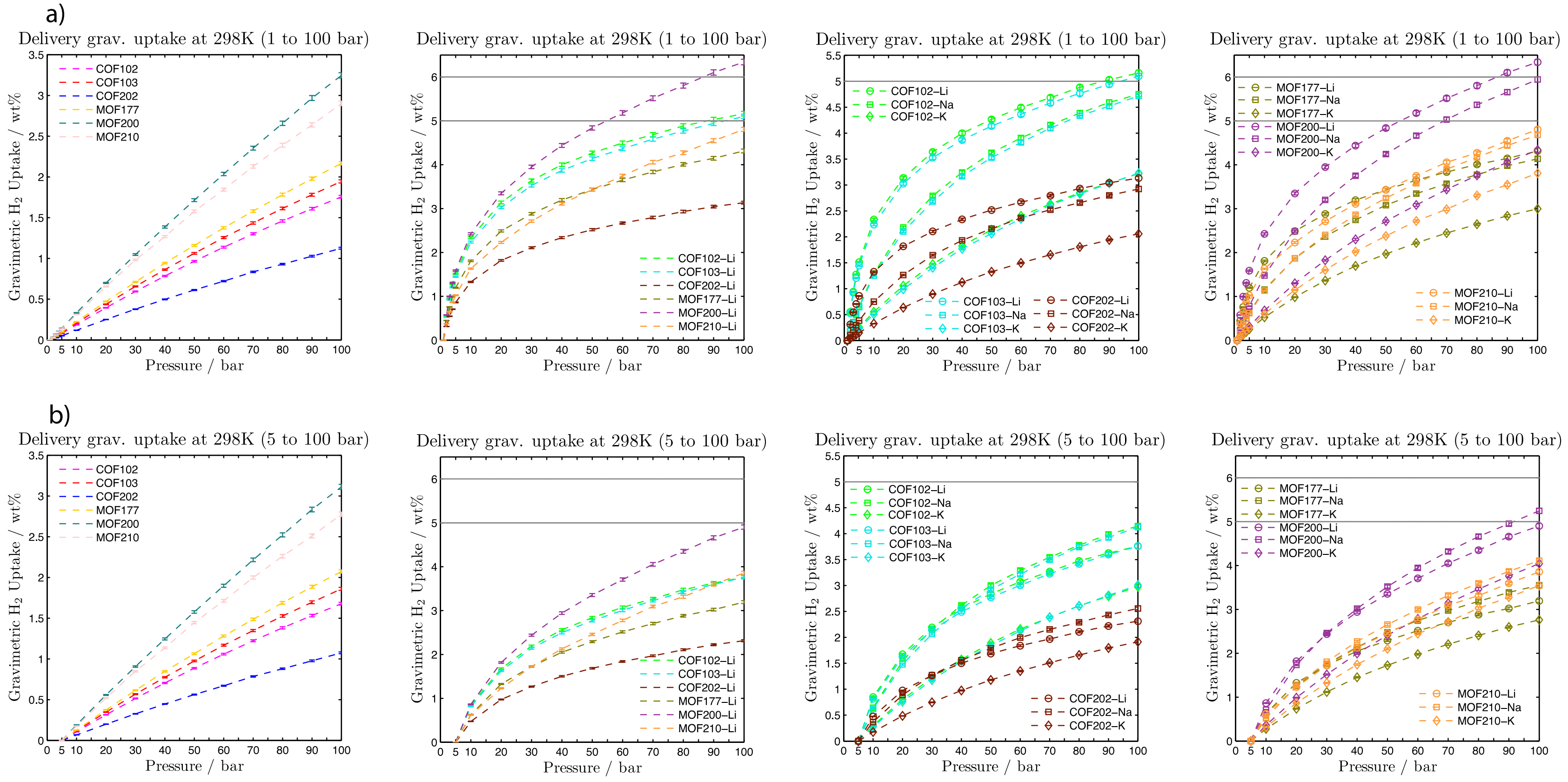

Figure 7.4: Delivery gravimetric uptake obtained for the studied COFs and MOFs, also the metalated analogs with Li, Na, and K are shown. MOF180 and MOF205 as well as the metalated cases are reported in the SI. In (a), we show the delivery amount using 1 bar as the basis, while in (b) we show the delivery amount using 5 bar as the basis. The error bars at each calculated point are shown, while on some cases they are too small to fit inside the symbols.

We conclude that at lower pressure (1-10 bar) the Li cases perform better because the slope of the curves (uptake vs V_P at constant pressure) is larger than the others, while the slope of the Na cases starts becoming larger than the Li cases as the pressure increases above 30 bar. Finally, the slope of the curves for the K cases starts becoming as large as the Na cases at 100 bar. In other words, the Li cases perform better in the range of 1-10 bar, while Na cases perform better in the range of 30-100 bar, and by extension, the K cases should perform better above 100 bar using 5 bar as the basis, all due to the dependence of their H_2 affinity at different pressures. This explains why Na cases leads to better performance than the Li cases above 30 bar; the higher performance obtained from 1 to 10 for the Li cases is diminished by removing the uptake up to 5 bar due to the basis. By extension, we can argue that the K cases will perform better than the Na cases above 100 bar.

We also calculated the *excess* gravimetric amount[85, 130] in wt% at 298 K. In the case of the pristine frameworks at 100 bar, we obtained the best performance for MOF177 with 0.87 excess wt%, followed by COF103 with 0.55 and MOF200 with 0.54. In our previous work, we compared the results from theory and experiment for different pristine MOFs and COFs to validate our methodology.[96, 120, 121].

For the metalated compounds at 100 bar and 298 K, we obtained the best results for MOF200-Li, with 4.87 excess wt% units, followed by COF102-Li, with 4.84, and by COF103-Li, with 4.68. We found that for this pressure range the Li-metalated cases have a better performance than the Na analogs, which have better performance than the K-metalated frameworks. Using the same general principle given for delivery gravimetric units, but for this case the delivery basis is 0 bar, we expect the Na-based frameworks will eventually outperform the Li cases, but at a pressure beyond 100 bar, as Figures S14 and S15 suggest.

In a related work, we reported that IRMOF-2-96-Li reaches 5.6 excess wt% at 100 bar and 298 K,[121] while IRMOF-1-30-Li reaches 5.16 excess wt% at 100 bar and 298 K.[120] However, for application purposes, the delivery amount is the important unit because it determines the usable amount and here we have proven high excess amount uptake does not guarantee a high delivery amount at different basis.

7.1.3.3 Volumetric Uptake

We also calculated the *total*, *excess*, and *delivery* amount based on volumetric units (g H_2/L) for all these compounds (Figure 7.6).

For the *delivery* volumetric amount, we found almost the same behavior as with delivery gravimetric units. When using the basis of 1 bar, the Na analogs overcome the Li analogs at pressures beyond 50 bar. The best performers at 100 bar and 298 K are COF102-Na with 24.9, followed by COF102-Li with 23.8, COF103-Na with 22.8, COF103-Li with 21.7, and MOF177-Na with 21.4, all

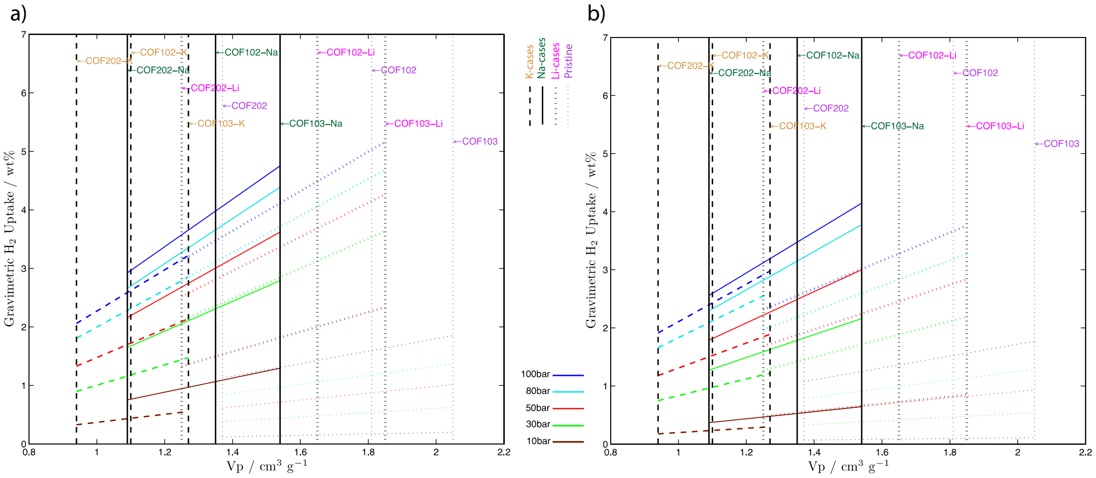

Figure 7.5: We show the correlation of pore volume (V_{P}) vs wt% delivery for different COFs: pristine (dotted line), COF-Li (double dotted line), COF-Na (continuous line), and COF-K (dashed line). In (a) 1 bar is used as the basis, while in (b) it is 5 bar. Different colors represent different pressures.

using delivery g H_2/L units.

On the other hand, when using the basis of 5 bar, the Na-based frameworks overcome the Li analogs at 20 bar. Also, the K-analogs overcome the Li-analogs at around 100 bar (at 60 bar in the case of MOF210) as we predicted it for the gravimetric uptake. At 100 bar and 298 K, we found the best performers are COF102-Na with 21.6, followed by COF103-Na with 19.8, MOF177-Na with 18.2, COF102-K with 17.2, and COF102-Li with 17.1, using delivery g H_2/L units and basis equal to 5 bar.

For the excess volumetric amount at 100 bar and 298 K, we found the best performers are COF102-Na with 23.3, followed by COF102-Li with 22.2, then COF103-Na with 20.6, COF103-Li with 19.8 and MOF177-Na with 19.5, with excess g H_2/L units. This is the same trend as the volumetric delivery amount using 1 bar as the basis. These new frameworks perform better than the best previously reported materials; MOF-C16-Li[120] (or IRMOF-1-16-Li) at 100 bar and 300 K reaches 17.3 excess g H_2/L, while IRMOF-2-54-Li[96] reaches 19.2 excess g H_2/L at the same thermodynamic conditions.

None of these compounds reach the volumetric 2010 DOE target of 28 g H_2/L, but the closest compounds to this quantity are COF102-Na and COF103-Na with 24.9 and 22.8 delivery g H_2/L from 1 to 100 bar (while 21.6 and 19.8 delivery g H_2/L from 5 to 100 bar) at 298 K, respectively. These are to the best of our knowledge the highest molecular hydrogen uptake for a porous material in volumetric units under these thermodynamic conditions. Therefore, if a high delivery volumetric uptake is to be targeted, these results still suggest that high S_{A} and V_{P} are both important, where it should be remembered if V_{P} is too large it could lead to a waste of space.

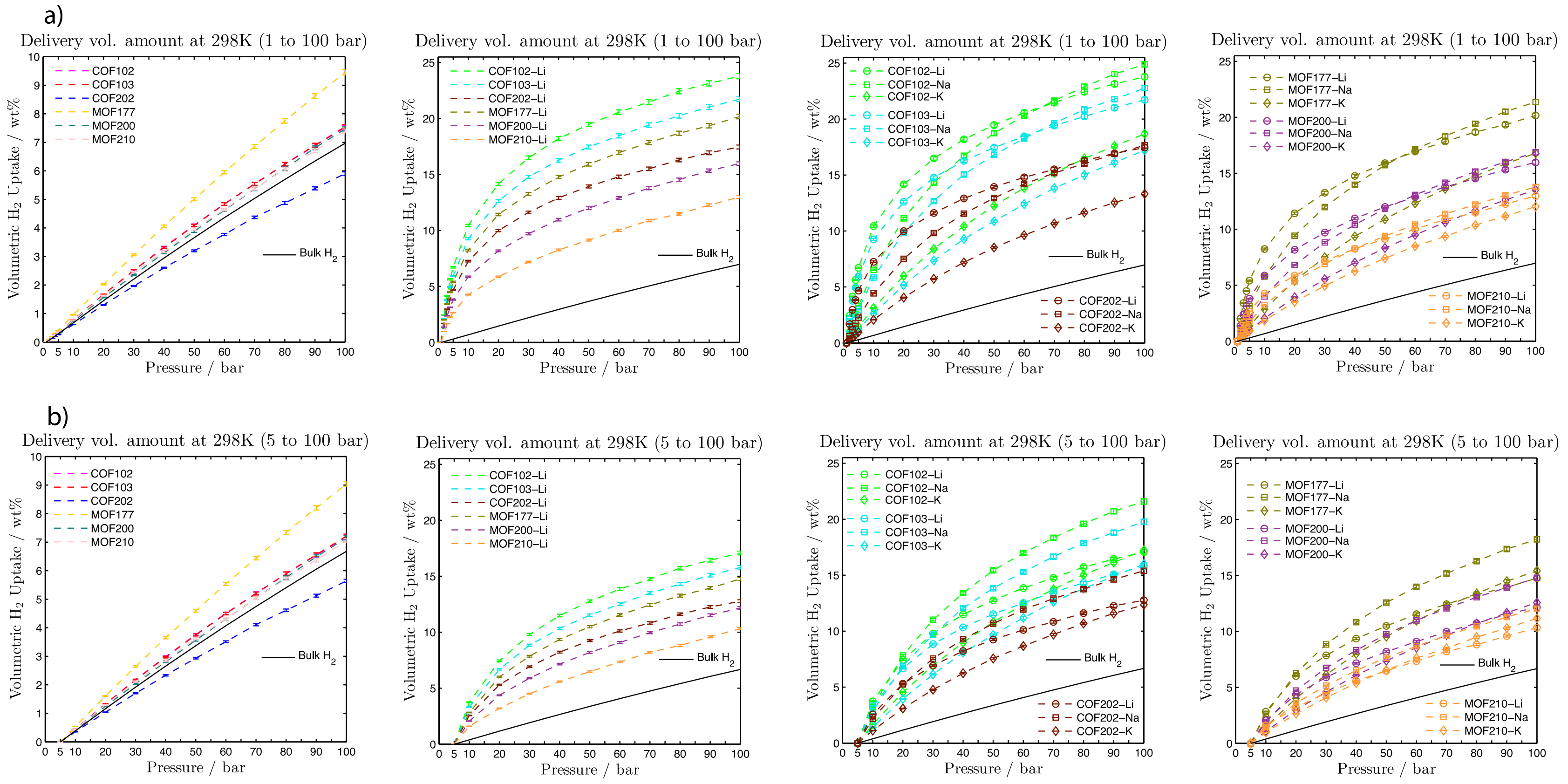

Figure 7.6: Delivery volumetric uptake obtained for the pristine, Li-, Na-, and K-metalated COFs and MOFs are shown. In (a) we used 1 bar as the basis, while in (b) we used 5 bar as the basis. The error bars at each calculated point are shown, and in some cases, they are too small to fit inside the symbols. Bulk H_2 is shown for comparison.

Current analyzed COFs composed mainly of aromatic rings (COF102 and COF103) perform better in volumetric units than analyzed MOFs because for the former most of the atoms are accessible to interact with H_2. In contrast, these MOFs with Zn clusters in their structures have zinc and oxygen atoms that are partially inaccessible (see inset of Figure 7.1). Also, a special case is COF202, where the t-butyl group used in the formation of the borosilicate has four carbons and one silicon atom per cab group that are partially unreachable as well (see Figure 7.1). This is, the more partially or totally inaccessible atoms the framework has, the worst performance in volumetric units, because these atoms that occupy space are not used to interact with H_2.

7.1.3.4 Isosteric Heat of Adsorption

We also calculated the isosteric heat of adsorption (Q_{st}) of these systems at 298 K. The unmetalated systems remain flat around 3.5-5 kJ/mol, while the Li-metalated cases vary from 13 to 21 kJ/mol, the Na-metalated cases are between 10 and 17 kJ/mol, and K-metalated frameworks window corresponds to 8-10 kJ/mol (see Figure 7.7). From these results we observe that a flat curve of Q_{st} with high absolute value is better for the delivery amount (this is of course aside from the ideal Q_{st} curve of increasing interaction at higher pressure). This is because for the delivery amount we do not want strong interaction energy at low pressure (below 1 or 5 bar), because this will bind a large number of molecules that will be difficult to remove after a cycle. For example, when discharging from 100 to 1 bar, the molecules absorbed from 0 to 1 bar will not be used. This can be seen in the Li cases, where they have the highest total uptake amount, but when we analyzed delivery units, they were overcome by the Na cases, which have a flatter Q_{st} curve. The K cases have a flatter curve than the Na analogs; however, the absolute Q_{st} value for Na cases is higher, therefore, they perform better than K-based frameworks at a pressure below 100 bar. This is another explanation for why the Na cases perform better at these delivery pressure ranges; Li cases bind too strongly to molecular hydrogen at lower pressure, while Na cases bind softer, resulting in a higher delivery amount. While K cases have a flatter surface, which is optimal for charge/discharge purposes, its absolute value is too low to compete with the Na cases. Therefore, this study suggests that the next generation of frameworks targeting hydrogen adsorption with high delivery amount should have a flatter Q_{st}, and the absolute value should be at least as high as 15 kJ to reach the DOE gravimetric targets.

7.1.3.5 Adsorption Mechanism of Molecular Hydrogen

The multiple configurations that the H_2 framework needs to explore at room temperature in the sorption process prompt us to analyze the mechanism from the ensemble average rather than single snapshots (Figures 7.8,7.9,7.10). After averaging the ensemble of all configurations, we found that the single layer mechanism is predominant for the metalated frameworks, while the pore filling mechanism appears after the sites surrounding the alkaline metals have been covered. On the other

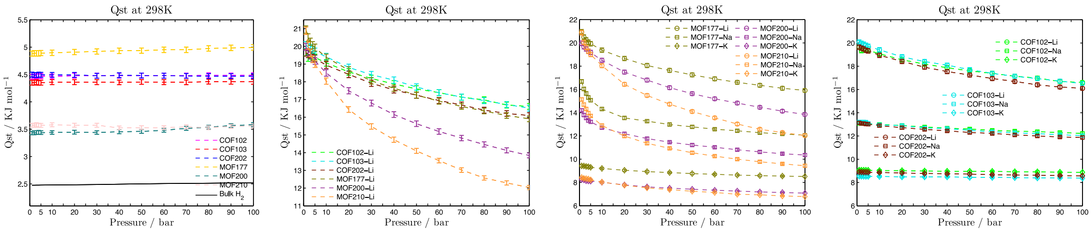

Figure 7.7: Heat of adsorption obtained for the pristine COFs and MOFs, as well as the analogs metalated with Li, Na, and K. MOF180 and MOF205 as well as for the metalated cases are reported in the SI. Top plots show the error bars at each calculated point, and in the bottom plots, the error bars are too small to fit inside the symbols.

hand, for pristine COFs and MOFs, the pore filling mechanism is predominant, while there are not clear evidence about the formation of single layers. Previous works on the topic did not address the problem of the mechanism of hydrogen adsorption at room temperature; however, it is important to discern if there is a characteristic mechanism because it provides a validation for which physical model can be used to represent each sorption curve. In this case, we have proved at the atomistic level, we can use the Langmuir model for metalated frameworks, while the BET model can be applied for pristine compounds both at low saturation uptakes. Although the connectivity and the topology of all these frameworks differ, the profile of the sorption at different pressures remains similar in all of them.

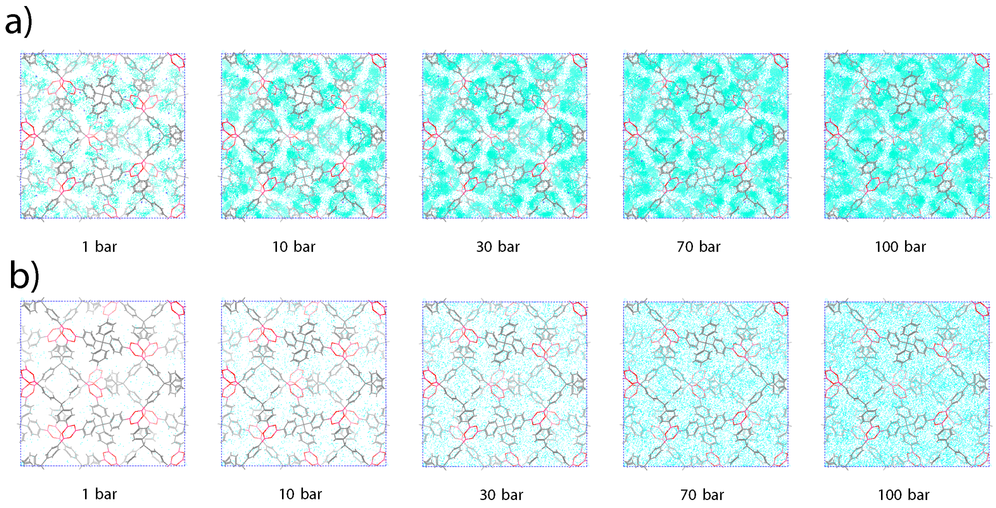

Figure 7.8: We show the ensemble average of molecular hydrogen for COF102 (bottom) and COF102-Li (top) at 298 K. Atom colors are C, gray; O, red; and B, pink; the average of molecular hydrogen is shown in green. COF103 and COF103-Li have the same mechanism as COF102 and COF102-Li, and they are not shown.

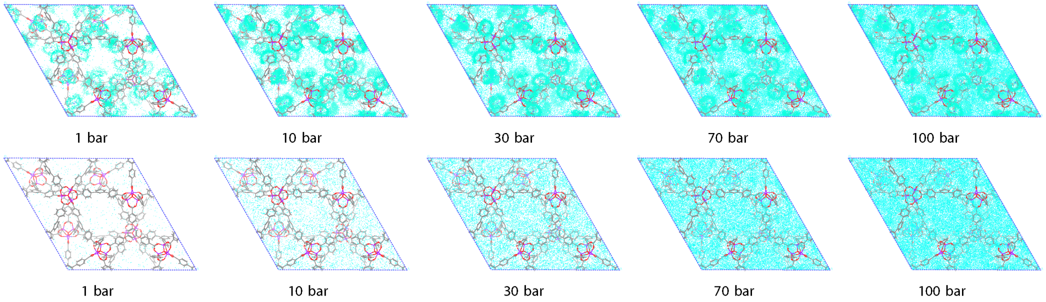

1 bar 10 bar 30 bar 70 bar 100 bar

1 bar 10 bar 30 bar 70 bar 100 bar

Figure 7.9: We show the ensemble average of molecular hydrogen for MOF177 (bottom) and MOF177-Li (top) at 298 K. Atoms colors are Zn, purple; C, gray; O, red; and the average of molecular hydrogen is shown in green. MOF200, MOF180, and MOF210 have a similar mechanism to MOF177 and they are not shown; the same applies to their metalated analogs.

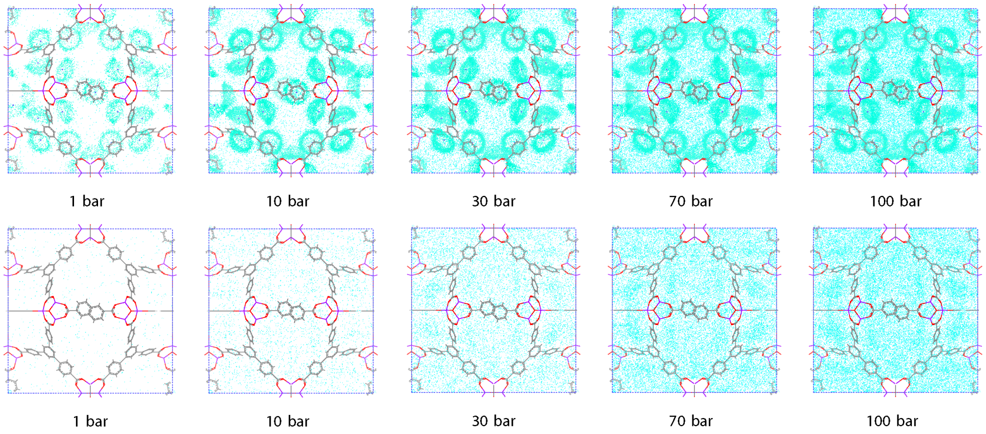

1 bar 10 bar 30 bar 70 bar 100 bar

1 bar 10 bar 30 bar 70 bar 100 bar

Figure 7.10: We show the ensemble average of molecular hydrogen for MOF205 (bottom) and MOF205-Li (top) at 298 K. Atom colors are the same as in Figure 7.9.

7.1.3.6 Comparisons to Previous Computational Studies

Subsequent to our work showing the Li-doped MOFs could lead to substantial H_2 adsorption at room temperature,[120] Blomqvist et al.[131] used the generalized gradient approximation to density functional theory by using the projector augmented wave (PAW) method to confirm our results for Li-MOF5. However, if it is assumed that two Li atoms per benzene ring could be stable (one in each face), then a corrected DFT functional for vdW interactions should be used such as M06, because a function such as B3LYP would predict otherwise (Figure 7.2). Recently, Cao et al.[132] reported the uptake on COF102-Li and COF103-Li using force field parameters obtained from DFT/PW91. However, it is well-known that this level of DFT does not account for the London dispersion, so these results likely underestimate the reversible binding.[122, 133] Therefore, these FF parameters have a lower quality than our CCSD(T) and MP2 calculations to estimate the dispersion interactions. This probably explains why they find a lower value for COF102-Li, with 4.25 effective wt% uptake, while from our calculation, we obtain 4.42 effective wt% (what is called in the literature effective amount[112] is what they define as excess amount), even though they report two Li atoms per benzene-BO_2 unit, while we report only one.

7.1.4 Concluding Remarks

We have calculated the gravimetric and volumetric uptake for the latest generation of COFs and MOF, as well as their Li-, Na-, and K-metalated analogs. We also calculated the thermodynamics for the formation of the Li-Bz adduct and found that its formation is favorable when THF is used.

We found that for the gravimetric delivery amount from 1 to 100 bar, eleven compounds reach the 2010 DOE target of 4.5 wt %, while only two compounds reach the 2015 DOE target of 5.5 wt % (MOF200-Li and MOF200-Na).

However, none of these compounds reach the volumetric 2010 DOE target of 28 g H_2/L, but the closest compound to this quantity is COF102-Na, with 24.9 delivery g H_2/L. In general, an increase in porosity (or pore volume) of MOFs or COFs leads to an increase in the gravimetric H_2 uptake but decrease in the volumetric H_2 uptake. This can be seen when comparing MOF-200 and COF-102. The best gravimetric H_2 uptake is found in MOF-200 analogs, where pore volume is larger than any other MOFs and COFs considered here; however, the best volumetric H_2 uptake is found in the COF-102 analogs, which have one of the smallest pore volumes. Therefore, to increase volumetric uptake, it is better to consider MOFs or COFs with low pore volume (of around 1.8, but smaller than 2 cm^3/g) at the expense of reducing the gravimetric uptake.

n summary, we recommend three ways to improve both gravimetric and volumetric delivery units: (a) by creating compounds with high S_{A} with all the atoms to be accessible, (b) by controlling the V_{P} to get the best compromise of used space (smaller V_{P} leads to better volumetric delivery, while bigger V_{P} leads to a better gravimetric delivery), and (c) by aiming for a flat Q_{st} curve, which can be obtained when several strong sorption sites exist. According to the present work, a constant Q_{st} value at least 15 kJ/mol should be obtained in order to reach the DOE gravimetric goal.

7.2 Dependence of the H_2 Binding Energies Strength on the Transition Metal and Organic Linker

Jose L. Mendoza-Cortes, Hiroyasu Furukawa, Omar M. Yaghi, William A. Goddard III, **2012**

7.2.1 Introduction

A current major obstacle to molecular hydrogen (H_2) as an alternative source of energy is the difficulty of storage at opera tional temperatures. The U.S. Department of Energy (DOE) has set the 2015 targets of 5.5 wt % and 40 g/L at 233-358 K and 3-100 bar (and ultimate 7.5 wt % and 70 g/L).[117, 118, 134] Among the most promising routes to obtain this goal is physisorption because is fully reversible and has fast kinetics at desired condi tions. However, current materials have been able to attain <10 kJ/mol at ambient conditions and this decays as the sorption sites get saturated.[121, 135] Thus, sorption sites that are able to ac commodate more H_2 molecules and have a stronger affinity for H_2 are needed. We and others have found that this necessary to keep a constant heat of adsorption (Qst) as the loading increase and to be efficient for the loading/unloading cycle, which are requirements for materials to attain the DOE targets.[135, 58] There have been several theoretical studies that try to put stronger interactions between H_2 and the material host, however they still have to be synthesized.[120, 115, 136, 137]

We have speculated that using transition metal sites in the structures of porous materials can reach this goal.[138, 139] Our trials have been focusing in using precious late transition metals (TM) such as Pd. In this paper we show that it is not necessary to use such precious and heavy TM to obtain good binding energies with H_2. We report the binding energy of 4 H_2 interacting with 60 compounds (6 linkers with 12 different transition metals). We found that early TM (Sc to Cu) can attain the same strength of interactions as precious late transition metals (Pd and Pt). We also report that the square planar coordination geometry is not necessary to obtain many strong interactions because the tetrahedral geometry gives similar affinity. This is maybe because we are dealing with mainly long range interactions and the local geometrical environments is not determinant as in the covalent bond formation. We focus on the ligands (building blocks) used for synthesizing porous materials since it is easier to calculate the binding energy to these smaller species and at the fundamental level, there is not a significant difference with the extended structure.

7.2.1.1 Types of Interactions for H_2

There are several interactions that H_2 can have with other atoms, molecules or solids, which are dispersion, electrostatics and orbital interactions.[140, 2] The nature and magnitude of these interactions are shown in Table 7.5 and Figure 7.11. The existence of each of these interactions can allow us to tune the $\Delta H^{\circ}{}_{\text{bind}}$ to obtain the optimal value.

Table 7.5: Different interactions H_2 can have with other entities that can be used to tune the $\Delta H^{\circ}{}_{\text{ads}}$

Interaction	Energy dependence	Typical values (kJ/mol)
Charge - quadropole	$1/r^3$	~3.5 [140]
Charge - induced dipole[a]	$1/r^4$	~6.8 [140]
Dipole - induced dipole[a]	$1/r^5$	~0.6 [140, 141]
Dispersion	$1/r^6$	~5-6 [58]
Orbital interaction	< vdW radii	~20-160 [2, 142, 143, 144]

[a] If a strong external field is present; a dipole can be induced in H_2 if a strong external field is present.

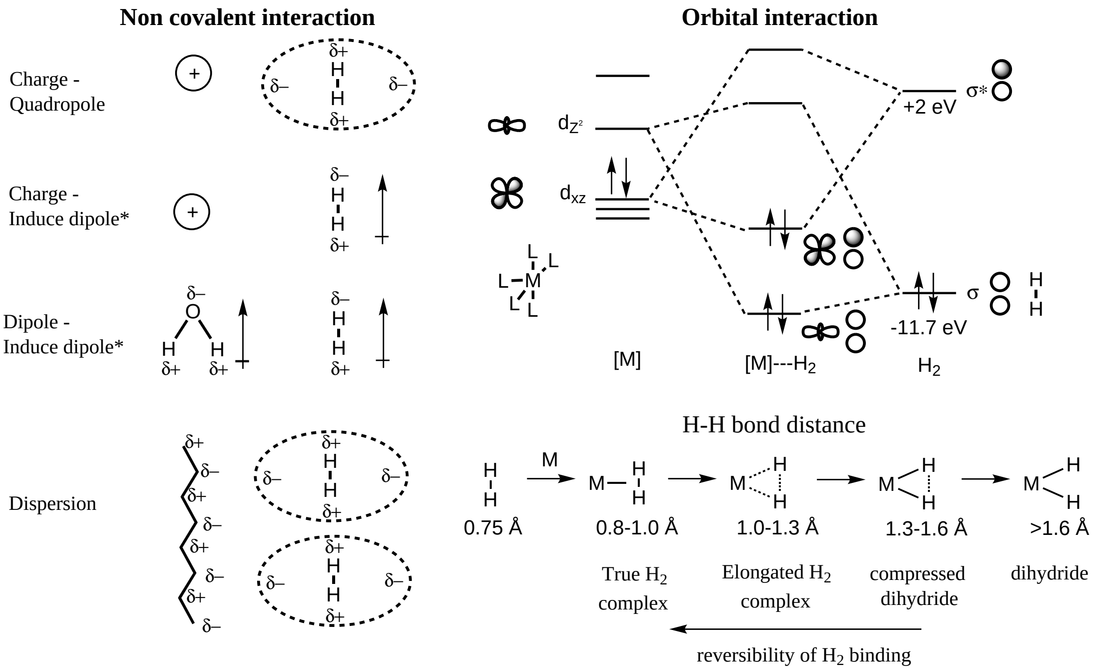

Figure 7.11: Interactions H_2 can have; noncovalent interactions and orbital interactions. The molecular orbital diagram and the H-H bond distances (from crystallography and NMR) are adapted from reference [2]. (*) A strong external field is needed to create a dipole in H_2.

Non covalent interactions (electrostatic and dispersion) have a typical $\Delta H^{\circ}{}_{\text{ads}}$ value of less than 10 kJ/mol while orbital interac tion have values larger than 20 kJ/mol.

The first non-zero multipole moment for H_2 is the quadrupole moment due to their non-spherical nature and this interaction is responsible for most interactions in bulk H_2. However if other species interact with H_2, other electrostatic interactions can appear such as charge - quadrupole. If a strong external field is applied, then a dipole can be induced in H_2 and generate other interactions such as charge - induced dipole and dipole - induced dipole.[140, 141] The charge - H_2 interactions are difficult to appear because we need unscreened coulombic interactions which are rarely present in many systems, although some examples have been discovered in the so called open metal sites.[145] The other ubiquitous non covalent interaction is dispersion, and this is responsible for the interaction of H_2 with carbonaceous materials such a graphite and carbon nanotubes.[58]

Orbital interactions require either a very high pressure of 490 GPa[146] or d-orbitals of transitions metals (TM) to appear.[2, 142, 143, 144] The use of the d-orbital of TM is the most obvious choice because of the constraint of using up to 100 bar of pressure. The orbital interactions have different magnitude depending on the TM and the ligands used, and ultimately affect the H-H bond. The more the H-H bond elongates the higher the interaction and the less reversible the binding is (Figure 7.11 and Table 7.5).

We need all these different kind of interaction in order to obtain strong interactions with H_2 but without modifying the H-H bond length significantly in order to obtain reversibility. For example combinations of charge - quadrupole, dispersion as well as orbital interactions can give us the interaction ion - H_2 and ligands - H_2 in a range 0.4-35 kJ/mol by changing the charge on the ligand or the ligand itself.[140] Thus ligands that bind to transition metals can have different binding sites and by designing the counteranion, we can obtain different kinds of strong enough interactions with H_2.

7.2.1.2 Langmuir Theory and the Optimal Enthalpy

In this paper we consider the single layer approximation of the Langmuir model to get an estimation of the optimal en thalpy needed for maximum delivery. Previous work done by Bathia et al.,[58] has shown that this approximation is a good estimation for the H_2 sorption on porous materials such as graphite and carbon nanotubes. This is an acceptable first order approximation because H_2 is a small molecule and the H_2 - H_2 interactions are not very important.

With the Langmuir theory we can determine the uptake (n) and we can determined the necessary properties to get the delivery amount (D):[147]

$$D(K, P_{max}, P_{min} = \frac{KP_{max}n_m}{1+KP_{max}} - \frac{KP_{min}n_m}{1+KP_{min}} \tag{7.2}$$

where K is the equilibrium constant from the Langmuir theory at certain temperature, P_{max} and P_{min} are the maximum and minimum pressure of the delivery and n_m is the adsorption capacity of the material. The maximum delivery amount can be found by finding the optimal K. Thus from $\partial D/\partial K = 0$, the optimal value is K_{opt}=$1/(\sqrt{P_{max}P_{min}})$.[58, 147, 148]

Therefore, from K_{opt}=$(e^{\Delta S^\circ/R})(e^{\Delta H^\circ/RT})/P_0$, where ΔS^0 is the entropy change, ΔH^0 is the enthalpy change and the reference pressure, $P_0 = 1$ bar, we obtain the optimal binding value;

$$\Delta H^\circ{}_{\text{opt}} = T\Delta S^\circ + \frac{RT}{2}\ln\left(\frac{P_{max}P_{min}}{P_0^2}\right) \tag{7.3}$$

Bathia et al. reported that for various porous adsorbents a typical value for the H_2 adsorption is $\Delta S^0 \approx$ -8R.[58] Assuming this ΔS^0 value for the temperatures range of the DOE targets, we can estimate the optimal values for $\Delta H^{\circ}{}_{\rm opt}$ for a homogenous material (same type of binding site).

In Table 7.6, we show the optimal values calculated for the 2015 DOE goals. We are going to focus on the Fuel Cell (FC) delivery condition for 3/100 atm delivery limits but the same arguments can be applied to the Internal Combustion Engine (ICE) case. At 233K the optimal enthalpy change ($\Delta H^{\circ}{}_{\rm opt}$) is equal to -10.0 kJ/mol. On the other hand at 358K the $\Delta H^{\circ}{}_{\rm opt}$ = -15.3 kJ/mol. A second order approximation is undergoing.

Table 7.6: DOE targets for H_2 storage system for light-duty vehicle and the estimation of the optimal $\Delta H^{\circ}{}_{\rm ads}$ under these conditions using the Langmuir model

Storage parameter	Units	2015
System gravimetric capacity	kg(H_2)/kg(System)	0.055
System volumetric capacity	kg/m3	40
Min/Max delivery temperature	K	233/358
Min/Max delivery pressure FC[a]	atm	3/100
Min/Max optimal ΔH°_{opt} (*This work*) FC[a]	kJ/mol	-10.0/-15.3

[a] FC = fuel cell

In order to show how ΔH° affects the delivery amount we plot the different uptakes at 298K in Figure 7.12. We can see how the optimal value strength of 12.8 kJ/mol at 298K offers the best enthalpy of adsorption for the delivery amount for the range from 3 to 100 bar. The maximum delivery value calculated with these assumptions is of 0.709 (Table 7.7).

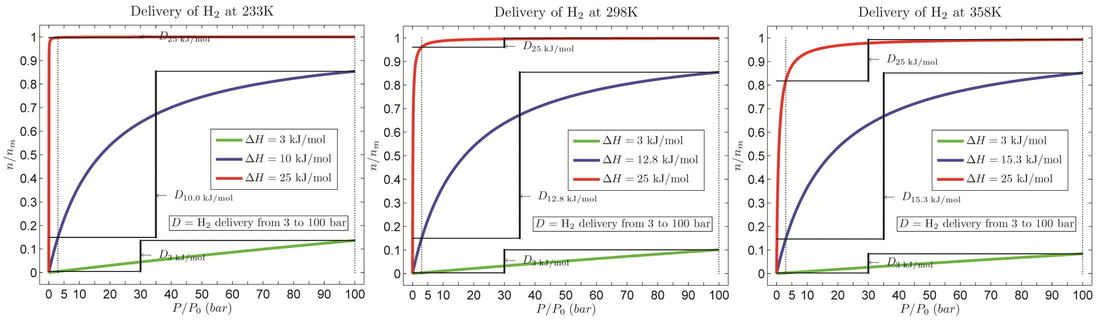

Figure 7.12: We show the normalized uptake (n/nm = uptake/sorption capacity) for three different temperature conditions (left: 233K, center: 298K, right: 358K) using the Langmuir model and ΔS° = -8R. We can see that the magnitude $\Delta H_{\rm ads}$ have a strong effect on the amount that can be delivered between 3 and 100 bar, i.e., a small value (3 kJ/mol) gives poor uptake and poor delivery, a large value (25 kJ/mol) gives high uptake but poor delivery. The ideal $\Delta H_{\rm ads}$ gives both a high uptake and high delivery.

Therefore, using these premises we embark ourselves in finding new ligands that can have a binding energy between 10 and 15.3 kJ/mol in order to get the optimal delivery amount for the DOE targets (233/358 K) by exploiting all the different types of interactions that the H_2 can have.

Table 7.7: Delivery amount obtained using ideals $\Delta H^{\circ}{}_{\text{ads}}$ and different temperatures

Temperature(/K)	$\Delta H^{\circ}{}_{\text{opt}}$ (/kJ mol-1)	Delivery[a] (3 to 100 bar)
233	-10	0.709
298	-12.8	0.709
358	-15.3	0.709

[a] We have normalized the Delivery amount using $D(K, P_{max}, P_{min}/n_m = \frac{KP_{max}}{1+KP_{max}} - \frac{KP_{min}}{1+KP_{min}}$, where the maximum delivery is close to 1.

7.2.2 Computational Details

To estimate the interactions between H_2 and the different linkers (with and without TM), we used the M06[122] hybrid DFT functionals that contains corrections for dispersion interactions as implemented in the Jaguar code.[9] Here we used the 6-31G**++ basis set for the light elements. For the TM we used the Los Alamos LACVP**++ electronic core potential which includes relativistic corrections.[10] The unrestricted open shell procedure for the self-consistent field calculations was used for all spin states. All geometries were optimized using the analytic Hessian to determine that the local minima have no negative curvatures (imaginary frequencies). The vibrational frequencies from the analytic Hessian were used to calculate the zero-point energy correction at 0 K.

For our calculations we used the following nomenclature,

$$\Delta H^{\circ}{}_{\text{bind}} = \Delta H^{\circ}{}_{\text{host+H2}} - \Delta H^{\circ}{}_{\text{host}} - \Delta H^{\circ}{}_{\text{H2}} \tag{7.4}$$

Where $\Delta H^{\circ}{}_{\text{bind}}$ is the binding enthalpy of H_2 to the host, and it represents our estimation of $\Delta H^{\circ}{}_{\text{ads}}$. $\Delta H^{\circ}{}_{\text{host}}$ is the enthalpy of the host or linker and $\Delta H^{\circ}{}_{\text{H2}}$ is the enthalpy of the free H_2. From here on, we use the term binding energy instead of binding enthalpy.

We first find the ground state for a given spin (s) according to the oxidation for the TM. For our cases we studied the most common oxidation state of the TM. We also explore the most favorable geometry given the electronic spin state; Tetrahedral (Tet) versus Square Planar (Sqr) when applicable or Trigonal bipyramidal (Tbi) versus Square pyramidal (Spy). The other geometries studied depending on the number ligands are Octahedral (Oct) and Pentagonal bipyramidal (Pbi). Therefore we used the first row transition metals from Sc to Cu because we consider they should be light and abundant. We also include Pd(II) and Pd(0) for comparison.

For the nucleophilic transition metals, we explore:

* Sc(III), geometry = Spy, Tbi with s = 0;

* Ti(IV), geometry = Oct with s = 0;

* V(V), geometry = Pbi with s = 0;

* Cr(III), geometry = Spy, Tbi with s = 1/2, 3/2;

While for the electrophilic transition metals, we studied:

* Mn(II), geometry = Tet, Sqr with s = 1/2, 3/2, 5/2;

* Fe(II), geometry = Tet with s = 0, 2/2;

* Co(II), geometry = Tet, Sqr and s = 1/2, 3/2;

* Ni(II), geometry = Tet, Sqr with s = 0,2/2;

* Cu(II), geometry = Sqr with s = 1/2;

* Pd(II) and Pd(0), geometry = Sqr with s = 0;

All the geometries and their energies are contained in the supplementary information. Pd is studied to get a comparison to precious metals. The geometry that we show is the ground state along with the spin state and all the $\Delta H^{\circ}{}_{\text{bind}}$ are calculated based on these structures. When the Square and Tetrahedral structure converge to the same coordinates (or Trigonal bipyramidal and Square pyramidal), only one of them is presented. For the V(V) case, we found that the metal does not bind to the linker but interacts mostly by columbic interactions.

7.2.3 Results and Discussion

7.2.3.1 Current Linkers Used in Porous Frameworks

With the objective of generating sites for metalation we have developed new COFs with the imine and hydrazide linkage.[149, 150] Also we have post-modified MOFs in order to have metals on the bridging ligands.[138, 139] Figure 7.13 summarize the linkers where we have purposely created sites to host metals on it. We also show the bipyridine ligands commonly used for the synthesis of MOFs and recently also in COFs.

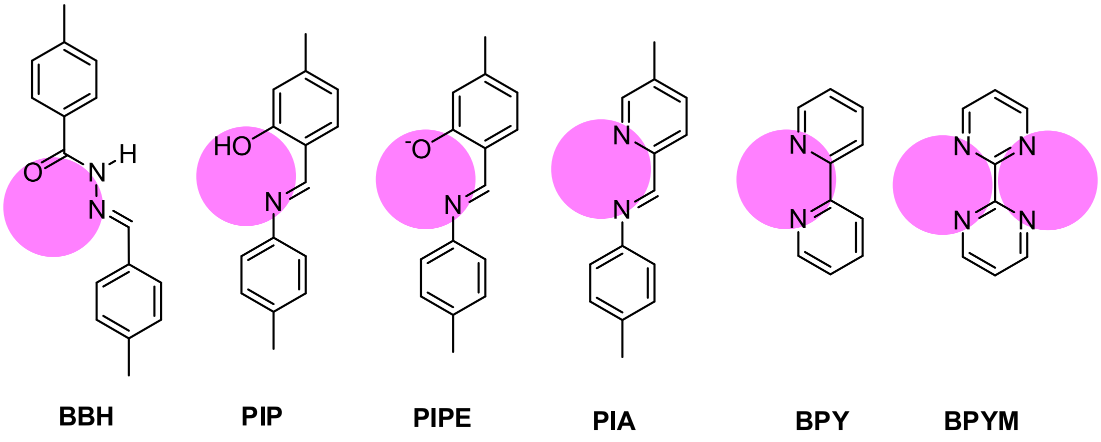

Figure 7.13: Connectivity developed in linkers used for COFs and MOFs where sites for metalation are present. The pink circle indicates the sites where transition metals can be placed.

Ligand Containing the Hydrazide binding group.

The first linker we calculate the binding energies for is the hydrazide containing linker; (E)-N'-benzylidenebenzohydrazide (**BBH**) shown in Figure 7.13. Our synthetic efforts have produced two Covalent Organic Frameworks with this connectivity which denominated COF-42 and COF-43.[150] In the spirit of knowing which transition metal would have the best binding energy to H_2, we calculate the interactions of such compounds using first row transition metals (Sc to Cu) as well as Pd. While Pd is a heavy precious metal, we wanted to explore if the square predominant geometry can have an effect given the closed shell electronic nature of this metal. Thus we include the Pd(II)Cl_2 case. The numerical results are shown in Table 7.8 and plotted in Figure 7.14.

Table 7.8: Binding energies ($\Delta H^{\circ}_{\mathrm{bind}}$) obtained for the ground state of linker **BBH** and different number of physisorbed H_2. We also show $\Delta H^{\circ}_{\mathrm{bind}}$ for the linker + TM(n)Cl_n + H_2. The H-H bond of isolated H_2 is 0.741 Å

Linker = **BBH**	Geom for M	Spin (s)	n H_2	$\Delta H^{\circ}_{\mathrm{bind}}$ (kJ/mol)	H-H bond (Å)
Linker	N/A	0	1, 2, 3, 4	-6.16, -6.13, -6.08, -6.05	0.745, 0.745, 0.745, 0.744
+ Sc(III)Cl_3	Spy	0	1, 2, 3, 4	-12.2, -12.1, -11.9, -11.6	0.745, 0.745, 0.745, 0.743
+ Ti(IV)Cl_4	Oct	0	1, 2, 3, 4	-12.7, -12.6, -12.5, -12.4	0.745, 0.745, 0.745, 0.744
+ V(V)Cl_5	Oct	0	1, 2, 3, 4	-11.7, -10.9, -10.4, -9.60	0.747, 0.746, 0.746, 0.745
+ Cr(III)Cl_3	Spy	3/2	1[a], 2, 3, 4	-17.6, -12.5, -12.2, -11.5	0.747, 0.746, 0.745, 0.744
+ Mn(II)Cl_2	Tet	5/2	1[a], 2, 3, 4	-20.1, -13.1, -13.0, -12.8	0.748, 0.747, 0.746, 0.746
+ Fe(II)Cl_2	Tet	2/2	1, 2, 3, 4	-12.4, -12.3, -12.3, -12.3	0.748, 0.748, 0.748, 0.748
+ Co(II)Cl_2	Tet	3/2	1, 2, 3, 4	-14.0, -13.2, -12.8, -12.3	0.749, 0.748, 0.747, 0.747
+ Ni(II)Cl_2	Tet	2/2	1[a], 2, 3, 4	-16.5, -16.3, -14.9, -14.0	0.747, 0.747, 0.746, 0.744
+ Cu(II)Cl_2	Sqr	1/2	1, 2, 3, 4	-14.0, -13.8, -13.6, -12.4	0.746. 0.746, 0.745, 0.744
+ Pd(II)Cl_2	Sqr	0	1, 2, 3, 4	-12.3, -12.0, -11.4, -11.3	0.746, 0.746, 0.745, 0.745

[a] The first H_2 interacts strongly with the metal but it does not form a hydride.

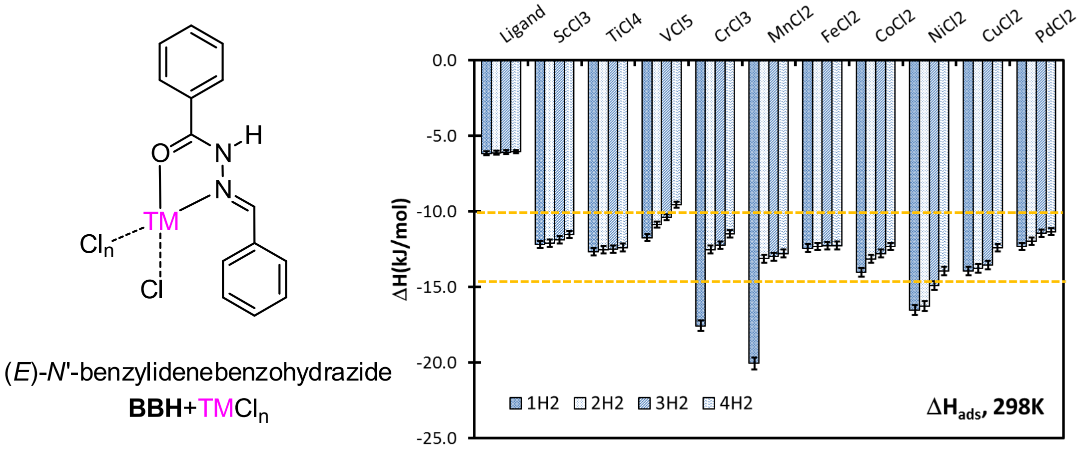

Figure 7.14: Different binding energies $\Delta H^{\circ}_{\mathrm{bind}}$ at 298K obtained for **BBH** ligand interacting with four physisorbed H_2. We have focused on isoelectronic TM. PdCl_2 is shown for comparison. The error bars estimate the different configurations. Mn(II), Cr(III) and Ni(II) show strong interactions with the first H_2 but there is no evidence of formation of hydride (Table 7.8).

We found that the ligand **BBH** alone does not interact strongly with the hydrogen molecule

($\Delta H^{\circ}{}_{\text{bind}}$ = -6.16, -6.13, -6.08 and -6.05 kJ/mol for the 1st to 4th H_2, respectively). However, we found that if this ligand is bound to the TM, this interaction energy increases. Also, all of studied TM interacting with H_2 have the correct energy to maximize the delivery amount for the temperature range needed by the DOE.

For all these cases, Sc to Cu and Pd(II), the H_2 does not bind chemically to the TM. We found strong interaction between the first H_2 with Cr(III), Mn(II) and Ni(II) but there is no evidence for the formation of hydride due to the still short H-H bond and the small value of the energetics. For the case of **BBH**-Cr(III)Cl_3, the first H_2 interacts strongly with the Cr(III)Cl_3 center forming an octahedral environment Cr(III)$Cl_3L_2(\eta^2\text{-}H_2)$, where L_2 represents the two binding sites of ligand **BBH**. This first H_2 has $\Delta H^{\circ}{}_{\text{bind}}$ = -17.6 kJ/mol while the H-H bond is 0.747 Å. The Cr-H_2 is long to be considered a true chemical bond; 2.57 and 2.58 Å. This quasi-complex **BBH**-Cr(III)$Cl_3(\eta^2\text{-}H_2)$ then serves as the host for other physisorbed H_2 with values of $\Delta H^{\circ}{}_{\text{bind}}$ = -12.5, -12.2 and -11.5 kJ/mol for the 2nd to 4th H_2, respectively. The H-H bond distance for these physisorbed H_2 are 0.746, 0.745, 0.744 Å, which are comparable to the isolated H_2 (0.741 Å).

The other strong interaction with the first H_2 occurs when using **BBH**-Mn(II)Cl_2. The first H_2 forms a quasi-complex Mn(II)$Cl_2L_2(\eta^2\text{-}H_2)$ with a distorted trigonal bipyramidal environment for the Mn(II) where L_2 represents the two binding sites of ligand **BBH** and with the $\eta^2\text{-}H_2$ occupying the equatorial positions. The $\Delta H^{\circ}{}_{\text{bind}}$ = -20.1 kJ/mol and the H-H bond for this first H_2 is of 0.748 Å, which shows there is no hydride formation. This also can be observed by the Mn-H_2 distances which are 2.48 and 2.49 Å. This shows that the strong interactions comes from dispersive forces and presumably to some coulombic interaction between the Mn(II)Cl_2 and the quadrupole moment of H_2. This quasi-complex formed by **BBH**-Mn(II)$Cl_2(\eta^2\text{-}H_2)$ then interacts with more H_2 to a smaller degree. The strength of the interaction with the 2nd, 3rd and 4th H_2 is -12.5, -12.2 and -11.5 kJ/mol, respectively. This is consistent with a short H-H bond of 0.747, 0.746 and 0.746 Å, respectively, on these H_2.

The third compound with a strong relative interaction with H_2 is the **BBH**-Ni(II)Cl_2. The first H_2 interacts strongly with the tetrahedral center formed by Ni(II)L_2Cl_2 where L_2 represents the two binding sites of ligand **BBH**. The strength for this interaction is $\Delta H^{\circ}{}_{\text{bind}}$ = -16.5 kJ/mol and the H-H bond for this H_2 is of 0.747 Å. For this case there is no $\eta^2\text{-}H_2$ binding to the metal center. Instead we found that the H_2 interacts mainly with the Cl^- ligand, this is observed because of the Cl^-H_2 distance of 2.86 and 3.60 Å, which are shorter than the Ni(II)-H_2 distances (3.90 and 4.50 Å). For this case, there is a second H_2 that interacts strongly with the **BBH**-Ni(II)Cl_2 center, which is located on the opposite side of the ligand. The interaction strength is very similar to the first H_2 as it can be observed with the $\Delta H^{\circ}{}_{\text{bind}}$ = -16.3 kJ/mol and the H-H bond of 0.747 Å. The distance for the Ni(II)-2ndH_2 are 2.89 and 3.63 Å, while the Ni-H_2 distances are longer (3.49 and 4.02 Å). This suggests that the same kind of interaction observed for the 1st H_2 occurs in the 2nd H_2. The

3^{rd} and 4^{th} H_2 interacts less strongly with the Ni(II)L_2Cl_2 as it can be observed by the values of $\Delta H°_{\text{bind}}$ = -14.9 and -14.0 kJ/mol, respectively. The H-H bonds distance for these physisorbed H_2 are 0.746 and 0.744 Å. This is an example of how the counter anion, in this case Cl^-, can work as center where the H_2 can interact strongly.

The rest of the TM studied exhibits a very similar behavior with $\Delta H°_{\text{bind}}$ that ranges from 11-14 kJ/mol for the 1^{st}-4^{th} interacting H_2 (Table 7.8 and Figure 7.14). These TM; Sc(III), Ti(IV), V(V), Fe(II), Co(II), Cu(II) and Pd(II) which have Cl as the counter anion, exhibit H-H bond for the interaction with H_2 in the range of 0.743-0.749 Å. All these elements have different coordination shell (Square pyramidal, Octahedral, Tetrahedral and Square planar) but similar $\Delta H°_{\text{bind}}$ which suggests that the interactions with H_2 do not depend strongly on the geometry that the TM adopts. These elements also have different oxidation states and the interaction strength is still in similar range, this also supports the hypothesis that the long range interactions depends poorly on the TM, oxidation state and geometry of the coordination shell when there is not η^2-H_2 interaction.

The case of the Fe(II) and Co(II) are puzzling because they have the largest H-H bond distance for the interacting H_2 but they have the energetics in the normal range of -14 to -12 kJ/mol. For the compound **BBH**-Fe(II)Cl_2 where the coordination geometry for the TM is tetrahedral, we have $\Delta H°_{\text{bind}}$ = -12.4, -12.3, -12.3 and -12.3 kJ/mol for the 1^{st} to 4^{th} H_2, respectively. And the H-H bond corresponds to each distance 0. 748 Å. A similar behavior occurs for the **BBH**-Co(II)Cl_2 case, where the $\Delta H°_{\text{bind}}$ = -14.0, -13.2, -12.8 and -12.3 kJ/mol and the H-H bond is 0.749, 0.748, 0.747, 0.747 Å, for the 1^{st} to the 4^{th} interacting H_2, respectively. These compounds combined with the **BBH**-Mn(II)Cl_2 and the **BBH**-Ni(II)Cl_2 cases which also have tetrahedral geometry for the TM, strongly propose that the TM tetrahedral generates the most distortion for the interacting H-H bond.

The square geometry for the TM can be observed for the cases of **BBH**-Cu(II)Cl_2 and **BBH**-Pd(II)Cl_2. The interaction strength for these cases is also ordinary, on the range of -14 to -11 kJ/mol for the four interacting H_2. There is also not a big distortion in the H-H bond, with this distance ranging from 0.744 to 0.746 Å. Contrary to what we should expect, the square geometry does not give a better interaction for more H_2 bounded to the complex. For example, for **BBH**-Cu(II)Cl_2, the first H_2 bind with $\Delta H°_{\text{bind}}$ = -14.0 kJ/mol while the interaction strength drops for the 4^{th} H_2 to $\Delta H°_{\text{bind}}$ = -12.4 kJ/mol. The same behavior is observed for the **BBH**-Pd(II)Cl_2 complex. The first H_2 bind with $\Delta H°_{\text{bind}}$ = -12.3 kJ/mol while the interaction strength drops to $\Delta H°_{\text{bind}}$ = -11.3 kJ/mol for the 4^{th} H_2. This supports the hypothesis that the geometrical coordination for the TM does not determinant the strength of the interactions with H_2 when there is not η^2-H_2 interaction.

In the case **BBH**-V(V)Cl_5, there is only a coordination with the O from the C=O of the **BBH** but not with the N of the imine. This can be observed by the long N-V of 3.93 Å, and the short O-V distance of 2.29 Å. However the V(V) is coordinated to the five Cl^- with a distance of 2.125, 2.208, 2.213, 2.218, and 2.290 Å. This complex has an octahedral geometry with $\Delta H^{\circ}_{\mathrm{bind}}$ = -11.7, -10.9, -10.4 and -9.6 kJ/mol. The other compounds with octahedral geometry is **BBH**-Ti(IV)Cl_4 where both coordination sites of **BBH** are used. The strength of the interaction with H_2 is $\Delta H^{\circ}_{\mathrm{bind}}$ = -12.7, -12.6, -12.5 and -12.4 kJ/mol which is similar to the V(V) analog. In both cases the H-H bond distance is around 0.745 Å. At the beginning of these studies we speculated that the octahedral geometry would hindrance the interaction of the TM with the H_2, however this interaction is still comparable to those interaction obtained from tetrahedral and square geometry.

While we focused on the ground state for the TM interacting with H_2, we also explore the effect of having other spin for the same oxidation state. The first example is **BBH**-Mn(II)Cl_2, where we found the ground state to be s = 5/2. However, if s = 1/2 would be synthesized, the interaction with H_2 will drop by 8 and 1 kJ/mol ($\Delta H^{\circ}_{\mathrm{bind}}$ = 12.3 and 12.1 kJ/mol) for the 1st and 2nd H_2, respectively. The second example we study is the case of **BBH**-Co(II)Cl_2 where the ground state was found to be s = 3/2, however if the s = 1/2 were synthesized, the interaction with H_2 would fall by more than 1 kJ/mol ($\Delta H^{\circ}_{\mathrm{bind}}$ = 13.0 and 12.8 kJ/mol) for the 1st and 2nd H_2. A similar trend occurs for **BBH**-Ni(II)Cl_2, where we found that the ground state is s = 2/2 but if the s = 0 were synthesized, the interaction to H_2 would decrease by more than 3 kJ/mol ($\Delta H^{\circ}_{\mathrm{bind}}$ = 12.8 and 12.8 kJ/mol for the 1st and 2nd H_2, respectively). For the Ni case, the geometry for s = 2/2 is tetrahedral while for s = 0 is square planar, therefore contrary to what should be expected even when the square environment can have a closer interaction than the tetrahedral case, the tetrahedral case interacts more strongly with H_2 due to their unpaired spin electrons.

Although the difference in energy is minimal, we can say that in general the high spin TM interact more strongly with H_2 than the slow spin analog. In all our cases the high spin was the ground state and this correspond to a Tet or Oct geometry however the Ni(II) low spin correspond to Sqr geometry and still gets less energy interaction with H_2. These observations suggest once again that geometrical difference in the coordination sphere influences to a lesser degree than the spin state for this kind of long range interactions.

Ligand containing the Imine binding group.

Our efforts to synthesis other kinds of COFs lead us to the developed the imine connectivity.[149] In this case the main linker used for the synthesis is (E)-2-((phenylimino)methyl)phenol (PIP). While the acid-basic conditions can varied we also explored the binding energy to H_2 of the un-protonated analog of this linker; (E)-2-((phenylimino)methyl)phenolate (**PIPE**). We studied the same TMs; Sc to Cu as well as Pd(II) for comparison between early transition metals and rare-earth elements. The results for the protonated and un-protonated linkers are shown in Table 7.9 and Figure 7.15.

The **PIP** and **PIPE** ligands do not interact strongly with the H_2. Our calculations show that **PIPE** interacts more strongly than **PIP** with H_2. **PIP** have $\Delta H^{\circ}_{\mathrm{bind}}$ = -5.96, -5.92, -5.90 and -5.88 kJ/mol for the 1st to the 4th interacting H_2. On the other hand, **PIPE** have $\Delta H^{\circ}_{\mathrm{bind}}$ = -9.25,

Table 7.9: Binding energies ($\Delta H^{\circ}{}_{\mathrm{bind}}$) obtained for the ground state of linkers **PIP** and **PIPE** and different number of physisorbed H_2. We also show $\Delta H^{\circ}{}_{\mathrm{bind}}$ for the linker + TM(n)Cl_n + H_2. The H-H bond of isolated H_2 is 0.741 Å

Linker = PIP	Geom for M	Spin (s)	n H_2	$\Delta H^{\circ}{}_{\mathrm{bind}}$ (kJ/mol)	H-H bond (Å)
Linker	N/A	0	1, 2, 3, 4	-5.96, -5.92, -5.90, -5.88	0.745, 0.745, 0.745, 0.744
+ Sc(III)Cl_3	Spy	0	1, 2, 3, 4	-12.7, -12.3, -12.1, -11.9	0.746, 0.745, 0.744, 0.744
+ Ti(IV)Cl_4	Oct	0	1, 2, 3, 4	-11.6, -11.4, -11.3, -10.5	0.745, 0.744, 0.744, 0.743
+ V(V)Cl_5	Oct	0	1, 2, 3, 4	-11.0, -10.9, -10.5, -10.2	0.745, 0.745, 0.745, 0.744
+ Cr(III)Cl_3	Spy	3/2	1[a], 2, 3, 4	-20.2, -11.6, -11.0, -11.9	0.747, 0.745, 0.745, 0.744
+ Mn(II)Cl_2	Tet	5/2	1[a], 2, 3, 4	-19.5, -13.0, -12.9, -12.5	0.748, 0.747, 0.746, 0.745
+ Fe(II)Cl_2	Tet	2/2	1, 2, 3, 4	-12.9, -12.9, -12.7, -12.4	0.747, 0.747, 0.746, 0.746
+ Co(II)Cl_2	Tet	3/2	1, 2, 3, 4	-14.2, -13.9, -12.4, -12.2	0.746, 0.746, 0.744, 0.743
+ Ni(II)Cl_2	Tet	2/2	1, 2, 3, 4	-11.9, -11.9, -11.7, -11.7	0.746, 0.745, 0.744, 0.743
+ Cu(II)Cl_2	Sqr	1/2	1[a], 2, 3, 4	-16.2, -16.1, -15.2, -13.4	0.746, 0.746, 0.746, 0.744
+ Pd(II)Cl_2	Sqr	0	1, 2, 3, 4	-13.4, -13.2, -12.7, -11.7	0.746, 0.745, 0.745, 0.744
Linker = **PIPE**	Geom for M	Spin (s)	n H_2	$\Delta H^{\circ}{}_{\mathrm{bind}}$ (kJ/mol)	H-H bond (Å)
Linker	N/A	0	1, 2, 3, 4	-9.25, -9.16, -9.08, -8.90	0.747, 0.747, 0.746, 0.745
+ Sc(III)Cl_3	Spy	0	1, 2, 3, 4	-12.8, -12.7, -12.3, -12.2	0.746, 0.746, 0.745, 0.745
+ Ti(IV)Cl_4	Oct	0	1, 2, 3, 4	-12.9, -12.7, -12.6, -12.0	0.746, 0.745, 0.745, 0.745
+ V(V)Cl_5	Oct	0	1, 2, 3, 4	-11.8, -11.6, -11.1, -10.8	0.745, 0.745, 0.745, 0.744
+ Cr(III)Cl_3	Spy	3/2	1[a], 2, 3, 4	-16.6, -13.1, -13.0, -12.6	0.747, 0.746, 0.746, 0.746
+ Mn(II)Cl_2	Tet	5/2	1[a], 2, 3, 4	-16.4, -13.9, -13.8, -13.7	0.749, 0.749, 0.749, 0.748
+ Fe(II)Cl_2	Tet	2/2	1, 2, 3, 4	-14.9, -14.8, -14.0, -13.7	0.748, 0.747, 0.746, 0.746
+ Co(II)Cl_2	Tet	3/2	1, 2, 3, 4	-14.4, -14.1, -14.1, -13.7	0.747, 0.747, 0.745, 0.745
+ Ni(II)Cl_2	Tet	2/2	1, 2, 3, 4	-14.6, -14.5, -14.2, -13.5	0.748, 0.747, 0.747, 0.744
+ Cu(II)Cl_2	Sqr	1/2	1[a], 2, 3, 4	-15.7, -15.4, -14.0, -13.8	0.747, 0.747, 0.746, 0.746
+ Pd(II)Cl_2	Sqr	0	1, 2, 3, 4	-14.5, -14.5, -13.6, -13.2	0.746, 0.746, 0.746, 0.745

[a] The first H_2 interacts strongly with the metal but it does not form a hydride

-9.16, -9.08 and 8.90 kJ/mol for the 1st to the 4th interacting H_2, this is more than 3kJ/mol stronger than the neutral analog. This is expected since unscreened coulombic interactions give around 3.5 kJ/mol of additional interaction with the quadrupole moment of H_2 (Table 7.5).

All of the ground states configurations were used to determine the interactions with H_2. The interaction with H_2 is only stronger for the negative ligand alone, since this trend is not universal when a TM is bound to the **PIPE** ligand, presumably because the negative charge of the O- is transferred to the TM center and there is no longer an effective negative charge (Table 7.9 and Figure 7.15).

We found that almost all the compounds of the form **PIP**+TM(n)Cl_n or **PIPE**+TM(n)Cl_n do not bind chemically to the first H_2. However we found that the Cr(III), Mn(II) and Cu(II) cases interact strongly with the first H_2. For example the complex **PIP**-Cr(III)Cl_3 interacts with the 1st H_2 giving $\Delta H^{\circ}{}_{\mathrm{bind}}$ = -20.2 kJ/mol. The analog case **PIPE**-Cr(III)Cl_3 gives a $\Delta H^{\circ}{}_{\mathrm{bind}}$ = -16.6 kJ/mol. In both of these cases, the geometry for the TM is Square pyramidal and the first H_2 binds

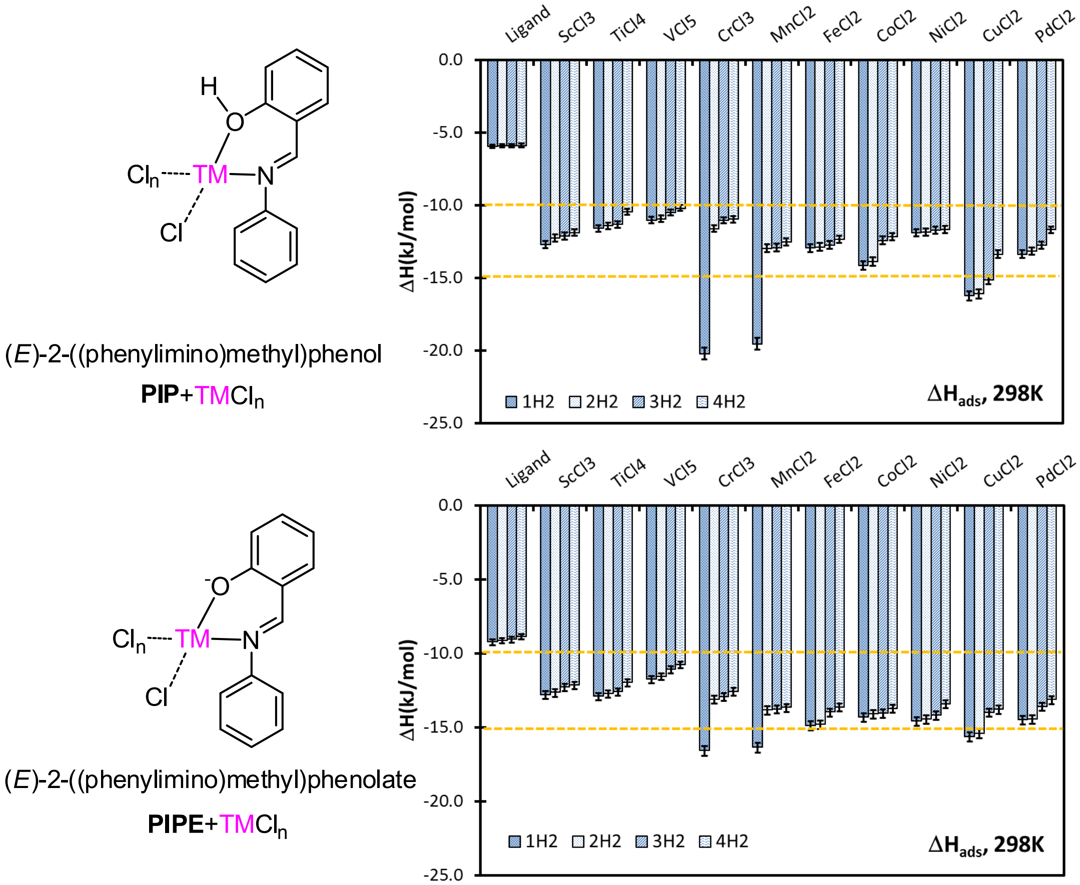
(*E*)-2-((phenylimino)methyl)phenol

PIP+TMCl$_n$

(*E*)-2-((phenylimino)methyl)phenolate

PIPE+TMCl$_n$

Figure 7.15: Different binding energies $\Delta H^{\circ}{}_{\mathrm{bind}}$ at 298K obtained for the **PIPE** ligand interacting with four physisorbed H_2. $PdCl_2$ is shown for comparison. The error bars estimates the different configurations. Mn(II), Cr(III) and Cu(II) show strong interactions with the first H_2 but there is no evidence of formation of hydride (Table 7.9).

to the bottom of the pyramid forming an octahedral environment for the TM where there is a η^2-H_2 interaction. In the case of **PIP**-Cr(III)Cl_3(η^2-H_2) the Cr-H_2 distance is 2.488 and 2.502 Å. For analog **PIPE**-Cr(III)Cl_3(η^2-H_2) the Cr-H_2 distance is longer with 2.525 and 2.544 Å. These ligand-Cr(III)Cl_3(η^2-H_2) complexes then serves as the host for the following 2nd to 4th H_2. The strength for these latter H_2 is around 11 to 13 kJ/mol with an H-H bond of 0.745-0.746 Å, with a slightly stronger interaction for the **PIPE** case.

In a similar fashion the **PIP**-Mn(II)Cl_2 complex interacts strongly with the 1st H_2 with $\Delta H^{\circ}{}_{\mathrm{bind}}$ = -19.5 kJ/mol, while **PIPE**-Mn(II)Cl_2 gives $\Delta H^{\circ}{}_{\mathrm{bind}}$ = -16.4 kJ/mol. In the case of the **PIP** complex the H_2 forms a **PIP**-Mn(II)Cl_2(η^2-H_2) where the geometry is a distorted trigonal bipyramidal with the η^2-H_2 and the binding sites of the **PIP** ligand occupy the equatorial positions while the Cl^- occupies the axial positions. The distances for the Mn-H_2 are 2.65 and 2.67 Å. The same geometry and type of interaction is obtained for the negative analog link that forms **PIPE**-Mn(II)Cl_2(η^2-H_2). The distances for the Mn-H_2 are 2.66 and 2.67 Å, which are similar to the **PIP** case. The following

2nd to 4th H_2 binds with a weaker $\Delta H^{\circ}{}_{\text{bind}}$ of around -13.9 to -12.5 kJ/mol. The H-H bonds in all these interactions ranges from 0.745 to 0.749 Å.

The other TM that has a strong interaction with the first H_2 is Cu(II). In this case, we observe that the 2nd H_2 also interacts as strong as the 1st one. The **PIP**-Cu(II)Cl_2 interacts with the 1st and 2nd H_2 with $\Delta H^{\circ}{}_{\text{bind}}$ = -16.2 kJ/mol and -16.1 kJ/mol, respectively. This is the same scenario for the complex **PIPE**-Cu(II)Cl_2 with $\Delta H^{\circ}{}_{\text{bind}}$ = -15.7 kJ/mol and -15.4 kJ/mol for the 1st and 2nd H_2, respectively. In any of these interactions there is no evidence for η^2-H_2. The distances for the Cu-1stH_2 in the **PIP**-Cu(II)Cl_2 are 2.785 and 3.182 Å, while for the Cu-2ndH_2 the distances are 3.438 and 3.963 Å. This shows the asymmetry of this interaction. On the other hand, the distances for the Cu-1stH_2 in the **PIPE**-Cu(II)Cl_2 case are 2.87 and 3.31 Å, while for the 2ndH_2, the distances are 2.93 and 3.49 Å. In this case, the square planar geometry for the Cu is distorted. For the next H_2 interacting with these complexes the $\Delta H^{\circ}{}_{\text{bind}}$ ranges from -15.2 to -13.4 kJ/mol. In general also the H-H bond is not perturbed significantly since the range for the distances are from 0.744 to 0.747 Å. Thus the square planar geometry for this ligand has a preference because the interaction with H_2 is mild but the interaction strength does not drops drastically for the subsequent H_2. The geometries for the Mn(II) and Cu(II) are Tetrahedral and Square planar, respectively, and the stronger interaction is for the Tetrahedral geometry when compared to the square geometry, as in the **BBH** ligand.

The other TMs have mild interactions with H_2, the $\Delta H^{\circ}{}_{\text{bind}}$ ranges from -14.9 to -10.2 kJ/mol. This is the ideal range for maximum delivery under the assumption presented in this work, and our results suggest that any of the TMs presented here with their respective oxidation state should give optimal delivery amount of H_2. In general the tetrahedral and square planar geometry for the TM gives the stronger interaction followed by the Square pyramidal and Octahedral geometry.

In most of the cases the TM coordinates to the **PIP** or **PIPE** ligand. However the V(V) does not coordinate with the **PIP** ligand and it weakly coordinates to the O in the **PIPE** ligand. In the formation of the interaction between **PIP** and V(V), the bonds are too long to be considered coordination bonds, the values for the V-O and V-N distances 3.53 and 3.81 Å. This makes the V(V)Cl_5 complex to have a quasi-square pyramidal geometry. A similar case happens for the **PIPE**-V(V)Cl_5 where the V(V) coordinates this time waekly to the O- of the **PIPE** ligand. The distance for the V-O and V-N are 1.77 and 3.86 Å. The interaction of the V(V)Cl_5 complex with the O of the **PIPE**, makes the geometry of the TM to be octahedral. Both cases (PIP V(V)Cl_5 and **PIPE**-V(V)Cl_5) have the lowest interaction with H_2, since their values ranges from $\Delta H^{\circ}{}_{\text{bind}}$ = -11.8 to -10.2 kJ/mol. This is probably because of the screened coulombic charge for the V(V)Cl_5 and the poor dispersion interaction that the octahedral geometry offers. The H-H bond length is not out of the ordinary, which can be observed by the constant values of 0.744 and 0.745 for all the four interacting H_2.

In general the negatively charged **PIPE** compounds have more interaction than the neutral analog **PIP** analogs except when the TM is bound directly to the negatively charged species and this TM is highly electrophilic. This makes the charged to be screened and then there will not be a strong charge quadrupole interaction. We also found that with these two linkers, all the TM falls in the ideal range of 10-15 kJ/mol interaction for maximum delivery uptake, thus if the gravimetric uptake needs to be optimized, we can use the lighter version of TM. We corroborated that the tetrahedral geometry in general gives slightly stronger interaction than the square geometry. And these geometries give slightly stronger interaction than the square bipyramidal followed by the octahedral geometry. This will serves for future design as a way to tune the H_2 interaction.

Ligand containing the Imine-Pyridine binding groups.

Our efforts to generate metalation sites include the (E)-N-(pyridin-2-ylmethylene)aniline (**PIA**) ligand which we used in a MOF to create metalation sites.[139] We explored for this linker the same TMs; Sc to Cu as well as Pd(II). The results are shown in Table 7.10 and Figure 7.16.

Table 7.10: Binding energies ($\Delta H^{\circ}{}_{\text{bind}}$) obtained for the ground state of linker **PIA** and different number of physisorbed H_2. We also show $\Delta H^{\circ}{}_{\text{bind}}$ for the linker + TM(n)Cl_n + H_2. The H-H bond of isolated H_2 is 0.741 Å

Linker = **PIA**	Geom for M	Spin (s)	n H_2	$\Delta H^{\circ}{}_{\text{bind}}$ (kJ/mol)	H-H bond (Å)
Linker	N/A	0	1, 2, 3, 4	-7.57, -7.53, -7.48, -7.40	0.746, 0.746, 0.745, 0.744
+ Sc(III)Cl_3	Spy	0	1[a], 2, 3, 4	-15.2, -12.3, -11.7, -10.9	0.747, 0.745, 0.745, 0.743
+ Ti(IV)Cl_4	Oct	0	1, 2, 3, 4	-11.9, -11.6, -10.9, -10.0	0.745, 0.745, 0.744, 0.743
+ V(V)Cl_5	Oct	0	1, 2, 3, 4	-10.9, -10.8, -9.78, -8.33	0.747, 0.747, 0.745, 0.745
+ Cr(III)Cl_3	Spy	3/2	1[a], 2, 3, 4	-18.5, -12.5, -10.9, -10.3	0.747, 0.745, 0.744, 0.744
+ Mn(II)Cl_2	Tet	5/2	1[a], 2, 3, 4	-15.7, -12.8, -12.7, -12.5	0.748, 0.747, 0.746, 0.746
+ Fe(II)Cl_2	Tet	2/2	1, 2, 3, 4	-14.0, -14.0, -14,0, -13.9	0.747, 0.747, 0.746, 0.746
+ Co(II)Cl_2	Tet	3/2	1, 2, 3, 4	-13.8, -13.6, -13.6, -13.4	0.746, 0.746, 0.746, 0.745
+ Ni(II)Cl_2	Tet	2/2	1, 2, 3, 4	-14.3, -14.2, -14.1, -14.1	0.747, 0.746, 0.746, 0.746
+ Cu(II)Cl_2	Sqr	1/2	1, 2, 3, 4	-13.9, -13.6, -13.5, -13.2	0.746, 0.746, 0.745, 0.744
+ Pd(II)Cl_2	Sqr	0	1, 2, 3, 4	-12.8, -12.8, -11.9, -11.9	0.745, 0.745, 0.745, 0.744

[a] The first H_2 interacts strongly with the metal but it does not form a hydride.

As in the other cases we found TM that interacts strongly with the 1st H_2 trough a η^2-H_2 interaction. For the first time in this series we found this interaction for the Sc(III)Cl_3 type complex. The 1st H_2 forms a **PIA**-Sc(III)Cl_3(η^2-H_2) complex with a $\Delta H^{\circ}{}_{\text{bind}}$ of -15.2 kJ/mol. The TM has an octahedral geometry with the η^2-H_2 occupying one of the sites. The distances for the Sc-H_2 are 2.77 and 2.81 Å, while the H-H bond is 0.747 Å. The following 2nd to 4th H_2 interact less strongly with this psedo-complex which is observed from $\Delta H^{\circ}{}_{\text{bind}}$ = -12.3, -13.3 and -12.7 kJ/mol. The H-H bond is also not distorted (0.745, 0745 and 0.743 Å, for 2nd to 4th H_2, correspondingly).

The other case where the TM interacts strongly with the first H_2 forming a η^2-H_2 complex is Cr(III). This interaction forms the **PIA**-Cr(III)Cl_3(η^2-H_2) complex where the Cr(III) forms an octahedral coordination center. The $\Delta H^{\circ}{}_{\text{bind}}$ for this interaction is -18.5 kJ/mol. The bond distances

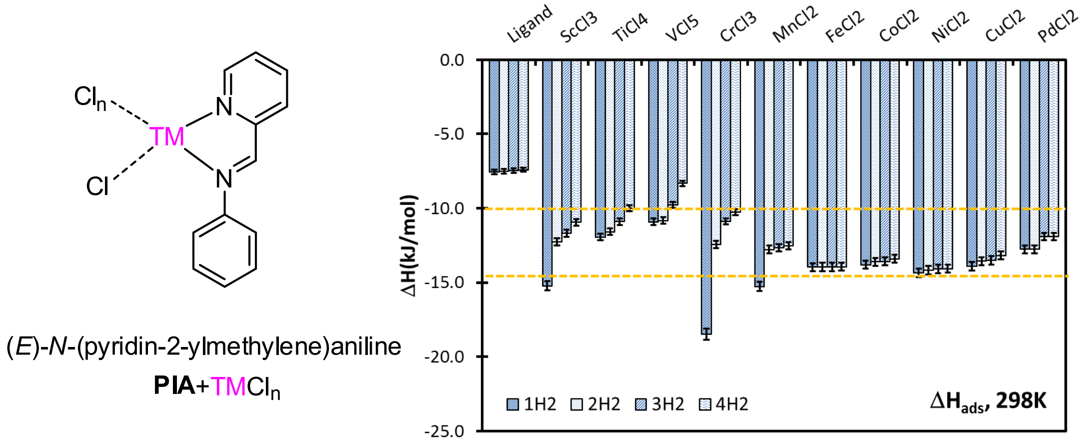

(*E*)-*N*-(pyridin-2-ylmethylene)aniline

PIA+TMCl$_n$

Figure 7.16: Different binding energies $\Delta H°_{\text{bind}}$ at 298K obtained for the **PIA** ligand interacting with four physisorbed H_2. We have focused on isoelectronic TM. $PdCl_2$ are shown for comparison. The error bars estimate the different configurations. Mn(II), Cr(III) and Sc(II) show strong interactions with the first H_2 but there is no evidence of formation of hydride (Table 7.10).

for the Cr-H_2 are 2.54 and 2.53 Å, which are shorter than the Sc(III) case. The next H_2 binds less strongly with $\Delta H°_{\text{bind}}$ = -12.5, -10.9 and -10.3 kJ/mol for the 2nd to 4th H_2, respectively. This is a drastic drop for the $\Delta H°_{\text{bind}}$. It is expected since now an octahedral geometry is being form and this coordination shell for the TM is the one that has the least binding energy towards H_2.

The last TM in this series that interacts strongly with the first H_2 is Mn(II). The strength of this interaction is $\Delta H°_{\text{bind}}$ = -12.3 kJ/mol and forms **PIA**-Mn(II)Cl_2(η^2-H_2). The TM gets transformed from a tetrahedral coordination shell to a distorted trigonal bipyramidal with the η^2-H_2 in the equatorial position. The Mn-H_2 distance is 2.70 Å, for both H_2 which show the symmetry of the interaction. The H-H bond is 0.748 Å. The following H_2 interacts less strongly with $\Delta H°_{\text{bind}}$ = -12.8, -12.7 and -12.5 kJ/mol for the 2nd to 4th H_2, respectively. The H-H bond is not significantly affected in these interactions since the bonds range from 0.747 to 0.746 Å.

All the other TM have an interactions in the ideal $\Delta H°_{\text{bind}}$ range of 10-15 kJ/mol, and the V(V) is in the limit. The results shown in Table 7.10 suggest the same trends as in the other ligands, when comparing the geometry of the TM. This is that the stronger interactions in general are for the tetrahedral coordinations shell, followed closely by the square planar geometry. Then the next geometry that gives strong interaction with H_2 is the square pyramidal coordination shell, and at the end, the octahedral geometry gives the worst interaction with H_2.

In V(V) case, there is not a coordination interaction between the **PIA** ligand and the V(V)Cl_5 cluster. This can be deducted because of the long V-N distances which are 3.39 and 3.90 Å. The V(V)Cl_5 adopts distorted square pyramidal geometry, however the **PIA** occupies a site making this coordination shell a distorted octahedral. The interactions with H_2 are the worst in this series with $\Delta H°_{\text{bind}}$ = -10.9, -10.8, -9.78 and -8.33 kJ/mol for the 1st to the 4th H_2, respectively. The second worst performance is for the other octahedral geometry and in this case there is a true coordination bond forming the **PIA**-Ti(IV)Cl_4 complex. The strength of interaction for this complex is $\Delta H°_{\text{bind}}$ = -11.9, -11.6, -10.9 and -10.0 kJ/mol for the four H_2 by order of interaction.

From this ligand we have confirmed that the tetrahedral geometry for the coordination shell gives the stronger interactions with H_2, followed closely by the square planar case. Then, the next strong interaction is given by the square pyramidal geometry and finally the octahedral coordination shell gives the worst interaction with H_2.

7.2.3.2 Proposed Linkers Based on Experimental Crystal Structures

We speculated that the square geometry was essential to obtain the maximum number of interacting H_2 with the linker versus tetrahedral or other geometry. Thus, we search the Cambridge Structural Database (CSD) for square geometry for TM with pyridine ligands. We were focused on these ligands because we believe they can be an easy metalation sites in a framework (Figure 7.13). We found the various numbers of synthesized compounds in the literature with these restrictions. This type of interaction sites are analogous to the COF synthesized with triazine linkage.[151]

Ligand containing the bipyridine group.

The first linker we studied with this approach was the 2,2'-bipirydine (BPY). Using the crystal structures we calculated the H_2 binding energy for all these TM; Ni(II)[152], Cu(II)[153], Pt(II)[154] and Pd(II)[155]. We include Pt(II) to have another comparison besides Pd(II) for precious late transition metal and also because Pt(II) in this coordination environment is ubiquitous in coordination chemistry. The results are shown in Table 7.11 and Figure 7.17.

Table 7.11: Binding energies ($\Delta H°_{\text{bind}}$) obtained for the ground state of linker **BPY** and different number of physisorbed H_2. We also show $\Delta H°_{\text{bind}}$ for the linker + TM(II)Cl_2 + H_2. The H-H bond of isolated H_2 is 0.741 Å

Linker = BPY	Geom for M	Spin (s)	n H_2	$\Delta H°_{\text{bind}}$ (kJ/mol)	H-H bond (Å)
Linker	N/A	0	1, 2, 3, 4	-5.33, -5.18, -4.90, -4.78	0.745, 0.744, 0.744, 0.744
+ Ni(II)Cl_2	Sqr	0	1, 2, 3, 4	-10.9, -10.1, -8.83, -7.64	0.746, 0.746, 0.745, 0.745
+ Cu(II)Cl_2	Sqr	1/2	1, 2, 3, 4	-14.7, -13.3, -13.0, -11.7	0.746, 0.746, 0.744, 0.744
+ Pt(II)Cl_2	Sqr	0	1, 2, 3, 4	-11.4, -11.1, -10.9, -10.4	0.744, 0.744, 0.744, 0.744
+ Pd(II)Cl_2	Sqr	0	1, 2, 3, 4	-9.89, -9.86, -9.81, -9.78	0.747, 0.747, 0.747, 0.746

The **BPY** ligand alone does not interact strongly with H_2. The $\Delta H°_{\text{bind}}$ ranges from -5.33 to -4.78 kJ/mol, which is the usual strength for interaction with an organic linker. The H-H bond distance for the H_2 are also in the usual range with 0.745, 0.744, 0.744 and 0.744 Å, for the 1st to the 4th H, respectively. However we increase this interaction by adding TM to the binding sites of this linker.

The best results are for the **BPY**-Cu(II)Cl_2 complex with $\Delta H°_{\text{bind}}$ = -14.7, -13.3, -13.0 and

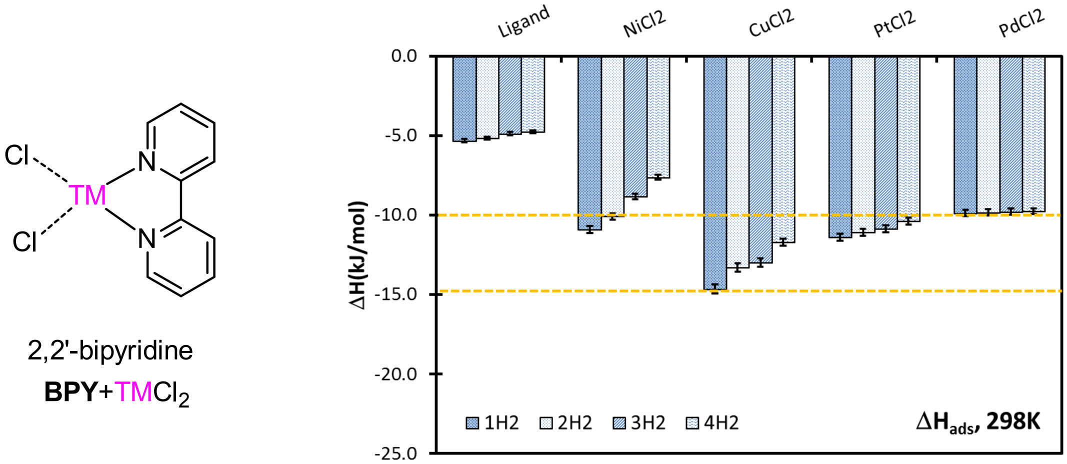

Figure 7.17: Different binding energies $\Delta H^{\circ}{}_{\text{bind}}$ at 298K obtained for the **BPY** ligand interacting with four physisorbed H_2. We have focused on isoelectronic TM. The error bars estimate the different configurations.

-11.7 kJ/mol. This is in the ideal range for maximum delivery H_2 for the 233/358 K under our current assumptions. The H-H are 0.746, 0.746, 0.744 and 0.744 for the 1^{st} to 4^{th} interacting H_2, this indicates that the H-H bond is not significantly distorted. The next best performance was the **BPY**-Pt(II)Cl_2 complex. We found that the $\Delta H^{\circ}{}_{\text{bind}}$ is slightly better than the Pd(II) case, as we explain below. For the 1^{st} to the 4^{th} H_2, we found that $\Delta H^{\circ}{}_{\text{bind}}$ = -11.4, -11.1, -10.9 and -10.4 kJ/mol, respectively. All the H-H bond for these H_2 are the same; 0.744 Å. We calculate the $\Delta H^{\circ}{}_{\text{bind}}$ for the **BPY**-Ni(II)Cl_2 in a square planar geometry, although the most common geometry is tetrahedral for this case. Our intention was to compare the square geometry among different elements. Our results under for this geometry is $\Delta H^{\circ}{}_{\text{bind}}$ = -10.9, -10.1, -8.83 and -7.64 kJ/mol. We observe a drastic drop in the binding energy when the number of H_2 increase, which is not desirable for a material in real application. Finally, the **BPY**-Pd(II)Cl_2 complex gives a worst performances with $\Delta H^{\circ}{}_{\text{bind}}$ in the range of -9.89 to -9.78 kJ/mol for the 1^{st} to the 4^{th} H_2, respectively.

Thus, except for the Ni(II) case, all the other TM have a constant $\Delta H^{\circ}{}_{\text{bind}}$ over the first four H_2, which is desirable for a host in real applications, and also the interactions are slightly larger than 10 kJ/mol. We show again the utility of metalation as a way to improve the interaction with H_2.

Ligand containing two bipyridine groups.

The first linker we studied with this approach was the 2,2'-bipirimidine (**BPYM**). Using the crystal structures we calculated the H_2 binding energy for all these TM; Ni(II)[156], Cu(II)[157], Pt(II)[158] and Pd(II)[159]. In this case we studied the effect of having an extra TM in the same ligand and if this effect is somehow additive. The results are shown in Table 7.12 and Figure 7.18.

The **BPYM** alone does not have strong interactions with H_2, which is shown by the $\Delta H^{\circ}{}_{\text{bind}}$

Table 7.12: Binding energies ($\Delta H^{\circ}_{\mathrm{bind}}$) obtained for the ground state of linker **BPYM** and different number of physisorbed H_2. We also show $\Delta H^{\circ}_{\mathrm{bind}}$ for the linker + TM(II)Cl_2 + H_2. The H-H bond of isolated H_2 is 0.741 Å

Linker = **BPYM**	Geom for M	Spin (s)	n H_2	$\Delta H^{\circ}_{\mathrm{bind}}$ (kJ/mol)	H-H bond (Å)
Linker	N/A	0	1, 2, 3, 4	-5.85, -5.74, -5.52, -5.23	0.745, 0.745, 0.745, 0.745
+ Ni(II)Cl_2	Sqr	0	1, 2, 3, 4	-10.3, -10.3, -10.2, -10.2	0.748, 0.748, 0.747, 0.746
+ Cu(II)Cl_2	Sqr	1/2	1, 2, 3, 4	-14.4, -14.2, -14.0, -13.7	0.746, 0.746, 0.746, 0.746
+ Pt(II)Cl_2	Sqr	0	1, 2, 3, 4	-11.5, -11.3, -11.0, -10.6	0.746, 0.746, 0.746, 0.746
+ Pd(II)Cl_2	Sqr	0	1, 2, 3, 4	-12.5, -12.5, -12.1, -12.1	0.745, 0.745, 0.745, 0.745

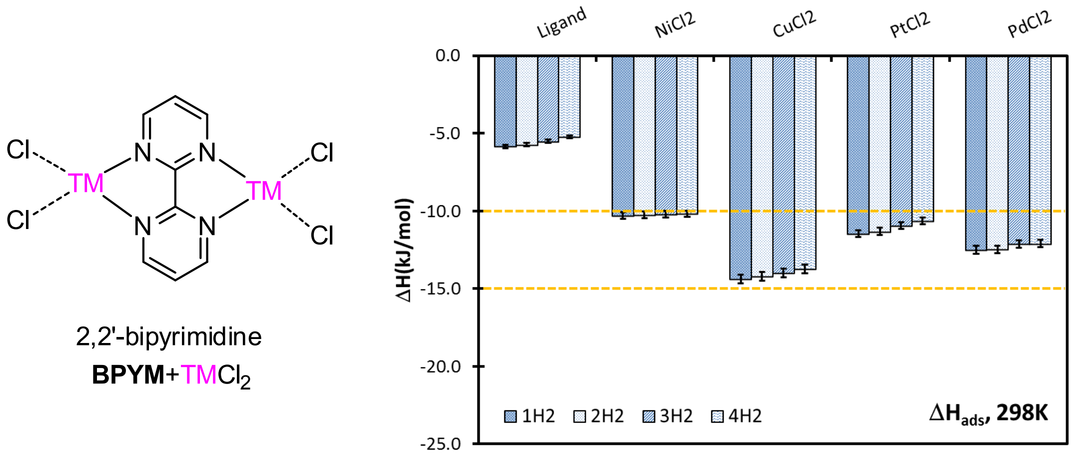

2,2'-bipyrimidine
BPYM+TMCl$_2$

Figure 7.18: Different binding energies $\Delta H^{\circ}_{\mathrm{bind}}$ at 298K obtained for the **BPYM** ligand interacting with four physisorbed H_2. We have focused on isoelectronic TM. The error bars estimate the different configurations.

= -5.85,-5.74, -5.52 and -5.23 kJ/mol, which is slightly higher than the **BPY** ligand. Also the H-H bonds are slightly higher with all the bonds being 0.745 Å. We then calculate the binding energy with other TM and we found that we the interaction strength is improved.

The best performance is for the **BPYM**-Cu(II)Cl_2 with a $\Delta H^{\circ}_{\mathrm{bind}}$ = -14.4, -14.2, -14.0 and -13.7 kJ/mol, with all the H-H bond being the same; 0.746 Å. The next best performance is for **BPYM**-Pd(II)Cl_2 complex with $\Delta H^{\circ}_{\mathrm{bind}}$ = -12.5, -12.5, -12.1 and -12.1 kJ/mol, for the 1st to the 4th H_2 respectively. The compound **BPYM**-Pt(II)Cl_2 has the third best performance where $\Delta H^{\circ}_{\mathrm{bind}}$ for the 1st to the 4th H_2 is in the range of -11.5 to -10.6 kJ/mol for the first four H_2. Finally the **BPYM**-Ni(II)Cl_2 case we have $\Delta H^{\circ}_{\mathrm{bind}}$ in the range of -10.3 to -10.2 for the first 4 H_2. Once again, we explored the square planar geometry for Ni(II) in order to compare among the same geometry, even when it is more common to find Ni(II) in the tetrahedral geometry.

We found that the additive effect for more $\Delta H^{\circ}_{\mathrm{bind}}$ given that two TM are close to each other was only found for the case of PdCl_2, while in the other cases we did not see this effect clearly. It is possible that more configurations need to be explored. The compound that offers the stronger interaction with H_2 is the Cu(II)Cl_2 for both ligands.

7.2.3.3 Alternative Strategy to Metalate COFs and MOFs

Until now we have explored the reaction of metal salts such as $Pd(CH_3CN)_2Cl_2$, $PdCl_2$ and $Cu(BF_4)_2$ with the organic linker,[138, 139] however another strategy is to react metallic atoms such as Pd(0) with the same ligands. This would create metallic center in the structure where the H_2 can interact strongly with.

We found that the reaction of any of the linkers described in this work reacts with Pd(0) exothermically as it can be seen in Figure 7.19. The most exothermic reaction is between Pd(0) and the **PIPE** ligand (ΔH_r° = -100.8 kJ/mol, ΔG_r° = -68.4 kJ/mol), presumably because this is the only ligand with a formal negative charge. In terms of neutral species, the most favorable interactions are for the ligands that contains the most nitrogen atoms, thus the most exothermic interaction is between Pd(0) and **BBH**, followed by Pd(0) and **BPY** which binds the Pd(0) to two N atoms. The linkers that interact the least strongly are **PIP** followed by **BBH**, each with only one N binding site and one OH binding site. The equilibrium between **PIP** and the **PIPE** ligand was studied trough the calculation of the pKa obtained with our ab-initio quantum mechanical methods.[160] We obtained that the pKa is equals to 8.7 in water which indicates that the **PIP** ligand is basic and that at normal neutral conditions in water, the **PIP** does not dissociates to create **PIPE** and H^+. It is important to study this equilibrium because the X-ray studies very rarely can determine if the H is in the structure or not, and it is more difficult when powder X-ray structure determinations is used.

We then proceed to study the reactivity of these Linker-Pd(0) complexes interacting with H_2. The results are shown in Figure 7.20 and Table 7.13. As we can observe there are chemical reactions between the first H_2 and all of the Linkers-Pd forming species that can be considered hydrides due to the H-H bond length and the energetics. The energetics for these reactions range from ΔH_r° = -53.5 kJ/mol (for **BBH**-Pd) to ΔH_r° = -106 kJ/mol (for **PIPE**-Pd). In a similar manner the H-H bond length ranges from 0.855 to 1.806 Å, with the shortest bond being for the least energetic reaction (**BBH**-Pd + H_2) and the largest H-H bond for the most energetic reaction (**PIPE**-Pd + H_2). The ligands in between have energetics that not necessarily correlates with the energetics, this is for examples the next strong reaction is the formation of **PIA**-Pd with ΔH_r° = -96.1 kJ/mol and the H-H bond of 0.868 Å, however the next reaction gives longer bonds but still smaller energetics for the reaction. **PIP**-Pd creates ΔH_r° = -91.7 kJ/mol and H-H bond of 0.869 Å, followed by **BPYM**-Pd with ΔH_r° = -80.7 kJ/mol and H-H bond of 0.870 Å, (this ligand in particular host two Pd per linker and the 2nd H_2 binds with ΔH_r° = -80.5 kJ/mol with H-H bond of 0.869 Å), followed by **BPY**-Pd with ΔH_r° = -77.1 and H-H bond of 0.871 Å. This shows that the H-H bond is sensitive to the energetics but also that the H-H bond with our methodology might have an error in the estimation

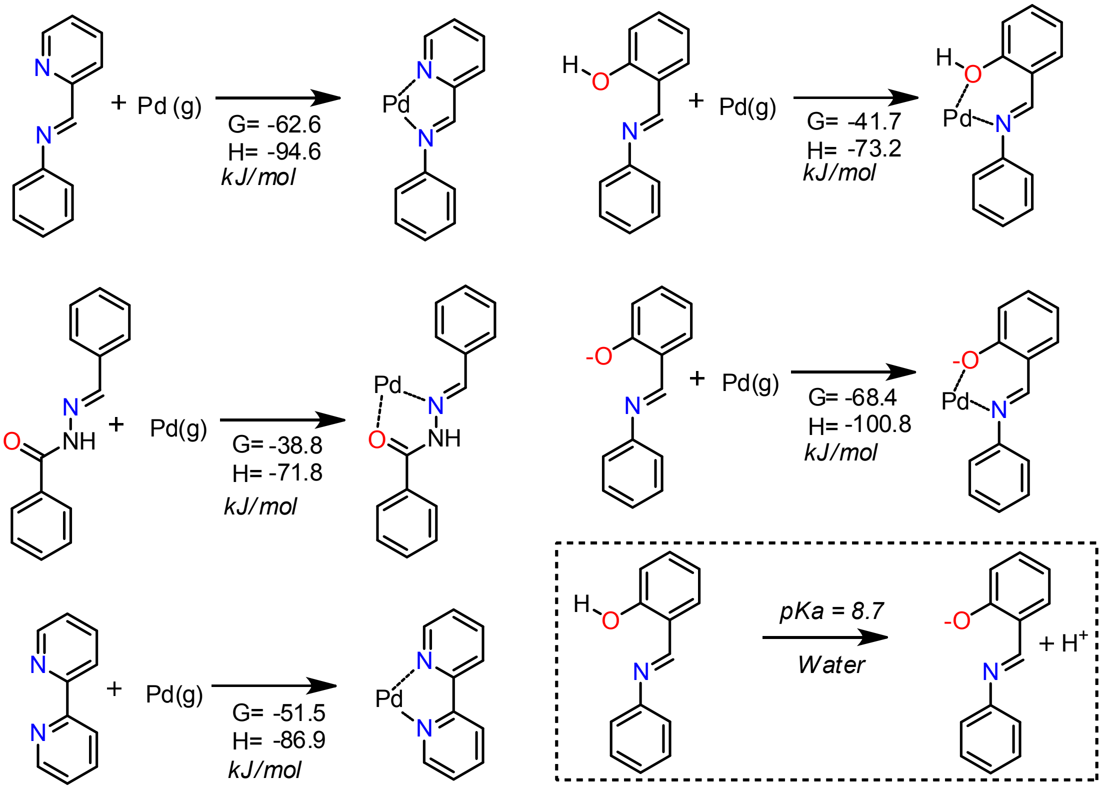

Figure 7.19: Alternative option for metalating the linkers using metallic Pd(0). Our calculations show that all these reactions are favorable, and therefore it should be a viable mode for putting metals inside extended structure. Note that in the reaction from **PIP** to **PIPE**, we did not consider a counter cation for **PIPE**; this makes the reaction with H^+ extremely favorable. The inset shows the calculated pKa for **PIP**/**PIPE**.

of the bond in the order of 0.003 Å, but it still sensitive enough to capture this direct correlation of H-H bond to the strength of ΔH_r°. In the paper by Kubas,14 the range for a true H_2 complex is given as 0.8 to 1.00 Å, while the elongated H_2 complex is estimated as the H-H bond distance from 1.0 to 1.3 Å. However our calculations show energetics for the formation of hydrides and H-H bond around 0.9 Å, while the only long bond is of 1.8 Å, for the **PIPE**-Pd. This discrepancy can be resolved by trusting the energetics of our QM method but considering our distances for H-H bond obtained from QM shorter than those described by Kubas. This can be seen in the following comparison, Kubas used the value of the isolated H-H of 0.75 Å, while our QM method found this value to be 0.741 Å.

Another evidence for the formation of hydride is the short H-Pd bond in all these linkers. The distances for the Pd-H bond in the **PIPE**-Pd-H_2 complex are 1.566 and 1.564 Å. We then obtained longer Pd-H bond distances for the **PIA**-Pd-H_2 complex with 1.722 and 1.717 Å. The **PIA**-Pd-H_2 complex gives Pd-H bond distances of 1.729 and 1.724 Å, these distances are longer than the **PIPE** ligand. The distances for the Pd-H bonds in the **BPYM**-Pd_2-H_2 complex are 1.713 and 1.712 Å,

Table 7.13: Binding energies ($\Delta H^{\circ}{}_{\mathrm{bind}}$) obtained for the ground state of all linkers (**BBH**, **PIP**, **PIPE**, **PIA**, **BPY**, and **BPYM**) + Pd shown in Figure 7.19 reacting with different number of H_2. For each case the spin is 0. The H-H bond of isolated H_2 is 0.741 Å

Linker-Pd	Geom for M	n H_2	$\Delta H^{\circ}{}_{\mathrm{bind}}$ (kJ/mol)	H-H bond (Å)
BBH-Pd	Sqr	1^{a}- 5	-53.5, -12.6, -12.5, -12.0, -12.1	0.855, 0.749, 0.748, 0.747, 0.744
PIP-Pd	Sqr	1^{a}- 5	-91.7, -13.7, -13.6, -13.6, -13.1	0.869, 0.749, 0.748, 0.748, 0.744
PIPE-Pd	Sqr	1^{a}- 5	-106, -14.8, -14.2, -13.8, -13.8	1.806, 0.748, 0.747, 0.747, 0.744
PIA-Pd	Sqr	1^{a}- 5	-96.1, -13.7, -13.0, -12.7, -12.0	0.868, 0.749, 0.747, 0.747, 0.743
BPY-Pd	Sqr	1^{a}- 5	-77.1, -11.4, -11.4, -11.0, -10.9	0.871, 0.746, 0.745, 0.743, 0.743
BPYM-Pd	Sqr	1^{a}- 5	-80.7, -80.5, -14.5, -14.5, -13.2	0.870, 0.869, 0.748, 0.748, 0.748

[a] The first H_2 react chemically and forms a linker-Pd-H_2 that resembles a hydride formation due to the energetics involved.

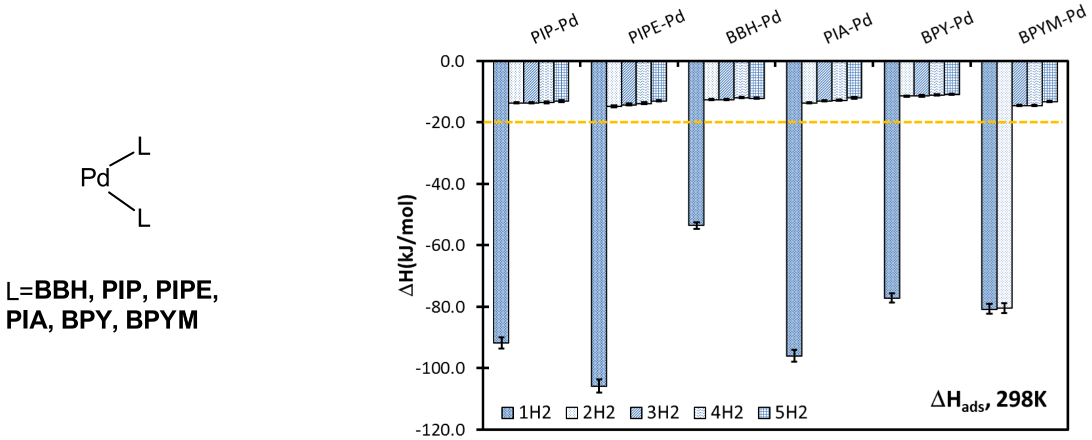

Figure 7.20: (left) Our calculations showed that Pd(0) binds to the different linkers studied here. (Right) The plot shows the energetics when the H_2 interacts with the compounds formed with Pd(0) shown in Figure 7.19. The first H_2 forms a hydride converting the Pd(0) into Pd(II). The subsequent H_2 interacts strongly by physisorption with the formed Pd(II)H_2. **BPYM** shows two H_2 bound chemically because it has two Pd per linker.

while for the second H_2 in the **BPYM**-Pd_2-$2H_2$ complex, the distance for the analog bonds are 1.713 and 1.713 Å. Then we have the **BPY**-Pd-H_2 complex with both Pd-H bond distances of 1.715 and 1.713 Å. Finally the bond distances for the Pd-H in the **BBH**-Pd-H_2 complex are 1.729 and 1.723 Å. This trend suggest that the longer the Pd-H bond the least energetics for the formation of the linker-Pd-H_2 (with the **PIA**-Pd-H_2 complex not quite following this trend, perhaps because the N in the pyridine ring makes this bond longer than the rest due to the pi electrons from the aromatic ring). For all these cases we found that the singlet is the final electronic ground state of the linker-Pd-H_2 complex and all the geometries are square planar.

Once the first H_2 is bound chemically to the linker-Pd system, the new complexes linker-Pd-H_2 serves as the host that interacts with other H_2. We show the energies for these other 4 H_2 in Table 7.13. In general the energies are very similar to the energies obtained for the physisorbed H_2 of the other ligands with transition metals and chlorines as the counter anion. This indicates that even when we have square planar geometries that allow more H_2 to interact with the metallic center, we do not obtain much gain, however the new concept of using the same coordinated metallic center for chemisorption and physisorption allows us to explore new types of hydrogen uptake.

A very important phenomenon happens when we absorb H_2 into **BPY** versus **BPYM**. While **BPY** has one site for hosting the Pd(0), the **BPYM** ligand has two sites and it turns out that the binding of the H_2 is stronger for the **BPYM**-Pd_2-$2H_2$ com-plex than with **BPY**-Pd-H_2 suggesting a cooperative interactions caused by having two Pd in the same ligand. This is the same effect observed for Pd(II)Cl_2, this suggest that late transition metals have this property but we have not observed in early TM. The physisorbed H_2 to **BPYM**-Pd_2-$2H_2$ have a stronger binding energy of around 14.5 kJ/mol while the analogs for the **BPY**-Pd-H_2 are around 11.4 kJ/mol. The same trends is observed when we analyzed the H-H bond; this bond distance is longer for the **BPYM**-Pd_2-$2H_2$ (around 0.748 Å) that for the **BPY**-Pd-H_2 case (around 0.745 Å). This is an effect not observed for the other cases and gives us a hint for using mult-binding sites for metals such as the **BPYM**, rather than the single-site binding sites such as the **BPY**. The overall gain is bigger when the metals are in the same ligand.

7.2.4 Concluding Remarks

We showed early TM (Sc to Cu) gives similar and superior van der Waals interactions than precious TM (Pd and Pt), therefore suggesting the viability for real applications.

We found high spin TM interacts more strongly with H_2 than the low spin analog. Another characteristic correlated with the spin state, is that we found that the tetrahedral geometry in general gives slightly stronger interaction than the square geometry. And these geometries give slightly stronger interaction than the square bipyramidal followed by the octahedral geometry. In general the negatively charged compounds have more interaction than the neutral analog analogs except when the TM is bound directly to the negatively charged species and this TM is highly electrophilic. This makes the charged to be screened and then there will not be a strong charge quadrupole interaction. The role of the ligand is also cooperative, since we observe that the Chlorine ligand interacts with the H_2, presumably due to charge-quadrupole interactions. Our results shows that most of the TM used falls in the ideal range of 10-15 kJ/mol interaction for maximum delivery uptake, thus if the gravimetric uptake needs to be optimized, we can use the lighter version such as the early TM. Among all studied the spins states, ligands and TM, bound to the Chlorine ligand, we found that they do not form hydrides when interacting with one H_2 but sometimes there is a strong affinity with the first H_2 forming a η^2-H_2 interaction. This will serves for future design as a way to tune the H_2 interaction.

This study also suggest that an material with heterogeneous sorption sites might be useful when a drastic change of temperature occurs in the environment since different $\Delta H^{\circ}{}_{\text{ads}}$ values between 10-15.3 kJ/mol will help the delivery amount. However if the system is maintained at the same temperature, then a homogenous material is the best option.

We also showed an alternative way of metalating the linkers of common COFs and MOFs, which is by using Pd(0). Our results showed that the formation of the complex linker-Pd(0) is favorable for all the linkers studied. When these complexes interact with H_2, the first H_2 forms a hydride with the Pd creating a linker-Pd-H_2 complex. The following H_2 interacts by non-covalent interactions forces (dispersion and coulombic) with the formed linker-Pd-H_2 complex. This new route shows a new form of using the coordinated transition metal as site for chemisorption and physorption, opening the door to new types of H_2 uptake. We also showed that having two metals in the same ligand gives a cooperative interaction with H_2, this can be observed for the cases of **BPY**-Pd-H_2 and the **BPYM**-Pd_2-$2H_2$ complexes.

With our results we predict that by metalating the existing COFs or MOFs with light or late TM with a tetrahedral or square geometry we will obtain a binding energy for optimal delivery amount of H_2. We also predict that if nucleophilic TM is used and it has a square pyramidal or octahedral geometry which is accessible to interact with H_2, then the $\Delta H^{\circ}{}_{\text{bind}}$ will also increase.

We believe that these results are of fundamental importance for the development of the next generation of H_2 storage porous materials. We are currently developing the Force Field for the most promising TM candidates.

Appendix A

Quantum Mechanical Calculations and Geometries on the Formation of Molecular Machines

A.1 All QM Calculations

Table A.1: Free energies in gas and solvated phase including quantum corrections. The solvent used is CH_3CN. Units:kcal/mol

Compound	H(gas)	G(gas)	G(solv)
F^-	-6.25912E+04	-6.26022E+04	-6.26928E+04
I^-	-7.18457E+03	-7.19727E+03	-7.25915E+03
PF6-	-5.90200E+05	-5.90224E+05	-5.90268E+05
1R	-9.95162E+05	-9.95221E+05	-9.95229E+05
D-2F	-8.96625E+05	-8.96676E+05	-8.96687E+05
D-2I	-7.85625E+05	-7.85676E+05	-7.85718E+05
D-2PF6	-1.95169E+06	-1.95175E+06	-1.95177E+06
D-2	-7.70993E+05	-7.71044E+05	-7.71203E+05
1R-D-2F	-1.89183E+06	-1.89192E+06	-1.89194E+06
1R-D-2I	-1.78082E+06	-1.78092E+06	-1.78095E+06
1R-D-2PF6	-2.94690E+06	-2.94699E+06	-2.94703E+06
1R-D-2	-1.76627E+06	-1.76636E+06	-1.76648E+06
2R-D-2F	-2.88703E+06	-2.88715E+06	-2.88719E+06
2R-D-2I	-2.77607E+06	-2.77619E+06	-2.77623E+06
2R-D-2PF6	-3.94215E+06	-3.94227E+06	-3.94231E+06
2R-D-2	-2.76152E+06	-2.76165E+06	-2.76175E+06
Dp-2F	-1.01694E+06	-1.01699E+06	-1.01700E+06
Dp-2I	-9.05930E+05	-9.05981E+05	-9.06021E+05
Dp-2PF6	-2.07199E+06	-2.07204E+06	-2.07207E+06
Dp-2	-8.91317E+05	-8.91368E+05	-8.91508E+05
1R-Dp-2F	-2.01213E+06	-2.01222E+06	-2.01224E+06
1R-Dp-2I	-1.90117E+06	-1.90126E+06	-1.90129E+06
1R-Dp-2PF6	-3.06723E+06	-3.06732E+06	-3.06735E+06
1R-Dp-2	-1.88657E+06	-1.88666E+06	-1.88678E+06
2R-Dp-2F	-3.00732E+06	-3.00745E+06	-3.00747E+06
2R-Dp-2I	-2.89636E+06	-2.89649E+06	-2.89653E+06
2R-Dp-2PF6	-4.06244E+06	-4.06256E+06	-4.06260E+06
2R-Dp-2	-2.88182E+06	-2.88194E+06	-2.88204E+06

Table A.2: Electronic Energy (E,scf), Zero Point Energy (ZPE), Solvation energy for CH_3CN (Esolv). Units:kcal/mol

Compound	E, scf	ZPE	Hvib	Htot	Svib	Stot	E(solv)
F^-	-6.25938E+04	0.00000E+00	0.00000E+00	2.61845E+00	0.00000E+00	3.69456E+01	-9.70695E+01
I^-	-7.18823E+03	0.00000E+00	0.00000E+00	3.65542E+00	0.00000E+00	4.26061E+01	-6.81235E+01
PF6-	-5.90217E+05	1.20070E+01	2.08100E+00	4.45100E+00	1.02720E+01	7.85360E+01	-5.61219E+01
1R	-9.95510E+05	3.28599E+02	1.70370E+01	1.94070E+01	1.19796E+02	1.97765E+02	-2.05595E+01
D-2F	-8.96967E+05	3.24753E+02	1.41130E+01	1.64830E+01	1.13238E+02	1.70006E+02	-2.02911E+01
D-2I	-7.85967E+05	3.24753E+02	1.41130E+01	1.64830E+01	1.13238E+02	1.70006E+02	-5.18886E+01
D-2PF6	-1.95204E+06	3.24753E+02	1.41130E+01	1.64830E+01	1.13238E+02	1.70006E+02	-3.43250E+01
D-2	-7.71334E+05	3.24753E+02	1.41130E+01	1.64830E+01	1.13238E+02	1.70006E+02	-1.68734E+02
1R-D-2F	-1.89252E+06	6.56066E+02	3.44260E+01	3.67960E+01	2.77676E+02	3.17215E+02	-2.30938E+01
1R-D-2I	-1.78152E+06	6.56066E+02	3.44260E+01	3.67960E+01	2.77676E+02	3.17215E+02	-3.65654E+01
1R-D-2PF6	-2.94759E+06	6.56066E+02	3.44260E+01	3.67960E+01	2.77676E+02	3.17215E+02	-4.64984E+01
1R-D-2	-1.76696E+06	6.56066E+02	3.44260E+01	3.67960E+01	2.77676E+02	3.17215E+02	-1.21114E+02
2R-D-2F	-2.88807E+06	9.85690E+02	5.16350E+01	5.40050E+01	3.89058E+02	4.30516E+02	-3.84228E+01
2R-D-2I	-2.77711E+06	9.85690E+02	5.16350E+01	5.40050E+01	3.89058E+02	4.30516E+02	-4.57423E+01
2R-D-2PF6	-3.94319E+06	9.85690E+02	5.16350E+01	5.40050E+01	3.89058E+02	4.30516E+02	-4.53417E+01
2R-D-2	-2.76256E+06	9.85690E+02	5.16350E+01	5.40050E+01	3.89058E+02	4.30516E+02	-1.10013E+02
Dp-2F	-1.01728E+06	3.24753E+02	1.41130E+01	1.64830E+01	1.13238E+02	1.70006E+02	-1.99386E+01
Dp-2I	-9.06271E+05	3.24753E+02	1.41130E+01	1.64830E+01	1.13238E+02	1.70006E+02	-4.95869E+01
Dp-2PF6	-2.07233E+06	3.24753E+02	1.41130E+01	1.64830E+01	1.13238E+02	1.70006E+02	-4.11532E+01
Dp-2	-8.91658E+05	3.24753E+02	1.41130E+01	1.64830E+01	1.13238E+02	1.70006E+02	-1.49998E+02
1R-Dp-2F	-2.01282E+06	6.56066E+02	3.44260E+01	3.67960E+01	2.77676E+02	3.17215E+02	-2.74249E+01
1R-Dp-2I	-1.90186E+06	6.56066E+02	3.44260E+01	3.67960E+01	2.77676E+02	3.17215E+02	-4.06581E+01
1R-Dp-2PF6	-3.06792E+06	6.56066E+02	3.44260E+01	3.67960E+01	2.77676E+02	3.17215E+02	-3.39980E+01
1R-Dp-2	-1.88726E+06	6.56066E+02	3.44260E+01	3.67960E+01	2.77676E+02	3.17215E+02	-1.21905E+02
2R-Dp-2F	-3.00836E+06	9.85690E+02	5.16350E+01	5.40050E+01	3.89058E+02	4.30516E+02	-3.06199E+01
2R-Dp-2I	-2.89740E+06	9.85690E+02	5.16350E+01	5.40050E+01	3.89058E+02	4.30516E+02	-4.74455E+01
2R-Dp-2PF6	-4.06348E+06	9.85690E+02	5.16350E+01	5.40050E+01	3.89058E+02	4.30516E+02	-4.66618E+01
2R-Dp-2	-2.88285E+06	9.85690E+02	5.16350E+01	5.40050E+01	3.89058E+02	4.30516E+02	-1.07737E+02

Table A.3: Free energies in gas and solvated phase including quantum corrections. The solvent used is CH_3CN. Units:kcal/mol

Compound	H(gas)	G(gas)	G(solv)
1R	-9.95162E+05	-9.95221E+05	-9.95229E+05
Bz(OCH3)2	-2.89325E+05	-2.89353E+05	-2.89348E+05
-NH2- site	-6.75272E+05	-6.75304E+05	-6.75316E+05
-NH2'- site	-8.20194E+05	-8.20231E+05	-8.20239E+05
1R-1R	-1.99035E+06	-1.99045E+06	-1.99047E+06
1R'-1R'	-1.99032E+06	-1.99044E+06	-1.99045E+06
1R-Bz(OCH3)2	-1.28450E+06	-1.28458E+06	-1.28458E+06
1R-NH2- site	-1.67048E+06	-1.67055E+06	-1.67057E+06
1R-NH2'- site	-1.81540E+06	-1.81548E+06	-1.81549E+06

Table A.4: Electronic Energy (E , scf), Zero Point Energy (ZPE), Solvation energy for CH_3CN (Esolv). Units:kcal/mol

Compound	E, scf	ZPE	Hvib	Htot	Svib	Stot	E(solv)
1R	-9.95510E+05	3.28599E+02	1.70370E+01	1.94070E+01	1.19796E+02	1.97765E+02	-2.05595E+01
Bz(OCH3)2	-2.89436E+05	1.04135E+02	4.08000E+00	6.45000E+00	2.34762E+01	9.39090E+01	-5.95564E+00
-NH2- site	-6.75361E+05	8.07760E+01	5.70600E+00	8.07600E+00	3.60639E+01	1.08914E+02	-2.32889E+01
-NH2'- site	-8.20336E+05	1.31735E+02	7.90500E+00	1.02750E+01	5.62807E+01	1.25741E+02	-1.93427E+01
1R-1R	-1.99105E+06	6.58173E+02	3.66040E+01	3.89740E+01	2.58352E+02	3.35071E+02	-2.83913E+01
1R'-1R'	-1.99102E+06	6.56478E+02	3.46260E+01	3.69960E+01	2.74323E+02	3.20944E+02	-4.45452E+01
1R-Bz(OCH3)2	-1.28496E+06	4.33114E+02	2.35260E+01	2.58960E+01	1.64741E+02	2.42929E+02	-1.63825E+01
1R-NH2- site	-1.67092E+06	4.11047E+02	2.41510E+01	2.65210E+01	1.76566E+02	2.42304E+02	-2.55056E+01
1R-NH2'- site	-1.81589E+06	4.62013E+02	2.68440E+01	2.92140E+01	1.95686E+02	2.63315E+02	-2.78585E+01

A.2 Geometries for the R Family (2R-D-2PF$_6$, 1R-D-2PF$_6$, 2R-D-2PF$_6$) and for the R’ Family (2R-Dp-2PF$_6$, 1R-Dp-2PF$_6$, 2R-Dp-2PF$_6$)

A.2.1 2R-D-2PF$_6$-M06L

```
201
2R-D-2PF6-M06L
  O        6.65680      13.70690       7.19040
  O        8.77290      14.71850       3.05630
  O       11.12290       2.53230       9.23700
  O       11.54530       2.32320       4.50430
  N       11.26060      11.17400       6.57730
  H       10.77290      10.85820       5.69690
  H       10.61740      10.91800       7.35690
  N       13.07910       6.72760       6.94840
  H       12.52050       6.56410       6.08110
  H       12.40160       6.64030       7.74060
  C        6.71560      13.13430       8.48340
  H        7.02580      12.08170       8.44270
  H        5.70650      13.19790       8.89030
  H        7.40790      13.68010       9.13850
  C        7.51370      15.07350       2.52230
  H        7.06910      15.92340       3.05670
  H        6.80950      14.23180       2.55550
  H        7.69190      15.35450       1.48410
  C       10.01820       1.65090       9.16010
  H        9.21760       2.06520       8.53380
  H        9.65340       1.53180      10.17990
  H       10.30910       0.67100       8.75960
  C       12.10430       2.83790       3.31010
  H       11.91940       3.91510       3.20460
  H       11.61470       2.30800       2.49350
  H       13.18820       2.66300       3.26160
  C        7.80380      13.71210       6.46580
  C        7.67680      14.21460       5.16340
```

H	6.69820	14.54830	4.83950
C	8.79270	14.26390	4.33620
C	10.03640	13.80450	4.79350
H	10.88120	13.79630	4.10880
C	10.14090	13.29610	6.07930
C	9.03300	13.25780	6.93560
H	9.13610	12.82770	7.92710
C	11.42050	12.65760	6.52850
H	11.73280	12.96340	7.53520
H	12.24350	12.85300	5.83330
C	12.55020	10.45630	6.73380
H	13.03090	10.84220	7.63780
H	13.17500	10.73090	5.87680
C	12.27150	8.97530	6.80050
H	11.71940	8.66690	5.90100
H	11.61830	8.76060	7.65860
C	13.53370	8.13560	6.91870
H	14.21610	8.25650	6.06670
H	14.09740	8.33220	7.83850
C	14.08770	5.63670	7.06880
H	14.61770	5.78480	8.01020
H	14.78990	5.75050	6.23930
C	13.29990	4.35800	7.01690
C	12.70190	3.87630	8.17170
H	12.91800	4.31060	9.14400
C	11.70830	2.89170	8.06670
C	11.34340	2.38400	6.82360
H	10.56060	1.64430	6.70550
C	11.98450	2.85830	5.67240
C	12.96830	3.83960	5.75940
H	13.41300	4.27490	4.87240
O	12.11740	10.57900	9.92590
O	14.01750	12.49770	9.04670
O	14.86780	13.55770	6.59740
O	14.29110	12.11260	4.25670
O	12.42110	10.18540	3.50890

N	9.84780	10.51390	4.11440
N	8.60720	9.86260	6.57560
N	9.57260	10.57140	9.11780
C	13.48030	10.55760	10.31000
H	13.97990	9.93520	9.55710
H	13.60790	10.05350	11.27990
C	14.09950	11.93490	10.33820
H	13.59430	12.59230	11.06420
H	15.15280	11.84950	10.66290
C	14.72640	13.71340	8.96850
H	15.81050	13.53040	9.07600
H	14.42830	14.39210	9.78580
C	14.43590	14.38180	7.65560
H	13.35500	14.58940	7.56610
H	14.95190	15.35810	7.62890
C	14.65240	14.18990	5.35620
H	15.21980	15.13540	5.29330
H	13.58550	14.44980	5.23060
C	15.08860	13.27540	4.24930
H	14.99260	13.80500	3.28610
H	16.15380	13.00900	4.37140
C	14.56050	11.30900	3.12860
H	15.63980	11.07900	3.06010
H	14.29550	11.86230	2.21440
C	13.80040	10.00640	3.24610
H	13.95630	9.39530	2.34360
H	14.17630	9.42210	4.09500
C	11.64430	10.68970	2.50500
C	12.08660	10.95190	1.20880
H	13.10440	10.72250	0.91570
C	11.20640	11.46470	0.25930
H	11.57000	11.66740	-0.74390
C	9.88120	11.71630	0.59090
H	9.19800	12.13680	-0.14030
C	9.43000	11.41270	1.86790
H	8.39620	11.59940	2.14560

C	10.28830	10.88010	2.83300
C	8.67950	9.97640	4.16790
H	8.11460	9.75390	3.25700
C	8.03140	9.56170	5.40440
C	6.81550	8.86820	5.29080
H	6.41950	8.64400	4.30670
C	6.17310	8.45730	6.44680
H	5.24330	7.89830	6.39560
C	6.74480	8.77050	7.67030
H	6.28540	8.47750	8.60720
C	7.95610	9.48080	7.68440
C	8.49260	9.88100	8.97870
H	7.90120	9.56280	9.84300
C	9.86350	10.97930	10.42930
C	8.86880	11.36600	11.33380
H	7.83370	11.35720	11.00220
C	9.18190	11.75940	12.62820
H	8.39180	12.05760	13.30950
C	10.50890	11.76080	13.03790
H	10.77120	12.05390	14.05030
C	11.51960	11.38500	12.15670
H	12.54370	11.36050	12.51090
C	11.20790	11.00460	10.85200
O	13.90950	6.68080	10.10760
O	15.97070	8.45160	9.30530
O	16.93550	9.52790	6.92050
O	16.27640	8.00840	4.62630
O	14.27220	6.19280	3.84310
N	11.64150	6.53900	4.34280
N	10.30670	6.03910	6.79220
N	11.31650	6.71090	9.33200
C	15.26120	6.53270	10.50930
H	15.71550	5.89180	9.74620
H	15.33100	6.00420	11.46950
C	16.02250	7.83620	10.57110
H	15.60550	8.51470	11.33590

H	17.06530	7.62150	10.86380
C	16.74770	9.62920	9.26470
H	17.81900	9.38310	9.35430
H	16.49310	10.29180	10.11130
C	16.48490	10.34700	7.97050
H	15.40890	10.57860	7.86240
H	17.01000	11.32020	7.97280
C	16.70600	10.11010	5.66330
H	17.28180	11.04830	5.54790
H	15.64090	10.38160	5.54130
C	17.13090	9.13260	4.60370
H	17.09400	9.62500	3.61550
H	18.17600	8.82210	4.77070
C	16.48000	7.19560	3.49370
H	17.54070	6.90330	3.40030
H	16.21980	7.75780	2.57970
C	15.64960	5.94040	3.62790
H	15.80260	5.28980	2.75520
H	15.97280	5.38290	4.51350
C	13.50550	6.58670	2.77550
C	13.98300	6.74970	1.47500
H	15.02180	6.54830	1.23770
C	13.12080	7.16780	0.45970
H	13.51250	7.29570	-0.54580
C	11.78390	7.42630	0.73520
H	11.10450	7.77830	-0.03510
C	11.30010	7.22930	2.02140
H	10.25800	7.43010	2.24440
C	12.13720	6.78660	3.05010
C	10.46270	6.01580	4.38570
H	9.93750	5.72050	3.47060
C	9.72520	5.76290	5.61770
C	8.42740	5.24070	5.50220
H	7.99510	5.09840	4.51590
C	7.71760	4.96710	6.66340
H	6.70240	4.58460	6.61430

C	8.31860	5.21770	7.88910
H	7.79620	5.05890	8.82820
C	9.61370	5.75880	7.90360
C	10.20340	6.07560	9.20030
H	9.61220	5.76530	10.06910
C	11.65150	7.10300	10.63730
C	10.67210	7.52640	11.54160
H	9.63960	7.57030	11.21410
C	11.00220	7.90380	12.83580
H	10.21480	8.23460	13.50600
C	12.32880	7.85870	13.24380
H	12.60580	8.14060	14.25600
C	13.32760	7.46030	12.35420
H	14.35510	7.42010	12.69820
C	13.00020	7.09970	11.04750
P	6.75150	6.95370	11.03650
F	7.55380	5.54810	11.27740
F	7.66180	7.68330	12.17950
F	6.02430	8.39750	10.73200
F	7.91330	7.35590	9.90930
F	5.89380	6.27020	9.82800
F	5.62790	6.56200	12.11590
P	7.34140	6.93290	2.09960
F	6.58400	8.38980	2.17540
F	8.15770	5.51130	2.08990
F	8.39640	7.55740	1.02260
F	8.35280	7.43980	3.32350
F	6.36660	6.43440	0.92310
F	6.33070	6.35230	3.24200

A.2.2 1R-D-2PF$_6$-M06L

137

1R-D-2PF6-M06L

O	5.83900	12.45040	6.35920
O	8.38000	14.66560	3.01660
O	10.99290	2.06900	9.17710
O	11.13640	2.39280	4.44260
N	10.86820	10.95550	6.50740
H	10.75640	10.68170	5.52830
H	10.06860	10.52490	7.01770
N	12.74070	6.60360	7.10790
H	12.26380	6.54070	6.17420
H	11.98570	6.39940	7.79040
C	5.79040	11.62200	7.51520
H	6.35370	10.69450	7.36860
H	4.73720	11.39320	7.67280
H	6.19230	12.13640	8.39460
C	7.17670	14.98770	2.34410
H	6.52480	15.61640	2.96360
H	6.62530	14.08550	2.05200
H	7.46740	15.53920	1.45050
C	9.94210	1.13250	9.05120
H	9.08160	1.56120	8.51980
H	9.64570	0.86810	10.06640
H	10.26420	0.22670	8.52130
C	11.53630	3.08220	3.27040
H	11.27810	4.14660	3.31680
H	10.98390	2.62620	2.45050
H	12.61630	2.98360	3.09210
C	7.06120	12.80410	5.91210
C	7.06440	13.54860	4.72300
H	6.10900	13.77550	4.26620
C	8.27000	13.95190	4.16480
C	9.48460	13.61040	4.78080
H	10.41540	13.92310	4.31730
C	9.46310	12.88500	5.96310

C	8.25760	12.47500	6.55070
H	8.26380	11.91470	7.48000
C	10.75110	12.45570	6.59690
H	10.80520	12.68920	7.66180
H	11.62270	12.87640	6.08770
C	12.11720	10.34170	7.06470
H	12.06500	10.48500	8.14630
H	12.96850	10.90160	6.66120
C	12.11930	8.87860	6.67510
H	12.22480	8.78350	5.58560
H	11.13660	8.46270	6.93450
C	13.17780	8.00490	7.33660
H	14.17780	8.13420	6.91040
H	13.23000	8.15380	8.42150
C	13.74510	5.50370	7.21900
H	14.21870	5.60370	8.19600
H	14.49110	5.67240	6.43700
C	12.97120	4.22260	7.05900
C	12.45400	3.59550	8.18410
H	12.71050	3.93260	9.18300
C	11.49770	2.58270	8.02290
C	11.08320	2.19500	6.75470
H	10.32350	1.43930	6.59450
C	11.63310	2.82110	5.62740
C	12.58670	3.82770	5.76970
H	12.96740	4.36510	4.90820
O	13.79180	5.61260	10.47120
O	15.70350	7.49910	9.67490
O	16.41800	9.14480	7.44400
O	15.63510	8.23090	4.94740
O	13.68070	6.47780	4.05400
N	11.08870	6.53440	4.69940
N	9.98830	5.89190	7.27390
N	11.27320	6.24430	9.76790
C	15.17410	5.40330	10.70170
H	15.50000	4.80630	9.84370

H	15.34260	4.79880	11.60470
C	15.98220	6.67840	10.78660
H	15.76190	7.22990	11.71490
H	17.05260	6.40740	10.82390
C	16.41490	8.71260	9.78140
H	17.50180	8.53010	9.72720
H	16.21280	9.18990	10.75620
C	16.00780	9.65910	8.68890
H	14.91270	9.81090	8.70430
H	16.47190	10.64300	8.87840
C	16.12200	10.02770	6.39140
H	16.68230	10.97350	6.49340
H	15.04580	10.28630	6.39540
C	16.46360	9.35970	5.08980
H	16.31120	10.07180	4.26010
H	17.52660	9.06520	5.08000
C	15.81880	7.58860	3.70720
H	16.88580	7.36870	3.52790
H	15.47700	8.24040	2.88560
C	15.05080	6.29040	3.74210
H	15.17010	5.73830	2.80030
H	15.44270	5.66020	4.54770
C	12.82670	6.82050	3.03390
C	13.22530	7.09000	1.72590
H	14.27400	7.07210	1.45090
C	12.26760	7.36680	0.74910
H	12.59380	7.57050	-0.26650
C	10.91610	7.37640	1.07240
H	10.15850	7.57410	0.32160
C	10.51650	7.11170	2.37580
H	9.45870	7.11130	2.62180
C	11.45720	6.82610	3.37240
C	9.96850	5.90890	4.84370
H	9.39610	5.56430	3.98000
C	9.36110	5.58260	6.12810
C	8.10840	4.94870	6.07860

H	7.64350	4.74760	5.11610
C	7.48140	4.63090	7.27470
H	6.50410	4.15800	7.27320
C	8.12560	4.93780	8.46430
H	7.67550	4.71230	9.42770
C	9.38260	5.55630	8.41980
C	10.05790	5.84060	9.68130
H	9.44980	5.66730	10.58180
C	11.72570	6.56460	11.05690
C	10.91230	7.22610	11.98280
H	9.93630	7.56710	11.65380
C	11.36270	7.50050	13.26830
H	10.71980	8.03440	13.96080
C	12.63540	7.09630	13.65240
H	12.99260	7.28220	14.66090
C	13.47550	6.46240	12.73810
H	14.46220	6.14090	13.05340
C	13.04260	6.22700	11.43440
P	9.21700	9.71590	9.48350
F	8.55400	8.27250	9.79070
F	9.47840	10.00530	11.04210
F	9.91470	11.16670	9.07090
F	10.69450	9.02340	9.33010
F	8.99450	9.45010	7.83490
F	7.77280	10.43980	9.52840
P	6.96990	5.49780	2.29980
F	5.61750	6.36010	2.11290
F	8.37180	4.64190	2.53540
F	7.74570	6.41480	1.19180
F	7.47340	6.55380	3.48000
F	6.51980	4.44150	1.16580
F	6.26330	4.59160	3.46920

A.2.3 0R-D-2PF$_6$-M06L

```
73
0R-D-2PF6-M06L
  O         5.40420        14.15650         5.39050
  O         7.20230        12.44640         1.34410
  O         9.15690         1.13250         8.23790
  O         8.85350         2.82370         3.80800
  N         9.31390        10.52530         6.18790
  H         9.36310         9.71410         5.55130
  H         8.33460        10.61550         6.46770
  N        10.29440         6.49520         7.46750
  H         9.74610         6.59990         6.60840
  H         9.66020         6.26190         8.25480
  C         5.50570        14.35770         6.78650
  H         5.54770        13.40480         7.32980
  H         4.60760        14.89870         7.08150
  H         6.38940        14.95480         7.04530
  C         6.05890        12.91740         0.65510
  H         5.96180        14.00740         0.73460
  H         5.14140        12.44980         1.03340
  H         6.20120        12.64200        -0.38900
  C         8.38690         0.01650         7.84270
  H         7.39580         0.31730         7.47930
  H         8.27200        -0.60290         8.73170
  H         8.88860        -0.56400         7.05730
  C         9.09220         3.87260         2.88550
  H         8.64600         4.81490         3.22210
  H         8.62900         3.56150         1.94950
  H        10.16460         4.03780         2.72310
  C         6.41600        13.48920         4.78420
  C         6.26680        13.31990         3.40150
  H         5.37570        13.72150         2.93450
  C         7.25270        12.65850         2.67830
  C         8.39230        12.15060         3.32450
  H         9.13370        11.61230         2.74640
  C         8.52680        12.32890         4.69020
```

C	7.54360	12.99860	5.43990
H	7.68770	13.15960	6.50480
C	9.70730	11.76990	5.42140
H	10.08940	12.47380	6.16760
H	10.52240	11.46500	4.76520
C	10.15290	10.23880	7.40160
H	9.95860	11.06020	8.09630
H	11.19050	10.31410	7.07030
C	9.82810	8.87790	8.00890
H	8.86910	8.52440	7.61240
H	9.66760	8.97040	9.08330
C	10.90840	7.81670	7.77140
H	11.54880	8.06200	6.92190
H	11.51080	7.67540	8.67070
C	11.26780	5.36680	7.26030
H	11.77450	5.21910	8.21210
H	11.97750	5.70970	6.50580
C	10.50730	4.15660	6.81310
C	10.17490	3.16930	7.72690
H	10.46430	3.24220	8.77080
C	9.42570	2.06500	7.29140
C	9.00290	1.97610	5.96970
H	8.41920	1.14030	5.60310
C	9.32520	2.99890	5.06780
C	10.08210	4.09450	5.47660
H	10.35260	4.88730	4.78620
P	9.52280	6.41320	11.02350
F	8.81500	4.96890	11.09380
F	8.33640	7.10610	11.85730
F	10.25050	7.87740	10.82170
F	10.40350	6.12870	12.33310
F	10.70880	5.76470	10.05510
F	8.66480	6.72440	9.59530
P	10.65360	8.13750	3.94910
F	9.70440	9.36510	3.42820
F	11.53290	6.95610	4.63970

F	11.74780	8.40800	2.82100
F	11.38680	9.22720	4.96580
F	9.85220	7.07260	3.05370
F	9.50020	7.91590	5.18550

A.2.4 2R-Dp-2PF$_6$-M06L

208

2R_Dp_2PF6

P	7.18400	6.68280	12.04600
F	6.05960	7.87550	11.89320
F	8.32140	5.50790	12.13170
F	8.08940	7.65210	12.98840
F	6.41390	6.08320	13.32560
F	7.96340	7.30060	10.71550
F	6.29980	5.73800	11.03460
P	6.17990	5.97110	2.86630
F	4.78940	6.74660	3.28510
F	7.59150	5.22700	2.50690
F	6.59230	7.24380	1.93140
F	6.94310	6.72070	4.14320
F	5.43760	5.24470	1.63870
F	5.79090	4.75220	3.88300
O	2.60860	11.11480	7.81140
O	3.01100	12.49330	3.28010
O	11.36110	2.45850	9.17750
O	10.93980	2.63740	4.44160
N	7.70190	12.09140	6.47670
H	7.50300	11.34690	5.75480
H	7.48780	11.67370	7.40700
N	12.62580	7.04630	6.96300
H	11.93900	6.96190	6.17640
H	12.09130	6.85330	7.84590
C	3.18200	10.95510	9.09580
H	4.09040	10.33970	9.05780
H	2.43040	10.45060	9.70280
H	3.43080	11.92220	9.55280
C	1.76260	11.88870	3.00790
H	0.95170	12.34980	3.58690
H	1.78050	10.81240	3.22390
H	1.57640	12.04040	1.94450
C	10.37270	1.44780	9.20930

H	9.42690	1.79550	8.77300
H	10.21750	1.20750	10.26090
H	10.69720	0.54610	8.67340
C	11.24540	3.27370	3.21430
H	10.96880	4.33630	3.22290
H	10.65880	2.76000	2.45340
H	12.31470	3.19100	2.97250
C	3.37570	11.70770	6.86190
C	2.78610	11.78540	5.59250
H	1.79220	11.37320	5.46600
C	3.48650	12.37780	4.54840
C	4.77830	12.88230	4.75650
H	5.32630	13.29050	3.91100
C	5.35580	12.77900	6.01370
C	4.65480	12.20970	7.08470
H	5.13830	12.12060	8.05250
C	6.76750	13.23540	6.22580
H	6.87750	13.90530	7.08590
H	7.15930	13.75150	5.34310
C	9.11280	12.53900	6.39950
H	9.21770	13.38330	7.08380
H	9.24930	12.94780	5.39300
C	13.17550	8.42060	7.02870
H	13.88190	8.52860	6.19580
H	13.76470	8.47840	7.95260
C	13.65580	5.96920	6.80440
H	14.35280	6.07730	7.63720
H	14.18640	6.18170	5.87190
C	12.93370	4.65300	6.78610
C	12.59920	4.02920	7.97910
H	12.95070	4.41030	8.93320
C	11.69330	2.95910	7.95860
C	11.15950	2.50400	6.75710
H	10.43580	1.69880	6.71000
C	11.53740	3.12460	5.55950
C	12.43090	4.19140	5.56380

H	12.66460	4.73290	4.65550
O	8.76690	13.20120	9.44200
O	8.48930	15.53050	7.84740
O	8.42200	16.04760	5.14170
O	9.24270	13.94360	3.45040
O	9.06390	11.24840	3.51000
N	6.80080	10.26400	4.45590
N	6.47260	9.50720	7.13200
N	7.05800	11.12170	9.34620
C	9.69300	14.27480	9.45200
H	10.42140	14.02680	8.67260
H	10.23580	14.31980	10.40490
C	9.05620	15.60850	9.13540
H	8.28760	15.87610	9.88000
H	9.83410	16.39160	9.17340
C	8.06940	16.78660	7.36340
H	8.93030	17.47460	7.30330
H	7.32770	17.24520	8.03960
C	7.45720	16.61050	5.99930
H	6.56060	15.96760	6.05380
H	7.12020	17.59440	5.62770
C	7.93840	15.89370	3.82740
H	7.66320	16.86970	3.39050
H	7.02810	15.26650	3.81370
C	9.01220	15.25610	2.99040
H	8.69170	15.23900	1.93410
H	9.93580	15.85710	3.04670
C	10.19820	13.27380	2.66170
H	11.19480	13.74030	2.76090
H	9.91780	13.36070	1.60070
C	10.29580	11.82020	3.11230
H	10.77300	11.21770	2.32370
H	10.91700	11.73850	4.01060
C	8.06650	11.11770	2.59210
C	8.19150	11.38430	1.22960
H	9.14840	11.67790	0.81430

C	7.09700	11.21960	0.38370
H	7.20880	11.43730	-0.67470
C	5.87710	10.77950	0.88410
H	5.01910	10.66690	0.22920
C	5.76560	10.46580	2.23130
H	4.82320	10.10610	2.63550
C	6.85190	10.60870	3.09770
C	6.07940	9.24610	4.77220
H	5.57930	8.63800	4.01420
C	5.94790	8.77000	6.14480
C	5.29410	7.54670	6.36410
H	4.89870	6.99790	5.51630
C	5.22650	7.05320	7.65730
H	4.74810	6.10010	7.86480
C	5.79680	7.78730	8.68760
H	5.78510	7.43750	9.71260
C	6.38870	9.01970	8.37840
C	6.81370	9.86290	9.48950
H	6.82920	9.37100	10.46790
C	7.14990	11.87990	10.52130
C	6.36020	11.60330	11.64420
H	5.69110	10.74730	11.61070
C	6.41150	12.40140	12.77920
H	5.78620	12.16520	13.63400
C	7.25930	13.50090	12.80330
H	7.30790	14.13930	13.68050
C	8.05030	13.80580	11.69760
H	8.70550	14.66830	11.74130
C	8.00120	13.00640	10.55660
O	14.02500	6.41440	9.97450
O	16.01790	8.05640	8.88160
O	16.51600	9.34180	6.40750
O	15.37260	8.23100	4.09250
O	13.09010	6.73230	3.55910
N	10.66260	6.78140	4.69360
N	9.93320	5.95190	7.28190

N	11.37260	6.62360	9.59590
C	15.40420	6.14100	10.14670
H	15.65950	5.47080	9.31830
H	15.58400	5.59480	11.08310
C	16.27540	7.37210	10.08590
H	16.08970	8.04230	10.94170
H	17.33250	7.05690	10.14620
C	16.85340	9.18500	8.75500
H	17.89860	8.87480	8.58640
H	16.83510	9.78510	9.68150
C	16.37610	10.04250	7.61890
H	15.32090	10.32630	7.78580
H	16.96220	10.97930	7.60100
C	16.10550	10.12620	5.31430
H	16.70960	11.04880	5.24220
H	15.05080	10.43660	5.43130
C	16.25190	9.33080	4.04950
H	16.01540	9.98350	3.19100
H	17.29420	8.99100	3.92580
C	15.24160	7.62810	2.82790
H	16.21990	7.29270	2.43920
H	14.84160	8.35900	2.10460
C	14.33620	6.42750	2.95970
H	14.19560	5.94510	1.98170
H	14.79830	5.69470	3.63140
C	12.08600	7.23780	2.77510
C	12.23720	7.65820	1.45470
H	13.20710	7.61670	0.97100
C	11.12910	8.11110	0.73360
H	11.26400	8.42940	-0.29640
C	9.87020	8.13700	1.32240
H	8.99570	8.47300	0.77240
C	9.71690	7.70550	2.63520
H	8.73510	7.70790	3.10040
C	10.81050	7.24700	3.37470
C	9.62660	6.04050	4.89740

H	8.98260	5.72520	4.07060
C	9.20860	5.58480	6.21720
C	8.03560	4.82000	6.31060
H	7.47530	4.58290	5.40950
C	7.59230	4.44320	7.57180
H	6.67410	3.87350	7.68560
C	8.32080	4.83680	8.68640
H	7.98660	4.62540	9.69840
C	9.49540	5.57770	8.49050
C	10.26390	5.97110	9.66420
H	9.83620	5.67040	10.62550
C	11.92080	7.00260	10.83420
C	11.11260	7.46670	11.87540
H	10.04400	7.55800	11.70830
C	11.66090	7.80940	13.10470
H	11.00760	8.16290	13.89610
C	13.02940	7.68160	13.30550
H	13.47160	7.93270	14.26540
C	13.85640	7.22860	12.27760
H	14.91900	7.11610	12.46140
C	13.31130	6.90280	11.03770
C	12.09040	9.46180	6.96280
C	12.43840	10.81140	6.84310
C	11.46370	11.79060	6.70900
C	10.10590	11.45250	6.67260
C	9.75730	10.11310	6.81760
C	10.73510	9.13540	6.97650
H	13.48890	11.09960	6.84460
H	11.75810	12.83410	6.59900
H	8.71290	9.80890	6.79190
H	10.41730	8.10270	7.08930

A.2.5 1R-Dp-2PF$_6$-M06L

```
144
1R_Dp_2PF6
  P        9.81150       7.60240      10.98440
  F        8.31060       7.82930      11.58480
  F       11.28450       7.36930      10.28140
  F       10.26100       9.07510      11.46710
  F       10.31150       6.91550      12.34290
  F        9.30740       8.26060       9.53480
  F        9.33700       6.14290      10.37600
  P        8.84370       6.05240       3.93390
  F        7.21760       6.06100       3.75780
  F       10.46530       6.07260       4.22240
  F        8.86320       7.66020       3.63820
  F        8.64050       6.39590       5.56320
  F        9.08450       5.73680       2.37600
  F        8.78890       4.47220       4.28620
  O        2.59060      10.46380       7.20330
  O        3.13980      12.42580       2.90310
  O        7.61890       1.93340       8.86150
  O       10.06300       1.76390       4.78810
  N        7.43730      12.12140       6.36790
  H        7.17580      11.40240       5.64990
  H        7.28030      11.65550       7.28270
  N       10.55800       6.49700       7.61890
  H        9.97270       6.33720       6.77950
  H        9.94710       6.89760       8.34650
  C        3.12230      10.18440       8.48480
  H        4.11700       9.72480       8.41440
  H        2.43020       9.48460       8.95330
  H        3.19660      11.08930       9.10310
  C        2.02900      11.68630       2.44120
  H        1.10770      11.96170       2.97130
  H        2.19130      10.60580       2.55110
  H        1.92270      11.92630       1.38290
  C        6.88200       0.80890       8.43240
```

H	6.33590	1.01060	7.50120
H	6.16940	0.58900	9.22770
H	7.52880	-0.06440	8.27420
C	11.01740	2.34430	3.91360
H	10.76250	3.38340	3.68230
H	10.98770	1.74720	3.00210
H	12.02870	2.29610	4.34040
C	3.31310	11.29370	6.40650
C	2.82260	11.43640	5.10030
H	1.92590	10.89190	4.82910
C	3.50720	12.24310	4.19840
C	4.68120	12.90490	4.58610
H	5.25090	13.45940	3.84480
C	5.14990	12.75470	5.88250
C	4.46580	11.95970	6.81150
H	4.88180	11.82460	7.80550
C	6.50060	13.28610	6.25610
H	6.52780	13.79420	7.22670
H	6.90480	13.96470	5.50010
C	8.88060	12.47780	6.24260
H	9.07350	13.26020	6.97800
H	8.99900	12.90760	5.24520
C	11.62610	7.50840	7.29100
H	12.16700	7.09040	6.43650
H	12.28460	7.54060	8.15990
C	11.13350	5.19040	8.12900
H	11.19730	5.29710	9.21100
H	12.14570	5.13610	7.71900
C	10.32930	4.00980	7.68820
C	9.31860	3.49260	8.48760
H	9.08890	3.91930	9.45790
C	8.59100	2.38840	8.02330
C	8.86880	1.82280	6.78390
H	8.31780	0.97510	6.39480
C	9.87920	2.37020	5.98410
C	10.62010	3.45830	6.43590

H	11.38370	3.91230	5.81290
O	8.65220	13.45640	9.34030
O	7.90770	15.79780	7.98490
O	6.90300	16.58500	5.46430
O	7.47120	14.76480	3.40620
O	7.87090	11.96960	3.18430
N	6.46900	10.07030	4.46630
N	6.68270	9.41570	7.21550
N	7.04790	11.27320	9.29970
C	9.48770	14.60430	9.29560
H	10.13250	14.43960	8.42620
H	10.13520	14.65580	10.18160
C	8.72610	15.89720	9.12430
H	8.10960	16.12310	10.01050
H	9.45510	16.72130	9.02370
C	7.17650	16.98810	7.78480
H	7.85830	17.82370	7.55230
H	6.62490	17.26040	8.70160
C	6.19720	16.79600	6.66310
H	5.53450	15.93850	6.87890
H	5.55170	17.68960	6.59080
C	6.02410	16.37920	4.38370
H	5.44120	17.29230	4.16730
H	5.29910	15.58130	4.62350
C	6.81900	15.99610	3.16790
H	6.13300	15.90650	2.30810
H	7.55680	16.77860	2.92450
C	8.00530	14.22600	2.22050
H	8.74270	14.91250	1.76770
H	7.19910	14.08540	1.48170
C	8.70240	12.92260	2.53610
H	9.14500	12.49920	1.62460
H	9.51920	13.10490	3.24180
C	6.96240	11.28320	2.42650
C	6.76070	11.48590	1.06250
H	7.35270	12.21130	0.51770

C	5.79950	10.74800	0.37610
H	5.65400	10.92710	-0.68510
C	5.02810	9.80600	1.04440
H	4.25800	9.24900	0.51940
C	5.24750	9.58290	2.39680
H	4.63620	8.86680	2.93910
C	6.22730	10.28700	3.10490
C	6.33060	8.86280	4.89040
H	6.15510	8.03190	4.19770
C	6.42730	8.47740	6.29110
C	6.24110	7.12230	6.60340
H	6.07130	6.41310	5.80030
C	6.36600	6.71200	7.92260
H	6.26880	5.66400	8.19180
C	6.65780	7.66720	8.88280
H	6.82090	7.40170	9.92230
C	6.79720	9.00690	8.48390
C	7.03690	10.00420	9.52170
H	7.19660	9.59740	10.52890
C	7.09430	12.08660	10.44320
C	6.31110	11.80100	11.56560
H	5.64810	10.94100	11.51800
C	6.34910	12.59880	12.70180
H	5.72390	12.35890	13.55590
C	7.19500	13.69870	12.72990
H	7.25240	14.32650	13.61410
C	7.97470	14.01590	11.61990
H	8.63930	14.87040	11.67110
C	7.91480	13.23370	10.46750
C	11.03250	8.84710	6.98450
C	10.98180	9.84090	7.96340
C	10.32330	11.03610	7.70380
C	9.71700	11.25560	6.46530
C	9.80040	10.27260	5.47490
C	10.45510	9.07600	5.73360
H	11.40010	9.65060	8.94770

H	10.23030	11.78510	8.48640
H	9.31780	10.42550	4.51140
H	10.48690	8.30330	4.97310

A.2.6 0R-Dp-2PF$_6$-M06L

```
80

0R_Dp_2PF6

  O        5.85140       15.08870        8.50220

  O        1.32500       14.45010        7.20960

  O       13.33310        0.63400        7.01450

  O       15.48120        4.71570        5.87090

  N        5.43870       10.81460        5.42190

  H        4.87070       10.38390        6.15930

  H        6.28880       11.08830        5.96610

  N       10.29560        5.52400        6.91490

  H       10.91390        6.24590        6.47740

  H       10.07760        4.91350        6.12310

  C        7.21370       14.68380        8.41830

  H        7.31820       13.60490        8.56430

  H        7.72950       15.21380        9.21810

  H        7.65310       14.97370        7.45500

  C        0.92870       15.33400        8.23970

  H        1.34270       16.33950        8.09120

  H        1.23820       14.96730        9.22650

  H       -0.15910       15.38190        8.19680

  C       14.44470       -0.07090        6.49930

  H       14.59670        0.13800        5.43280

  H       14.22110       -1.12930        6.63170

  H       15.36650        0.17620        7.04150

  C       15.43870        6.13490        5.76180

  H       14.57280        6.46650        5.18250

  H       16.35570        6.41880        5.24700

  H       15.42310        6.60520        6.75360

  C        4.98260       14.49280        7.65980

  C        3.63350       14.81230        7.86700

  H        3.39340       15.50270        8.66620

  C        2.65640       14.21820        7.07830

  C        3.01240       13.29880        6.08020

  H        2.22910       12.83230        5.49060

  C        4.35470       13.01050        5.87560
```

C	5.35420	13.61760	6.64140
H	6.39390	13.34500	6.50250
C	4.75020	12.01510	4.83140
H	5.46310	12.42910	4.10970
H	3.88610	11.64350	4.27290
C	5.81540	9.77690	4.38660
H	6.32730	10.32840	3.59200
H	4.87760	9.38520	3.98160
C	9.04310	6.15600	7.45870
H	9.36880	6.78300	8.29620
H	8.43850	5.34330	7.87190
C	11.04470	4.77080	7.98600
H	10.32780	4.08540	8.44740
H	11.31190	5.52800	8.73070
C	12.24090	4.04720	7.45600
C	12.26110	2.65860	7.46280
H	11.43450	2.07500	7.85660
C	13.38580	1.99030	6.95780
C	14.45380	2.70890	6.43550
H	15.32840	2.22580	6.01720
C	14.40850	4.11030	6.42140
C	13.31600	4.78850	6.95780
H	13.26390	5.86970	6.92220
C	8.26220	6.97640	6.48160
C	8.82630	8.11760	5.91170
C	8.04410	8.97480	5.16120
C	6.68200	8.72150	4.98890
C	6.13090	7.54900	5.50230
C	6.92150	6.67790	6.24200
H	9.87340	8.35230	6.06590
H	8.49250	9.87400	4.74680
H	5.07300	7.33660	5.36280
H	6.48030	5.78250	6.67400
P	7.01490	10.53680	8.63190
F	6.52830	9.86800	10.00720
F	7.49310	11.22860	7.14670

F	8.03440	11.54010	9.37910
F	8.18630	9.43230	8.44710
F	5.83280	11.65260	8.69580
F	5.98920	9.57060	7.76010
P	11.77290	7.00400	3.97600
F	10.97210	8.40350	3.83860
F	12.53660	5.59560	4.25420
F	13.18750	7.75640	3.78830
F	11.89150	7.31390	5.66370
F	11.62720	6.68730	2.41340
F	10.34340	6.23800	4.30900

Appendix B

Generalization of the Sorption Process with Multilayers for Non-Self-Interacting Atoms and Molecules

Jose L. Mendoza-Cortes, **2012**

In this section a formulation to generalize the sorption process of any gas in any framework is developed. The only restriction is the topology or connectivity of the framework. The parameters needed are the interaction energies of the guest molecule to the framework. Such parameters will be reported elsewhere based on DFT calculation. In this paper we only present the formal derivation of the statistical mechanics of the process and the case of H_2 sorption in any framework is studied.

B.1 Given a Topology

The following derivation of the sorption process is solely restricted by the topology and it is focused in a H_2 gas. By the topological constraint we mean the connnectivity in the 3D dimensional space of periodic structure.

An example is shown below:

B.2 Determine the Occupancy

The topology is going to determine the number of absorption sites that we are going to have for our system. For our model we use connection that have the same width/distance in every direction this can be applied to any other model. This can be easily seen in the following picture.

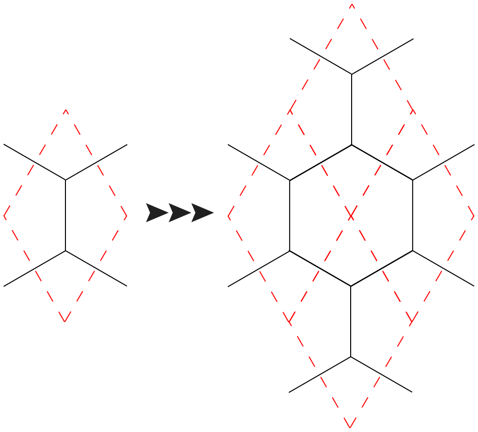

Figure B.1: Topological constrain

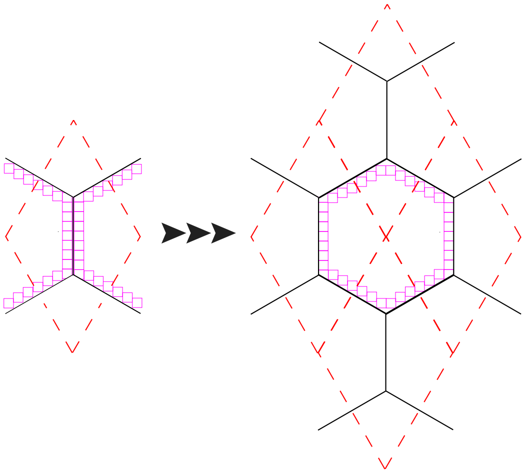

Figure B.2: Determination of number of adsorption sites

B.3 Gibbs Ensemble

In the following subsection we will explain how every step is derived and how we can build the Langmuir theory and the Brunauer-Emmett-Teller (BET) theory with this model. At the end we will see that the restrictions imposed by these two theories are overcomed, which are monolayer for the the Langmuir theory and infinite layers for the BET case.

We make the following definition and assumptions based on the postulates above:

- Equivalent sites B
- The system has N molecules distributed in B sites
- there are not interaction between molecules
- The lattice may be one-, two-,three- periodic

- Let the relation between V and B be $V = B \times \alpha$

B.3.1 Monolayer Theory

Using the the Gibbs ensamble (also known as Grand Canonical distribution) we have

$$\begin{aligned}\Xi(\mu,\tau) &= \sum_{N=0}^{\infty}\sum_{S(N)} \exp[(n\mu - \epsilon_{S(N)})/\tau] \\ &= \sum_{[S(N),N=0]} \exp[(n\mu - \epsilon_{S(N)})/\tau] \qquad \text{(B.1)}\end{aligned}$$

Where,

- $[S(N), N = 0]$ is for all states of the system for all number of partciles
- $\epsilon_{S(N)}$ = each ϵ_S depends on the number of particles. $\epsilon_{S(N)}$ is the energy of the state $S(N)$ of the exact N = particle Hamiltonian.

Now we can calculate the thermal average number of particles by

$$\langle N\rangle = \frac{\sum_{S,N} N\exp[(n\mu - \epsilon_{S(N)})/\tau]}{\Xi} \qquad \text{(B.2)}$$

that combining with

$$\frac{\partial \Xi}{\partial \mu} = \frac{1}{\tau}\sum_{S,N} N\exp[(n\mu - \epsilon_{S(N)})/\tau] \qquad \text{(B.3)}$$

we obtain:

$$\langle N\rangle = \frac{\tau}{\Xi}\frac{\partial \Xi}{\partial \mu} = \tau\frac{\partial \log\Xi}{\partial \mu} \qquad \text{(B.4)}$$

From the definition of $\lambda = \exp\mu/\tau$ we have

$$\frac{\langle N\rangle}{B} = \lambda\frac{\partial \log\Xi}{\partial \lambda} \qquad \text{(B.5)}$$

Now taking into account the assumption from the Langmuir theory as two energy states for each particle as shown in the following figure

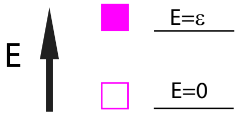

Figure B.3: Assumption from Langmuir theory

Then we can derive the partition function as

$$\Xi = 1 + \lambda \exp\left(\frac{-\epsilon}{\tau}\right) \tag{B.6}$$

Using this result into eq B.5 we have:

$$\begin{aligned} \frac{\langle N \rangle}{B} &= \frac{\lambda \exp(-\epsilon/\tau)}{1 + \lambda \exp(-\epsilon/\tau)} \\ \frac{\overline{N}}{B} &= \frac{1}{\lambda^{-1} \exp(\epsilon/\tau) + 1} \end{aligned} \tag{B.7}$$

Multilayer Theory

In the following sections the multilayer theory generalization is shown and the special case of the BET theory is shown to be an special case as well as the Langmuir theory.

Given that a gas molecule can be absorbed on each site B, with partition function j_1 that can named "first layer". Also that this first molecule can be used as a site for another for a "second layer" molecule and so on. The partition funtion for these other second and beyond molecules is j_∞. If given N total number of molecules and N_1 are in the first layer and N^* are in higher layers (more details can be found elsewhere [161][162]).

Using the grand canonical partition function, we have

$$\begin{aligned} \Xi(B,\mu,T) &= \sum_{N\geq 0} \exp[(N\mu)/k\tau] Q(N,B,T) \\ &= 1 + \sum_{N_1=1}^{B} \frac{B!(j_1 \exp(\mu/(kT)))^{N_1}}{N_1!(B-N_1)!(N_1-1)!} \\ \times & \sum_{N^*=0}^{\infty} \frac{(N_1+N^*-1)!(j_\infty \exp(\mu/(kT)))^{N^*}}{N^*!} \end{aligned} \tag{B.8}$$

And

$$\Xi(B,\mu,T) = \sum_{N_1=0}^{B} \frac{B!(y)^{N_1}}{N_1!(B-N_1)!} = (1+y)^B \tag{B.9}$$

where we have defined,

$$y = \frac{j_1 \exp(\mu/kT)}{1 - j_\infty \exp(\mu/kT)} \tag{B.10}$$

.

Using again

$$\overline{N} = kT\left(\frac{\partial \log \Xi}{\partial \mu}\right)_{T,B} \tag{B.11}$$

and applying it to eqn. B.9 we have

$$\frac{\overline{N}}{B} = \frac{cx}{(1-x+cx)(1-x)} \tag{B.12}$$

given $c = \frac{j_1}{j_\infty}$ and $x = j_\infty \exp(\mu/kT)$. This is also known as the BET adsorption isotherm equation.

B.3.2 Restricted Multilayer Theory

If the adsorption is restricted to n layers,

$$\begin{aligned}\Xi(B,\mu,T) = &\sum_{N_1=0}^{B}\sum_{N_2=0}^{N_1}\sum_{N_3=0}^{N_2}\cdots\sum_{N_n=0}^{N_{n-1}}\frac{B!}{(B-N_1)!N_1!}\\ &\times\frac{N_1!}{(N_1-N_2)!N_2!}\\ &\times\frac{N_{n-1}!(cx)^{N_1}x^{N_2+\ldots+N_n}}{(N_{n-1}-N_n)!N_n!}\end{aligned} \tag{B.13}$$

Summing in turn over N_n, N_{n-1}, …, N_1 we find

$$\begin{aligned}\Xi &= [1+cx(1+x+x^2+\ldots+x^{n-1})]^B\\ &= \left[1+cx\left(\frac{1-x^n}{1-x}\right)\right]\end{aligned} \tag{B.14}$$

Using this into eqn. B.11 we find the BET equation for restricted adsorption

$$\frac{\overline{N}}{B} = \frac{cx[1-(n+1)x^n+nx^{n+1}]}{(1-x)(1-x+cx-cx^{n+1})} \tag{B.15}$$

This equation is more general since

$$\frac{\overline{N}}{B} \overset{n=\infty}{\rightarrow} \frac{cx}{(1-x+cx)(1-x)} \tag{B.16}$$

the BET equation, and

$$\frac{\overline{N}}{B} \overset{n=1}{\rightarrow} \frac{j_1 \exp(\mu/kT)}{1 + j_1 \exp(\mu/kT} \tag{B.17}$$

the Langmuir equation.

B.4 Hydrogen Molecule Case

For the hydrogen gas we assume ideal behaviour, therefore

$$\lambda = \frac{n}{n_q} = \frac{p}{\tau n_q} = \frac{p}{k_B T n_q} \tag{B.18}$$

and

$$n_q = \left(\frac{M\tau}{2\pi\hbar^2}\right)^{3/2} = \left(\frac{M k_B T}{2\pi\hbar^2}\right)^{3/2} \tag{B.19}$$

B.4.1 Monolayer Theory in H_2

If we apply these assumptions to eqn. B.7 we get the Langmuir equation for H_2

$$\begin{aligned} \frac{\langle N \rangle}{B} &= \frac{1}{(n_q\tau/p)\exp(\epsilon/\tau) + 1} \\ \frac{\overline{N}}{B} &= \frac{p}{(n_q\tau)\exp(\epsilon/\tau) + p} \\ &= \frac{p/p_0}{(n_q\tau)\exp(\epsilon/\tau)/p_0 + p/p_0} \end{aligned} \tag{B.20}$$

where $p_0 = 1$ bar. The results are plotted in fig. B.4.

A more complete plot can be seen in fig. B.5 It can bee seen that for $\Delta H = 20$ KJ/mol the delivery amount has the largest value.

These results can be compared to those published by Bhatia and Myers [58], they reached a close result but there is an underestimation of the entrophy, The result obtained by them can be seen in the fig. B.6.

B.4.2 Multilayer Theory in H_2

In order to obtain the j_1 and j_∞ the procedure illustrated in fig. B.7 was used.

In the following sections no interaction between H_2 molecules are considered.

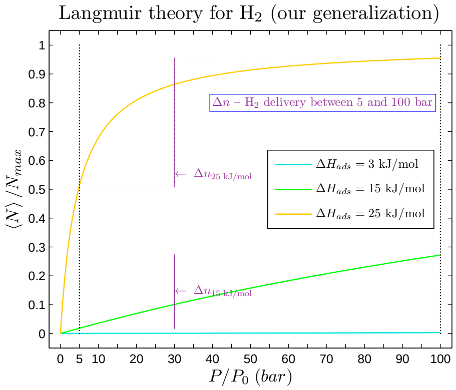

Figure B.4: Isotherms of H_2 uptake using our generalization

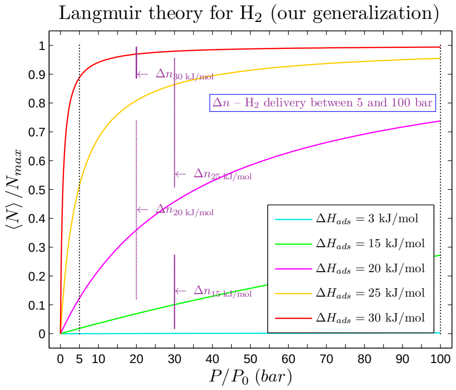

Figure B.5: Isotherms of H_2 uptake using our generalization

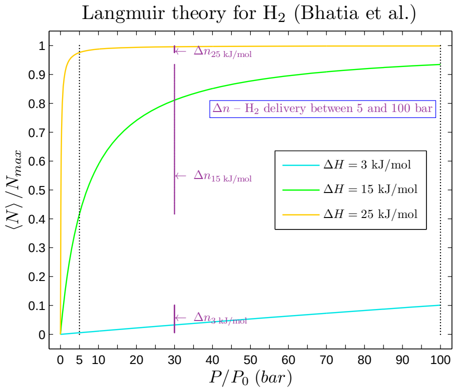

Figure B.6: Isotherm of H_2 uptake using the theory by Bhatia and Myers

$$j_1 \cong e^{-\epsilon_1/kT} \cong e^{-\Delta H_{ads}/kT} \tag{B.21}$$

$$j_2 \cong e^{-\epsilon_\infty/kT} \cong e^{-\Delta H^*_{ads}/kT} \tag{B.22}$$

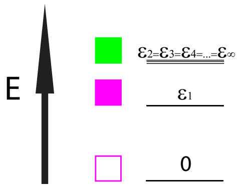

Figure B.7: Assumption for the multilayer theory

$$\begin{aligned} \Delta H_{ads}/kT &= \text{Surface} \cdots \text{H}_2 \qquad (B.23) \\ \Delta H^{*}_{ads}/kT &= \text{H}_2 \cdots \text{H}_2 \qquad (B.24) \end{aligned}$$

This can also be observed in fig. B.8

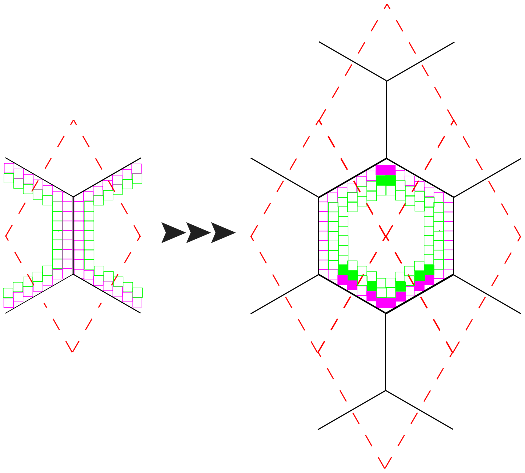

Figure B.8: Assumption for the multilayer theory

We performed ab initio quantum mechanics to investigate the interaction of the H_2 molecules with different building blocks for potential COFs. We decided to use density functional theory (DFT) at the M06 level which has been shown to predict accurately interaction energies for non covalent interactions including that of H_2. We used the algorithm as implemented in Jaguar 7.0 using the effective core potentials (ECP) for heavy atoms and 6-31G basis set for the outermost core orbitals when the atoms are not described by ECP. This is also known as LACVP^{**++}. Some of the models are shown in fig. B.9.

Thefore using this interaction energy into Eq B.15 we can, in principle, calculate the sorption isotherm of any framework composed given the ligand. This will be useful to know a priori if a lot of resources are to be invested in synthesizing certain porous material.

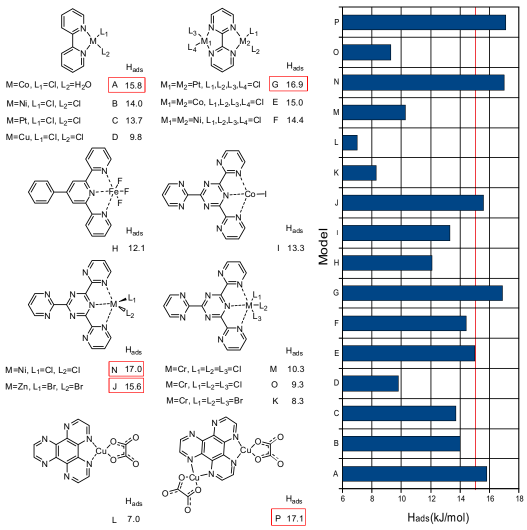

Figure B.9: Models studied with DFT/MO6

B.5 Supplementary Information

B.5.1 NIST Data for H_2

NIST have reported the experimental entalphy and entrophy for H_2 with respect to standard conditions (298 K, 1 bar) [163].

The data is reported as a empirical formula:

$$\Delta H = At + \frac{Bt^2}{2} + \frac{Ct^3}{3} + \frac{Dt^4}{4} - \frac{E}{t} + F - H \tag{B.25}$$

in KJ/mol.

and

$$S = A\log(t) + Bt + \frac{Ct^2}{2} + \frac{Dt^3}{3} - \frac{E}{2t^2} + G \tag{B.26}$$

Given:

A = 33.066178

B = -11.363417

C = 11.432816

D = -2.772874

E = -0.158558

F = -9.980797

G = 172.707974

H = 0.000000

and t = Temperature(K)/1000.

The results for 298-1000 K are shown in fig. B.10 and fig. B.11.

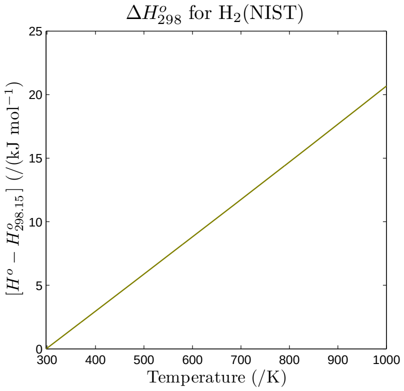

Figure B.10: Experimental data for ΔH of H_2

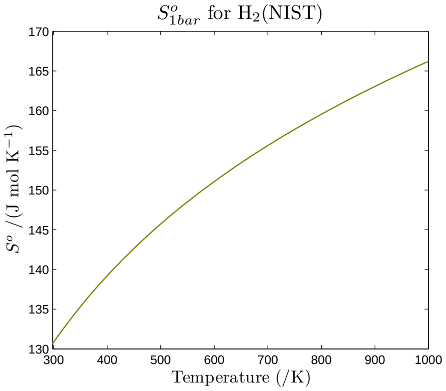

Figure B.11: Experimental data for $S^\circ_{1\ bar}$ of H_2

Bibliography

[1] F. Jensen, *Introduction to Computational chemistry.* John Wiley & Sons, 2007.

[2] G. J. Kubas, "Fundamentals of h(2) binding and reactivity on transition metals underlying hydrogenase function and h(2) production and storage," *Chemical Reviews*, vol. 107, no. 10, pp. 4152–4205, 2007.

[3] C. J. Cramer, *Essentials of Computational chemistry, Theories and Models.* John Wiley & Sons, 2004.

[4] C. Kittel and H. Kroemer, *Thermal Physics.* W. H. Freeman and Company, 2002.

[5] T. L. Hill, *An Introduction to Statistical Thermodynamics.* Dover Pub., 1986.

[6] P. Vairaprakash, H. Ueki, K. Tashiro, and O. M. Yaghi, "Synthesis of metal-organic complex arrays," *Journal of the American Chemical Society*, vol. 133, no. 4, pp. 759–761, 2011.

[7] Y. Zhao and D. G. Truhlar, "The m06 suite of density functionals for main group thermochemistry, thermochemical kinetics, noncovalent interactions, excited states, and transition elements: two new functionals and systematic testing of four m06-class functionals and 12 other functionals," *Theoretical Chemistry Accounts*, vol. 120, no. 1-3, pp. 215–241, 2008.

[8] A. D. Becke, "Density-functional thermochemistry .3. the role of exact exchange," *Journal of Chemical Physics*, vol. 98, no. 7, pp. 5648–5652, 1993.

[9] *Jaguar, version 7.6, Schrdinger, LLC, New York, NY, 2011.*

[10] P. J. Hay and W. R. Wadt, "Ab initio effective core potentials for molecular calculations - potentials for k to au including the outermost core orbitals," *Journal of Chemical Physics*, vol. 82, no. 1, pp. 299–310, 1985.

[11] A. K. Rappe, C. J. Casewit, K. S. Colwell, W. A. Goddard, and W. M. Skiff, "Uff, a full periodic-table force-field for molecular mechanics and molecular-dynamics simulations," *Journal of the American Chemical Society*, vol. 114, no. 25, pp. 10024–10035, 1992.

[12] A. K. Rappe and W. A. Goddard, "Charge equilibration for molecular-dynamics simulations," *Journal of Physical Chemistry*, vol. 95, no. 8, pp. 3358–3363, 1991.

[13] J. Emsley, "Very strong hydrogen-bonding," *Chemical Society Reviews*, vol. 9, no. 1, pp. 91–124, 1980.

[14] G. A. Jeffrey and W. Saenger, *Hydrogen Bonding in Biological Structures.* Springer-Verlag, 1991.

[15] M. O. Sinnokrot, E. F. Valeev, and C. D. Sherrill, "Estimates of the ab initio limit for pi-pi interactions: The benzene dimer," *Journal of the American Chemical Society*, vol. 124, no. 36, pp. 10887–10893, 2002.

[16] G. A. Jeffrey, *An introduction to hydrogen bonding.* Oxford University Press, 1997.

[17] R. L. Lieberman and A. C. Rosenzweig, "Crystal structure of a membrane-bound metalloenzyme that catalyses the biological oxidation of methane," *Nature*, vol. 434, no. 7030, pp. 177–182, 2005.

[18] R. Balasubramanian, S. M. Smith, S. Rawat, L. A. Yatsunyk, T. L. Stemmler, and A. C. Rosenzweig, "Oxidation of methane by a biological dicopper centre," *Nature*, vol. 465, no. 7294, pp. 115–U131, 2010.

[19] J. Fritsch, P. Scheerer, S. Frielingsdorf, S. Kroschinsky, B. Friedrich, O. Lenz, and C. M. T. Spahn, "The crystal structure of an oxygen-tolerant hydrogenase uncovers a novel iron-sulphur centre," *Nature*, vol. 479, no. 7372, pp. 249–U134, 2011.

[20] Y. Umena, K. Kawakami, J. R. Shen, and N. Kamiya, "Crystal structure of oxygen-evolving photosystem ii at a resolution of 1.9 angstrom," *Nature*, vol. 473, no. 7345, pp. 55–U65, 2011.

[21] J. P. Gong, Y. Katsuyama, T. Kurokawa, and Y. Osada, "Double-network hydrogels with extremely high mechanical strength," *Advanced Materials*, vol. 15, no. 14, pp. 1155–1158, 2003.

[22] A. Jaramillo-Botero, M. Blanco, Y. Y. Li, G. McGuinness, and W. A. Goddard, "First-principles based approaches to nano-mechanical and biomimetic characterization of polymer-based hydrogel networks for cartilage scaffold-supported therapies," *Journal of Computational and Theoretical Nanoscience*, vol. 7, no. 7, pp. 1238–1256, 2010.

[23] R. Auhl, R. Everaers, G. S. Grest, K. Kremer, and S. J. Plimpton, "Equilibration of long chain polymer melts in computer simulations," *The Journal of chemical physics*, vol. 119, no. 24, p. 12718, 2003.

[24] E. R. Duering, K. Kremer, and G. S. Grest, "Relaxation of randomly cross-linked polymer melts," *Physical Review Letters*, vol. 67, no. 25, pp. 3531–3534, 1991.

[25] S. L. Mayo, B. D. Olafson, and G. W. A., "Dreiding: a generic force field for molecular simulations," *Journal of Physical Chemistry*, vol. 94, no. 26, pp. 8897–8909, 1990.

[26] K. Kremer and G. S. Grest, "Dynamics of entangled linear polymer melts: a moleculardynamics simulation," *Journal of Chemical Physics*, vol. 92, no. 8, pp. 5057–5087, 1990.

[27] H. Eyring, "The activated complex in chemical reactions," *Journal of Chemical Physics*, vol. 3, no. 2, pp. 107–115, 1935.

[28] D. J. Tannor, B. Marten, R. Murphy, R. A. Friesner, D. Sitkoff, A. Nicholls, M. Ringnalda, W. A. Goddard, and B. Honig, "Accurate first principles calculation of molecular charge-distributions and solvation energies from ab- initio quantum-mechanics and continuum dielectric theory," *Journal of the American Chemical Society*, vol. 116, no. 26, pp. 11875–11882, 1994.

[29] B. Marten, K. Kim, C. Cortis, R. A. Friesner, R. B. Murphy, M. N. Ringnalda, D. Sitkoff, and B. Honig, "New model for calculation of solvation free energies: Correction of self-consistent reaction field continuum dielectric theory for short-range hydrogen-bonding effects," *Journal of Physical Chemistry*, vol. 100, no. 28, pp. 11775–11788, 1996.

[30] L. Fang, M. A. Olson, D. Benitez, E. Tkatchouk, W. A. Goddard, and J. F. Stoddart, "Mechanically bonded macromolecules," *Chemical Society Reviews*, vol. 39, no. 1, pp. 17–29, 2010.

[31] F. Arico, J. D. Badjic, S. J. Cantrill, A. H. Flood, K. C. F. Leung, Y. Liu, and J. F. Stoddart, *Templated synthesis of interlocked molecules*, vol. 249 of *Topics in Current Chemistry*, pp. 203–259. Berlin: Springer-Verlag Berlin, 2005.

[32] M. Horn, J. Ihringer, P. T. Glink, and J. F. Stoddart, "Kinetic versus thermodynamic control during the formation of 2 rotaxanes by a dynamic template-directed clipping process," *Chemistry-a European Journal*, vol. 9, no. 17, pp. 4046–4054, 2003.

[33] P. A. Brady and J. K. M. Sanders, "Selection approaches to catalytic systems," *Chemical Society Reviews*, vol. 26, no. 5, pp. 327–336, 1997.

[34] P. T. Corbett, J. Leclaire, L. Vial, K. R. West, J. L. Wietor, J. K. M. Sanders, and S. Otto, "Dynamic combinatorial chemistry," *Chemical Reviews*, vol. 106, no. 9, pp. 3652–3711, 2006.

[35] C. D. Meyer, C. S. Joiner, and J. F. Stoddart, "Template-directed synthesis employing reversible imine bond formation," *Chemical Society Reviews*, vol. 36, no. 11, pp. 1705–1723, 2007.

[36] M. E. Belowich, C. Valente, R. A. Smaldone, D. C. Friedman, J. Thiel, L. Cronin, and J. F. Stoddart, "Positive cooperativity in the template-directed synthesis of monodisperse macromolecules," *Journal of the American Chemical Society*, vol. 134, no. 11, pp. 5243–61, 2012.

[37] T. Clark, J. Chandrasekhar, G. W. Spitznagel, and P. V. Schleyer, "Efficient diffuse function-augmented basis-sets for anion calculations .3. the 3-21+g basis set for 1st-row elements, li-f," *Journal of Computational Chemistry*, vol. 4, no. 3, pp. 294–301, 1983.

[38] M. J. Frisch, J. A. Pople, and J. S. Binkley, "Self-consistent molecular-orbital methods .25. supplementary functions for gaussian-basis sets," *Journal of Chemical Physics*, vol. 80, no. 7, pp. 3265–3269, 1984.

[39] D. Benitez, E. Tkatchouk, I. Yoon, J. F. Stoddart, and W. A. Goddard, "Experimentally-based recommendations of density functionals for predicting properties in mechanically interlocked molecules," *Journal of the American Chemical Society*, vol. 130, no. 45, pp. 14928–14929, 2008.

[40] W. L. Jorgensen, D. S. Maxwell, and J. TiradoRives, "Development and testing of the opls all-atom force field on conformational energetics and properties of organic liquids," *Journal of the American Chemical Society*, vol. 118, no. 45, pp. 11225–11236, 1996.

[41] Y. Umena, K. Kawakami, J. R. Shen, and N. Kamiya, "Crystal structure of oxygen-evolving photosystem ii at a resolution of 1.9 angstrom," *Nature*, vol. 473, no. 7345, pp. 55–U65, 2011.

[42] J. P. McEvoy and G. W. Brudvig, "Water-splitting chemistry of photosystem ii," *Chemical Reviews*, vol. 106, no. 11, pp. 4455–4483, 2006.

[43] J. P. McEvoy and G. W. Brudvig, "Structure-based mechanism of photosynthetic water oxidation," *Physical Chemistry Chemical Physics*, vol. 6, no. 20, pp. 4754–4763, 2004.

[44] M. Haumann, P. Liebisch, C. Muller, M. Barra, M. Grabolle, and H. Dau, "Photosynthetic o-2 formation tracked by time-resolved x-ray experiments," *Science*, vol. 310, no. 5750, pp. 1019–1021, 2005.

[45] J. Clausen and W. Junge, "Detection of an intermediate of photosynthetic water oxidation," *Nature*, vol. 430, no. 6998, pp. 480–483, 2004.

[46] W. Junge and J. Clausen, "Photosynthetic oxygen production," *Science*, vol. 312, no. 5779, pp. 1470–1470, 2006.

[47] A. D. Becke, "Density-functional thermochemistry .3. the role of exact exchange," *Journal of Chemical Physics*, vol. 98, no. 7, pp. 5648–5652, 1993.

[48] C. T. Lee, W. T. Yang, and R. G. Parr, "Development of the colle-salvetti correlation-energy formula into a functional of the electron-density," *Physical Review B*, vol. 37, no. 2, pp. 785–789, 1988.

[49] J. L. Mendoza-Cortes, S. S. Han, H. Furukawa, O. M. Yaghi, and W. A. Goddard, "Adsorption mechanism and uptake of methane in covalent organic frameworks: Theory and experiment," *Journal of Physical Chemistry A*, vol. 114, no. 40, pp. 10824–10833, 2010.

[50] J. L. Mendoza-Cortes, T. A. Pascal, and W. A. Goddard, "Design of covalent organic frameworks for methane storage," *Journal of Physical Chemistry A*, vol. 115, no. 47, pp. 13852–13857, 2011.

[51] J. Sun, T. D. Jarvi, L. F. Conopask, S. Satyapal, M. J. Rood, and M. Rostam-Abadi, "Direct measurements of volumetric gas storage capacity and some new insight into adsorbed natural gas storage," *Energy & Fuels*, vol. 15, no. 5, pp. 1241–1246, 2001.

[52] A. Celzard and V. Fierro, "Preparing a suitable material designed for methane storage: A comprehensive report," *Energy & Fuels*, vol. 19, no. 2, pp. 573–583, 2005.

[53] V. C. Menon and S. Komarneni, "Porous adsorbents for vehicular natural gas storage: A review," *Journal of Porous Materials*, vol. 5, no. 1, pp. 43–58, 1998.

[54] R. F. Cracknell, P. Gordon, and K. E. Gubbins, "Influence of pore geometry on the design of microporous materials for methane storage," *Journal of Physical Chemistry*, vol. 97, no. 2, pp. 494–499, 1993.

[55] J. M. Fox, "The different catalytic routes for methane valorization - an assessment of processes for liquid fuels," *Catalysis Reviews-Science and Engineering*, vol. 35, no. 2, pp. 169–212, 1993.

[56] D. A. Hickman and L. D. Schmidt, "Production of syngas by direct catalytic-oxidation of methane," *Science*, vol. 259, no. 5093, pp. 343–346, 1993.

[57] R. A. Periana, D. J. Taube, S. Gamble, H. Taube, T. Satoh, and H. Fujii, "Platinum catalysts for the high-yield oxidation of methane to a methanol derivative," *Science*, vol. 280, no. 5363, pp. 560–564, 1998.

[58] S. K. Bhatia and A. L. Myers, "Optimum conditions for adsorptive storage," *Langmuir*, vol. 22, no. 4, pp. 1688–1700, 2006.

[59] A. P. Cote, A. I. Benin, N. W. Ockwig, M. O'Keeffe, A. J. Matzger, and O. M. Yaghi, "Porous, crystalline, covalent organic frameworks," *Science*, vol. 310, no. 5751, pp. 1166–1170, 2005.

[60] A. P. Cote, H. M. El-Kaderi, H. Furukawa, J. R. Hunt, and O. M. Yaghi, "Reticular synthesis of microporous and mesoporous 2d covalent organic frameworks," *Journal of the American Chemical Society*, vol. 129, no. 43, pp. 12914–12915, 2007.

[61] H. M. El-Kaderi, J. R. Hunt, J. L. Mendoza-Cortes, A. P. Cote, R. E. Taylor, M. O'Keeffe, and O. M. Yaghi, "Designed synthesis of 3d covalent organic frameworks," *Science*, vol. 316, no. 5822, pp. 268–272, 2007.

[62] R. W. Tilford, W. R. Gemmill, H. C. zur Loye, and J. J. Lavigne, "Facile synthesis of a highly crystalline, covalently linked porous boronate network," *Chemistry of Materials*, vol. 18, no. 22, pp. 5296–5301, 2006.

[63] G. Garberoglio, A. I. Skoulidas, and J. K. Johnson, "Adsorption of gases in metal organic materials: Comparison of simulations and experiments," *Journal of Physical Chemistry B*, vol. 109, no. 27, pp. 13094–13103, 2005.

[64] G. Garberoglio and R. Vallauri, "Adsorption and diffusion of hydrogen and methane in 2d covalent organic frameworks," *Microporous and Mesoporous Materials*, vol. 116, no. 1-3, pp. 540–547, 2008.

[65] G. Garberoglio, "Computer simulation of the adsorption of light gases in covalent organic frameworks," *Langmuir*, vol. 23, no. 24, pp. 12154–12158, 2007.

[66] T. Duren, L. Sarkisov, O. M. Yaghi, and R. Q. Snurr, "Design of new materials for methane storage," *Langmuir*, vol. 20, no. 7, pp. 2683–2689, 2004.

[67] Y. H. Jhon, M. Cho, H. R. Jeon, I. Park, R. Chang, J. L. C. Rowsell, and J. Kim, "Simulations of methane adsorption and diffusion within alkoxy-functionalized irmofs exhibiting severely disordered crystal structures," *Journal of Physical Chemistry C*, vol. 111, no. 44, pp. 16618–16625, 2007.

[68] Q. Y. Yang and C. L. Zhong, "Molecular simulation of carbon dioxide/methane/hydrogen mixture adsorption in metal-organic frameworks," *Journal of Physical Chemistry B*, vol. 110, no. 36, pp. 17776–17783, 2006.

[69] A. Tkatchenko and O. A. von Lilienfeld, "Popular kohn-sham density functionals strongly overestimate many-body interactions in van der waals systems," *Physical Review B*, vol. 78, no. 4, p. 6, 2008.

[70] M. P. Waller, A. Robertazzi, J. A. Platts, D. E. Hibbs, and P. A. Williams, "Hybrid density functional theory for pi-stacking interactions: Application to benzenes, pyridines, and dna bases," *Journal of Computational Chemistry*, vol. 27, no. 4, pp. 491–504, 2006.

[71] Y. S. Bae and C. H. Lee, "Sorption kinetics of eight gases on a carbon molecular sieve at elevated pressure," *Carbon*, vol. 43, no. 1, pp. 95–107, 2005.

[72] R. Ahlrichs, M. Bar, M. Haser, H. Horn, and C. Kolmel, "Electronic-structure calculations on workstation computers - the program system turbomole," *Chemical Physics Letters*, vol. 162, no. 3, pp. 165–169, 1989.

[73] F. Weigend and M. Haser, "Ri-mp2: first derivatives and global consistency," *Theoretical Chemistry Accounts*, vol. 97, no. 1-4, pp. 331–340, 1997.

[74] F. Weigend, M. Haser, H. Patzelt, and R. Ahlrichs, "Ri-mp2: optimized auxiliary basis sets and demonstration of efficiency," *Chemical Physics Letters*, vol. 294, no. 1-3, pp. 143–152, 1998.

[75] C. Hattig, "Optimization of auxiliary basis sets for ri-mp2 and ri-cc2 calculations: Core-valence and quintuple-zeta basis sets for h to ar and qzvpp basis sets for li to kr," *Physical Chemistry Chemical Physics*, vol. 7, no. 1, pp. 59–66, 2005.

[76] S. Simon, M. Duran, and J. J. Dannenberg, "How does basis set superposition error change the potential surfaces for hydrogen bonded dimers?," *Journal of Chemical Physics*, vol. 105, no. 24, pp. 11024–11031, 1996.

[77] A. Pianwanit, C. Kritayakornupong, A. Vongachariya, N. Selphusit, T. Ploymeerusmee, T. Remsungnen, D. Nuntasri, S. Fritzsche, and S. Hannongbua, "The optimal binding sites of ch4 and co2 molecules on the metal-organic framework mof-5: Oniom calculations," *Chemical Physics*, vol. 349, no. 1-3, pp. 77–82, 2008.

[78] D. J. Adams, "Chemical potential of hard-sphere fluids by monte-carlo methods," *Molecular Physics*, vol. 28, no. 5, pp. 1241–1252, 1974.

[79] J. L. Soto and A. L. Myers, "Monte-carlo studies of adsorption in molecular-sieves," *Molecular Physics*, vol. 42, no. 4, pp. 971–983, 1981.

[80] O. Delgado-Friedrichs, M. O'Keeffe, and O. M. Yaghi, "Three-periodic nets and tilings: edge-transitive binodal structures," *Acta Crystallographica Section A*, vol. 62, pp. 350–355, 2006.

[81] R. Schmid and M. Tafipolsky, "An accurate force field model for the strain energy analysis of the covalent organic framework cof-102," *Journal of the American Chemical Society*, vol. 130, no. 38, pp. 12600–12601, 2008.

[82] O. M. Yaghi, M. O'Keeffe, N. W. Ockwig, H. K. Chae, M. Eddaoudi, and J. Kim, "Reticular synthesis and the design of new materials," *Nature*, vol. 423, no. 6941, pp. 705–714, 2003.

[83] H. Furukawa and O. M. Yaghi, "Storage of hydrogen, methane, and carbon dioxide in highly porous covalent organic frameworks for clean energy applications," *Journal of the American Chemical Society*, vol. 131, no. 25, pp. 8875–8883, 2009.

[84] A. P. Nelson, O. K. Farha, K. L. Mulfort, and J. T. Hupp, "Supercritical processing as a route to high internal surface areas and permanent microporosity in metal-organic framework materials," *Journal of the American Chemical Society*, vol. 131, no. 2, pp. 458–460, 2009.

[85] H. Furukawa, M. A. Miller, and O. M. Yaghi, "Independent verification of the saturation hydrogen uptake in mof-177 and establishment of a benchmark for hydrogen adsorption in metal-organic frameworks," *Journal of Materials Chemistry*, vol. 17, no. 30, pp. 3197–3204, 2007.

[86] H. K. Chae, D. Y. Siberio-Perez, J. Kim, Y. Go, M. Eddaoudi, A. J. Matzger, M. O'Keeffe, and O. M. Yaghi, "A route to high surface area, porosity and inclusion of large molecules in crystals," *Nature*, vol. 427, no. 6974, pp. 523–527, 2004.

[87] S. S. Han, W. Q. Deng, and W. A. Goddard, "Improved designs of metal-organic frameworks for hydrogen storage," *Angewandte Chemie-International Edition*, vol. 46, no. 33, pp. 6289–6292, 2007.

[88] J. H. Lan, D. P. Cao, and W. C. Wang, "High uptakes of methane in li-doped 3d covalent organic frameworks," *Langmuir*, vol. 26, no. 1, pp. 220–226, 2010.

[89] J. L. C. Rowsell, E. C. Spencer, J. Eckert, J. A. K. Howard, and O. M. Yaghi, "Gas adsorption sites in a large-pore metal-organic framework," *Science*, vol. 309, no. 5739, pp. 1350–1354, 2005.

[90] Z. A. Kaszkur, R. H. Jones, D. Waller, C. R. A. Catlow, and J. M. Thomas, "Combined rietveld molecular-dynamics powder diffraction approach to the location of molecules in porous solids - application to 1,4-dibromobutane in zeolite-y," *Journal of Physical Chemistry*, vol. 97, no. 2, pp. 426–431, 1993.

[91] P. L. Llewellyn and G. Maurin, "Gas adsorption microcalorimetry and modelling to characterise zeolites and related materials," *Comptes Rendus Chimie*, vol. 8, no. 3-4, pp. 283–302, 2005.

[92] Z. M. Rong, A. P. Terzyk, P. A. Gauden, and P. Vadgama, "Effective diffusion coefficient determination within cylindrical granules of adsorbents using a direct simulation method," *Journal of Colloid and Interface Science*, vol. 313, no. 2, pp. 449–453, 2007.

[93] S. Biloe, V. Goetz, and S. Mauran, “Dynamic discharge and performance of a new adsorbent for natural gas storage,” *Aiche Journal*, vol. 47, no. 12, pp. 2819–2830, 2001.

[94] D. Lozano-Castello, J. Alcaniz-Monge, M. A. de la Casa-Lillo, D. Cazorla-Amoros, and A. Linares-Solano, “Advances in the study of methane storage in porous carbonaceous materials,” *Fuel*, vol. 81, no. 14, pp. 1777–1803, 2002.

[95] T. Burchell, “Low pressure storage of natural gas for vehicular applications,” *SAE Tech. Pap.*, vol. 01, p. 2205, 2000.

[96] S. S. Han, H. Furukawa, O. M. Yaghi, and W. A. Goddard, “Covalent organic frameworks as exceptional hydrogen storage materials,” *Journal of the American Chemical Society*, vol. 130, no. 35, pp. 11580–11581, 2008.

[97] S. S. Kaye, A. Dailly, O. M. Yaghi, and J. R. Long, “Impact of preparation and handling on the hydrogen storage properties of zn4o(1,4-benzenedicarboxylate)(3) (mof-5),” *Journal of the American Chemical Society*, vol. 129, no. 46, pp. 14176–14177, 2007.

[98] A. R. Millward and O. M. Yaghi, “Metal-organic frameworks with exceptionally high capacity for storage of carbon dioxide at room temperature,” *Journal of the American Chemical Society*, vol. 127, no. 51, pp. 17998–17999, 2005. ISI Document Delivery No.: 997PK Times Cited: 443 Cited Reference Count: 22 Millward, AR Yaghi, OM Amer chemical soc Washington.

[99] M. Eddaoudi, J. Kim, N. Rosi, D. Vodak, J. Wachter, M. O’Keeffe, and O. M. Yaghi, “Systematic design of pore size and functionality in isoreticular mofs and their application in methane storage,” *Science*, vol. 295, no. 5554, pp. 469–472, 2002.

[100] J. R. Hunt, C. J. Doonan, J. D. LeVangie, A. P. Cote, and O. M. Yaghi, “Reticular synthesis of covalent organic borosilicate frameworks,” *Journal of the American Chemical Society*, vol. 130, no. 36, pp. 11872–11873, 2008.

[101] H. Furukawa, N. Ko, Y. B. Go, N. Aratani, S. B. Choi, E. Choi, A. O. Yazaydin, R. Q. Snurr, M. O’Keeffe, J. Kim, and O. M. Yaghi, “Ultrahigh porosity in metal-organic frameworks,” *Science*, vol. 329, no. 5990, pp. 424–428, 2010.

[102] J. Lelieveld, P. J. Crutzen, and F. J. Dentener, “Changing concentration, lifetime and climate forcing of atmospheric methane,” *Tellus Series B-Chemical and Physical Meteorology*, vol. 50, no. 2, pp. 128–150, 1998.

[103] S. Plimpton, “Fast parallel algorithms for short-range molecular-dynamics,” *Journal of Computational Physics*, vol. 117, no. 1, pp. 1–19, 1995.

[104] S. J. Plimpton, R. Pollock, and M. Stevens, "Particle-mesh ewald and rrespa for parallel molecular dynamics simulations," in *Proc of the Eighth SIAM Conference on Parallel Processing for Scientific Computing*.

[105] W. Shinoda, M. Shiga, and M. Mikami, "Rapid estimation of elastic constants by molecular dynamics simulation under constant stress," *Physical Review B*, vol. 69, no. 13, pp. 1341031–1341038, 2004.

[106] G. J. Martyna, D. J. Tobias, and M. L. Klein, "Constant-pressure molecular-dynamics algorithms," *Journal of Chemical Physics*, vol. 101, no. 5, pp. 4177–4189, 1994.

[107] M. Parrinello and A. Rahman, "Polymorphic transitions in single-crystals - a new molecular-dynamics method," *Journal of Applied Physics*, vol. 52, no. 12, pp. 7182–7190, 1981.

[108] M. E. Tuckerman, J. Alejandre, R. Lopez-Rendon, A. L. Jochim, and G. J. Martyna, "A liouville-operator derived. measure-preserving integrator for molecular dynamics simulations in the isothermal-isobaric ensemble," *Journal of Physics a-Mathematical and General*, vol. 39, no. 19, pp. 5629–5651, 2006.

[109] H. Wu, W. Zhou, and T. Yildirim, "High-capacity methane storage in metal-organic frameworks m(2)(dhtp): The important role of open metal sites," *Journal of the American Chemical Society*, vol. 131, no. 13, pp. 4995–5000, 2009.

[110] S. Q. Ma, D. F. Sun, J. M. Simmons, C. D. Collier, D. Q. Yuan, and H. C. Zhou, "Metal-organic framework from an anthracene derivative containing nanoscopic cages exhibiting high methane uptake," *Journal of the American Chemical Society*, vol. 130, no. 3, pp. 1012–1016, 2008.

[111] A. U. Czaja, N. Trukhan, and U. Muller, "Industrial applications of metal-organic frameworks," *Chemical Society Reviews*, vol. 38, no. 5, pp. 1284–1293, 2009. ISI Document Delivery No.: 453GD Times Cited: 121 Cited Reference Count: 87 Czaja, Alexander U. Trukhan, Natalia Mueller, Ulrich Royal soc chemistry Cambridge.

[112] W. Zhou, H. Wu, M. R. Hartman, and T. Yildirim, "Hydrogen and methane adsorption in metal-organic frameworks: A high-pressure volumetric study," *Journal of Physical Chemistry C*, vol. 111, no. 44, pp. 16131–16137, 2007.

[113] W. Zhou, H. Wu, and T. Yildirim, "Structural stability and elastic properties of prototypical covalent organic frameworks," *Chemical Physics Letters*, vol. 499, no. 1-3, pp. 103–107, 2010.

[114] H. Li, M. Eddaoudi, M. O'Keeffe, and O. M. Yaghi, "Design and synthesis of an exceptionally stable and highly porous metal-orgboysanic framework," *Nature*, vol. 402, no. 6759, pp. 276–279, 1999.

[115] T. Yildirim and M. R. Hartman, “Direct observation of hydrogen adsorption sites and nanocage formation in metal-organic frameworks,” *Physical Review Letters*, vol. 95, no. 21, 2005.

[116] S. Q. Ma, X. S. Wang, C. D. Collier, E. S. Manis, and H. C. Zhou, “Ultramicroporous metal-organic framework based on 9,10-anthracenedicarboxylate for selective gas adsorption,” *Inorganic Chemistry*, vol. 46, no. 21, pp. 8499–8501, 2007.

[117] USDOE *Office of Energy Efficiency and Renewable Energy, The FreedomCAR and Fuel Partnership Targets for Onboard Hydrogen Storage, https://www1.eere.energy.gov/targets onboard hydro storage explanation.pdf*, no. November 2010, 2009.

[118] USDOE, USCAR, Shell, BP, ConocoPhillips, Chevron, and ExxonMobil *The FreedomCAR http://www1.eere.energy.gov/hydrogenandfuelcells/mypp/pdfs/storage.pdf*, 2009.

[119] S. S. Han, J. L. Mendoza-Cortes, and W. A. Goddard, “Recent advances on simulation and theory of hydrogen storage in metal-organic frameworks and covalent organic frameworks,” *Chemical Society Reviews*, vol. 38, no. 5, pp. 1460–1476, 2009.

[120] S. S. Han and W. A. Goddard, “Lithium-doped metal-organic frameworks for reversible h-2 storage at ambient temperature,” *Journal of the American Chemical Society*, vol. 129, no. 27, pp. 8422–8423, 2007.

[121] S. S. Han and W. A. Goddard, “High h-2 storage of hexagonal metal-organic frameworks from first-principles-based grand canonical monte carlo simulations,” *Journal of Physical Chemistry C*, vol. 112, no. 35, pp. 13431–13436, 2008.

[122] Y. Zhao and D. G. Truhlar, “Density functionals with broad applicability in chemistry,” *Accounts of Chemical Research*, vol. 41, no. 2, pp. 157–167, 2008.

[123] J. R. Hart and A. K. Rappe, “Vanderwaals functional forms for molecular simulations,” *Journal of Chemical Physics*, vol. 97, no. 2, pp. 1109–1115, 1992.

[124] J. M. Hayes, J. C. Greer, and D. A. Morton-Blake, “A force-field description of short-range repulsions for high density alkane molecular dynamics, simulations,” *Journal of Computational Chemistry*, vol. 25, no. 16, pp. 1953–1966, 2004.

[125] S. S. Han, S. H. Choi, and W. A. Goddard, “Improved h-2 storage in zeolitic imidazolate frameworks using lit, na+, and k+ dopants, with an emphasis on delivery h-2 uptake,” *Journal of Physical Chemistry C*, vol. 115, no. 8, pp. 3507–3512, 2011.

[126] M. Tacke, “Direct synthesis of organometallics .4. the mechanism of the activation of aromatic hydrocarbons with lithium atoms: Spectroscopic results and their ab initio interpretation,” *Chemische Berichte*, vol. 129, no. 11, pp. 1369–1371, 1996.

[127] M. Tacke, “Carbonyl and benzene complexes of lithium: Transition-metal-like behaviour of lithium in organolithium compounds,” *European Journal of Inorganic Chemistry*, no. 5, pp. 537–541, 1998.

[128] S. Krieck, H. Gorls, and M. Westerhausen, “Alkali metal-stabilized 1,3,5-triphenylbenzene monoanions synthesis and characterization of the lithium, sodium, and potassium complexes,” *Organometallics*, vol. 29, no. 24, pp. 6790–6800, 2010.

[129] S. F. Boys and F. Bernardi, “Calculation of small molecular interactions by differences of separate total energies - some procedures with reduced errors,” *Molecular Physics*, vol. 19, no. 4, pp. 553–566, 1970.

[130] *Excess Uptake. In sorption experiments the excess amount is obtained but the absolute amount can only be estimated. The absolute adsorbed amount can be estimated from experimental data by using* $N_{\text{total}} = N_{\text{excess}} + V_P \times Density(\text{bulk})$ *where* N_{excess} *is the excess mass* V_P *is the pore volume* N_{total} *is total adsorbed amount of molecular hydrogen.* $Density(\text{bulk})$ *is the bulk density of molecular hydrogen. However from our GCMC calculations we obtain* N_{total} *directly.*

[131] A. Blomqvist, C. M. Araujo, P. Srepusharawoot, and R. Ahuja, “Li-decorated metal-organic framework 5: A route to achieving a suitable hydrogen storage medium,” *Proceedings of the National Academy of Sciences of the United States of America*, vol. 104, no. 51, pp. 20173–20176, 2007.

[132] D. P. Cao, J. H. Lan, W. C. Wang, and B. Smit, “Lithium-doped 3d covalent organic frameworks: High-capacity hydrogen storage materials,” *Angewandte Chemie-International Edition*, vol. 48, no. 26, pp. 4730–4733, 2009.

[133] Y. Zhao, N. E. Schultz, and D. G. Truhlar, “Design of density functionals by combining the method of constraint satisfaction with parametrization for thermochemistry, thermochemical kinetics, and noncovalent interactions,” *Journal of Chemical Theory and Computation*, vol. 2, no. 2, pp. 364–382, 2006.

[134] S. Satyapal, J. Petrovic, C. Read, G. Thomas, and G. Ordaz, “The us department of energy’s national hydrogen storage project: Progress towards meeting hydrogen-powered vehicle requirements,” *Catalysis Today*, vol. 120, no. 3-4, pp. 246–256, 2007.

[135] J. L. Mendoza-Cortes, S. S. Han, and W. A. Goddard, “High h-2 uptake in li-, na-, k-metalated covalent organic frameworks and metal organic frameworks at 298 k,” *Journal of Physical Chemistry A*, vol. 116, no. 6, pp. 1621–1631, 2012.

[136] M. Yoon, S. Y. Yang, C. Hicke, E. Wang, D. Geohegan, and Z. Y. Zhang, “Calcium as the superior coating metal in functionalization of carbon fullerenes for high-capacity hydrogen storage,” *Physical Review Letters*, vol. 100, no. 20, 2008.

[137] Y. Y. Sun, K. Lee, Y. H. Kim, and S. B. Zhang, “Ab initio design of ca-decorated organic frameworks for high capacity molecular hydrogen storage with enhanced binding,” *Applied Physics Letters*, vol. 95, no. 3, pp. 33109–4, 2009.

[138] C. J. Doonan, W. Morris, H. Furukawa, and O. M. Yaghi, “Isoreticular metalation of metal-organic frameworks,” *Journal of the American Chemical Society*, vol. 131, no. 27, pp. 9492–9493, 2009.

[139] E. D. Bloch, D. Britt, C. Lee, C. J. Doonan, F. J. Uribe-Romo, H. Furukawa, J. R. Long, and O. M. Yaghi, “Metal insertion in a microporous metal-organic framework lined with 2,2 ’-bipyridine,” *Journal of the American Chemical Society*, vol. 132, no. 41, pp. 14382–14384, 2010.

[140] R. C. Lochan and M. Head-Gordon, “Computational studies of molecular hydrogen binding affinities: The role of dispersion forces, electrostatics, and orbital interactions,” *Physical Chemistry Chemical Physics*, vol. 8, no. 12, pp. 1357–1370, 2006.

[141] T. A. Pascal, C. Boxe, and W. A. Goddard, “An inexpensive, widely available material for 4 wt % reversible hydrogen storage near room temperature,” *Journal of Physical Chemistry Letters*, vol. 2, no. 12, pp. 1417–1420, 2011.

[142] A. A. Gonzalez, K. Zhang, S. P. Nolan, R. L. Delavega, S. L. Mukerjee, C. D. Hoff, and G. J. Kubas, “Thermodynamic and kinetic-studies of the complexes w(co)3(pcy3)2(h2) w(co)3(pcy3)2(n2), w(co)3(pcy3)2(ncch3), w(co)3(pcy3)2(pyridine), w(co)3(pcy3)2(p(ome)3), w(co)3(pcy3)2(co),” *Organometallics*, vol. 7, no. 12, pp. 2429–2435, 1988.

[143] J. Y. Shen, C. M. Haar, E. D. Stevens, and S. P. Nolan, “Synthetic and thermochemical studies of reactions of the 16-electron ruthenium complex (ph2pnmenmepph2)(2)rucl bf4 with h-2, ch3cn and co,” *Journal of Organometallic Chemistry*, vol. 571, no. 2, pp. 205–213, 1998.

[144] D. M. Heinekey, M. H. Voges, and D. M. Barnhart, “Rhenium dihydrogen complexes with isonitrile coligands: Novel displacement of chloride by hydrogen,” *Journal of the American Chemical Society*, vol. 118, no. 44, pp. 10792–10802, 1996.

[145] W. Zhou and T. Yildirim, “Nature and tunability of enhanced hydrogen binding in metal-organic frameworks with exposed transition metal sites,” *Journal of Physical Chemistry C*, vol. 112, no. 22, pp. 8132–8135, 2008.

[146] V. Labet, R. Hoffmann, and N. W. Ashcroft, “A fresh look at dense hydrogen under pressure. iii. two competing effects and the resulting intra-molecular h-h separation in solid hydrogen under pressure,” *Journal of Chemical Physics*, vol. 136, no. 7, pp. 074503–10, 2012.

[147] K. R. Matranga, A. L. Myers, and E. D. Glandt, “Storage of natural-gas by adsorption on activated carbon,” *Chemical Engineering Science*, vol. 47, no. 7, pp. 1569–1579, 1992.

[148] J. Purewal, *Hydrogen Adsorption by Alkali Metal Graphite Intercalation Compounds*. Dissertation (ph.d.), 2010.

[149] F. J. Uribe-Romo, J. R. Hunt, H. Furukawa, C. Klock, M. O’Keeffe, and O. M. Yaghi, “A crystalline imine-linked 3-d porous covalent organic framework,” *Journal of the American Chemical Society*, vol. 131, no. 13, pp. 4570–4571, 2009.

[150] F. J. Uribe-Romo, C. J. Doonan, H. Furukawa, K. Oisaki, and O. M. Yaghi, “Crystalline covalent organic frameworks with hydrazone linkages,” *Journal of the American Chemical Society*, vol. 133, no. 30, pp. 11478–11481, 2011.

[151] P. Kuhn, M. Antonietti, and A. Thomas, “Porous, covalent triazine-based frameworks prepared by ionothermal synthesis,” *Angewandte Chemie-International Edition*, vol. 47, no. 18, pp. 3450–3453, 2008.

[152] H. P. Wu, C. Janiak, G. Rheinwald, and H. Land, “5,5-dicyano-2,2 ’-bipyridine silver complexes: discrete units or co-ordination polymers through a chelating and/or bridging metal-ligand interaction,” *Journal of the Chemical Society-Dalton Transactions*, no. 2, pp. 183–190, 1999.

[153] M. Ghosh, P. Biswas, U. Florke, and K. Nag, “Halogen exchange and scrambling between c-x and m-x ’ bonds in copper, nickel, and cobalt complexes of 6,6 ’-bis(bromo/chloromethyl)-2,2 ’-bipyridine. structural, electrochemical, and photochemical studies,” *Inorganic Chemistry*, vol. 47, no. 1, pp. 281–296, 2008.

[154] R. S. Osborn and D. Rogers, “Crystal-structure of red form of 2,2’-bipyridyl dichloroplatinum(ii),” *Journal of the Chemical Society-Dalton Transactions*, no. 9, pp. 1002–1004, 1974.

[155] M. Maekawa, M. Munakata, S. Kitagawa, and M. Nakamura, “Crystal-structure of (2,2’-bipyridine)dichloropalladium(ii),” *Analytical Sciences*, vol. 7, no. 3, pp. 521–522, 1991.

[156] G. Demunno, M. Julve, F. Lloret, and A. Derory, “2,2’-bipyrimidine (bipym)-bridged dinuclear complexes .1. preparation, crystal-structure, and magnetic-properties of ni2(h2o)8(bipym) no3 4 and ni2(h2o)8(bipym) so4 2.2h2o,” *Journal of the Chemical Society-Dalton Transactions*, no. 8, pp. 1179–1184, 1993.

[157] G. Yucesan, J. E. Valeich, H. X. Liu, W. Ouellette, C. J. O'Connor, and J. Zubieta, "Solid state coordination chemistry of the oxovanadium-diphosphonate/copper-bipyrimidine system," *Inorganica Chimica Acta*, vol. 362, no. 6, pp. 1831–1839, 2009.

[158] W. B. Connick, R. E. Marsh, W. P. Schaefer, and H. B. Gray, "Linear-chain structures of platinum(ii) diimine complexes," *Inorganic Chemistry*, vol. 36, no. 5, pp. 913–922, 1997.

[159] C. M. Fitchett and P. J. Steel, "Synthesis and x-ray crystal structures of metal complexes of three isomeric bibenzodiazines: Discrete and polymeric assemblies," *Polyhedron*, vol. 27, no. 5, pp. 1527–1537, 2008.

[160] J. J. Klicic, R. A. Friesner, S. Y. Liu, and W. C. Guida, "Accurate prediction of acidity constants in aqueous solution via density functional theory and self- consistent reaction field methods," *Journal of Physical Chemistry A*, vol. 106, no. 7, pp. 1327–1335, 2002.

[161] T. L. Hill, "Statistical mechanics of multimolecular adsorption .1," *Journal of Chemical Physics*, vol. 14, no. 4, pp. 263–267, 1946.

[162] T. Keii, "Rates of formation of different deuteroethylenes and deuteroethanes in the reaction of ethylene and deuterium," *Journal of Chemical Physics*, vol. 22, no. 1, pp. 144–145, 1954.

[163] M. W. Chase, "Nist-janaf themochemical tables," *Journal of Physical and Chemical Reference Data*, vol. 27, no. 6, pp. I–II, 1998.